NORTHWESTERN UNIVERSITY

Synthesis and Optimization of Cell-Permeable Contrast Agents for Magnetic Resonance Imaging

A DISSERTATION

SUBMITTED TO THE GRADUATE SCHOOL

IN PARTIAL FULFILLMENT OF THE REQUIREMENTS

for the degree

DOCTOR OF PHILOSOPHY

Field of Chemistry

By

Paul Joseph Endres

EVANSTON, ILLINOIS

June 2008

ABSTRACT

Synthesis and Optimization of Cell-Permeable Contrast Agents for Magnetic Resonance Imaging

Paul J. Endres

Magnetic resonance imaging (MRI) is a technique widely used in both clinical and experimental settings to produce high-resolution images of opaque living organisms without utilizing ionizing radiation. Currently, MR imaging is augmented by contrast agents; however, these small molecule Gd(III) chelates are confined to extracellular and vascular regions of the specimen, reducing their ability to provide information about cell physiology or molecular pathology. However, as compared to other imaging modalities, MRI has a relatively low sensitivity to exogenous contrast agents. As a result, the system has an inherent difficulty exploiting any newly developed contrast agent, especially if the probe shows specificity and selective image contrast enhancement on a molecular level.

This thesis describes the synthesis, visualization, and optimization of several MR contrast agents prepared on varying scaffolds that display cell membrane permeability or elicit enhanced image contrast over current clinical imaging probes. Section 1 (Chapters 2 and 3) describes the synthesis, cell culture, and optimization of six contrast agents that possess the capability to cross cell membranes in sufficient quantity for detection via MR imaging. Four agents are based on the conjugation of a Gd(III) chelator with an 8-amino acid polyarginine oligomer or an amphipathic stilbene molecule, 4-amino-4'-(*N*,*N*-dimethylamino) stilbene. However, transport of these contrast agents was determined to be bidirectional, allowing them to efflux rapidly from cultured

cells. Therefore, a disulfide linkage was incorporated between the transduction moiety (polyarginine 8-mer) and the Gd(III) chelate (either DOTA or DTPA) to create thiol sensitive derivatives of the cell-permeable contrast agents. These second generation imaging agents successfully displayed prolonged cellular retention via synchrotron radiation X-ray fluorescence (SR-XRF) and MR imaging. Section 2 (Chapters 4 and 5) describes the synthesis of MR contrast agents with elevated relaxivities and versatile scaffolds for potential conjugation of cell-penetrating moieties. These novel contrast agents hold particular promise for the development of multifunctional imaging probes by exploiting metal-based nanoparticles (TiO_2) and ring-opening metathesis polymerization (ROMP). Each scaffold allows for attachment of multiple Gd(III) imaging agents via increased surface area (TiO_2 nanoparticles) or polymerizable functionalities (ROMP-accessibility) while maintaining additional synthetic handles for fluorophore or cell-penetrating moiety conjugation.

ACKNOWLEDGEMENTS

It is not everyday that you get to thank someone for making the last five years of your life a success, but here is my humble attempt. Since the spring of 2003 when he captivated me and probably a hundred other perspectives with his nimble humor and Quicktime movies, Tom Meade has been my advisor, mentor, and friend. Without his constant scientific and financial support, it would have been impossible to complete this tremendous undertaking. I simply cannot imagine a more constructive, collaborative, and ultimately rewarding environment. I have learned how to become a thorough scientist, a patient and understanding mentor, and a concise 20/10 writer under his tutelage. Please accept my most grateful thanks.

I also thank the rest of my committee members; Professors Karl Scheidt, Amy Rosenzweig, and Thomas O'Halloran. It has been a pleasure to have such dedicated and renowned scientists guiding me through my graduate career.

More thanks must go to the current members of the Meade group. In their own ways, they have each guided, taught, and helped me achieve so much over the years. I owe a tremendous debt to those who helped get me acquainted and started in lab, namely, Matthew Allen, Brad Ulrich, Joe Duimstra, Frank Femia, Jody Major, Kylie Barker, Amanda Eckermann, Paul Lee, Elise Schultz-Sikma, and Peijiao Wang. Matt, it's obvious that you left me more than just your hood— your advice has been a tremendous help, and your friendship has never been dull. Brad, your help with solid phase synthesis will never be forgotten, neither will your death metal music that shattered many a calm Friday morning. Joe, there is a special place in my heart for our labor intensive HPLC afternoons. Frank, well, Delilah's and the diner just haven't been the same since you left.

As part of a multidisciplinary group, I have worked closely with some biologists, chemists, and physicists. In particular, Keith MacRenaris has made all the cell work presented here possible. He has been an invaluable resource, a great friend, and a terrific roommate. I must also thank Luca Frullano for his ^{17}O-NMR expertise, Stefan Vogt for his undying devotion to all things mathematical and synchrotron-based, Ellen Kohlmeir for her many MRI troubleshooting sessions, and Lauren Urbanczyk-Pearson for her help concerning my lack of immaculate grammatical prose. However, individuals are nothing without the group, so I must thank Ying Song, Dave Ballweg, Dan Mastrone, Dan Feld, Emily Testa, Allison Harney, Renee Cilliers, Preeti Sukaker, Paul Sillitti, and my undergrad, Sarah Moum, for always making the lab a productive and exciting place.

Collaborations are a large part of a graduate career in science, and I have been able to contribute to some of the best Northwestern has to offer. First, I must thank Gayle Woloshak and Tanja Paunesku for all the time and effort they put in the TiO_2 project, and second, DeeDee Smith and SonBinh Nguyen for enduring what has been a bumpy yet rewarding road on the ROMP contrast agent project.

Now that all of my mentors and colleagues have been introduced, I must thank those of you who proofread my thesis chapters. As with any large piece of scientific writing, there is always a better, more concise way of stating your observations, therefore, these individuals have earned a paragraph all to their own: Brad, Matt, Amanda, Stefan, Ellen, Keith, Elise, DeeDee, Kylie, and Owen Priest.

My labmates and collaborators are not the only people I have met while in Chicago. I definitely have enjoyed my afternoon lifting sessions with Dave Frattarelli, the lunches at Rollin' to Go with Emma Kate Payne, and my first Chicago roommate, Chris Oliveri. I also thank my

Chicago MPC friends, Mike Huang, Kevin Vakil, Shaun Tang, and honorary members, Chris Ferguson, Keith Berman and Eddie Hong. They have kept my struggling social life alive these past few years (and probably my sanity as well).

Now, with a most sincere heart, I thank my family. My mother and father have not only supported me financially, but emotionally on this journey. I thank my father for never giving up on me, even when I made decisions that he thought were a little risky, maybe even down right ridiculous. I thank my mother for her valuable advice and unconditional support that always came with a loving smile. I thank my sister for the kind thoughts and birthday package pick-me-ups, and Tori Green for her friendship and support. This would not be possible without each one of you, and I hope that I have made you proud.

LIST OF ABBREVIATIONS

Abbrevation	Full Name
AD	Alzheimer's disease
AETP	*s*-(2-aminoethylthio)-2-thiopyridine hydrochloride
Arg	arginine
ATCC	American Type Culture Collection
BAPTA	1,2-*bis*(o-aminophenoxy)ethane-*N*,*N*,*N*',*N*'-tetraacetic acid
bm	broad multiplet
br	broad
bs	broad singlet
CAT	computer-assisted tomography
CBS	calf bovine serum
CEST	chemical exchange saturation transfer
CLIO	cross linked iron oxide
CPP	cell penetrating peptide
CT	computer tomography
d	doublet
DCM	dichloromethane
DIEA	*N*,*N*-diisopropylethylamine
DMEM	Dulbecco's modified Eagle's medium
DMF	*N*,*N*-dimethylformamide
DMSO	dimethylsulfoxide
DNA	deoxyribonucleic acid
DO3A	*N,N',N''*-tricarboxymethylene cyclen
DOPA-DO3A	Gd(III)-4,7-bis-carboxymethyl-10-{[2-(3,4-dihydroxy-phenyl)-ethylcarbamoyl]-methyl}-1,4,7,10-tetraazacyclododecyl-acetic acid
DOTA	1,4,7,10-tetraazacyclododecane-1,4,7,10 tetraacetic acid
DOTA-mono-NHS	1,4,7,10-tetraazacyclododecane-1,4,7,10-tetraacetic acid mono(*N*-hydroxysuccinimide ester)
DOTA-tris-TB	1,4,7-tris(acetic acid-*tert*-butyl ester)-10-acetic acid-1,4,7,10-tetraazacyclododecane
DP	degree of polymerization

Abbrevation	Full Name
DPBS	Dulbecco's phosphate buffered saline
DRIFT	diffuse reflectance infrared Fourier transform
DTPA	diethylenetriaminepentaacetic acid
DTPA-BMA	diethylenetriamine pentaacetic acid-bismethylamide
DTT	dithiothreitol
EA	elemental analysis
ECM	extracellular matrix
EDT	1,2-ethanedithiol
EDTA	ethylenediaminetetraacetic acid
EMEM	Eagle's minimum essential medium
ENDOR	electron-nuclear double resonance
ESI	electrospray ionization
EtOAc	ethyl acetate
EtOH	ethyl alcohol
FBS	fetal bovine serum
Fmoc	fluorenyl-methoxy-carbonyl
FOV	field of view
FT	Fourier transform
GPC	gel-permeation chromatography
GRID	gadolinium rhodamine dextran
GSH	glutathione
HATU	*N,N,N′,N′*-tetramethyl-*O*-(7-azabenzotriazol-1-yl)uronium hexafluorophosphate
Hex	hexane
HIV-1 TAT	human immunodeficiency virus transactivator
HOPO	hydroxypyridinone
HP-DO3A	1,4,7-tris(carboxymethy1)-10-(2-hydroxypropyl)-1,4,7,10-tetraazacyclododecane
HPLC	high performance liquid chromatography
HR	high resolution
HSA	human serum albumin

Abbrevation	Full Name
ICP	inductively coupled plasma
IR	infrared
LC	liquid chromatography
LIPOCEST	liposome CEST
LRET	lanthanide resonance energy transfer
m	multiplet
mAbs	monoclonal antibodies
MALDI-TOF	matrix assisted laser desorption ionization time of flight
MDCK	canine kidney epithelial cells
MeCN	acetonitrile
MeOH	methyl alcohol
MION	magnetic iron oxide nanoparticle
MOPS	4-morpholinepropanesulfonic acid
MR	magnetic resonance
MRI	magnetic resonance imaging
MS	mass spectrometry
MTBE	methyl *tert*-butyl ether
MTT	4-methyl trityl
MWC	molecular weight cutoff
NADH	nicotinamide adenine dinucleotide (reduced form)
NGR	asparagine-glycine-arginine
NIH/3T3	mouse fibroblast cells
NMR	nuclear magnetic resonance
NO	nitric oxide
NP	nanoparticle
PARACEST	paramagnetic chemical exchange saturation transfer
Pbf	pentamethyldihydrobenzofuran-5-sulfonyl
p-Bn-NH_2-DOTA	2-*p*-aminobenzyl-1,4,7,10-tetraazacyclododecane-1,4,7,10-tretraacetic acid
p-Bn-NH_2-DTPA	2-*p*-aminobenzyldiethylenetriaminepentaacetic acid
PBS	phosphate buffered saline

Abbrevation	Full Name
PC12	rat pheochromocytoma cells
PC3M	human prostate cancer cells (metastatic)
PDA	photo-diode array
PDI	polydispersity index
PEG	polyethylene glycol
PET	positron emission tomography
PTD	protein transduction domain
RAW 264.7	mouse macrophage cells
RF	radiofrequency
RMS	root mean squared
RNA	ribonucleic acid
ROMP	ring-opening metathesis polymerization
RP	reverse-phase
s	singlet
SCF	self-consistent field
SPECT	single positron emission computerized tomography
SPIO	superparamagnetic iron oxide
SR-XRF	synchrotron radiation X-ray fluorescence
TEA	triethylamine
TFA	trifluoroacetic acid
THF	tetrahydrofuran
TIC	total ion count
TIS	triisopropylsilane
TLC	thin-layer chromatography
TMS	trimethylsilyl
Trt	trityl
UV	ultraviolet

Symbol	Description
$\boldsymbol{B}_0$	static magnetic field vector
$\boldsymbol{B}_1$	radio frequency (RF) generated field
c	molal concentration
ΔE_{T1e}	activation energy of T_{1e}
$\Delta H^{\ddagger}$	activation enthalpy
g	electron g-factor
h	hour
h	Plank's constant
I, $\boldsymbol{I}$	spin quantum number of an element
k	rate
k_B	Boltzmann constant
k_{D2O}	the rate of luminescence decay in a solution of D_2O
K_f	formation constant
k_{H2O}	the rate of luminescence decay in a solution of H_2O
M	molar
M, $\boldsymbol{M}$	net magnetization vector
m/z	mass to charge ratio
μ_B	the Bohr magneton
MHz	megahertz
min	minute
mL	milliliter
mM	millimolar
μM	micromolar
mmol	millimole
mol	mole
N_0	total number of spins
nm	nanometer
ns	nanosecond
P	octanol-water partition coefficient
q	number of coordinated water molecules

Symbol	Description
r	distance
r_1	longitudinal relaxivity
s	second
S	the spin of the ion
t	triplet
T	Tesla
T_1	longitudinal nuclear relaxation time
T_{1e}	the longitudinal electron spin relaxation time of the metal ion
T_2	transverse nuclear relaxation time
T_{2e}	the transverse electron spin relaxation time of the metal ion
τ_c	total correlation time
T_E	echo delay time
τ_m	water residency lifetime
τ_R	rotational correlation time
T_R	recycle time
ω_I	the nuclear Larmor frequency
ω_L	the Larmor frequency
ω_S	the electron Larmor frequency
η	refractive index
λ_{em}	emission wavelength
λ_{ex}	excitation wavelength

I dedicate this work to my family.

Without you, this would never have been possible.

TABLE OF CONTENTS

LIST OF FIGURES

LIST OF SCHEMES

LIST OF TABLES

CHAPTER 1: Introduction

Introduction

This chapter will focus on the topics and principles needed to understand magnetic resonance imaging (MRI) and its applications. After a discussion of the basic magnetic properties governing this imaging technique, focus will be shifted to a review of synthetically prepared complexes, termed contrast agents, that have been shown to enhance image contrast-noise ratios. This section will then address the mechanisms that allow these complexes to advance MR imaging.

MRI and Associated Principles

MR imaging is a technique used in clinical and experimental settings to produce high quality images of opaque living organisms without the need for harmful ionizing radiation. Its non-invasive images are not limited by tissue depth, as those from light-based microcopy are, nor do they require radioactive drugs or X-ray sources as in standard X-ray, CAT scans, or heavy atom angiography. Instead, MR derives its images from the local concentrations and relaxation rates of water protons within an applied magnetic field and takes advantage of the quantum mechanical property of nuclear spin. However, it is sometimes easier to visualize this process in the classical sense of angular momentum vectors.[1] Essentially, the nuclear spins of elements with odd mass numbers (e.g. ^{1}H, ^{13}C, ^{17}O, ^{23}Na, and ^{31}P) can be combined to yield a vector that has a magnitude, ***I***, defined in **Equation 1.1**.

$$|\boldsymbol{I}| = \hbar \sqrt{I\ (\ I+1\ )} \quad , \quad \hbar = h/2\pi \qquad \textbf{Equation 1.1}$$

where h is Plank's constant and I is the spin quantum number. If placed in an external magnetic field ($\boldsymbol{B}_0$), nuclei with angular momentum vectors (***I***) will align themselves in one of two directions, against the magnetic field vector (down) or with the magnetic field vector (up). They

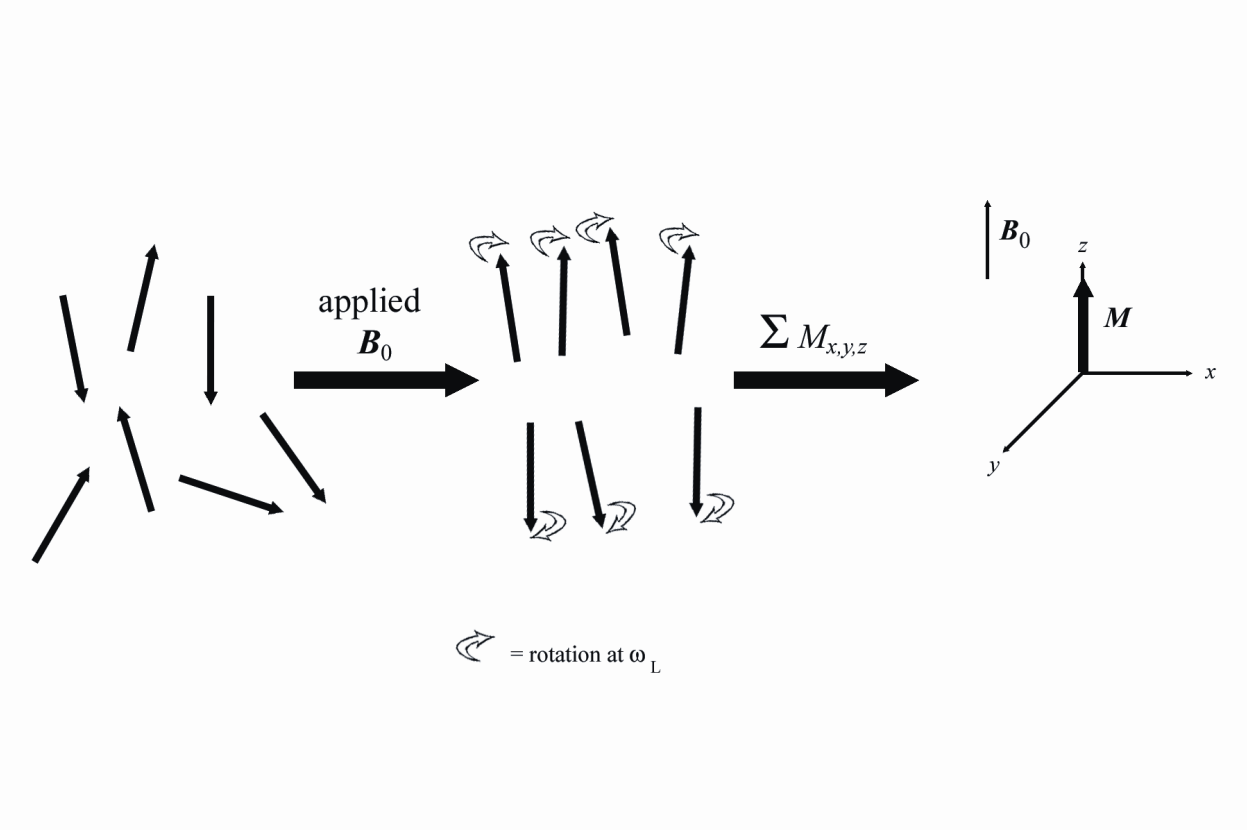

Figure 1.1 A representation of hydrogen nuclei (vector arrows) before and after placement in an external magnetic field, $\boldsymbol{B}_0$. Throughout the alignment, the nuclei are constantly spinning at the Larmor frequency, ω_L. Due to **Equations 1.2** and **1.4**, slightly more nuclei orient themselves in the 'up' or lower energy state, allowing the formation of a net magnetization vector, $\boldsymbol{M}$.

will populate these two allowed states according to a Boltzmann distribution (**Equation 1.2**) where k_B is the Boltzmann constant. Individually these vectors are the basis of MRI, but it is their summation that allows facile understanding of MRI physics (**Figure 1.1**).

$$\frac{N_{up}}{N_{down}} = \exp\left(\frac{\gamma\hbar \boldsymbol{B}_0}{k_B\ T}\right) \qquad \textbf{Equation 1.2}$$

$$\boldsymbol{M} = \sum \gamma I \qquad \textbf{Equation 1.3}$$

$$\boldsymbol{M} = M_x + M_y + M_z \qquad \textbf{Equation 1.4}$$

Shown in **Equation 1.3**, $\boldsymbol{M}$ is the vector sum of all the individual protons' magnetic moments where γ is the gyromagnetic ratio characteristic for each spinning angular momentum vector. In an unexcited or ground state sample, the distribution of individual spins comprising $\boldsymbol{M}$ will have collective components of M_x, M_y and M_z (**Equation 1.4**). Due to random phase incoherence of these individual spins, M_x and M_y will go to zero, however, restrictions placed on M_z will make its value non-zero. Therefore, as shown in **Figure 1.1**, when a nuclei such as hydrogen (I = ½) is placed within an external magnetic field ($\boldsymbol{B}_0$), it can effectively be depicted as a vector possessing a magnitude equal to **Equation 1.5** in only the M_z direction (where N_0 is the total number of spins).

$$\boldsymbol{M} = M_z = \frac{N_0\ \gamma^2\ \hbar^2\ I\ (I+1)}{3\ k_B\ T}\boldsymbol{B}_0 \qquad \textbf{Equation 1.5}$$

A variety of radio frequency (RF) pulses, which generate magnetic fields, can be applied to these conglomerate spins causing $\boldsymbol{M}$ to flip away from the z axis and take on x and y components. Deemed $\boldsymbol{B}_1$, this perpendicularly induced magnetic field (consequence of the RF

pulse) causes the spins to display a detectable rotating magnetization (M_{xy}). Upon completion of this RF pulse, the nuclear spins will return to their ground state energy by interacting with the surroundings in a process called relaxation. Broken down into two main processes, relaxation rates are the mathematical basis of the MR images we see. The first process, designated spin-lattice or T_1, is the mechanism responsible for describing the return of magnitude to M_z (immediately following the RF pulse). The second relaxation process, termed spin-spin or T_2, is responsible for describing the return to zero of M_{xy} (immediately following the RF pulse). Both of these processes are presented in detail in the following section.

Introduction to T_1 and T_2 Relaxivity

T_1 relaxation is affected by several processes. However, all of these processes are characterized by one underlying principle, the generation of magnetic noise which gives rise to fluctuating magnetic fields. These fluctuating fields allow the RF pulsed nuclei to release energy and return to their ground state. The time needed for M_z to return to the original magnitude recorded before the RF pulse is called T_1.

T_2 relaxation is brought about by a phenomenon known as spin dephasing. Immediately following the RF pulse, the individual spins compromising $\boldsymbol{M}$ will be coherent and rotating about $\boldsymbol{B}_0$. The fluctuating magnetic field caused by random particle motion and the bulk $\boldsymbol{B}_0$ inhomogeneities will result in loss of spin phase coherence and induce neighboring spin pairings, respectively. Neither contributes to overall system energy loss, but both diminish signal in the *xy* plane.

To create images from these measurable rates, MR imaging exploits magnetic time-varying, linear magnetic field gradients. These gradients create unique, infinitesimally small magnetic environments for each part of a sample placed within the magnetic field (the strength

of $\boldsymbol{B}_0$ and the gradient coil determine the number of unique fields). This system allows the MR hardware to encode positional data about the sample that can later be used to reconstruct an image. A computer can now use the relaxation rates (T_1 or T_2) along with calculated nuclei densities to determine pixel intensities via mathematical functions called continuous Fourier transforms (FTs). By concurrently mapping the data set against the 3D array of frequencies created by the field gradients, non-invasive, cross-sectional images of most biological samples can be acquired.[1]

T_1 Contrast Agent Parameters

Earlier in this chapter, inherent sample parameters and outcomes were discussed. However, like PET, SPECT, and CT, MR image contrast can be improved by the introduction of exogenous contrast agents. In the case of MRI, such compounds decrease the T_1 or T_2 relaxation times of neighboring nuclei, causing local increases or decreases of signal intensity. If a particular complex has a more pronounced effect on the T_1 or T_2 relaxation processes of hydrogen nuclei, it is deemed a T_1- or T_2-agent, respectively. This thesis deals exclusively with Gd(III)-based T_1 contrast agents, therefore, only T_1 processes and Gd(III)-based agents will be described from this point forward. Information regarding T_2 processes can be found in reference 1.

The general equations governing solvent relaxation rate in the presence of paramagnetic ions (e.g. gadolinium) were developed by Solomon and Bloembergen and are expressed in **Equation 1.6**.[2, 3] The observed longitudinal relaxation rate ($1/T_1$) is the sum of the diamagnetic ($1/T_{1,dia}$) and paramagnetic relaxation rates ($1/T_{1,para}$). However, this equation holds true for only very dilute solutions of paramagnets. A more applicable relationship for systems involving a contrast agent, **Equation 1.7**, takes into account the relaxation rate enhancement (r_1) and

concentration of gadolinium present. In the presence of Gd(III) complexes, the paramagnetically-induced relaxation of water protons is a direct result of dipole-dipole interactions between the nuclear spins of hydrogen and the fluctuating field of the unpaired Gd(III) electrons.

$$\left(\frac{1}{T_1}\right)_{obs} = \left(\frac{1}{T_1}\right)_{dia} + \left(\frac{1}{T_1}\right)_{para} \qquad \textbf{Equation 1.6}$$

$$\left(\frac{1}{T_1}\right)_{obs} = \left(\frac{1}{T_1}\right)_{dia} + r_1\ [\mathrm{Gd}] \qquad \textbf{Equation 1.7}$$

$$\left(\frac{1}{T_1}\right)_{para} = \left(\frac{1}{T_{1\,para}}\right)^{IS} + \left(\frac{1}{T_{1\,para}}\right)^{OS} \qquad \textbf{Equation 1.8}$$

$$\left(\frac{1}{T_1}\right)^{IS} = \frac{cq}{55.5}\left(\frac{1}{T_{1m} + \tau_m}\right) \qquad \textbf{Equation 1.9}$$

This interaction is strongly dependent on distance and thus can be described by two terms (**Equation 1.8**); the direct-contact inner sphere contribution $(1/T_1)^{IS}$ and the proximity-influenced outer sphere contribution $(1/T_1)^{OS}$. Due to our inability to control and influence outer sphere contributions, this discussion will focus on inner sphere relaxivity.[1] The inner sphere term can be expressed by **Equation 1.9**, where c is the molal concentration of Gd(III) ions, q is the number water molecules coordinated to the Gd(III) ion, τ_m is the mean residence lifetime of a water molecule in the inner sphere, and $(1/T_{1m})$ is the longitudinal proton relaxation rate of the bound water molecule. The longitudinal proton relaxation rate, $(1/T_{1m})$, is governed by the dipole-dipole (DD) and scalar (SC) mechanisms of relaxation as shown in **Equations 1.10** and **1.11**. However, the scalar mechanism contributes little to the overall relaxation rate at field

strengths above 10 MHz, so they can be ignored in the case of virtually all medical scanners.[1] Symbols found in **Equation 1.11** are defined as follows: g is the electron g-factor, μ_B is the Bohr magneton, r_{GdH} is the electron spin-proton distance, and ω_I and ω_S are the nuclear and electron Larmor frequencies, respectively. As shown in **Equation 1.11**, the dipolar term from **Equation 1.10** is dependent on several factors, one of which is the overall correlation time, τ_{c1}. The overall correlation time is governed by the rotational correlation time of τ_R, the longitudinal electron spin relaxation time, T_{1e}, and τ_m from **Equation 1.12**. Upon closer examination of **Equations 1.9 and 1.12**, the parameters q, r_{GdH}, τ_m, τ_R, and T_{1e} can be synthetically manipulated; hence, their optimization will lead to maximum relaxation rates (parameters depicted in **Figure 1.2**).[4]

$$\left(\frac{1}{T_{1\,m}}\right) = \left(\frac{1}{T_1}\right)^{DD} + \left(\frac{1}{T_1}\right)^{SC} \qquad \textbf{Equation 1.10}$$

$$\left(\frac{1}{T_1}\right)^{DD} = \frac{2}{15}\left(\frac{\gamma_I^2\ g^2\ \mu_B^2}{r_{GdH}^6}\right) S(S+1) \left(\frac{\mu_0}{4\ \pi}\right)^2 \left(7\frac{\tau_{c2}}{1+\omega_s^2\ \tau_{c2}^2} + 3\frac{\tau_{c1}}{1+\omega_I^2\ \tau_{c1}^2}\right) \qquad \textbf{Eqn 1.11}$$

$$\left(\frac{1}{\tau_{c1}}\right) = \left(\frac{1}{\tau_R}\right) + \left(\frac{1}{T_{1e}}\right) + \left(\frac{1}{\tau_m}\right) \qquad \textbf{Equation 1.12}$$

Each of these parameters has a physical meaning that is important in the design of contrast agents. Inner sphere relaxivity is directly proportional to the number of bound water molecules (q). Therefore, increasing q to its highest value would result in the highest relaxivity for any Gd(III) contrast agent (**Equation 1.9**). However, due to the toxic effects of the Gd(III) aqua ion in physiological environments, care must be taken so as not to allow the Gd(III) ion to dissociate from its chelator.[4] Generally this requires a minimum of seven to eight moieties

chelating the metal center, which allows for a maximum *q* value of 2.[5] Another parameter of interest is r_{GdH}. It can be seen from **Equation 1.11** that r_{GdH} has a $(1/r^6)$ dependence. Theoretically, this allows sub-angstrom decreases in Gd-H distances to drastically improve relaxivity. However, electron-nuclear double resonance (ENDOR) spectroscopy studies have shown that for several 8 and 9-coordinate Gd(III) complexes, this distance is quite stable and is therefore an unlikely source for increased relaxivity.[4, 6] With an optimal value of 10 ns, the mean residence lifetime of protons, τ_m, is a parameter which requires strict optimization to achieve maximum relaxivities.[4] If the τ_m is too short, protons of the bound water molecules cannot sufficiently be relaxed by the Gd(III) ion. If τ_m is too long, water exchange is not happening efficiently, and the relaxivity values will again suffer (**Figure 1.3**). Several factors influence the mean residence lifetime, and a detailed description of these can be found in literature reviews.[5, 7]

The rotational correlation time, τ_R, also possesses an optimal value. For most small molecule contrast agents at clinical field strengths, ($\leq$ 1.5 T) decreasing τ_R, slowing down the molecular tumbling rate, will increase relaxivity. Conversely, in higher field settings (typically > 1.5 T), τ_R exhibits an optimal value, and below that, relaxivity decreases with decreasing τ_R. Therefore, τ_R must be appropriately optimized for the desired imaging field strength (**Figure 1.3**).[5] Unlike the previous molecular parameters and correlation times, the longitudinal electronic relaxation time (T_{1e}) is a very complex and little understood parameter. Although studies have shown that T_{1e} is magnetic field dependent and, like τ_R, possesses a maximum value at a given field strength, much has yet to be learned about this attribute of Gd(III) contrast agents.[8, 9] Modulation of these parameters (excluding T_{1e}) and other advances in Gd(III) complexes as MRI contrast agents are presented within the proceeding sections of this chapter.

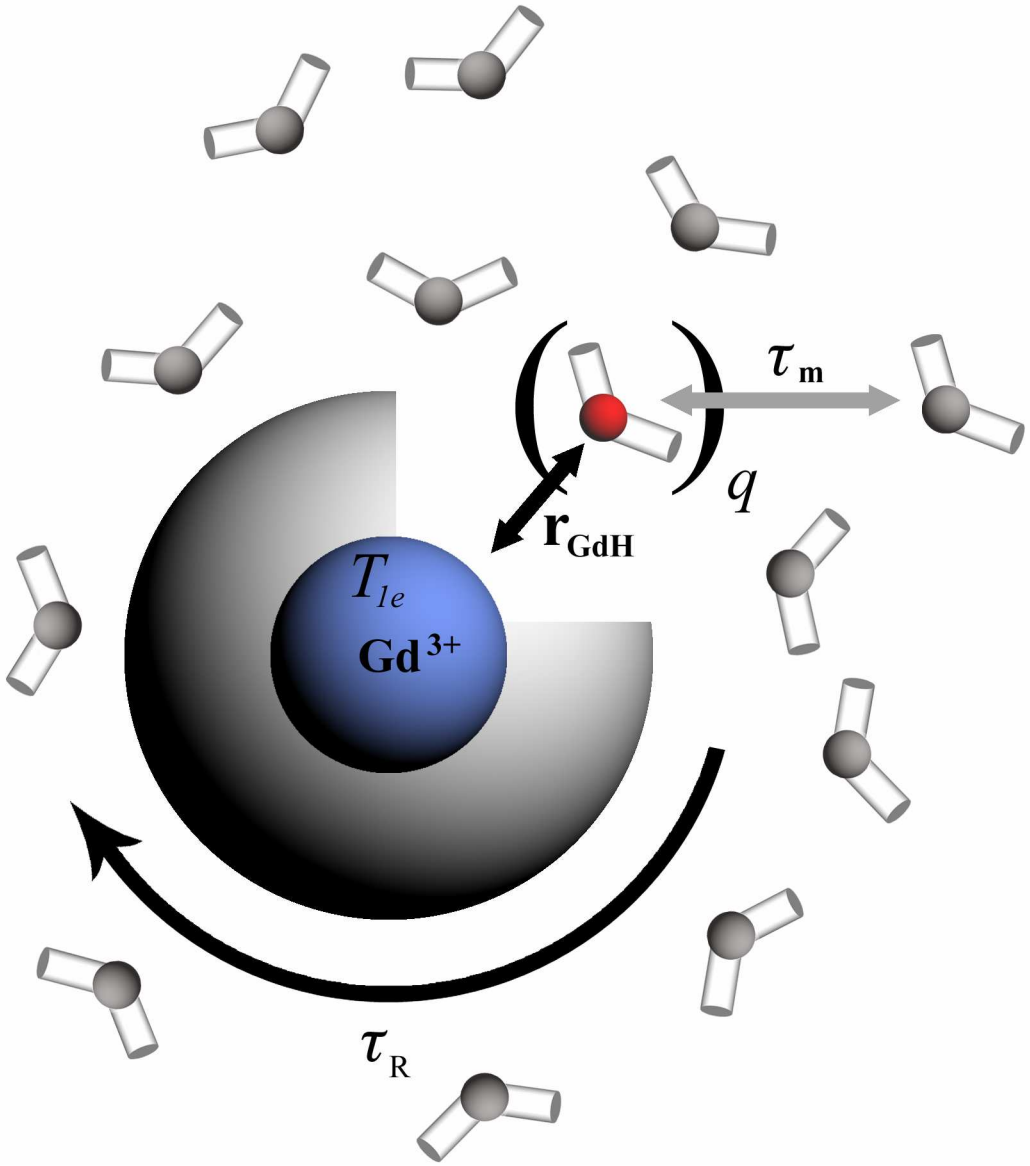

Figure 1.2 Parameters affecting the relaxivity of Gd(III)-based contrast agents.

q = number of bound water molecules

r_{GdH} = electron spin-proton distance

τ_m = mean residence lifetime of a water molecule in the inner sphere

τ_R = rotational correlation time

T_{1e} = longitudinal electronic relaxation time

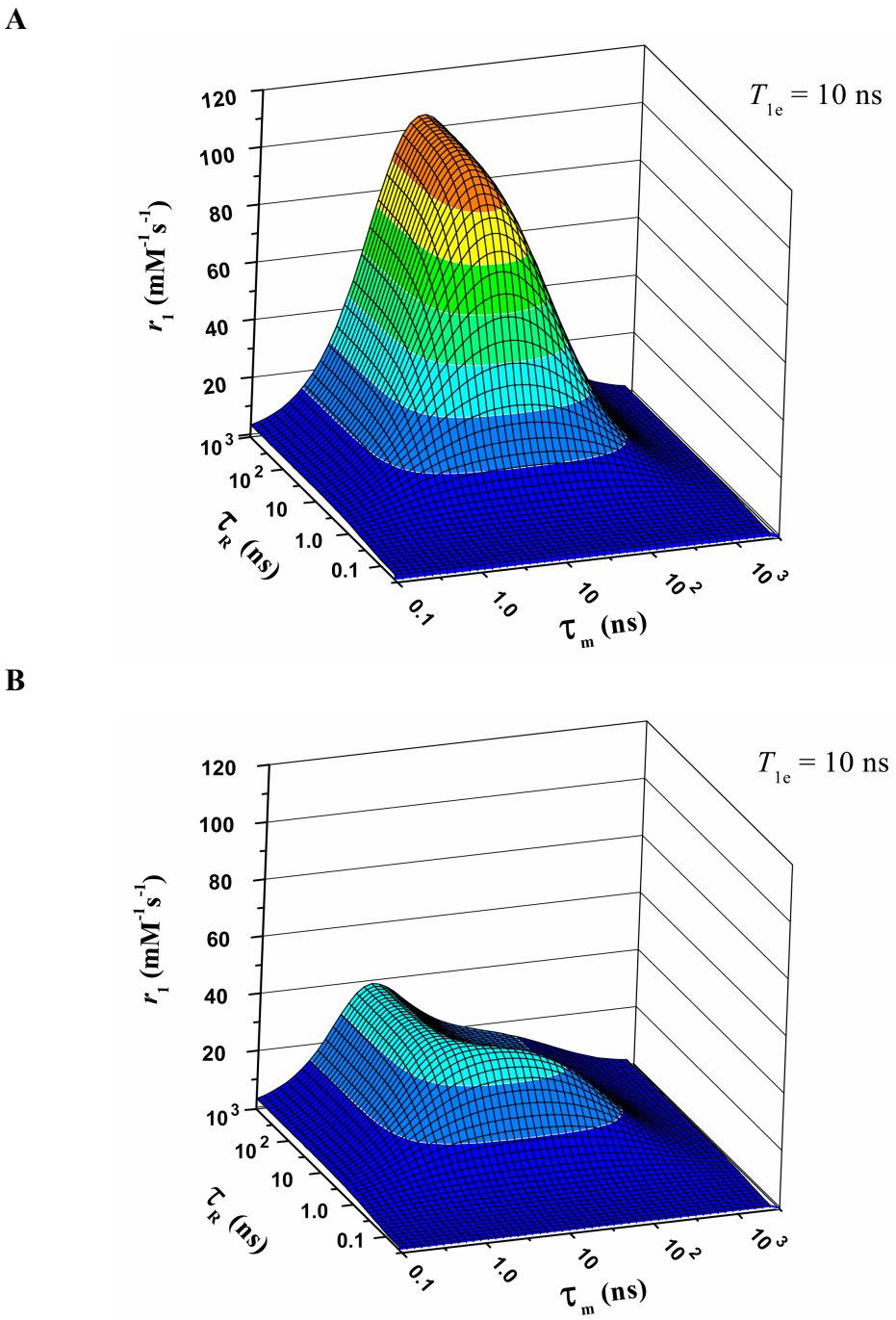

Figure 1.3 Inner sphere relaxivities calculated as a function of τ_m and τ_R with a static T_{1e} (10 ns) and q (1.0) at 20 and 60 MHz. (A) Calculations at 20 MHz (0.5 T). (B) Calculations at 60 MHz (1.5 T). Both simulations are reproduced with permission from reference 4.

Current Gd(III) MRI Contrast Agents

The evolution of improved pulse sequences, magnets, gradients, and contrast agents has made MR imaging one of the most popular imaging modalities of the clinical diagnostic community. Frequently, in clinical exams the inherent contrast between tissues is augmented by the use of paramagnetic, poly(amino-carboxylate) contrast agents such as Dotarem (Gd(III)-DOTA), ProHance (Gd(III)-HP-DO3A), Magnevist (Gd(III)-DTPA), and Omniscan (Gd(III)-DTPA-BMA), all of which consist of a Gd(III) metal ion and a small molecule chelator (**Figure 1.4**). Through the exploitation of the symmetrical electronic ground state and high magnetic moment created by the seven unpaired electrons of chelated Gd(III), current clinical agents accelerate the relaxation rate of water protons that interact with the metal ion. Although these small molecule gadolinium complexes display non-specific biodistributions and are confined to vascular regions of the body, their high formation constants (e.g. $K_f = 10^{25}$ for Gd(III)-DOTA) and favorable pharmacokinetics make them excellent candidates for clinical usage.[1, 4] Therefore, a majority of the novel contrast agents described herein are derivatizations of their high stability, poly(amino-carboxylate) chelating scaffolds.

Targeted T_1 Contrast Agents

Due to the non-specific biodistribution associated with many Gd(III)-DTPA and Gd(III)-DOTA-based contrast agents, much effort has been put into developing agents with biologically relevant targets. This allows the contrast agent to accumulate and create a virtual MR image 'hotspot' in a specific region of interest. One can imagine the utility of such MR active probes in preventative medicine. With the ability to selectively bind pathological cells and processes, these agents can visualize tumor formation, vessel blockages, and scar-forming fibrin.[10]

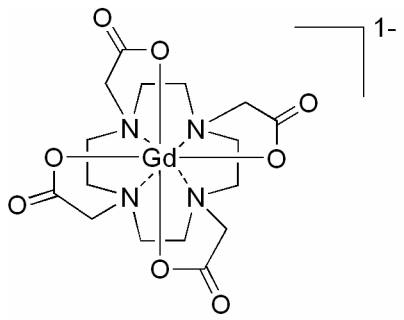

Dotarem®

Gd(III)-DOTA

$r_1 = 3.13\ mM^{-1}s^{-1}$

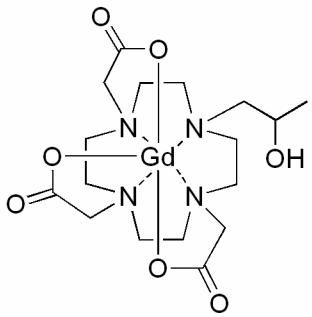

Prohance®

Gd(III)-HP-DO3A

$r_1 = 3.20\ mM^{-1}s^{-1}$

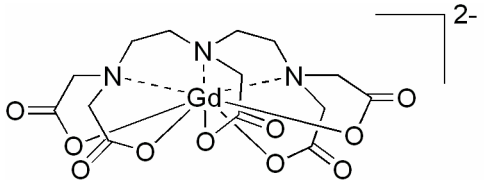

Magnevist®

Gd(III)-DTPA

$r_1 = 3.10\ mM^{-1}s^{-1}$

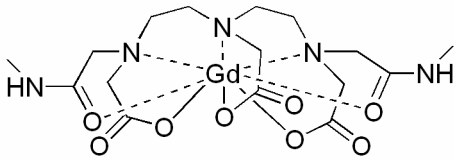

Omniscan®

Gd(III)-DTPA-BMA

$r_1 = 3.10\ mM^{-1}s^{-1}$

Figure 1.4 Examples of clinically-approved MRI contrast agents and their relaxivity data at 60 MHz and 37 °C.[4]

The most widely studied form of targeting contrast agents is those used for tumor visualization.[10, 11] Initial attempts by Aime and coworkers exploited the characteristically increased negative charge present on brain and lung tumor cell surfaces.[12] By electrostatically attaching Gd(III)-DOTA-based phosphonate complexes to positively charged peptides like polyornithine and polyarginine, they created one of the first clinically viable, targeted contrast agent candidates. However, the drawbacks of non-covalent attachment and the difficulties experienced with competitive, blood plasma anion binding to the peptides led other groups to take a more molecular approach to tumor cell targeting.

It is known that tumor cells overexpress certain receptors and proteins, several of which have been targeted with appropriate ligand-bound Gd(III) contrast agents to create protein and cell receptor-targeted probes (**Figure 1.5**).[4, 11] For example, the asparagine-glycine-arginine (NGR) peptide sequence was shown to have an increased affinity towards CD13, a protein needed for angiogenesis, while bisphosphonate groups are preferentially absorbed on bone growths.[13, 14] Other studies have shown that monoclonal antibodies (mAbs) functionalized with MR contrast agents can label cell receptors. Once bound, these contrast agents display increases in relaxivity due to the slower rotational correlation times of the contrast agent-receptor adducts.[10] Examples include contrast agents bound to an anticarcinoembryonic antigen, an anti-human T-cell antibody, and the $\alpha_v\beta_3$ integrin (a protein used to indirectly monitor tumor growth) antibody (**Figure 1.5**). However, this is not an exhaustive list, and the reader is directed to two comprehensive reviews on the topic.[10, 11]

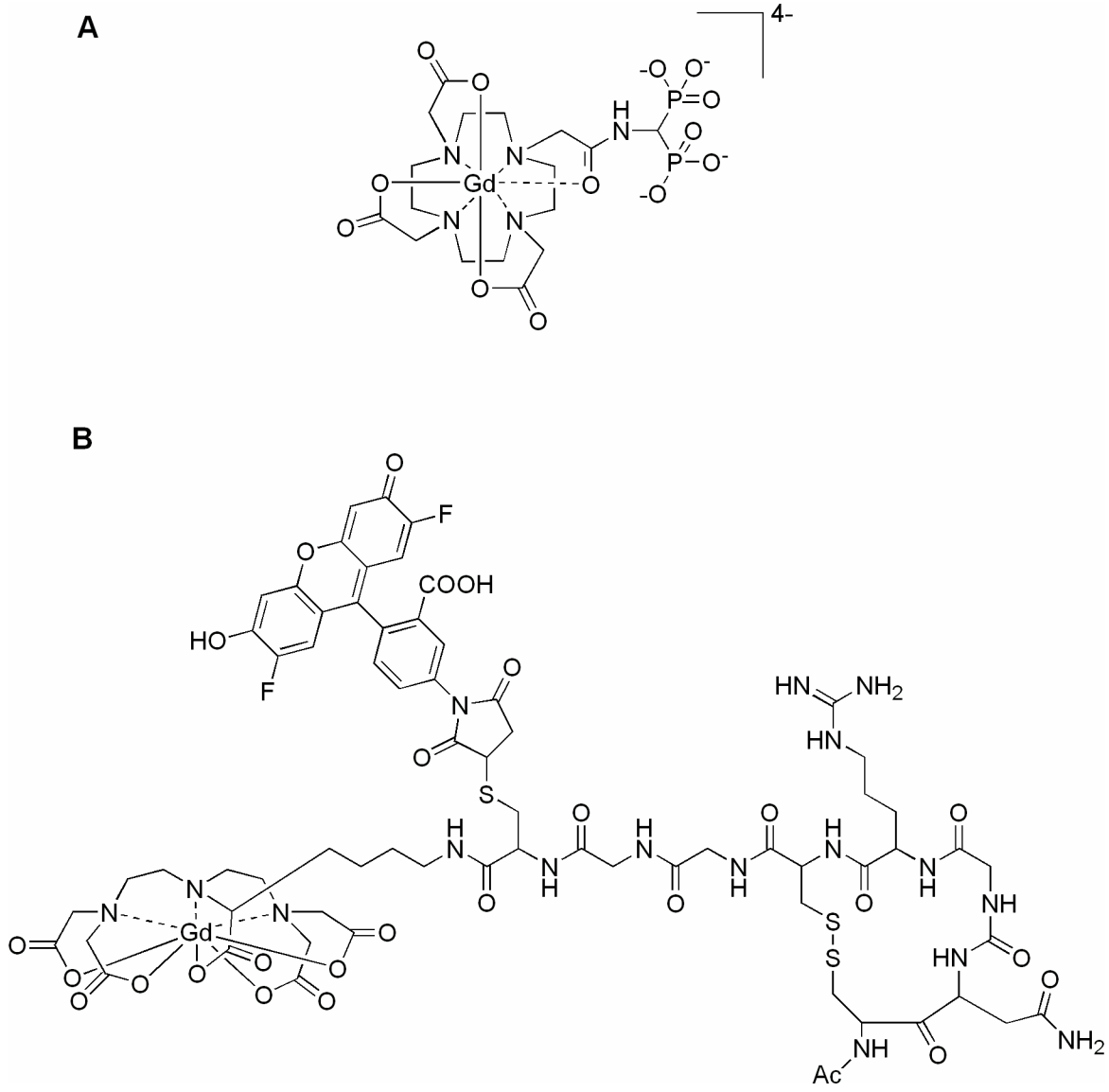

Figure 1.5 Examples of targeted MR contrast agents. (A) A Gd(III)-DOTA-based, bisphosphonate agent that is preferentially absorbed on pathological bone growths.[14] (B) A peptide (NGR) sequence functionalized Gd(III)-DTPA agent that was shown to have an increased affinity towards CD13, a protein involved in angiogenesis.[13]

Biochemically Active T_1 Contrast Agents

As the resolution of MR imaging approaches the cellular level, it has become advantageous to synthesize contrast agents that are sensitive to changes in the physiological environment. Such probes could allow clinicians to monitor disease states via enzymatic activity, pH fluctuations, pO_2 flux, and metal ion concentration.

Enzyme sensitive MR contrast agents are generally constructed to increase their relaxivity values upon interaction with the appropriate enzyme. For instance, Bertini and colleagues substituted one carboxylic acid arm of Gd(III)-DTPA with an arylsulfonamide to create a contrast agent that acts as an inhibitor of carbonic anhydrase.[15] When bound, the contrast agent exhibited a five-fold increase in relaxivity due to the slower molecule rotation (influence on τ_R) caused by the high molecular weight of the adduct. A similar system was explored by Lauffer and coworkers, who synthesized a Gd(III)-DTPA based chelate with a phosphate group terminated-hydrophobic pendant arm. Cleavage of the phosphate group by alkaline phosphotase allowed the hydrophobic arm to associate with human serum albumin (HSA), increasing τ_R and relaxivity (**Figure 1.6**).[16] Later, this same group exploited the protease activity of human carboxypeptidase B to cleave a hydrophilic peptide masking a similar hydrophobic pendant arm on Gd(III)-DTPA. Once cleaved, the agent binds to HSA.[17]

Unlike these systems, our group has visualized enzyme activity via modulation of the number of water molecules coordinated to the Gd(III) ion, q. By arranging large, enzyme-cleavable moieties on a Gd(III) chelate, the contrast agent is unable to efficiently interact with inner sphere water protons, giving the complex a $q = 0$ (*off*) state with low relaxivity. Once the enzyme removes the cleavable moiety, the Gd(III) ion is able to influence water molecules ($q = 1$ or *on* state). Examples include an agent that detects the well-known gene reporter

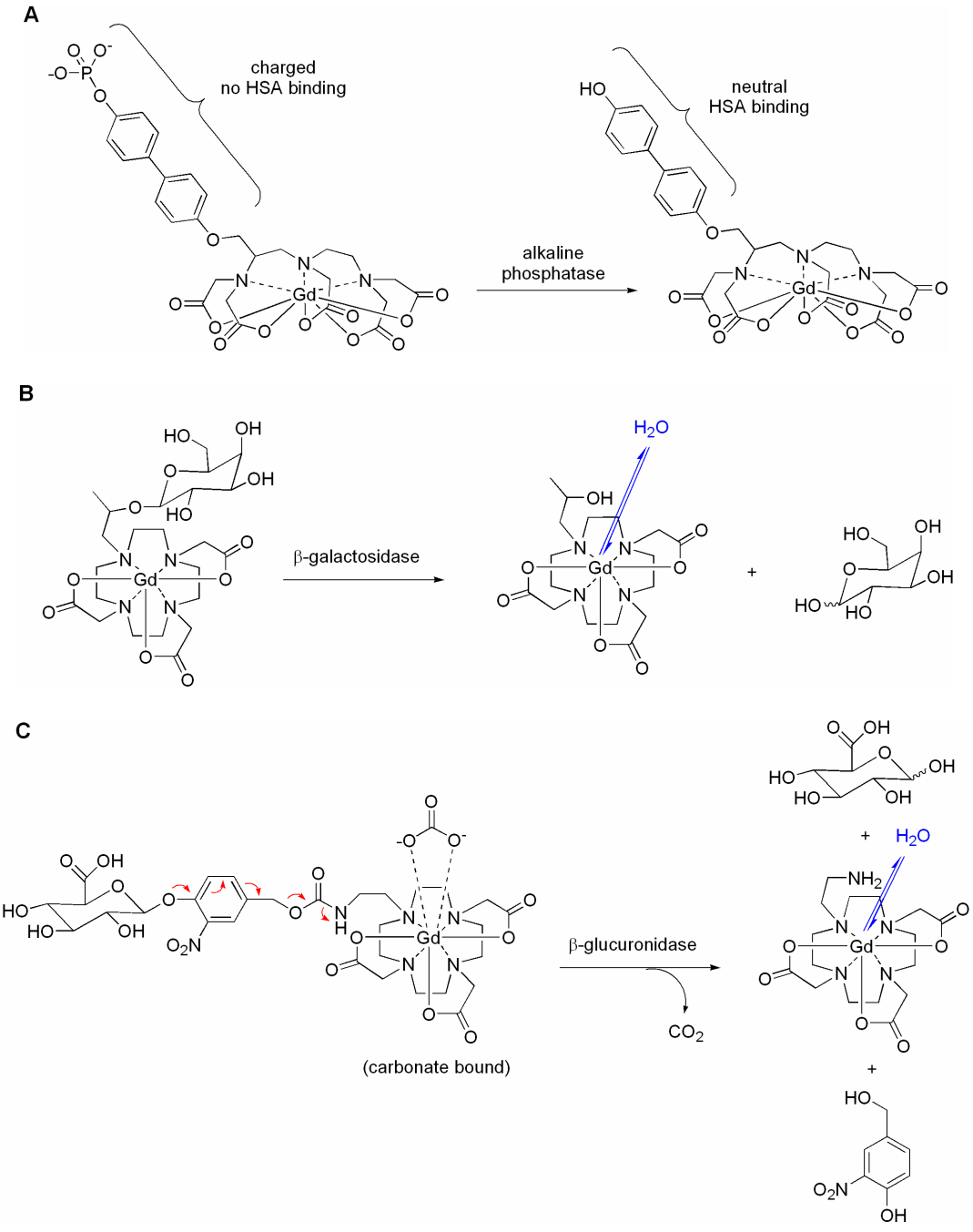

Figure 1.6 Examples of enzyme cleavable contrast agents. (A) An alkaline phosphatase sensitive MRI contrast agent developed by Lauffer and colleagues.[16] (B) and (C) Respectively, a β-galactosidase and β-glucuronidase activatable contrast agent synthesized by the Meade group.[18, 19]

β-galactosidase via β-galactose cleavage and another that detects tumor cell expressing β-glucuronidase via cleavage of β-glucuronic acid (**Figure 1.6**).[18-20]

Besides relying on enzyme kinetics for contrast agent activation, several groups have explored the ability of functionalized Gd(III) chelates to elicit relaxivity changes in response to pH. Such a system has an easily justifiable clinical endpoint because of the known pH gradient that exists in the acidic extracellular space of tumors.[21] Prepared by the groups of Sherry and Aime, several DOTA based tri- and tetraamide structures have shown pH-dependent relaxivity values.[22-24] A different approach was taken by Toth and Sitharaman where they used water soluble Gd(III)-fullerenes and Gd(III)-nanotubes to detect changes in pH.[25-27] These structures are susceptible to multiple protonation states and proton exchange rates, exhibiting increased relaxivities with decreased pH. Although often governed by complex mechanisms, these contrast agents have proven that careful modification of a Gd(III)-chelating structure can provide novel pH-dependent molecular probes (**Figure 1.7**).

Similar to enzyme kinetics and pH, the partial pressure of oxygen within the blood has been linked to several pathologies including stroke and angiogenesis.[10] Therefore, a method for measuring the relative blood oxygenation levels using contrast agent enhanced MRI has been examined. Shown in **Figure 1.7**, both contrast agents developed by Aime and coworkers show preferential affinity to the low oxygen binding T-form of hemoglobin. Therefore, areas of low oxygen partial pressure, dominated by T-form hemoglobin, would display higher relaxivities via adduct formation and an increase in the contrast agent's τ_R.[28, 29]

Another important class of biochemical markers is metal ions, and much progress has been made towards the design of MR contrast agents that change their relaxivities in response to

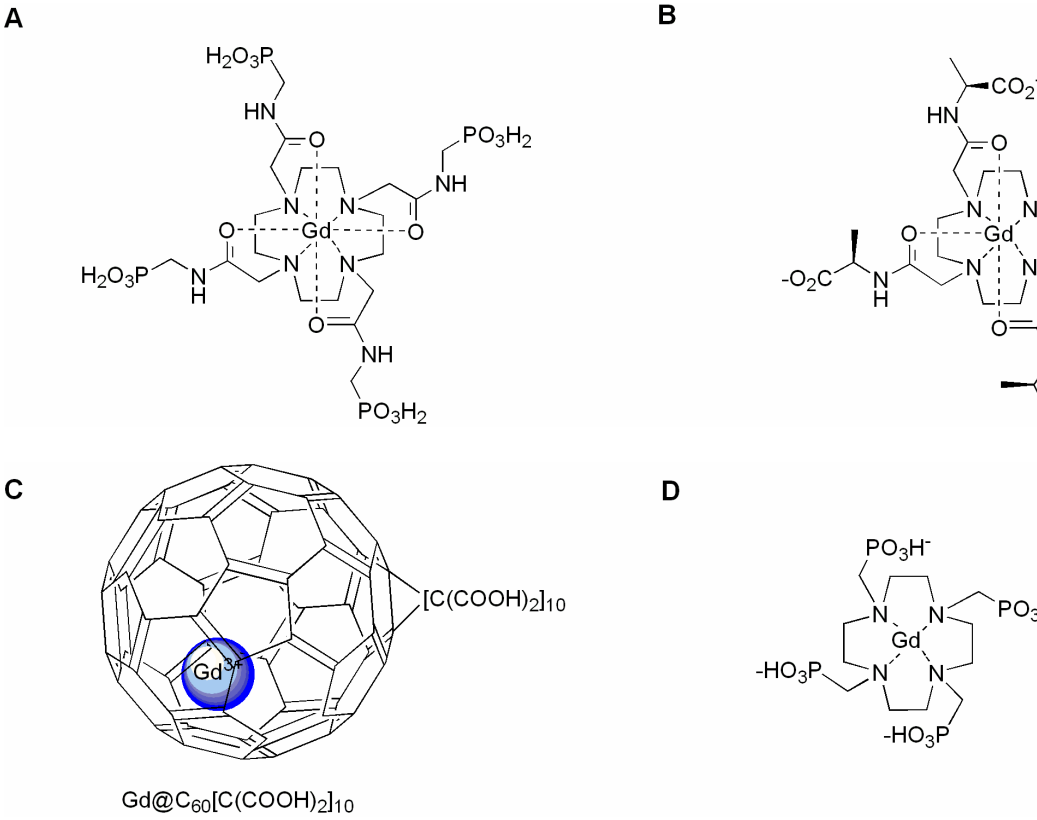

Figure 1.7 Examples of pH and pO_2 sensitive MR contrast agents. (A) Sherry and coworkers' tetraamide-DOTA-based pH sensitive contrast agent.[24] (B) A triamide-DOTA-based, pH sensitive contrast agent.[23] (C) The assumed structure of Toth's and Sitharaman's pH sensing Gadofullerene contrast agent.[27] (D) and (E) Respectively, Aime and coworkers' pO_2 sensitive DOTA-phosphonate and DTPA-boronic acid-based contrast agents.[28, 29]

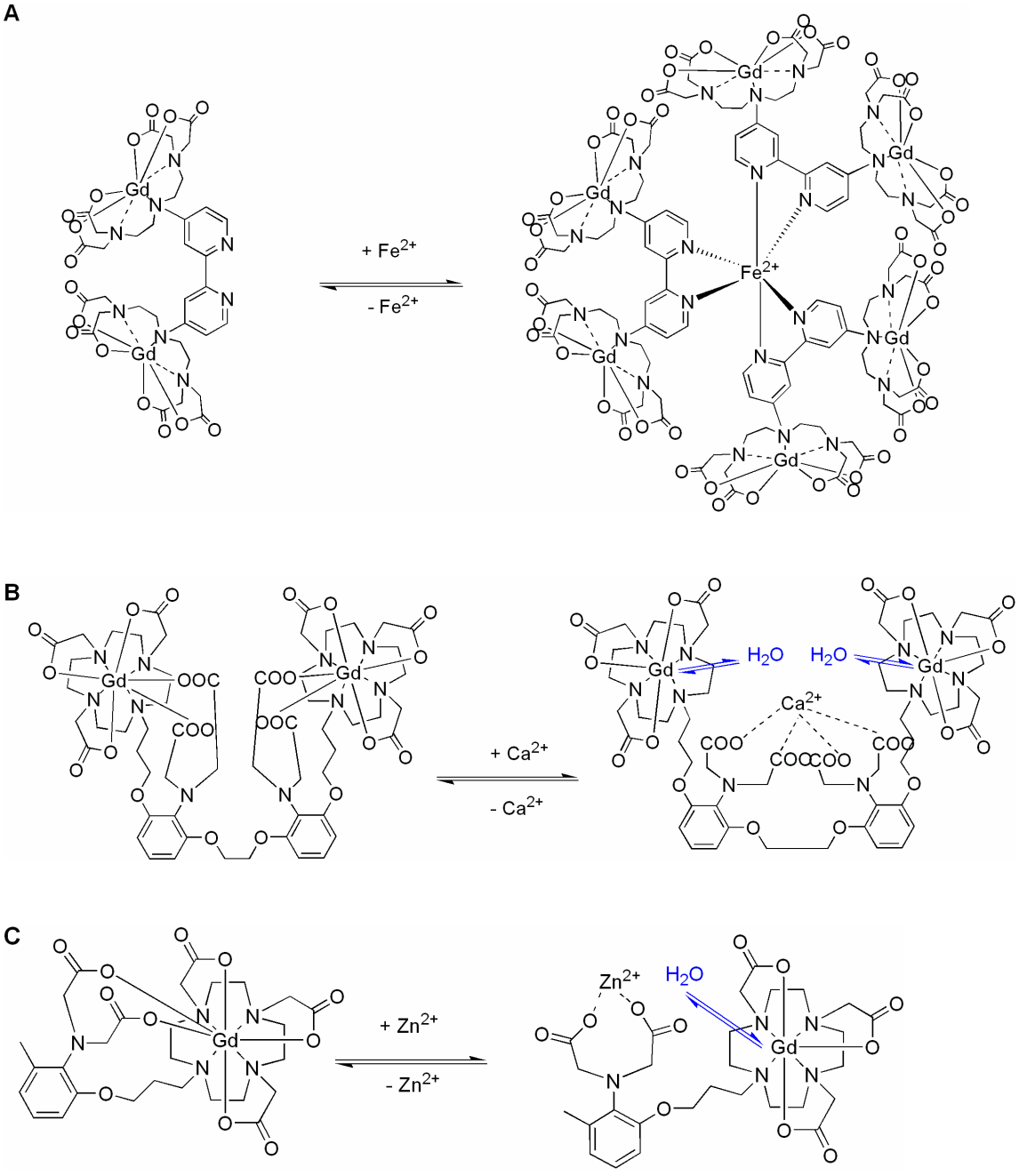

Figure 1.8 Examples of metal ion sensitive MR contrast agents. (A). Livramento and coworkers' Fe(II) sensitive, metallostar contrast agent.[30] (B) A 1,2-*bis*(o-aminophenoxy)ethane-*N*,*N*,*N*',*N*'-tetraacetic acid (BAPTA)-based Ca(II) sensitive contrast agent.[31] (C) Major and colleagues' selective Zn(II) sensing agent.[32]

metal ion gradients. Varying iron concentrations, linked to anemia and siderosis, have successfully been imaged, with a Gd(III)-DTPA based, self-assembling bipyridyl ligand.[30] Calcium, necessary for muscular contraction, neural cell communication, and hormonal secretion, was the target of work by Li and colleagues.[31] By linking 1,2-*bis*(o-aminophenoxy)ethane-*N*,*N*,*N*',*N*'-tetraacetic acid (BAPTA) between two Gd(III)-DOTA-based chelates, they synthesized a contrast agent capable of imaging calcium at physiological concentrations.

Another prevalent biological metal, zinc, has also been effectively imaged by both Nagano's and, later, Meade's groups.[32, 33] Based off half of the BAPTA molecule, Major and coworkers' contrast agent showed selective chelation of zinc in the presence of calcium and magnesium. Shown in **Figure 1.8**, all three of these agents show an increase in relaxivity upon binding of their respective metal ions.

Paramagnetic Chemical Exchange Saturation Transfer Contrast Agents

Built upon the same nuclear magnetic resonance (NMR) principles of MRI, chemical exchange saturation transfer (CEST) is a technique that uses presaturation pulse sequences (RF pulses) in order to create spectroscopically induced image contrast via magnetic resonance. All tissues have two pools of protons, those tightly associated with proteins, lipids, and subcellular structures (low pKa, -NH and -OH protons) and those considered to be the bulk water. These pools of protons are in constant communication with one another, hence their net magnetization vectors can be dependently decreased with the introduction of RF pulses at selected frequencies.[34] Initial studies showed that diamagnetic molecules could demonstrate the CEST effect because their -NH and -OH group protons slowly exchanged with the bulk water.[35] However, it was soon discovered that paramagnetic ion chelates with unusually slow water exchange rates ($1/\tau_m$) could augment the CEST images to an even greater extent.[36] Named

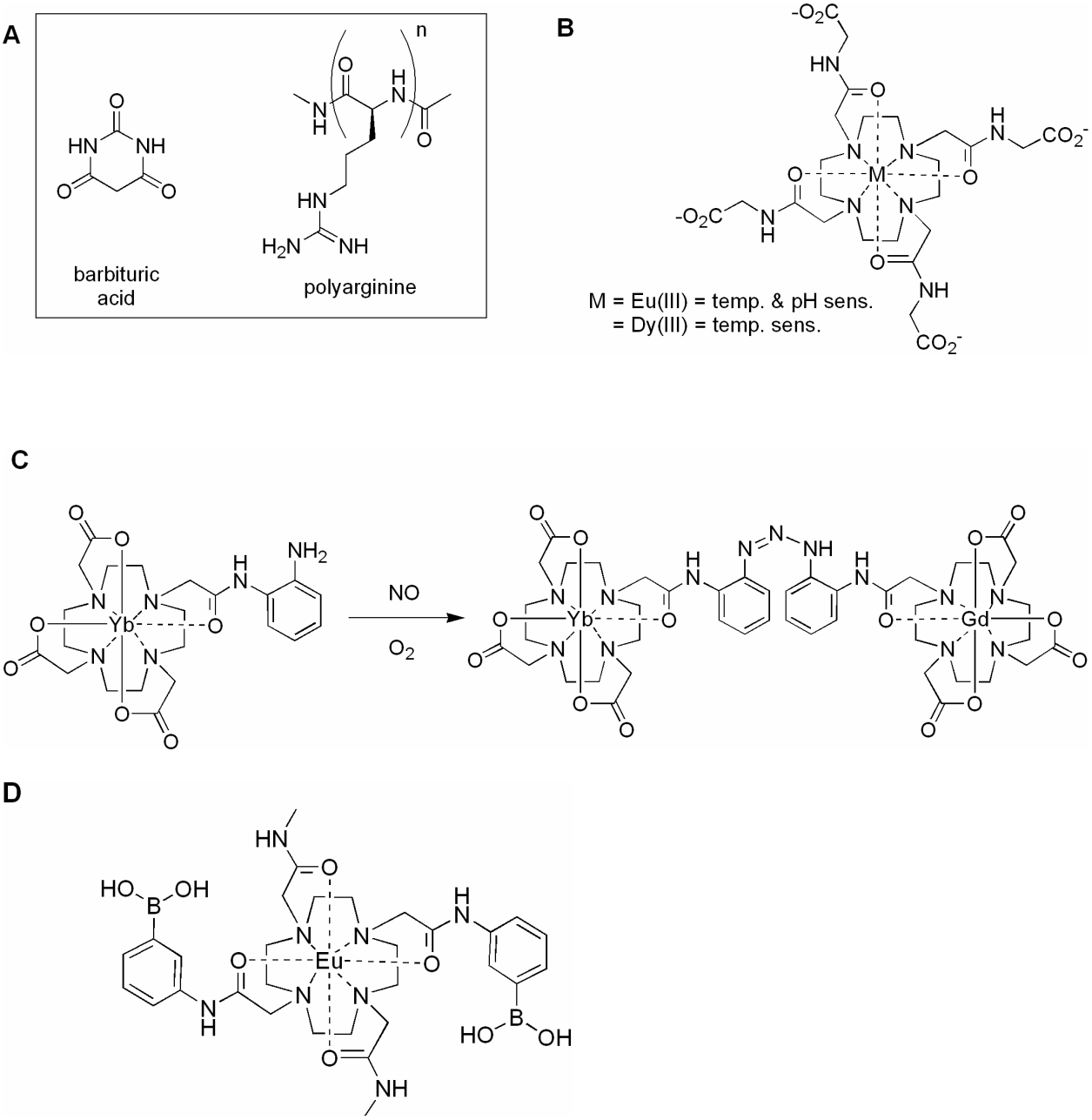

Figure 1.9 Examples of CEST and biochemically-active PARACEST contrast agents. (A) Biologically endogenous CEST contrast agents (barbituric acid and polyarginine oligomers). (B) A metal-dependant, pH and temperature sensitive PARACEST contrast agent.[37, 38] (C) A nitric oxide sensing PARACEST contrast agent.[39] (D) A glucose sensitive PARACEST contrast agent.[40]

PARACEST contrast agents, these paramagnetic compounds are usually built upon existing lanthanide chelating moieties and offer the ability to be fine tuned based upon lanthanide ion properties.[41]

Of special interest are the more recently developed PARACEST contrast agents that are responsive to biochemical environments. Similar to the biochemically-active T_1 contrast agents, these probes offer a change in PARACEST detectable intensities or frequencies upon pH changes, temperature variations, enzymatic cleavage, nitric oxide (NO) presence, and glucose concentrations.[37-40, 42] Shown in **Figure 1.9**, these agents are able to report on biologically relevant events without the need to efficiently relax water protons like their Gd(III) chelating counterparts. However, PARACEST agents do have one distinct limitation. Due to the inherent decreased sensitivity of CEST, approximately 100 times the amount of contrast agent is necessary over the conventional Gd(III) augmented imaging to elicit the same visible contrast enhancement. Therefore, this technique is in need of a more effective imaging system by which exogenous CEST agents can be fully utilized to aid in image contrast enhancement.[41]

Macromolecular and Alternative High Relaxivity T_1 Contrast Agents

As discussed, Gd(III)-based T_1 contrast agents are usually constructed of poly(amino-carboxylate) chelating backbones. However, such structures are generally limited to lower relaxivities due to their rapid tumbling (fast τ_R rates) and low values of q (Gd(III)-bound inner sphere water molecules). Understanding these limitations, several strategies have been investigated to increase contrast agent relaxivity.

First reported by Xu and coworkers, the oxygen-rich moiety of hydroxypyridinone (HOPO) has proven to be a promising candidate as a high relaxivity, small molecule Gd(III) chelate.[43] By exploiting the oxophilic nature of Gd(III), this sub-set of lanthanide chelates

A

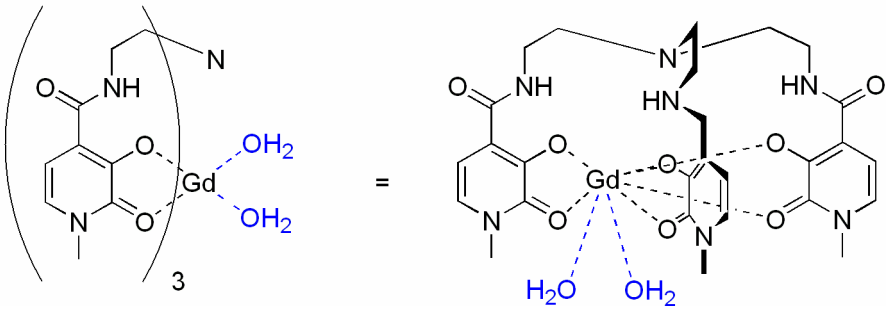

[Gd(III)-TREN-1-Me-3,2-HOPO]

r_1 = 10.5 $mM^{-1}s^{-1}$

τ_m = not measurable due to lack of H_2O solubility

B

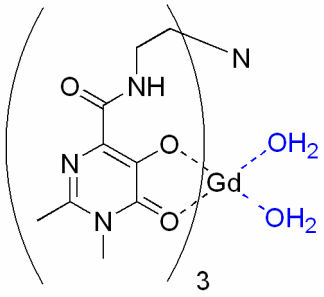

[Gd(III)-TREN-Me_2-5,4-HOPY]

r_1 = 9.0 $mM^{-1}s^{-1}$

τ_m = 2 ns

Figure 1.10 Examples of HOPO-based Gd(III) contrast agents and their relaxivities measured at 20 MHz, 25 °C, and pH 7. (A) The original HOPO-based, Gd(III) chelating contrast agent.[43] (B) A HOPO agent with improved water solubility.[44]

provides acceptable complex stabilities while allowing $q = 2$. This increase in q, along with the near-optimal water exchange rates of 2-31 ns, gives ligand relaxivities that, on average, are 8.0 $mM^{-1}s^{-1}$.[45] Shown in **Figure 1.10**, this system has been plagued with one major drawback: its poor water solubility. Given the high local concentration of Gd(III) needed to elicit image contrast enhancement, the first HOPO ligands were clinically unacceptable.[45] Since that time, much effort has been spent functionalizing the HOPO ligand with hydrophilic pendant arms.[46] One agent, shown in **Figure 1.10**, was particularly successful, displaying markedly increased water solubility while retaining a near-optimal value of τ_m.[44] While such work is interesting and novel, attachment of the necessary solubilizing groups decreases the overall chelate stability and has not been able to fully alleviate the issues associated with fast, small molecule tumbling rates.[47, 48]

The most common approaches to combating the fast τ_R times of low molecular weight Gd(III) contrast agents have been the conjugation of functionalized chelates to polymers, dendrimers, and the previously described biological molecules. Among the studies performed, derivatization of commercially available polylysine with DTPA-based chelating moieties has shown that up to 70 Gd(III) ions can be attached to a single molecule.[49] However, these agents exhibited high toxicity, and were later modified with polyethylenegycol (PEG) to modulate their pharmacokinetic downfall.[50] Still, the system consistently produced relaxivities per gadolinium that were lower than expected (based on τ_R measurements). This was speculated (and later proven by Toth and colleagues) to be a result of the polymer's flexible nature, creating fast local rotation.[51] Attempts by Modo and coworkers to functionalize dextran, a large molecular weight polysaccharide of glucose, resulted in similar relaxometric properties (**Figure 1.11**).[52] Therefore, other synthetic schemes, such as high molecular weight dendrimers, were employed.

In contrast to flexible linear polymers, dendrimers have a relatively rigid structure and their overall tumbling rate will, in most cases, contribute favorable to τ_R. Gadomer-17, shown in **Figure 1.11**, is an example of such a system. Built upon a polyamide dendrimer, the 17 kDa contrast agent has a relaxivity that is 65% higher per Gd(III) ion than its linear counterpart.[53] (The author directs the reader to the literature for more information on this topic.[1, 4, 5])

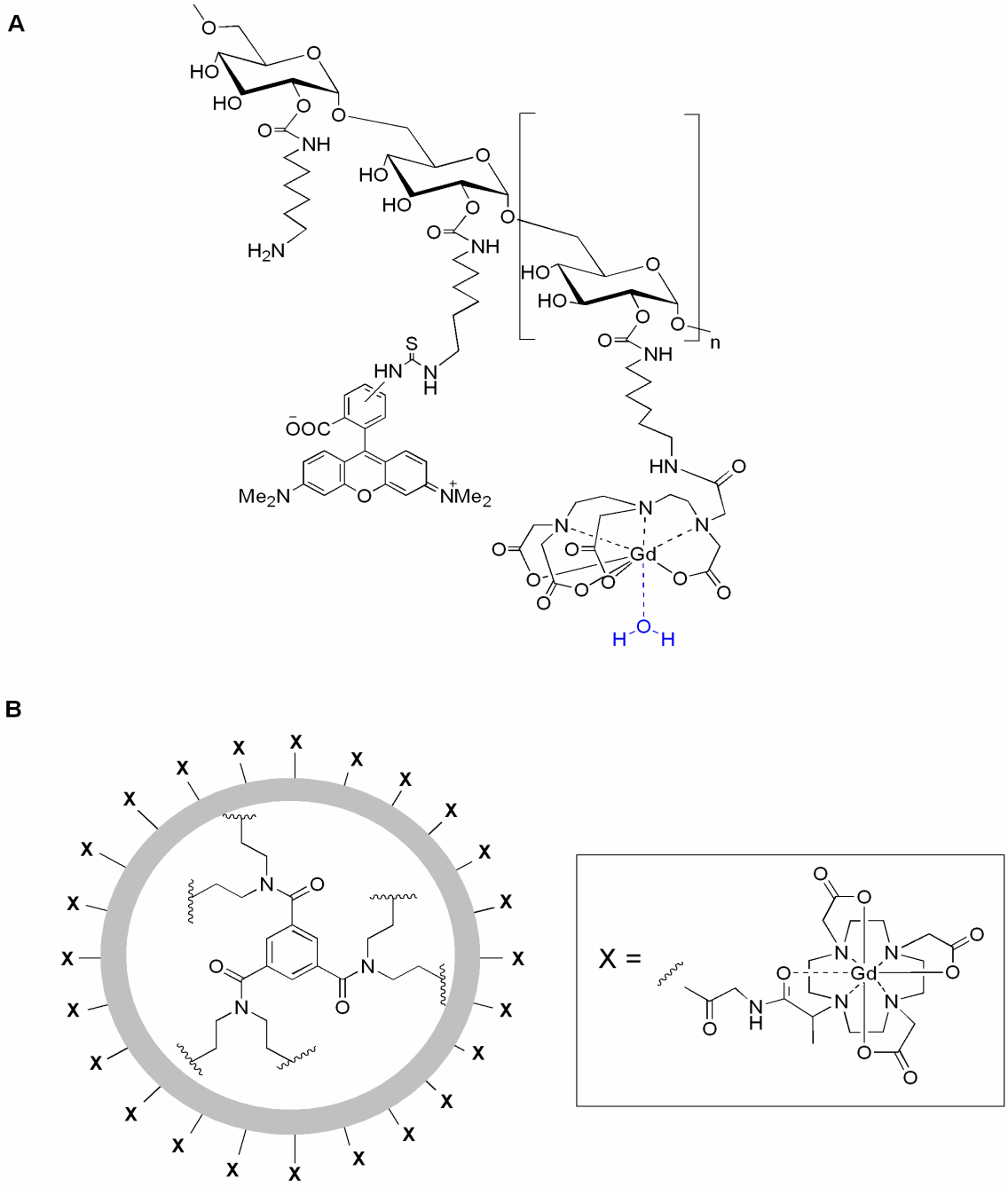

Figure 1.11 Examples of macromolecular Gd(III) contrast agents. (A) Modo and coworkers' macromolecular gadolinium rhodamine dextran (GRID) contrast agent.[52] (B) A representation of Gadomer-17, the dendritic agent developed by Rohrer and colleagues.[53]

Conclusions and Outlook

As this chapter has outlined, much work and progress has been made in the field of MRI and consequently on its image enhancing contrast agents. Perhaps the most exciting of which is the understanding now possessed on the intrinsic parameters that influence relaxivity. Although T_{1e} and relaxivity of 2nd sphere water molecules has received little attention, modulation and optimization of inner sphere water exchange, hydration number, and molecular rotation have been added to the community's collective knowledge base. Made possible by the collaborative efforts of coordination chemists, organic chemists, biophysics, and clinicians, the design and implementation of novel contrast agents for targeted, smart, intracellular, and molecular MRI promises to bring the clinical imaging community new and more efficient methods of non-invasive, in vivo diagnosis.

Scope of Thesis

This thesis focuses on the development and testing of cell-permeable contrast agents for molecular MR imaging. To realize the full potential of this imaging modality, chemists and biologists need to focus on the interdisciplinary work of synthesizing and testing contrast agents that can exploit such a powerful system. Considering the opportunities for exploratory research in MR imaging and the optimization accompanying contrast agents, the work presented here will focus on the functionalization, characterization, and optimization of several advanced imaging probes that enhance MR image contrast.

Chapter 1 will familiarize the reader with the physics that make MR imaging possible by discussing the principles that govern nuclear spin orientations and behaviors within a magnetic field. This is followed by a background on paramagnetic contrast agents that will allow an

increased understanding of the compounds, chelation chemistries, and relaxometric parameters described throughout Chapters 2-5.

Chapter 2 introduces and describes cell-permeable contrast agents. The discussion begins with the advantages over current clinical contrast agents and the difficulties associated with visualizing such systems. This chapter includes an introduction to synchrotron radiation X-ray fluorescence (SR-XRF) and is the first published use of SR-XRF to identify the locations of MR contrast agents in cells. Augmented with synthetic methodologies, cell uptake data, MR images, and a novel approach to lanthanide-fluorescence resonance energy transfer (L-FRET) probes, this chapter explicitly demonstrates the utility of polyarginine and 4-amino-4'-(*N*,*N*-dimethylamino)stilbene to increase cell uptake of Gd(III)-DOTA and Gd(III)-DTPA-based MR contrast agents.

Chapter 3 is a continuation of Chapter 2. It focuses on optimizing the cell retention of the polyarginine agents previously introduced. Specifically, the long-term cell retention of the Gd(III)-DOTA-Arg_8 and Gd(III)-DTPA-Arg_8 intracellular contrast agents introduced in Chapter 2 have been significantly increased by incorporating disulfide linkages between the Gd(III) chelate and the arginine transduction moiety. The inherent disulfide reducing environment of mammalian cells, directly related to the intracellular concentration of glutathione (GSH), is hypothesized to be responsible for these findings. Synthetic methodologies, pH stability, in vitro kinetics, cell studies, SR-XRF, and MR images of these agents are presented.

Chapter 4 explores the feasibility of a nanoparticle scaffold to selectively deliver MR contrast agents to subcellular organelles. This type of multifunctional system allows for the attachment of multiple (approximately 20) Gd(III) contrast agents as well as targeting vectors and therapeutics. The scaffold (TiO_2 nanoparticles) was functionalized with a Gd(III)-DOTA-

based contrast agent and DNA targeting vectors. The result was the first nanoparticle system capable of targeting subcellular structures while being simultaneously imaged via MRI. Synthesis and characterization of the nanoparticles, the Gd(III) chelate, and the subsequent conjugation reactions are supplemented by SR-XRF and MR images of the conjugates in cell culture are presented.

Chapter 5 reviews optimization of contrast agent relaxivity by increasing the rotational correlation time, τ_R. Synthetic methodologies and preliminary examination of Gd(III)-DOTA and Gd(III)-DTPA-based contrast agents susceptible to ring opening metathesis polymerization (ROMP) are presented. Although several monomers were synthesized, difficulties during the polymerization process afforded only a small selection of polymers; however, the resulting increases in relaxivity are promising.

CHAPTER 2:

Synthesis and Visualization of a Series of Cell-Permeable MRI Contrast Agents

The text in this chapter was taken in part from:

Endres, P. J.; MacRenaris, K. W.; Vogt, S.; Allen, M. J.; Meade, T. J., Quantitative Imaging of Cell-Permeable Magnetic Resonance Contrast Agents Using X-Ray Fluorescence. *Mol. Img.* **2006,** 5, (4), 485-497.

Introduction

Advances in magnetic resonance imaging (MRI) have provided a new tool for the study of developmental biological processes such as cell lineage and fate mapping.[1, 2] The ability to observe these long-term developmental events in whole animals from descendants of individual precursors is significantly impacting our understanding of these crucial and intricate processes. For example, an intact embryo can be labeled by microinjection of a stable, nontoxic MR lineage tracer and images acquired.[3] As a result, a complete time series of high-resolution three-dimensional MR images can be analyzed forward or backward in time to reconstruct cell divisions and movements. A principle barrier to the development of new lineage tracers and contrast agents is the inherent inability of these complexes to cross cell membranes.[4-8] Upon cell transduction, these agents must then produce an observable effect on the MR signal. Ideally, the agent has adequate synthetic versatility to allow for modification with a small-molecule (nonviral) delivery vehicle that does not increase toxicity and is efficient enough to deliver a detectable quantity of the imaging probe.

The development of cell-permeable peptides and small molecules has led to the identification of numerous carrier molecules. A number of reports have described delivery vehicles that direct the agent to a particular cell type, such as transferrin and folate-receptor-targeted agents.[9-14] Similar to receptor mediated delivery, cationic protein transduction domains (PTDs) such as polyarginine and HIV-1 TAT have been extensively used as translocation vehicles to facilitate delivery of all classes of modified contrast agents.[15-21] In general, such agents have been visualized via fluorophore conjugation and light microscopy or lanthanide luminescence and two-photon imaging. However, neither imaging system offers both high resolution and absolute quantification. Therefore, the focus of this chapter is two fold: the

development of highly efficient and passive vehicles for the intracellular transport of MR contrast agents and the testing of new quantitative methods for evaluating uptake.

To explore these goals, four cell permeable agents have been synthesized (**Figure 2.1**) and their translocation efficacy has been characterized by synchrotron radiation X-ray fluorescence (SR-XRF), inductively coupled plasma mass spectrometry (ICP-MS), and MR imaging. Accompanied by the synthetic schemes that afforded cell-permeable contrast agents **1-4**, this chapter compares the cellular transduction efficiencies of two different cell-permeable vehicles with entirely different translocation properties and mechanisms.

SR-XRF uses photoelectric absorption of incident hard X-rays to cause the ejection of K shell electrons from an atom (**Figure 2.2A**). With high atomic weight elements, this electron vacancy creates an excited state that relaxes with emission of a photon.[22] Owing to the monochromatic X-ray beam and zone plate optics available with SR-XRF, two dimensional images with single cell resolution (0.3 x 0.3 μm) can be recorded (**Figure 2.2B**). A major advantage of SR-XRF over standard fluorescence microscopy is that images are obtainable without altering the agent by attachment of an organic fluorophore. Although gamma counting augmented by emitters such as ^{153}Gd and ^{125}I offer the same advantage, the technique requires handling and preparation of radioactive compounds and the best resolution currently obtainable is (190 x 190 μm).[23]

Studies aimed at the elucidation of in vivo cellular processes and in vivo fate mapping could improve our knowledge of key biological processes such as immune defense mechanisms and tumorigenesis.[24] Therefore, modification of a contrast agent with a cellular transduction moiety and quantitative analysis of its translocation efficacy is a key step in the development of biologically compatible intracellular contrast agents.[2, 15, 16, 24-26]

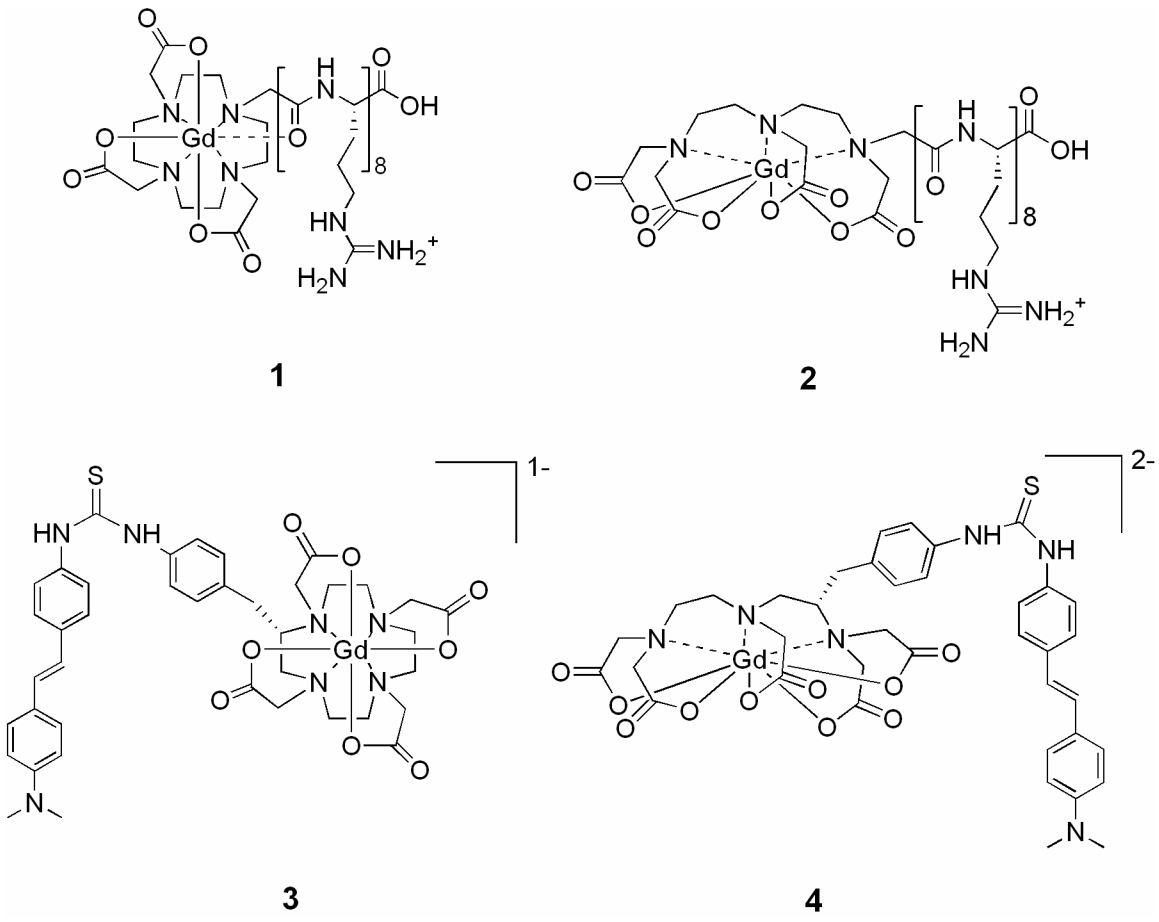

Figure 2.1 Structures of the intracellular MRI contrast agents. (**1**) An 8-amino acid polyarginine oligomer coupled to Gd(III)-DOTA. (**2**) An 8-amino acid polyarginine oligomer coupled to Gd(III)-DTPA. (**3**) A 4-amino-4'-(*N*,*N*-dimethylamino)stilbene coupled to Gd(III)-*p*-Bn-NH_2-DOTA. (**4**) A 4-amino-4'-(*N*,*N*-dimethylamino)stilbene coupled to Gd(III)-*p*-Bn-NH_2-DTPA.

A

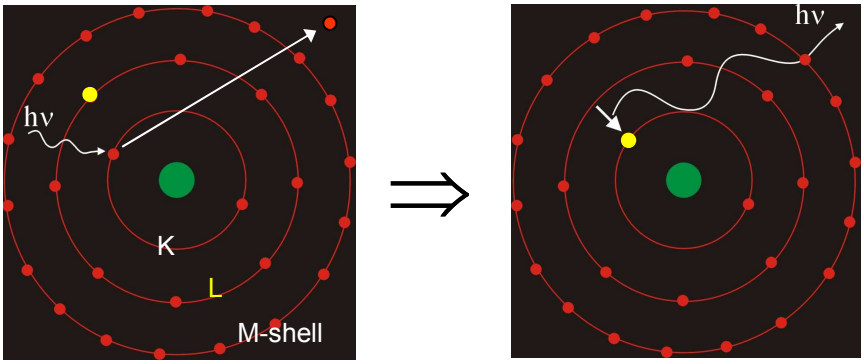

elemental absorption of monochromatic hard X-rays

characteristic X-ray fluorescence

B

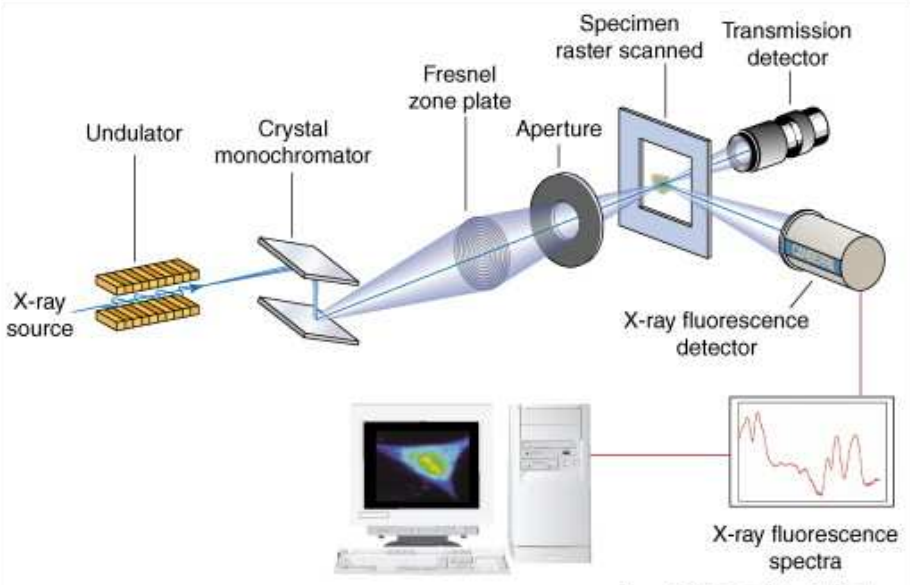

Figure 2.1 Selected diagrams of synchrotron radiation X-ray fluorescence. (A) Diagram depicting X-ray absorption and subsequent electron ejection from a high Z element by SR-XRF (courtesy of Stefan Vogt). (B) Reproduced schematic of experimental SR-XRF hardware.[27]

Results

Synthesis of the Cell-Permeable Contrast Agent Series

The four cell-permeable agents (**1-4**) were synthesized by the addition of either a cationic octamer of polyarginine or a 4 amino-4'-(*N*,*N*-dimethylamino)stilbene molecule (**Figure 2.1**) to either a DTPA or DOTA based Gd(III) chelating moiety. The final coupling step of the stilbene complexes was previously outlined; however, a more cost effective route yielding products of higher purity has been developed (**Scheme 2.1** and **2.2**).[28-30] Built from inexpensive and commercially available *L*-phenylalanine, both **1** and **2** have been produced with overall synthetic yields of 16 and 2%, respectively. These low yields are a consequence of the ring-closing reaction needed to form the macrocycle in **1**, and of aromatic nitration followed by carbonyl reduction in **2**. The coupling of the chelators to the arginine octamer in the case of **3** and **4** was done using standard fluorenyl-methoxy-carbonyl (Fmoc) protected solid phase peptide synthesis on Wang resin. The overall yields for contrast agents **3** and **4** were 82% and 88%, respectively (**Scheme 2.3**).[2]

Cellular Uptake Studies

Following full characterization, the four model cell-permeable contrast agents were tested for in vivo cellular transduction efficiency in three different mammalian cell lines. Each compound was solubilized in the corresponding media and the cell lines were incubated in that media for 4 h at several different concentrations. To quantitatively determine the uptake trend of **1**-**4** within the three cell lines, ICP-MS was utilized to determine the amount of Gd associated with cultures of these cell lines. As expected, per cell Gd content is directly correlated with cell size: MDCK cells being the largest in volume and highest in Gd ion uptake, followed by NIH/3T3, and RAW 264.7 cells. Another important attribute of uptake, cell viability, remained

Scheme 2.1 Synthesis of 4-isothiocyanato-4'-(*N*,*N*-dimethylamino)stilbene (**5**).

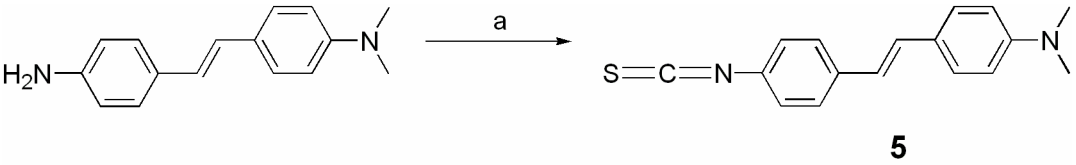

5

(a) K_2CO_3, $CSCl_2$, $CHCl_3$, 0 ºC

Scheme 2.2 Synthesis of Gd(III)-*p*-Bn-DOTA-stilbene (**3**) and Gd(III)-*p*-Bn-DTPA-stilbene (**4**).

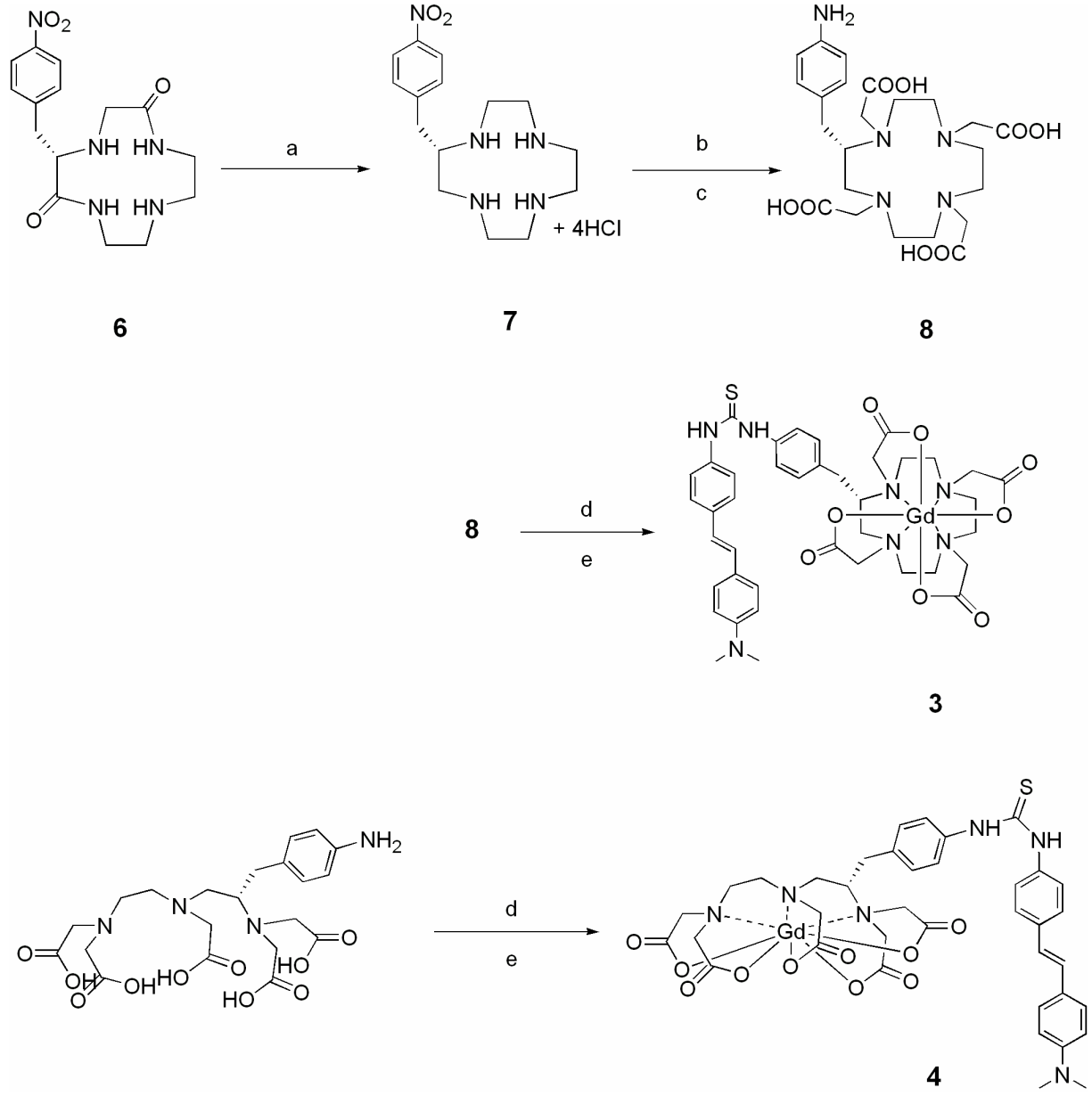

(a) BH_3•THF; (b) $BrCH_2CO_2H$, H_2O pH 10.0, 70 °C; (c) Pd/C, H_2; (d) **5**, DMF, 80 ºC; (e) $GdCl_3$, H_2O, pH 7.0.

Scheme 2.3 Synthesis of Gd(III)-DTPA-Arg_8 (**2**).

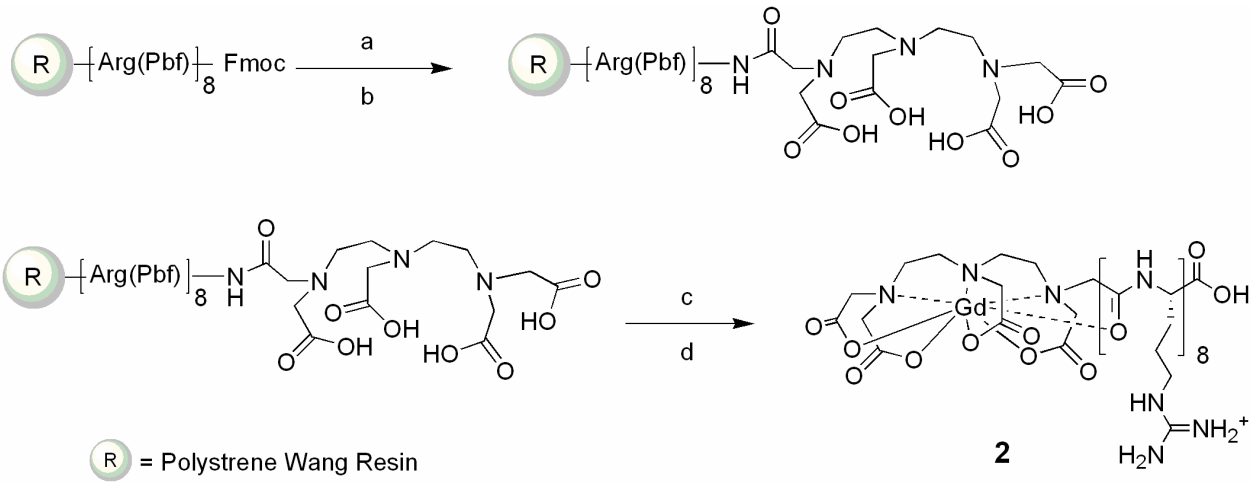

(a) Piperdine; (b) DTPA-dianhydride, DIEA; (c) 95% TFA, 2.5% H_2O, 2.5% TIS; (d) $Gd(OH)_3$, H_2O, 80 ºC.

stable compared to the controls, not decreasing more than 2% (3.0 mM) or 5% (10 mM). Special attention should be drawn to the relative transduction efficiencies of the agents within each cell line (**Figure 2.3**). The obtained data set shows that **1**-**4** are associating with the following cell dependent trends: NIH/3T3, **4** > **2** > **3** > **1**; RAW 264.7, **2** > **4** > **1** > **3**; MDCK, **4** > **3** > **1** > **2**. These results could be a function of overall molecular charge or three dimensional chelator conformations, and will be addressed in detail in the discussion section of this chapter.

Synchrotron Radiation X-Ray Fluorescence (SR-XRF) Analysis

SR-XRF analysis was performed to determine the cellular association pattern of **1**-**4**. For each combination of cell line, contrast agent, and concentration, five randomly chosen cells were raster scanned at coarse resolution (2.0 μm x 2.0 μm pixel size). From these randomly chosen cells, two cells per group were raster scanned at fine resolution (0.30 μm x 0.30 μm pixel size). All cells incubated with contrast agent and scanned revealed that Gd was present; however, we observed large standard deviations in the Gd content between different cells of the same population. The acquired high-resolution elemental maps provide pixel by pixel data sets that were used to globally confirm, map, and quantify the Gd distribution within each sample (**Figure 2.4**). These X-ray fluorescence maps were integrated over all the scanned pixels in the cell area to yield a quantitative elemental spectrum for the corresponding cell. The spectra of a cell (NIH/3T3) incubated with **4** (10 mM) and a control cell (NIH/3T3) are shown in **Figure 2.5**. Whereas fluorescence peaks corresponding to elements naturally occurring in cells are present in both of the samples (e.g. Fe and Zn), the cells treated with **4** show peaks corresponding to the characteristic $L_{\alpha 1,2}$, $L_{\beta 1}$, and $L_{\beta 2}$ fluorescence lines for Gd, at $E_{\alpha 1,2}$ = 6,057.2, 6,025.0 eV, $E_{\beta 1}$ = 6,713.2 eV, and $E_{\beta 2}$ = 7,102.8 eV.

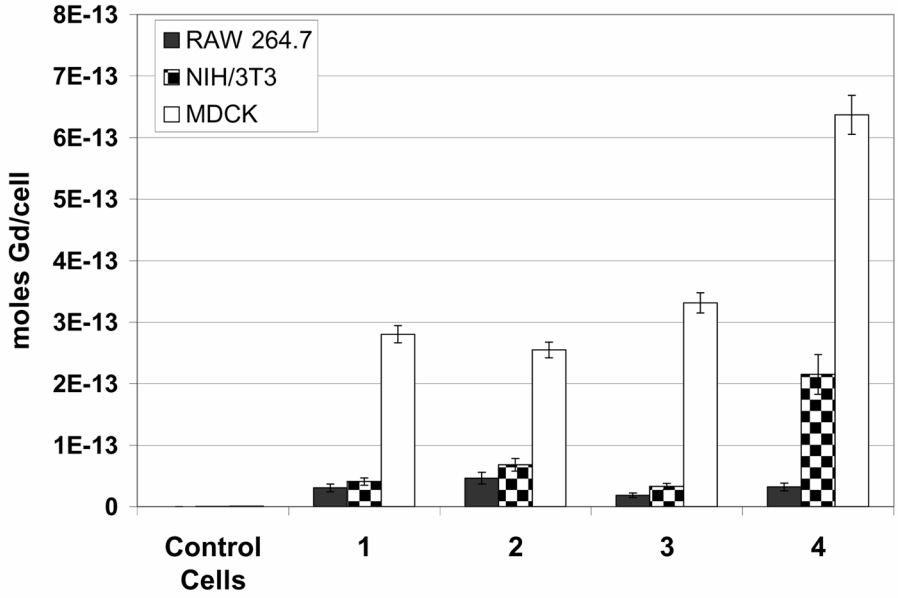

Figure 2.3 Average Gd concentrations determined via ICP-MS of the NIH/3T3, RAW 264.7, and MDCK cells incubated with compounds **1**–**4** at 3.0 mM for 4 h. The average cell count for RAW 264.7, NIH/3T3, and MDCK cells is 2,000,000, 750,000, and 600,000 cells, respectively. All samples were run in triplicate with error bars representing one standard deviation (the same parameters as the SR-XRF imaging study).

*Cell culture performed by Keith W. MacRenaris

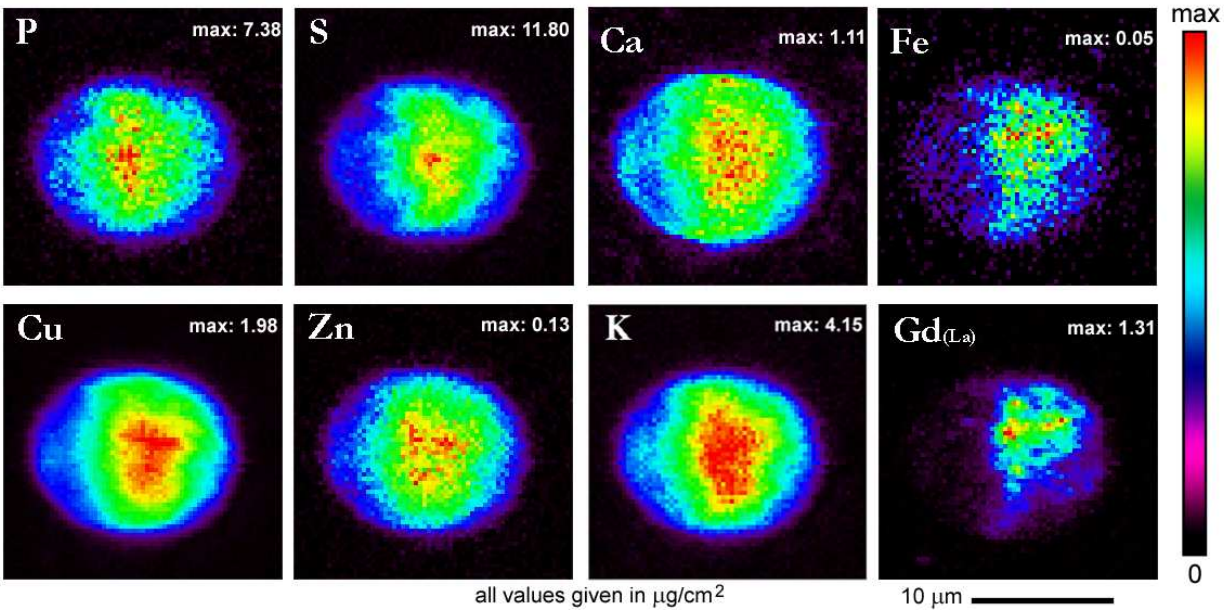

Figure 2.4 SR-XRF intensity weighted elemental maps of an MDCK cell incubated with **3** (10 mM for 4 h). Each image indicates the relative distribution of the specified element. The P, S, Ca, Zn, and K images reveal cell boundaries within which the Gd distribution pattern is detectable. The spectrum depicting the relative concentrations in each map are scaled to differing values (maximum value given within each map).

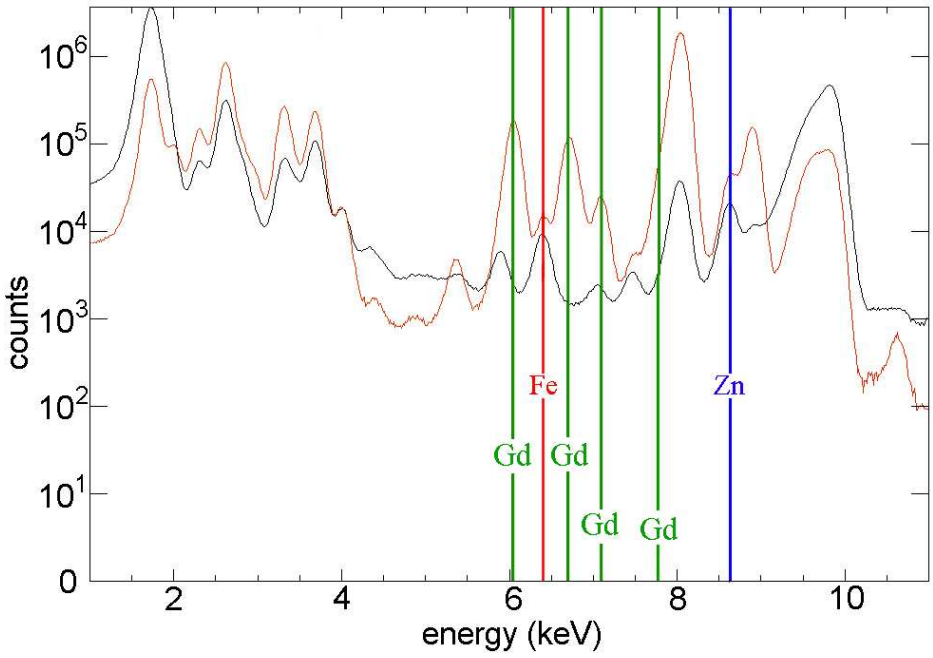

Figure 2.5 Comparison between the integrated X-ray fluorescence spectrums of all scanned pixels of an untreated NIH/3T3 cell (black spectrum) with that of an NIH/3T3 cell incubated with 3.0 mM of **4** for 4 h (orange spectrum). While peaks that correspond to elements normally present in cells are visible in both spectra (e.g. Fe ($K_{\alpha 1}$ = 6.403 keV) and Zn ($K_{\alpha 1}$ = 8.636 keV)), cells treated with **4** show sharp peaks corresponding to the characteristic $L_{\alpha 1}$ (6.058 keV), $L_{\beta 1}$ (6.713 keV), and $L_{\beta 2}$ (7.034 keV) energy levels for Gd fluorescence.

The Zn, Fe, and Gd columns of **Figures 2.6** and **2.7** show the respective elemental distributions within one chosen cell of each cell type incubated with **1**, **2**, **3** or **4** at 3.0 or 10 mM for 4 h. The colocalization (Colocal.) column combines the data from the three elemental maps (Zn, Fe, and Gd columns) to provide information on the areas of multi-element overlap. Owing to the proximity of the Gd and Fe fluorescence energy levels (**Figure 2.5**), it is important to deconvolute potential peak overlap between Fe and Gd fluorescence. This was accomplished using modified Gaussian curves that were fitted at each scan position to the acquired X-ray fluorescence spectra.[31] Comparison to NIST standards allowed the extrapolation of elemental concentrations (Experimental Procedures).

MR Imaging and T_1 Analysis

Spin-lattice relaxation times (T_1) of unlabeled cells ranged from 2.45 to 2.87 seconds whereas the T_1 values of cells incubated with **1**-**4** were 0.28 – 1.73 seconds (**Figure 2.8A**). As shown in **Figure 2.8B**, the trend remains that the samples with the highest total concentration of Gd(III) show the shortest T_1, corroborating the hypothesis that the relaxation rate is a function of the cellularly associated Gd(III) concentration and not an anomaly of cell packing. These differences were visualized using a T_1-weighted spin-echo imaging sequence of RAW 264.7 cells incubated with **1**, **2**, and **4**. The results of the imaging experiment show that the control cell image is considerably darker than the image of the cells treated with the contrast agents (**Figure 2.9**).

To demonstrate the T_1 differences between cell lines and their corresponding media, a sample of each cell line incubated with **3** at 3.0 mM was allowed to gravity settle within a coaxial insert. This insert was placed within a larger tube (5 mm OD) filled by the

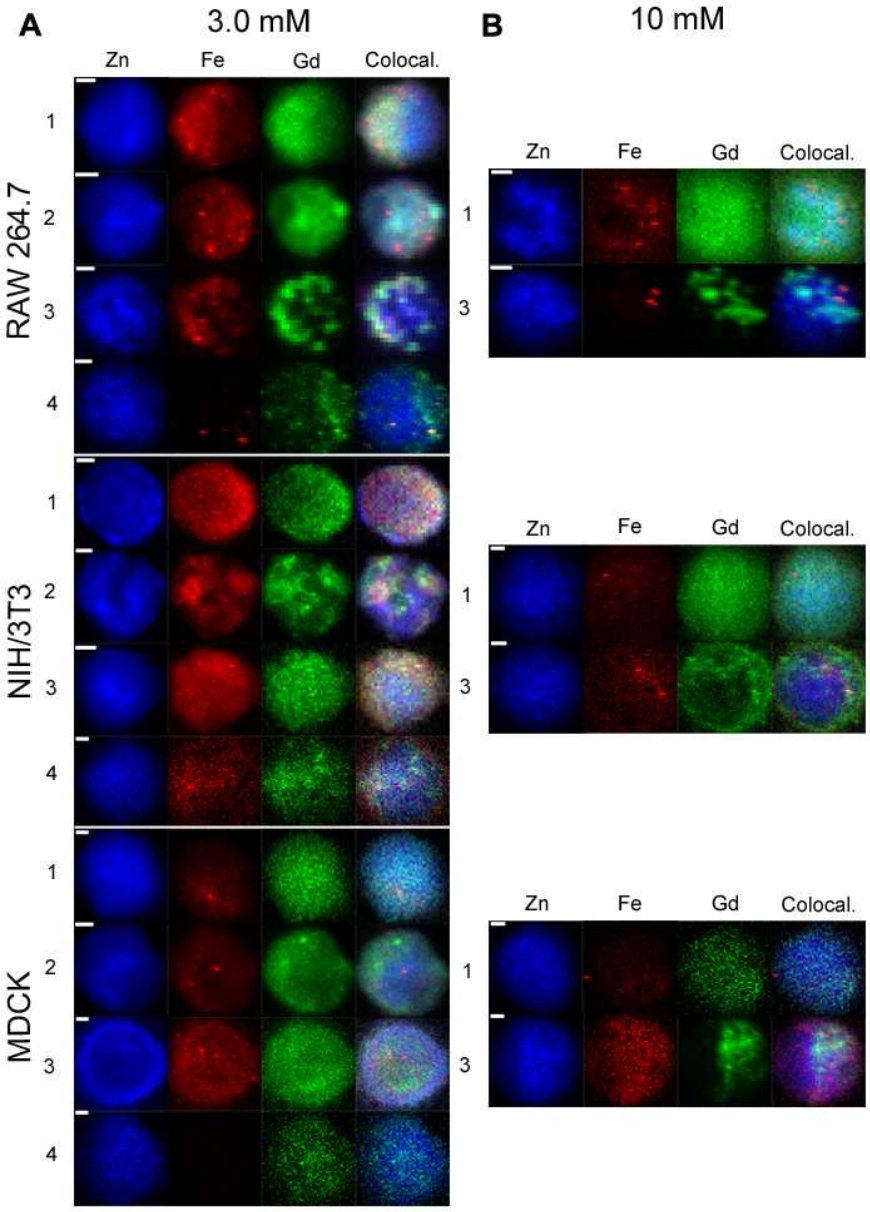

Figure 2.6 SR-XRF elemental maps of RAW 264.7, NIH/3T3, and MDCK cells incubated with contrast agents **1**-**4**. (A) SR-XRF determined 3 element overlay maps (Zn = blue, Fe = red and Gd = green) of one cell for each specific cell line incubated with **1**, **2**, **3** or **4** at 3.0 mM for 4 h. (B) A background subtracted 3 element overlay map of one cell for each specific cell line incubated with an arginine (**1**) or stilbene (**3**) modified contrast agent at 10 mM for 4 h. Scale bars represent 2.0 μm.

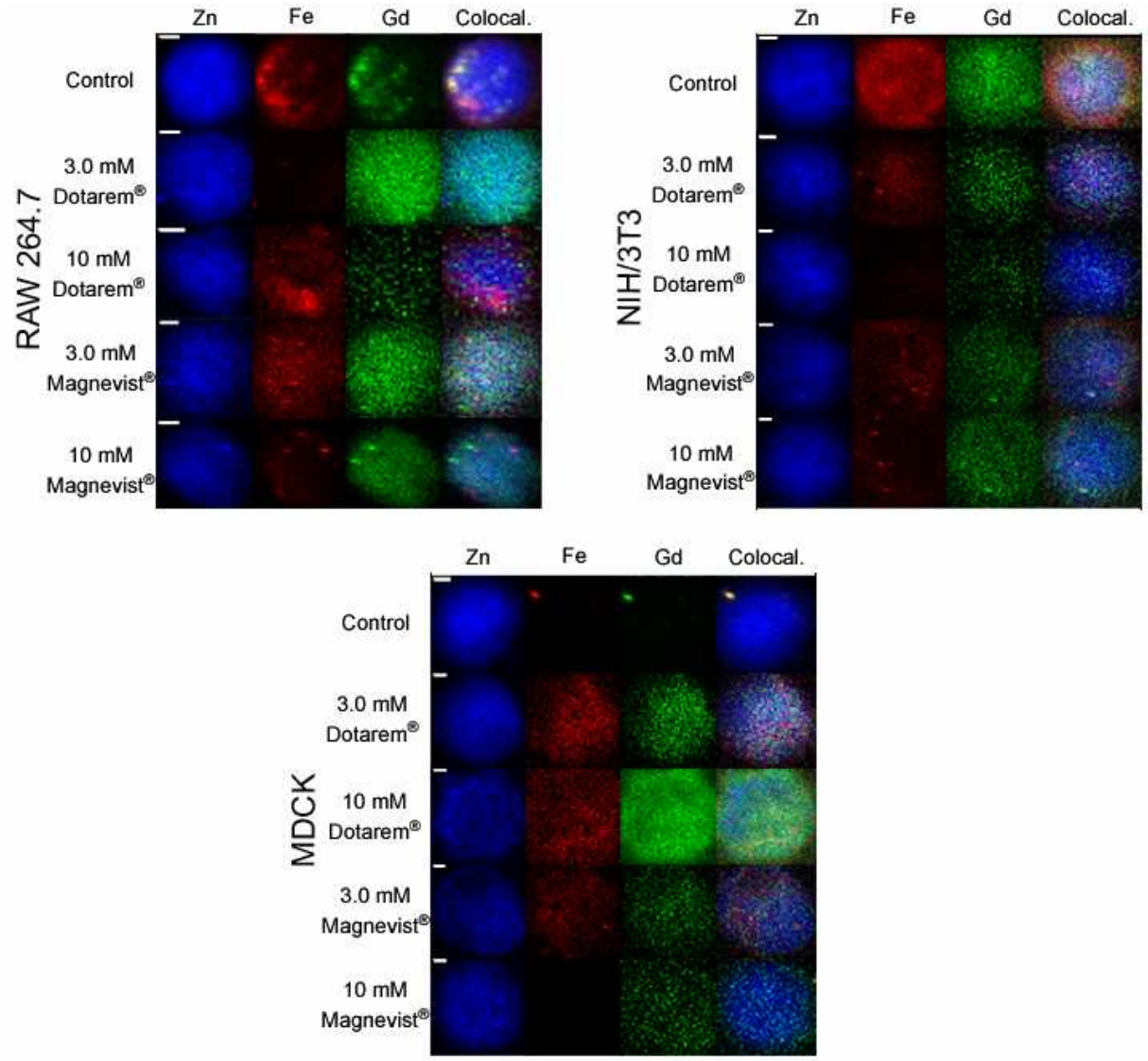

Figure 2.7 Control SR-XRF elemental maps of RAW 264.7, NIH/3T3, and MDCK cells incubated with Dotarem and Magnevist. An SR-XRF background subtracted 3 element overlay map (Zn = blue, Fe = red and Gd = green) of cells incubated with Dotarem (Gd(III)-DOTA) or Magnevist (Gd(III)-DTPA) at 3.0 or 10 mM for 4 h. Scale bars represent 2.0 μm. Notice the cell boundaries are outlined in the Zn map, however, the Gd distribution shows no discernable pattern. Note that each image is scaled to its respective maximum value; therefore, the Gd distribution falsely highlights the background.

corresponding cell media. Images show that the media phantoms provide an internal reference that has a much longer T_1 (darker image) than the cells treated with contrast agent (**Figure 2.9**).

Discussion

Upon successful synthesis and characterization of the cell-permeable contrast agents, in vitro testing of the complexes was performed. The results indicate variable uptake of contrast agents **1**-**4** between the different cell lines. This disparity is hypothesized to be attributed to three variables: transduction domain (polyarginine or stilbene), Gd(III) chelator (DOTA or DTPA), and cell type (NIH/3T3, RAW 264.7, or MDCK). Of these variables, choice of transduction moiety has been studied most rigorously. Polyarginine complexes have been shown to enter cells through a charge facilitated, endocytic pathway, whereas the uptake mechanism of stilbene complexes is not well understood.[15, 17, 18, 32] Both Kung and coworkers and Skovronsky et el. have demonstrated that stilbene based compounds cross the blood brain barrier which may be an indication of a passive uptake mechanism.[33, 34] The second variable which plays an important role in the cellular transduction efficiency of these contrast agents is the Gd(III) chelator. Changing the Gd(III) chelate from DOTA to DTPA leads to an overall molecular charge decrease from *n* to *n*-1. These variables represent two molecular properties that were systematically varied to determine the transduction efficiencies of a cationic polyarginine peptide (**1**, **2**) and derivatives of 4-amino-4'-(*N*, *N*-dimethylamino)stilbene (**3**, **4**) to associate DOTA and DTPA-based Gd(III) contrast agents with cells of differing morphologies and uptake mechanisms.[35-38] However, such molecular attributes and variables are only one side of the system. The physiology and inherent cell line characteristics must also be considered.

A

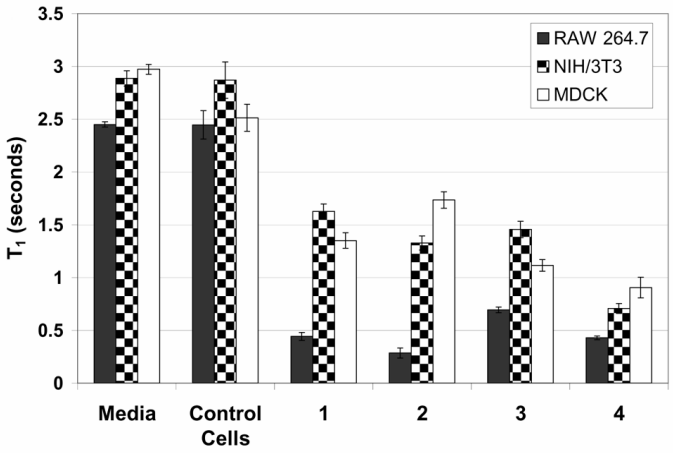

B

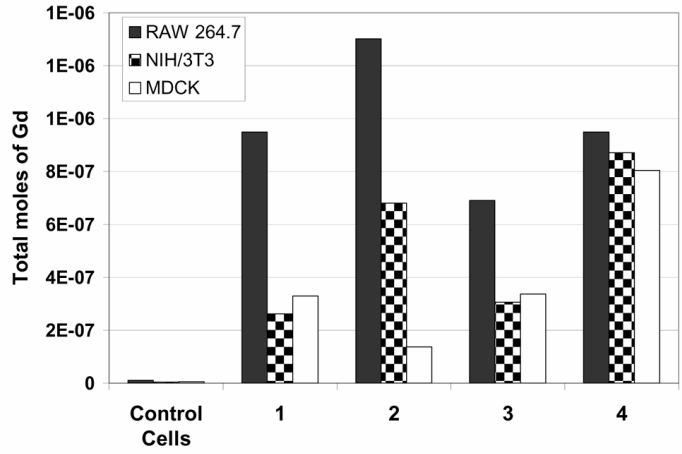

Figure 2.8 A T_1 study and the corresponding ICP-MS calculated gadolinium concentrations of NIH/3T3, RAW 264.7, and MDCK cells incubated with contrast agents **1**-**4**. (A) T_1 study of NIH/3T3, RAW 264.7, and MDCK cells incubated with 3.0 mM of **1**-**4** as well as untreated cells and media. Error bars represent one standard deviation of the slices taken (minimum 5 slices with 1 mm thickness). (B) ICP-MS calculated amount of Gd associated with the cells from the T_1 analysis. Total moles of Gd is shown in order to emphasize the inverse trend demonstrating that the relaxation rate is a function of the cellularly associated Gd concentration and not an anomaly of cell packing.

As the data shows, MDCK cells appear to be transport molecule dependent; allowing **3** and **4** to accumulate with increased efficiency (**Figure 2.3**). This dependency could be due to the differentiation of MDCK cells into columnar epithelium which may restrict active transport and limit the charge interaction between the cell membrane and molecules with multiple charges (**1** and **2**).[39, 40] In contrast, NIH/3T3 and RAW 264.7 transduction appears to be Gd(III) chelator dependent preferring DTPA (**2**, **4**) to DOTA based contrast agents (**1**, **3**).

In order to corroborate the quantitative cell studies and determine their utility as MR contrast agents, **1**-**4** (at the lowest incubated concentration, 3.0 mM) were tested for contrast enhancement via MRI. Comparison of the cells incubated with **1**-**4** in each image with either control cells or media (**Figure 2.9**) reveals increased signal intensity. Examination of **Figure 2.8** provides transduction efficiencies (given by T_1 values) that are identical to those outlined in the ICP-MS cell study (**Figure 2.3**).

The weak fluorescence quantum yield of Gd(III) and the current inability to directly visualize its in vitro location with sub-micron resolution required the use of SR-XRF to validate cellular uptake of the modified agents. Currently, hard, high-brilliance SR-XRF microprobes that employ Fresnel zone plates to focus incident X-rays can achieve sub-micron spatial resolution on comparatively thick (e.g., 10-20 μm) samples.[41, 42] The calculated attenuation length of similar organic material to the examined cells is 18.1 mm, therefore, only 0.06% of incident X-rays are absorbed by a 10 μm thick target cell.[43] This high elemental sensitivity and spatial resolution of SR-XRF microprobes make them well-suited for studying the interactions of Gd(III)-based contrast agents and single cells in vitro. By mapping individual cells, SR-XRF microprobe analyses complement bulk measurements performed by ICP-MS and MR imaging.

A

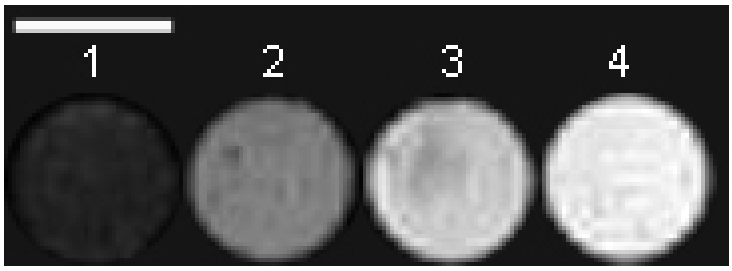

B

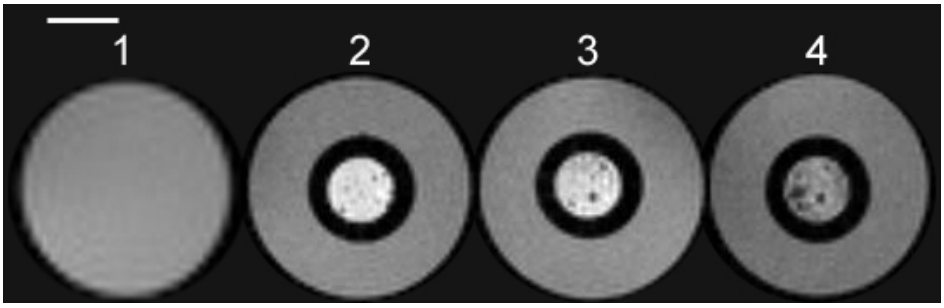

Figure 2.9 T_1-weighted, spin-echo MR images of NIH/3T3, RAW 264.7, and MDCK cells incubated with **1**-**4** at 9.4 T. (A) Incubations were performed on RAW 264.7 cells at 3.0 mM for 4 h. (1) Untreated cells; (2) cells incubated with **1**; (3) cells incubated with **2**; (4) cells incubated with **4**. (B) Samples (2–4) were incubated with **3** at 3.0 mM for 4 h. (1) Deionized water in 5 mm OD NMR tube; (2) NIH/3T3 cells (center) with an external phantom of NIH/3T3 media (outer ring); (3) RAW 264.7 cells (center) with an external phantom of RAW 264.7 media (outer ring); (4) MDCK cells (center) with an external phantom of MDCK media (outer ring). The dark spots throughout the cell images are due to air pockets created during cell packing. Images were obtained using a spin echo pulse sequence of T_R = 300 ms and T_E = 15 ms (FOV = 22 mm and slice thickness = 0.5 mm). The scale bars represent 1.5 mm.

Importantly, SR-XRF allows elemental mapping of the agents (**1**-**4**) without the use of organic fluorophores that may alter the transport properties of the agents.

As shown in **Figure 2.6**, each scanned cell incubated with complexes **1**-**4** dispalys substantial Gd fluorescence as compared with the control cells incubated with Gd(III)-DOTA, Gd(III)-DTPA, or in the absence of contrast agent (**Figure 2.7**). As expected, when the incubation concentration was increased to 10 mM, the Gd distribution patterns associated with the cells became more pronounced (**Figure 2.6B**). Complex **1** (arginine moiety) has a more diffuse pattern inside the cell whereas complex **3** (stilbene moiety) exhibits a more punctate pattern. This distribution may be explained by the amphipathic nature of the stilbene agents and their affinity to aggregate in aqueous media, or it may be due to cell specific uptake mechanisms.[26] However, the mechanism of uptake cannot be determined based on the data presented in this work as it focuses on the uptake efficiency of cell-permeable contrast agents and the quantification of the Gd associated with the cells.

As previously stated, SR-XRF can map and quantify elemental concentrations at femtogram levels.[31] However, due to the size of the cells (22 x 22 μm for MDCK cells), the resolution of the acquired elemental maps (raster scanned at 0.3 x 0.3 μm with a dwell time of 1.0 s/pixel), sample focusing (~ 1 h/cell), and total scan time per cell (~ 2.5 h/cell) made rigorous quantification of associated Gd by this technique feasible for only a small numbers of samples (see the Experimental Procedures Section). As expected, the ability to sample only a small number of cells gave rise to large variances in Gd concentration within a population. Nonetheless, these large standard deviations are simply an indication that contrast agent uptake is not homogenous within a given cell line even at a constant concentration and time.[44]

Conclusions

The data obtained from testing **1**-**4** with ICP-MS, SR-XRF, T_1 analyses, and MR imaging each provide unique information while corroborating the same transduction efficacy of the transport moieties. For example, the SR-XRF images demonstrate association of the agents with single cells and the ICP-MS data is quantitative evidence that the T_1 values and SR-XRF maps are a consequence of the Gd(III) contrast agents. The MRI and T_1 analyses prove that **1**-**4** are viable agents for MRI at the tested concentrations, and the images from **Figure 2.9** demonstrate the utility of ICP-MS and SR-XRF in prediction of relevant MR image enhancement

In conclusion, this investigation shows the ability of a polyarginine and stilbene functionalized MR contrast agent set to label three cell lines effectively enough to be visualized via MRI. The data obtained from ICP-MS, T_1 analyses, and acquired MR images covalidates the transduction efficiency of **1**-**4** within each cell line. SR-XRF was used to supplement these quantitative measurements by visualizing contrast agent association with single cells. The transduction efficiencies are not consistent across cells lines, therefore, selection of transduction moiety and Gd(III) chelator is an important consideration when developing intracellular MRI contrast agents.

Future Directions

Although SR-XRF is a powerful technique for assessing the feasibility and visualizing the location of cell-permeable MRI contrast agents, it requires equipment and personnel that are found in limited locations. Therefore, it would be advantageous to develop an agent that could be detected with greater ease. Given that the stilbene complexes of **3** and **4** have broad, long wavelength UV excitation spectra, an alternative to SR-XRF visualization, could be lanthanide resonance energy transfer (LRET). Based on possible luminescence sensitization by aromatic

A

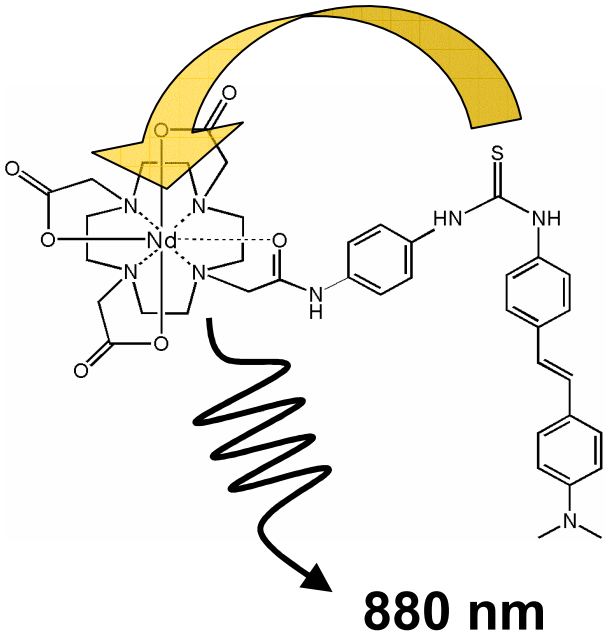

B

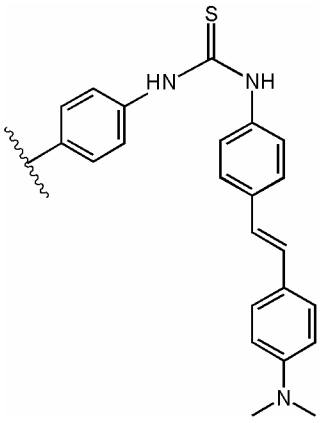

calculated
triplet excited state
is 13,380.75 cm^{-1}

Figure 2.10 Proposed lanthanide resonance energy transfer (LRET) probe. (A) Proposed structure of a cell-permeable LRET and MRI tunable contrast agent. (B) The truncated version of the stilbene moiety submitted to *ab initio* calculations.

antennas and the long-lived luminescent lifetimes of lanthanide ions,LRET systems involving DOTA and DTPA chelates have been the focus of many reports.[45-49]

In theory, each lanthanide-organic antenna couple emits a photon via a three-step process: antenna excitation, antenna to lanthanide energy transfer, and lanthanide luminescence. Optimally, the energy of the triplet excited state of the antenna needs to lie around 1500-1700 cm^{-1} above the emissive energy level of the accepting lanthanide.[46] If the energy gap is lower than 1500 cm^{-1}, then competing back-energy transfer occurs, if the gap is much higher than 1700 cm^{-1}, then efficiency of the energy transfer step is compromised. In addition to optimized energy states, the antenna should also be as spatially close to the lanthanide as possible.[50] Considering these parameters, cell-permeable contrast agent **3** was synthetically modified to decrease the lanthanide-stilbene distance, and the triplet excited state of a truncated version of the new complex was determined using *ab initio* calculations with a STO-3G basis set (**Figure 2.10**).[51, 52] Comparison of the calculated triplet state (13,380.75 cm^{-1}) to the lanthanide emissive levels of **Figure 2.11** highlighted one lanthanide that should be excited by the stilbene antenna, neodymium (emissive energy level at 11,460 cm^{-1}). In view of these results, the synthesis of a cell-permeable LRET contrast agent is proposed in **Scheme 2.4**. When metalated with Nd(III), this complex should have the ability to transduce cell membranes and be visualized with time-gated fluorescence microscopy at 880 nm. Now, if Gd(III) is used to metalate the complex, it will not only maintain identical cell membrane permeability, but it will be viable as a live-animal MR imaging probe. In summary, this agent will hypothetically be tunable to near-IR detection or non-invasive imaging (via MRI) while displaying identical cell uptake characteristics.

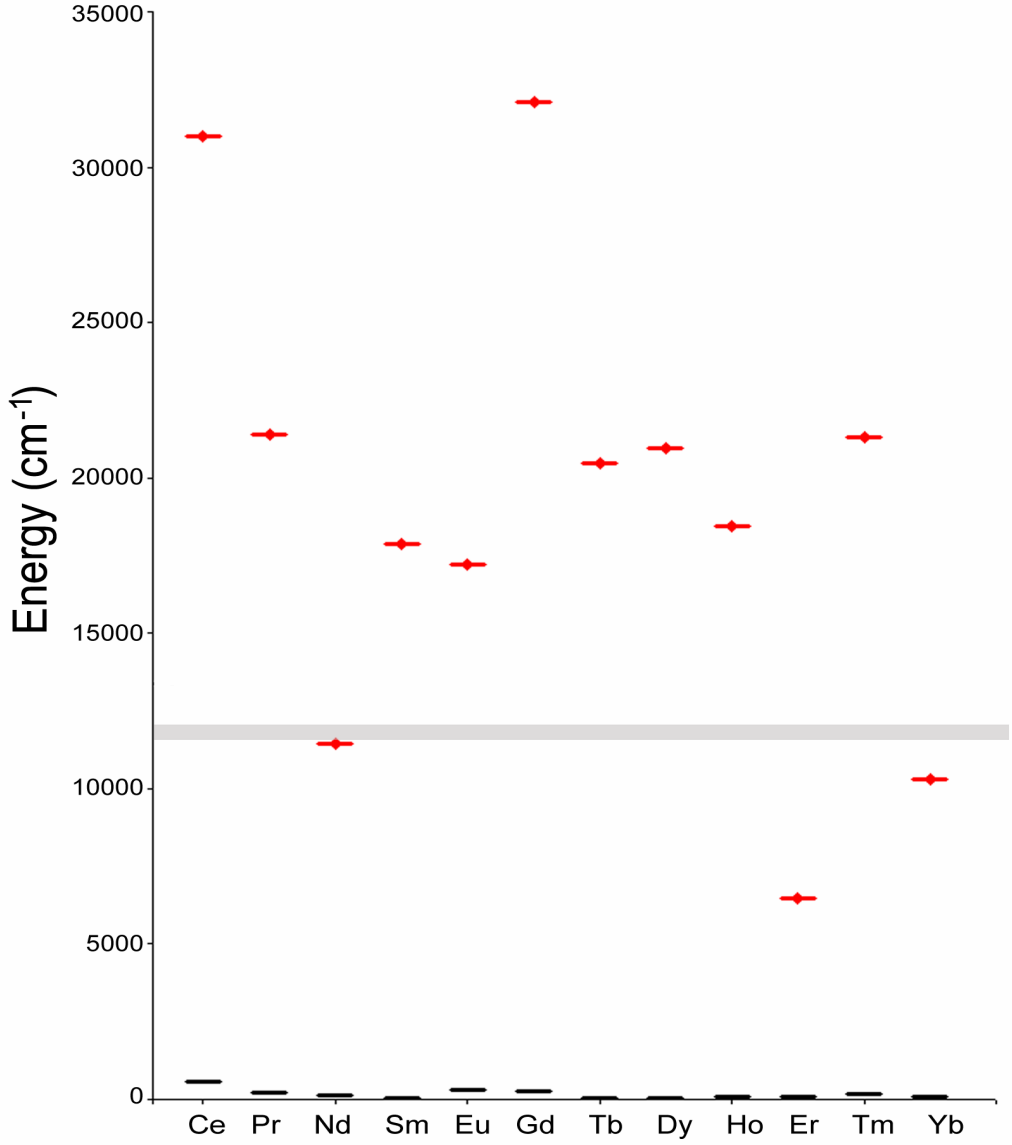

Figure 2.11 Chart of emissive lanthanide energy levels.[49, 53-56] The gray bar indicates the calculated triplet energy state of the truncated stilbene contrast agent (13,380.75 cm^{-1}) and an accompanying 1500 cm^{-1}. Neodymium's emissive energy state lies slightly below the optimal value for antenna-lanthanide transfer; therefore, LRET should be possible in this system.

Scheme 2.4 Proposed synthesis of tunable LRET and MRI contrast agent.

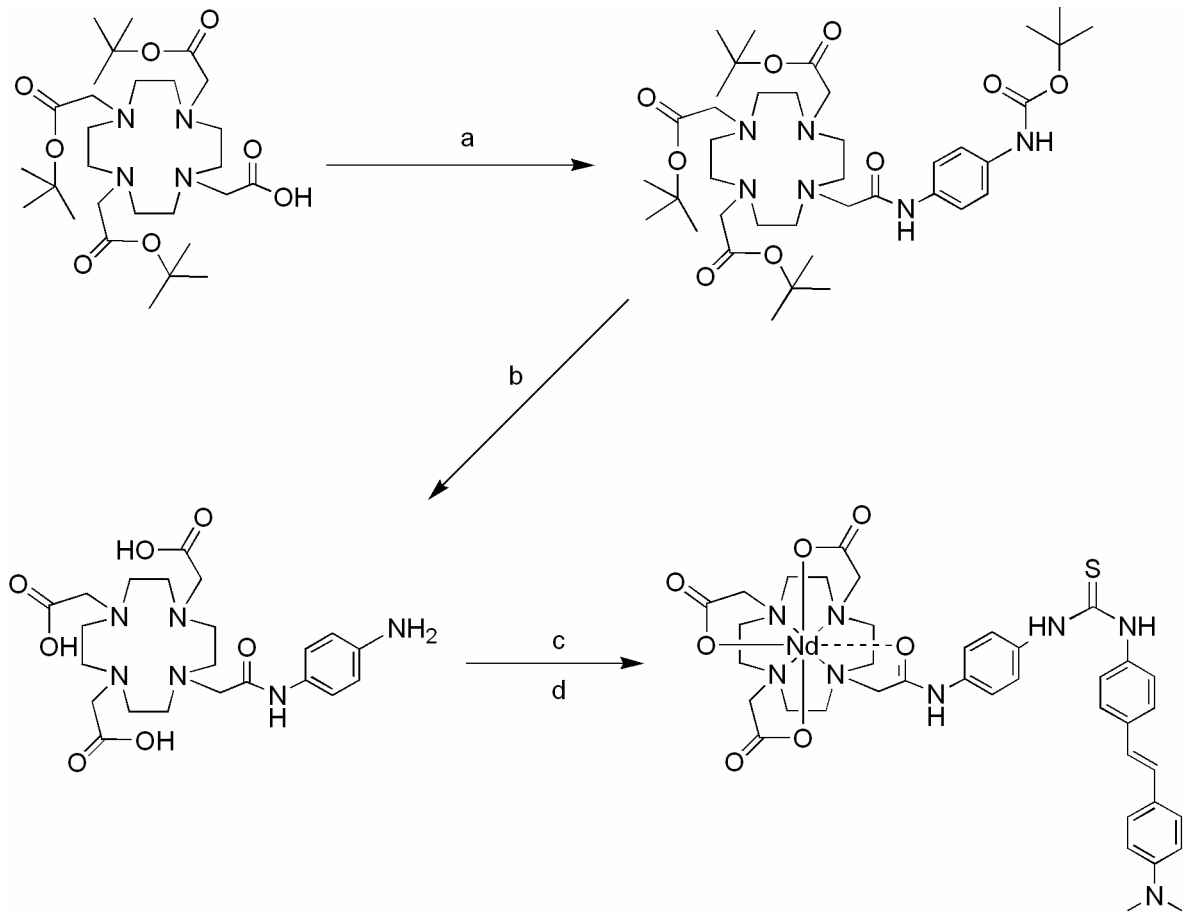

(a) N-*boc*-1,4-phenylenediamine, HATU, DIEA, DMF; (b) 95% TFA, 2.5% H_2O, 2.5% TIS; (c) **5**, DMF, 80 ºC; (d) $NdCl_3$, H_2O, pH 7.0

Experimental Procedures

All reagents and solvents were of the highest purity attainable from Aldrich (Milwaukee, WI) and TCI America (Portland, OR) unless otherwise noted. Modified Wang resin and amino acids were purchased from Novabiochem (San Diego, CA). NIH/3T3 cells, MDCK cells, and RAW 264.7 cells were purchased from ATCC (Manassas, VA). Also purchased from ATCC were Dulbecco's modified Eagle's medium (DMEM, with 4 mM L-glutamine modified to contain 4.5 g/L glucose and 1.5 g/L sodium carbonate) and Eagle's minimum essential medium (EMEM, with Earle's BSS and 2 mM L-glutamine modified to contain 1.0 mM sodium pyruvate, 0.1 mM nonessential amino acids, and 1.5 g/L sodium bicarbonate). Fetal bovine serum (FBS), calf bovine serum (CBS), and 0.25% trypsin/ethylenediaminetetraacetic acid (EDTA) solution were purchased from ATCC. Trypan blue, vent-cap flasks, multiwell plates, cell scrapers, and Dulbecco's phosphate buffered saline (DPBS) w/o calcium and magnesium were purchased from Fisher Scientific. 200 mesh London finder gold grids coated with a polymer backing (formvar) were purchased from Electron Microscopy Sciences (Hatfield, PA). Stem coaxial inserts with a reference capacity of 60 μL and 2 mm OD were obtained from Wilmad LabGlass (Buena, NJ, Catalog # WGS-5BL).

^{1}H and ^{13}C NMR spectra were obtained on a Varian Inova spectrometer at 400 and 100 MHz, respectively. Compounds were run in either $CDCl_3$ (7.27 and 77.23 ppm used as internal references for ^{1}H and ^{13}C NMR spectra, respectively) or due to solubility issues, D_2O with MeOH (4.80 and 49.00 ppm for ^{1}H and ^{13}C NMR spectra, respectively). Mass spectrometry samples were analyzed using electrospray ionization (ESI), single quadrupole mass spectrometry on a Varian 1200L spectrometer. Results reported for *m/z* are for $[M+H^+]^+$ or $[M-H^+]^-$. Elemental Analyses were performed at Desert Analytics Laboratory (Tuscon, AZ).

MR measurements were performed on a General Electric/Bruker Omega 400WB 9.4 T imaging spectrometer fitted with Accustar shielded gradient coils at 20 °C. Spin lattice relaxation times (T_1) were measured using a saturation recovery pulse sequence. Images were acquired using a T_1-weighted spin-echo pulse sequence on freshly harvested cells. ICP-MS was performed on a computer controlled PQ ExCell Inductively Coupled Plasma Mass Spectrometer. Cells were counted using a Bright-Line hemacytometer.

Complex **1** and **5** were synthesized following previously published procedures. Compound **7** was converted to **8** by following previously published procedures. [26, 28, 30]

Computational Parameters

Hyperchem 7.0 (Hypercube, Inc.; Gainesville, FL) was used to carry out all reported calculations. The triplet and singlet energies states were determined using a single-determinant self-consistent field (SCF) calculation with a STO-3G basis set and MP2 correlation energy.[51, 52] Additionally, an RMS gradient of 0.01 and SCF convergence of 0.0001 were set.

HPLC-MS

Analytical HPLC-MS was performed on a computer controlled Varian Prostar system consisting of a 410 autosampler equipped with a 100 μL sample loop, two 210 pumps with 5 mL/min heads, a 363 fluorescence detector, a 330 photodiode array (PDA) detector, and a 1200L single quadrupole ESI-MS. All separations were executed with a 1.0 mL/min flow rate using a Waters 4.6 x 250 mm 5 μm Atlantis C18 column, with a 3.1:1 split directing one part to the MS and 3.1 parts to the series-connected light and fluorescence detectors. Mobile phases consisted of Millipore Synthesis grade water (solvent A) and HPLC-grade acetonitrile (MeCN) (solvent B). Preparative HPLC was accomplished using a Varian Prostar system. Two Prostar 210 pumps with 25 mL/min heads fed a 5 mL manual inject sample loop. Detection was performed after a

20:1 split by a two-channel Prostar 325 UV-visible detector and, on the low-flow side, a HP 1046A fluorescence detector. The mobile phases were the same as in the HPLC-MS instrument. Preparative runs were on a Waters 19 x 250 mm 10 μm Atlantis C18 column.

Synchrotron Radiation X-Ray Fluorescence (SR-XRF) Analysis

Each of the three cell lines (NIH/3T3, MDCK, and RAW 264.7) was incubated with **1-4** at 3.0 mM or 10 mM concentrations. A matrix of varying contrast agents, cell lines, and incubation concentrations produced 24 unique samples. Mouse fibroblast cells (NIH/3T3) were grown in modified DMEM containing 10% CBS. Canine kidney epithelial cells (MDCK) were grown in modified EMEM containing 10% FBS. Mouse monocyte macrophage cells (RAW 264.7) were grown in modified DMEM containing 10% FBS. The NIH/3T3, MDCK, and RAW 264.7 cells were plated at 250,000, 150,000, and 500,000 cells/mL, respectively, in tissue culture treated Costar 12 well plates for 48 h. Compounds **1-4** were solubilized in the corresponding cell media for each cell line (described previously in this section) at a concentration of 3.0 and 10 mM (corroborated by ICP-MS; data not shown), filtered through a 0.2 μm syringe filter, and added to the cells. Following media addition, the cells were incubated at 37 °C in a 5% CO_2 atmosphere for 4 h. The media was removed, and the cells were rinsed in triplicate with room temperature DPBS. NIH/3T3 cells and MDCK cells were incubated with 250 μL of 0.25% trypsin/EDTA and collected. RAW 264.7 cells were harvested by cell scraping in 250 μL of RAW 264.7 media. The cells were counted with a hemacytometer and checked for viability using a trypan blue assay.[57] Cell suspensions were centrifuged (at 1,000 G) and the supernatant was removed leaving ~50 μL. Approximately 15 μL of this suspension was applied to formvar coated gold grids with a sterile glass Pasteur pipette for 1 min and the excess supernatant removed. The grids were then treated with ~15 μL of room temperature ethanol, followed by

removal of the ethanol, and drying at ambient temperature for 15 h. The cell coverage was approximately 15-30 cells/grid. The rest of the cell suspension was exposed to 500 μL of neat nitric acid at 70 °C for 4 h. The dissolved cells were diluted to 10 mL in a solution of 3% nitric acid and 5 ppb of indium as an internal standard. The samples were analyzed by ICP-MS. EM grids with cells were mounted onto a kinematic specimen mount for both visible light and X-ray fluorescence microscopy. The samples were examined on a light microscope (Leica DMXRE) and the cells to be scanned with SR-XRF were located on the grid relative to a reference point using a high spatial resolution motorized x/y stage (Ludl Bioprecision).

Synchrotron based scanning X-ray fluorescence microscopy was carried out at the 2-ID-E beamline of the Advanced Photon Source at Argonne National Laboratory (IL, USA). Hard X-rays (10 keV) from an undulator source were monochromatized using a single bounce Si <111> monochromator. The energy was selected to allow for efficient excitation of the Gd L lines, and also to enable the detection of the Zn K lines. A Fresnel zone plate (320 μm diameter, focal length f = 250 mm, X-radia, Concord, CA) was used to focus the monochromatic X-ray beam to a spot size of ~0.3 x 0.3 μm^2 on the specimen. The sample was raster scanned through the beam at room temperature under a helium atmosphere. At each scan position, a full fluorescence spectrum was acquired using an energy dispersive germanium detector (Ultra-LEGe detector, Canberra, Meriden, CT). Elemental content was determined by comparison of fitted sample spectra with NBS thin film standards 1832 and 1833 (NIST, Gaithersburg, MD) using MAPS software supplemented with fitting of fluorescence spectra at every pixel.[31]

MR Imaging and T_1 Analysis

NIH/3T3 cells, MDCK cells, and RAW 264.7 cells were grown in Corning brand tissue culture flasks (75 cm^2 with vent cap) and incubated in a 5% carbon dioxide incubator at 37 °C.

Cells were incubated with no contrast agent (incubated with corresponding media as controls) or 3.0 mM of compound **1**, **2**, **3** or **4** for 4 h at 37 °C in a 5% CO_2 atmosphere. Cells were rinsed in triplicate with room temperature DPBS. NIH/3T3 and MDCK cells were collected after exposure to 1 mL of 0.25% trypsin/EDTA and RAW 264.7 cells were harvested by exposure to 1 mL of RAW 264.7 media followed by cell scraping. Viable cells were then counted using a hemacytometer and a trypan blue stain. An average of 5,000,000 NIH/3T3 cells, 2,000,000 MDCK cells, and 12,000,000 RAW 264.7 cells were loaded into NMR tube coaxial inserts after centrifugation of the cell suspensions and removal of the supernatant there was approximately 100 μL of total volume left to add to the coaxial inserts. The cells were allowed to settle for 18 h into the 2 mm OD stem (60 μL reference capacity) of the insert. All MR data were collected at ambient temperature in a General Electric/Bruker Omega 400WB 9.4 T magnet (83 mm bore size) fitted with Accustar shielded gradient coils. Spin lattice relaxation times (T_1) were measured using a saturation recovery pulse sequence. Images were acquired using a T_1-weighted spin-echo pulse sequence with a repetition time (T_R) of 300.8 ms and an echo time (T_E) of 15.0 ms. After the T_1 measurements and spin echo images were acquired, the cell suspensions (100 μL) were removed from the coaxial inserts using a 20 gauge stainless steel needle. These suspensions were diluted to 1 mL with H_2O. Cell count and viability was then determined. After cell counting, the cell suspensions were digested at 70 °C for 4 h in 1 mL of concentrated nitric acid. The dissolved cells were diluted to 10 mL in a final solution of 3% nitric acid and 5 ppb of indium as an internal standard. The samples were analyzed by ICP-MS.

Synthesis of Gd(III)-DTPA-$(Arg)_8$ (**2**)

Polystyrene-based Wang resin containing a Fmoc protected arginine residue (3.0 g, 0.58 mmol/g) was swelled in CH_2Cl_2 (3 x 10 min) and washed with peptide synthesis grade

dimethylformamide (DMF) (4 x 10 min). The resin was treated three times with a solution of 20% piperdine in DMF (10 min) and the deprotected resin was washed with DMF (4 x 10 min). In a separate vial, Fmoc protected Pbf-arginine (2.82 g 4.35 mmol), *o*-(7-Azabenzotriazol-1-yl)-*N*,*N*,*N*',*N*'-tetramethyluronium hexafluorophosphate (HATU) (1.32 g, 3.48 mmol), and *N*,*N*'-diisopropylethylamine (DIEA) (1.12 g, 8.70 mmol) were dissolved in approximately 3 mL of DMF. The resulting solution was added to the deprotected resin and nitrogen was bubbled through the mixture for 6-8 h. The peptide solution was removed from the resin which was subsequently rinsed with DMF (4 x 10 min). This procedure was repeated a total of seven times in order to achieve the synthesis of an 8 amino acid polyarginine oligomer bound to the Wang resin.

The resin (1.0 g, 0.58 mmol/g) was deprotected with the piperdine solution and washed with DMF as described above. In a separate vial, diethylenetriamine-*N*,*N*,*N*',*N*',*N*''-pentaacetic dianhydride (DTPA-dianhydride) (0.720 g, 2.00 mmol) and DIEA (0.369 g, 2.90 mmol) were dissolved in a minimal amount of anhydrous DMF. The resulting solution was added to the deprotected resin and nitrogen was bubbled through the mixture for 6-8 h. The peptide solution was removed and the resin was washed with DMF, CH_2Cl_2, and MeOH (4 x 10 min each). Following the methanol washes, the resin was dried under vacuum. A solution of 95% trifluoroacetic acid (TFA), 2.5% triisopropylsilane (TIS), and 2.5% H_2O (50 mL) was added to the resin and nitrogen was bubbled through the mixture for 1 h. The resin was filtered and to the filtrate was added methyl tert-butyl ether (MTBE) (40 mL) to precipitate a white solid that was subsequently washed with MTBE (3 x). The solid was dissolved in 30 mL of water and freeze-dried to yield white flaky crystals of the chelate-peptide conjugate, DTPA-Arg_8 (0.42 g 44%) with ESI-MS (*m/z*): 1643.02; calc. for $C_{62}H_{119}N_{35}O_{18}+H^+$: 1642.83.

To a solution of DTPA-Arg_8 (0.289 g, 0.176 mmol) in water, was added $Gd(OH)_3$ (0.0410 g, 0.176 mmol). The reaction mixture was heated to 80 ºC and stirred for 16 h. The mixture was allowed to cool to room temperature and the pH was adjusted to 11.0 with concentrated NH_4OH. The resulting suspension was filtered using a 0.2 μm syringe filter and purified using preparatory HPLC with the Waters Atlantis column. An elution profile of a linearly increasing MeCN gradient from 0-98% over 45 min was used. The desired fraction (retention time: 8.43 min by UV at 220 nm with Gd fluorescence at Ex. λ = 274 and Em. λ = 315) was collected and freeze-dried to yield a white powder which was found to be **2** (0.275 g, 87%) by ESI-MS (*m/z*): 1797.00 with Gd(III) isotope pattern; calc. for $C_{62}H_{115}GdN_{35}O_{18}+H^+$: 1796.84.

Synthesis of 4-isothiocyanato-4'-(N,N-dimethylamino)stilbene (**5**)

To a stirring solution of 4-amino-4'-(*N*,*N*-dimethylamino)stilbene (1.00 g, 8.39 mmol) in $CHCl_3$ (50 mL) at 0 ºC were added simultaneously a solution of K_2CO_3 (1.16 g, 8.39 mmol) in H_2O (30 mL) and a solution of thiophosgene (0.640 mL, 8.39 mmol) in $CHCl_3$ (30 mL). The reaction was allowed to warm to ambient temperature over 5 h. The organic layer was separated, washed with H_2O, dried over $MgSO_4$, filtered through celite, and concentrated *in vacuo* to yield an orange solid (1.04 g, 93%). ^1H NMR ($CDCl_3$): δ = 2.99 (s, 6H), 6.70 (d, *J* = 8.0 Hz, 2H), 6.84 (d, *J* = 15.6 Hz, 1H), 7.04 (d, *J* = 15.6 Hz, 1H), 7.17 (d, *J* = 8.0 Hz, 2H), 7.41 (d, *J* = 8.0, 2H), 7.44 (d, *J* = 8.0 Hz, 2H); ^{13}C NMR (CDCl3): δ = 40.59, 112.53, 122.83, 125.42, 126.22, 127.03, 127.99, 128.79, 130.49, 134.84, 137.71, 150.40; ESI-MS (m/z): 281.00; calc. for $C_{17}H_{16}N_2S+H^+$: 281.10. Anal. Calcd for $C_{17}H_{16}N_2S$: C, 72.82; H, 5.75; N, 9.99. Found: C, 73.12; H, 5.72; N, 9.80.

Synthesis of 2-(4-nitrobenzyl)- 1,4,7,10-tetraazacyclododecane tetrahydrochloride (**7**)

Using a modified literature procedure, macrocycle **6** (1.61 g, 4.79 mmol) was dissolved in 140 mL of anhydrous THF at 0 ºC and treated with dropwise addition of a solution of BH_3-THF (1.0 M, 33.5 mL, 33.5 mmol) under a nitrogen atmosphere.[28, 30] After addition was complete, the reaction mixture was heated to reflux for 24 h and concentrated *in vacuo*. The resulting residue was dissolved in 200 mL of MeOH and refluxed for 12 h. This mixture was dried *in vacuo*, dissolved in MeOH (100 mL) and refluxed for 12 h. This procedure was repeated with 100 mL of EtOH, and the remaining residue was dissolved in 90 mL of EtOH. HCl gas was continuously bubbled through the EtOH solution at 0 ºC until the temperature stopped rising. Upon complete addition of HCl, the resulting chalky white mixture was brought to reflux for 12 h and concentrated *in vacuo* to approximately 30 mL. This reaction mixture was cooled to 0 ºC and the resulting white precipitate was filtered under nitrogen, washed with cold diethyl ether (Et_2O), and dried under vacuum. Recrystallization of **7** was accomplished from boiling MeOH to yield white crystals (1.06 g, 65%). ^{1}H NMR (D_2O): δ = 2.90-3.22 (m, 20H), 3.42 (m, 1H), 7.50 (d, *J* = 8.5 Hz, 2H), 8.20 (d, *J* = 8.5 Hz, 2H); ^{13}C NMR (D_2O with MeOH reference): δ = 38.06, 42.20, 43.88, 44.36, 45.35, 45.58, 46.00, 49.12, 55.64, 125.44, 131.90, 146.32, 148.07; ESI-MS (*m/z*): 308.18; calc. for $C_{15}H_{25}N_5O_2+H^+$: 308.20.

Synthesis of Gd(III) {4,7,1-triscarboxymethyl-6-[4-(3-{4-[2-(4-dimethylaminophenyl)-vinyl]phenyl}-thioureido)benzyl]-1,4,7,10-tetraazacyclododec-1-yl}-acetic acid (**3**)

Compound **7** (0.497 g, 0.758 mmol) was added to a stirring solution of 4-isothiocyanato-4'-(*N*,*N*-dimethylamino)stilbene (0.233 g, 0.834 mmol) in anhydrous DMF (10 mL). This solution was brought to 80 ºC for 12 h. The crude mixture was concentrated to dryness and dissolved in 10 mL of H_2O. $GdCl_3 \cdot 6H_2O$ (0.282 g, 0.758 mmol) was added, and the pH of the

solution was adjusted to 7.0 with 1 M NaOH. This solution was allowed to stir for 12 h at which the pH was adjusted to 11.0 with 1 M NaOH. The resulting yellow solution was filtered with a 0.2 μm syringe filter and freeze-dried to yield a crude yellow/brown solid. This solid was purified via a Sephadex G-25 size exclusion column in H_2O. The fractions containing pure product were combined and freeze-dried to yield a light yellow solid (0.645 g, 77%). ESI-MS (m/z): 942.30 with Gd(III) isotope pattern; calc. for $C_{40}H_{47}GdN_7O_8S$-H^+: 942.24. Anal. Calcd for $C_{40}H_{47}GdN_7O_8S \bullet Na \bullet 2\ H_2O$: C, 47.94; H, 5.13; N, 9.78. Found: C, 47.76; H, 4.92; N, 9.61.

Synthesis of Gd(III) -thioureido)phenyl]propyl}-carboxymethylamino)ethyl]-carboxymethyl-amino}-acetic acid (**4**)

p-Aminobenzyl diethylenetriaminepentaacetic acid (0.560 g, 1.12 mmol) was prepared via a literature procedure and was added to a stirring solution of **5** (0.410 g, 1.46 mmol) in anhydrous DMF (10 mL).[30] The resulting solution was brought to 80 ºC for 12 h. The crude mixture was concentrated to dryness and dissolved in 10 mL of H_2O. $GdCl_3 \cdot 6H_2O$ (0.417 g, 1.12 mmol) was added, and the pH of the solution was adjusted to 7.0 with 1 M NaOH. This suspension was allowed to stir for 12 h after which the pH was adjusted to 11.0 with 1 M NaOH. This solution was filtered with a 0.2 μm syringe filter and freeze-dried to yield a brown solid that was purified via a Sephadex G-25 size exclusion column in H_2O. The fractions containing pure product were combined and freeze-dried to yield a light orange solid (0.647 g, 56%). ESI-MS (m/z): 930.30 with Gd(III) isotope pattern; calc. for $C_{38}H_{41}GdN_6O_{10}S$ -H^+: 930.18. Anal. Calcd for $C_{38}H_{41}GdN_6O_{10}S \bullet 3\ Na \bullet 2\ H_2O$: C, 44.05; H, 4.38; N, 8.11. Found: C, 43.87; H, 4.50; N, 8.22.

CHAPTER 3:

Cell-Permeable MRI Contrast Agents with Increased Cell Retention

The text in this chapter was taken in part from:

Endres, P. J.; MacRenaris, K. W.; Vogt, S.; Meade, T. J., Cell-Permeable MRI Contrast Agents with Increased cell Rentention via Disulfide Exchange. *in preparation for Bioconj. Chem.*

Introduction

With the advent of wide-bore, high field magnets and improved pulse sequences, the technique of magnetic resonance imaging (MRI) is revolutionizing the field of molecular imaging.[1-3] This versatile, non-invasive technique is now capable of producing images with submicron resolution using routine conditions on commercially available instruments.[4] These exciting advances have been supplemented with an array of Gd(III) contrast agents, some conjugated to scaffolds (nanoparticles, antibodies, and proteins), others sensitive to biochemical markers (metal ion concentration, enzyme kinetics, or pH), and some with the ability to permeate cellular membranes (via cell penetrating peptides or active surface receptor uptake).[5-11] The focus of this work is upon this latter group of cell-permeable contrast agents, specifically the optimization of MR signal contrast longevity via disulfide bond incorporation.

The biological role of thiol-containing molecules has been actively explored and described in the literature, therefore, much is known about the major active species and their relative concentrations.[12] The pseudo-tripeptide of glutathione (GSH) is generally recognized as the most abundant and subsequently most active thiol species in biological environments. Previous work has shown that due to the drastically higher intracellular GSH concentration (~ 1-10 mM) of living cells compared to the extracellular blood plasma (~ 2 μM), thiol levels can be exploited to create a chemical release switch for selective intracellular cargo delivery.[13-15] Similar chemistry has been applied to the previously reported intracellular MR contrast agents (Chapter 2) in order to combat the recently observed cellular leaching.[16] This has produced a set of imaging probes that retain their cell permeability while displaying significantly longer intracellular lifetimes. Such an agent could passively label and non-invasively track the fate of

transplanted tissues and cells as well as lead to the design of other novel MR contrast agents with the ability to penetrate and be retained beyond vascular spaces.

Based on previous work by our group and others, an octamer of arginine residues allows cell membrane transduction of various cargo molecules, including fluorophores and contrast agents (e.g. fluorescein and Gd(III)-DOTA, respectively).[17-19] However, as will be shown, the ability of these current compounds to cross cell membranes is not unidirectional. Once inside the cell, the arginine-modified agents begin to leach out of the cell, forming a decay curve of intracellular contrast agent concentration, consequently decreasing the MR signal over time. Therefore, novel contrast agents containing a disulfide bond between the Gd(III) chelating moiety (either a DOTA or DTPA based molecule) and the transduction moiety (octamer of arginine residues) were synthesized and tested for improved cell-associated retention (**Figure 3.1**). By exploiting the inherent disulfide reducing environment of mammalian cells, these new contrast agents will be cleaved from their cellular transduction domains upon passage across the cellular membrane. This separation shows prolonged cellular lifetime of the Gd(III) by leaving the chelated metal with no method of cellular exit.

Results

Synthesis of the Thiol-Reactive Contrast Agents

The synthesis of the pyridyl-activated Gd(III) chelators was accomplished by coupling the amine terminated AETP to an activated form of either the DTPA or DOTA chelate (**Scheme 1**). The commercially available diethylenetriaminepentaacetic acid-dianhydride (DTPA-dianhydride) is inherently activated to amide bond formation, and the 1,4,7-tris(acetic acid-*tert*-butyl ester)-10-acetic acid-1,4,7,10-tetraazacyclododecane (DOTA-tris-TB) was activated *in situ* by the commonly used aminium salt, HATU. Both reactions required an excess of the base

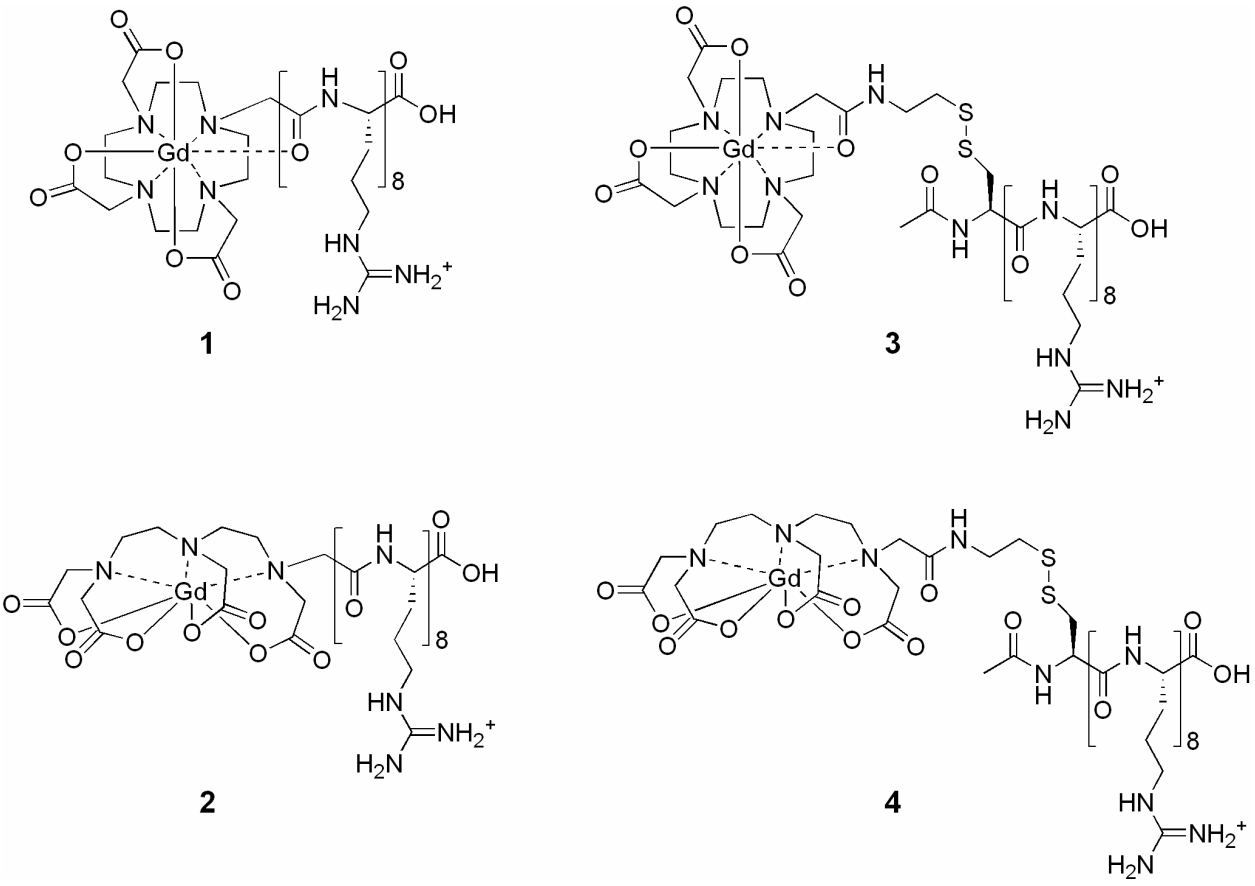

Figure 3.1 Structures of the first generation arginine-modified, cell-permeable contrast agents and second generation disulfide functionalized, cell-permeable contrast agents. (**1**) Gd(III)-DOTA-Arg_8; (**2**) Gd(III)-DTPA-Arg_8; (**3**) Gd(III)-DOTA-SS-Arg_8; and (**4**) Gd(III)-DTPA-SS-Arg_8.

DIEA, in order to deprotonate the hydrochloride salt starting material (AETP) and to aid in amide bond formation. Upon purification via preparative RP-HPLC, compounds **4** and **5** were afforded with acceptable yields (68 and 63%, respectively). The peptide RRRRRRRRC was synthesized without automation using standard Fmoc solid-phase synthesis methodology on pre-loaded Wang resin.[16, 17] After the addition of the cysteine residue, the resin was treated with acetic anhydride to end-cap the peptide's terminal amine. Due to the envisioned proximity of this terminal free amine to the later conjugated Gd(III) ion and to create peptide sequences with minimal structural differences as compared to the previously published Arg_8-MRI contrast agents, (e.g. charge and no terminal amine) this end-capping step was performed prior to cleavage and deprotection from the resin.[16, 17]

In order to optimize the thiol exchange reaction needed to produce **8** and **9**, the pyridyl-activated chelates (**6** or **7**) were added quickly to stirring solutions of the end-capped Arg_8-Cys oligomer under a nitrogen atmosphere in degassed phosphate buffer at pH 8.0 (**Scheme 3.2**). The optimal synthetic yields for these reactions were achieved when **6** and **7** were added in equimolar quantities to the thiol-containing peptide (**5**). It was found that adding higher amounts of the free thiol (**5**) actually lowered overall yield by facilitating increased disulfide oxidation and disulfide exchange of the desired product. This effect was also seen in previous disulfide exchange reactions.[20] Metalation of the cell-permeable contrast agents was achieved by adding $Gd(OH)_3$ to the phosphate buffered solutions of **8** and **9**. To ensure that Gd(III) chelation was maximized, the buffered solutions were lowered to pH 6.0 and allowed to stir for 7 days under a nitrogen atmosphere. The structures of the peptide conjugates **5**, **8**, and **9** were confirmed by NMR, ESI-MS, and HPLC, while the small molecule chelates were characterized by NMR, ESI-MS, HPLC and EA.

Scheme 3.1 Synthesis of the pyridyl-activated Gd(III) chelators.

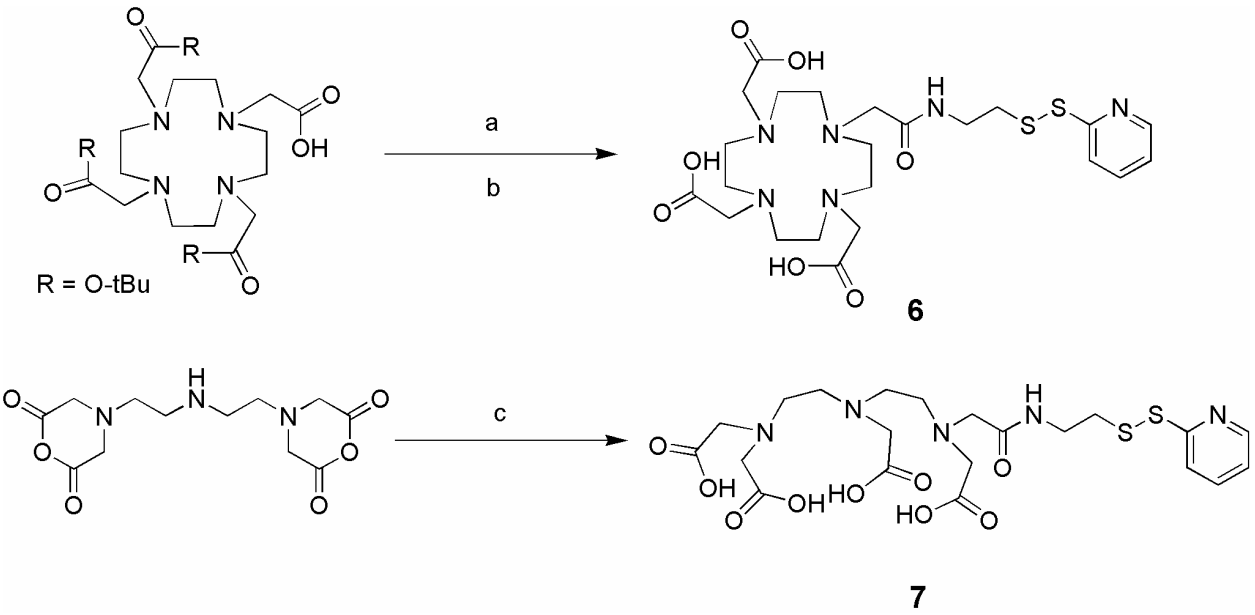

(a) AETP, HATU, DIEA, DMF; (b) 95% TFA, 2.5% H_2O, 2.5% TIS; (c) AETP, DMSO, and H_2O.

Scheme 3.2 Synthesis of the disulfide functionalized, intracellular contrast agents (**3**) Gd(III)-DOTA-SS-Arg_8 and (**4**) Gd(III)-DTPA-SS-Arg_8.

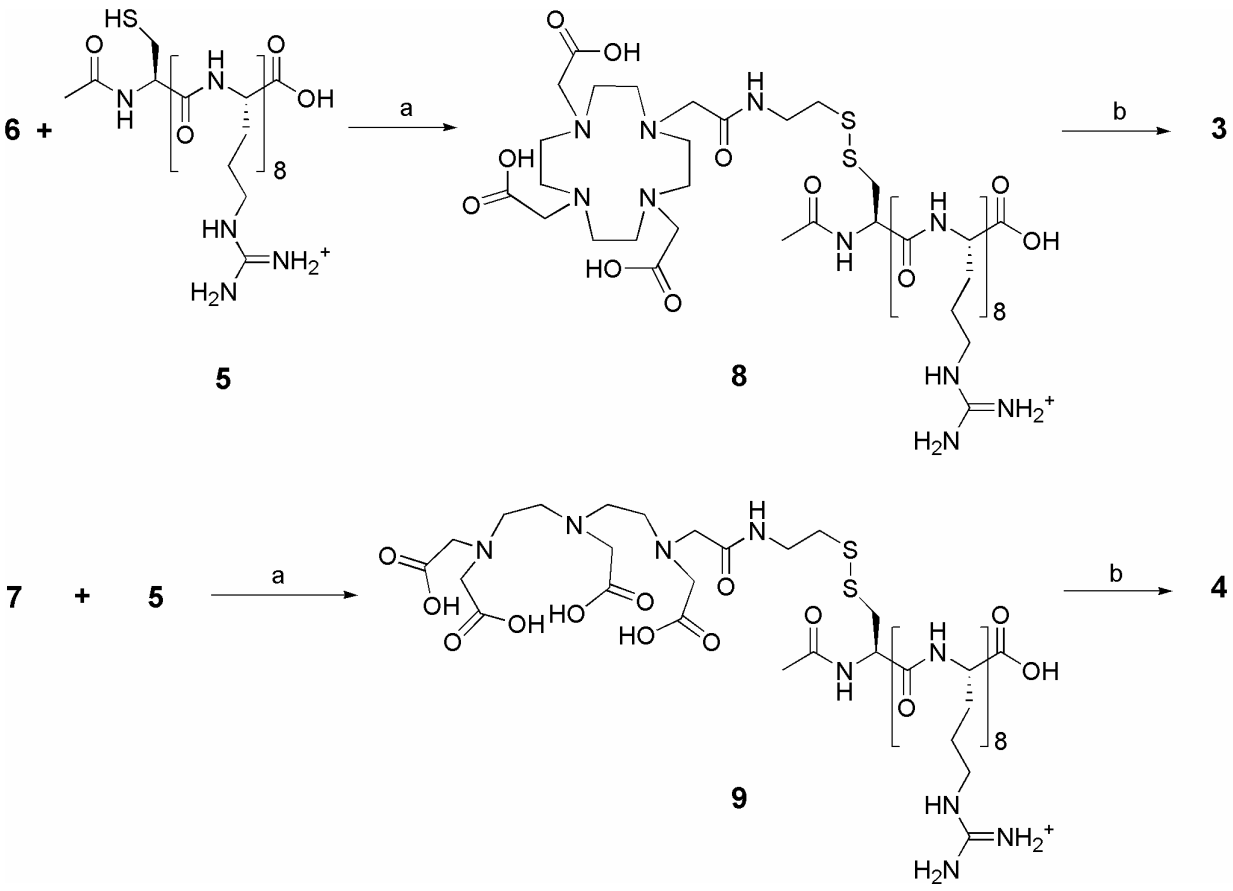

(a) stirring for 3 days under N_2 atmosphere in 10 mM phosphate buffer at pH 8.0; (b) $Gd(OH)_3$, 5 days, pH 6.0.

Contrast Agent Relaxivity, *q*, and τ_m

The relaxivity measurements (r_1, $mM^{-1}s^{-1}$) provided in **Table 3.1** show the relative enhancement of water proton relaxation rates per Gd(III) ion for complexes **1**-**4**. These rates were measured at 1.5 and 14.1 T in order to provide data at both clinical and research-oriented field strengths. As expected, the r_1 rates are strongly field dependant; however, **1**-**4** maintain higher relaxation rates than the currently available contrast agents Gd(III)-DOTA and Gd(III)-DTPA at both measured field strengths. The relaxation rates of **1**-**4** were then tested over a wide pH range (1.0-12.5) in order to determine the feasibility of these agents to relax water molecules at almost any biologically relevant pH (**Figure 3.2**). At very low pH (~ 1-4), the relaxivity for contrast agents **1**-**4** is consistent with Gd(III) disassociation from the chelating cage. Conversely, at high pH (~ 9-13), the relaxivity shows a decrease that is most likely attributable to a slightly open structure (more so in the case of **1** and **2** than in **3** and **4**) which allows carbonate ion binding or association of the metal center to the slowly exchanging hydroxyl ions.[15, 21, 22] However, in the applicable biological range of pH 4-8, all four of the cell-permeable agents display relatively constant relaxivity values.

The Tb(III) analogs of complexes **1**-**4** (complexes **10**-**13**) were subjected to fluorescence measurements so that the number of complex-associated water molecules could be determined. These measurements provided the following data (ms^{-1}): 10: k_{H2O} = 0.566, k_{D2O} = 0.315; 11: k_{H2O} = 0.635, k_{D2O} = 0.331; 12: k_{H2O} = 0.644, k_{D2O} = 0.397; 13: k_{H2O} = 0.671, k_{D2O} = 0.390. These values were applied to an equation listed in the Experimental Procedures section, resulting in the *q* values provided in **Table 3.1**. As with most small molecule DOTA and DTPA-based contrast agents where one carboxylic acid arm has been replaced with an amide, these values all reflect one bound water molecule within the acceptable experimental error of ±0.5.[2, 23]

Table 3.1 Relaxometric properties of the Arg_8-conjugated complexes **1-4** at pH 7.4 and 37 °C.

	Relaxivity ($mM^{-1}s^{-1}$)[a]		q	τ_m (ns)[c]
	60 MHz (1.5 T)	600 MHz (14.1 T)[b]		
(Gd(III)-DOTA-Arg_8) **1**	6.8	3.50	1.0	916
(Gd(III)-DTPA-Arg_8) **2**	7.8	3.45	1.2	1105
(Gd(III)-DOTA-SS-Arg_8) **3**	6.9	3.52	0.9	840
(Gd(III)-DTPA-SS-Arg_8) **4**	7.4	3.46	1.1	1327
Gd(III)-DOTA	3.2	2.12	1.2[d]	243[e]
Gd(III)-DTPA	3.8	2.09	1.2[d]	303[e]

[a] Measured in 100 mM phosphate buffer, [b] measured at ambient temperature (~ 25 °C), [c] calculated at 25 °C, [d] data from ref 24, [e] data from ref 25.

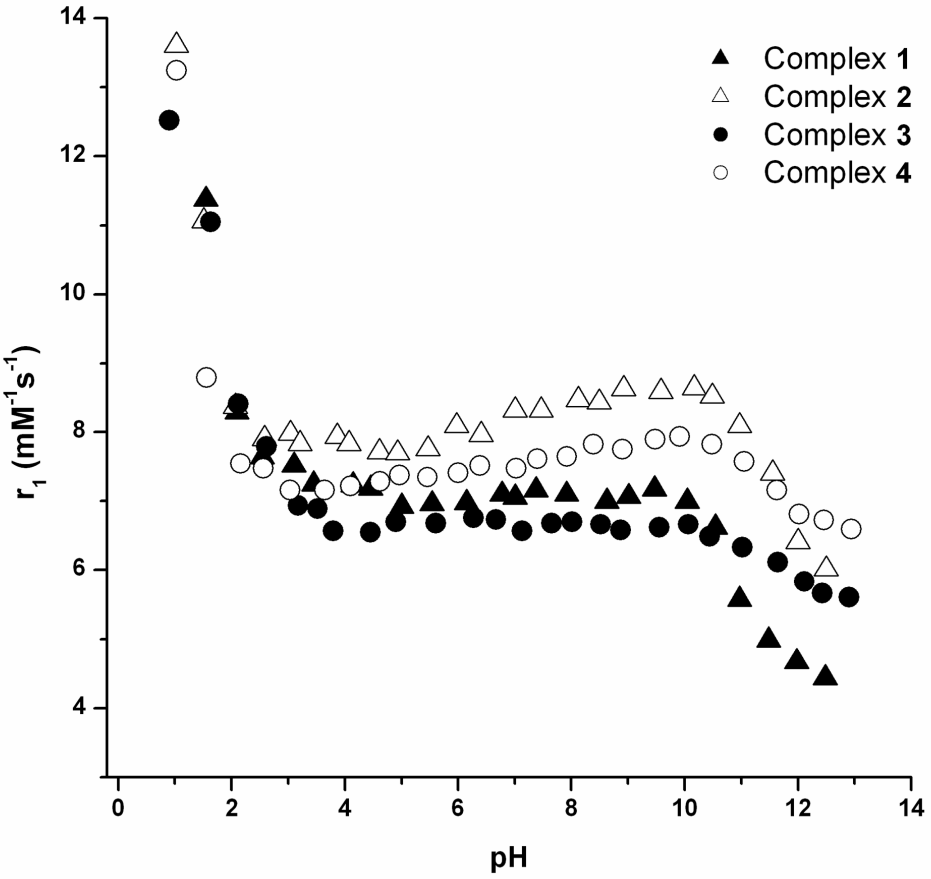

Figure 3.2 The millimolar relaxivities (r_1, $mM^{-1}s^{-1}$) of contrast agents **1-4** plotted against pH.Values were measured at 60 MHz and 37 °C. The contrast agents are represented as: **1** (closed triangles), **2** (open triangles), **3** (closed circles), and **4** (open circles). Comparison of closed data point markers allows facile correlation of the two DOTA-based ligands as does open data point markers for the two DTPA-based ligands.

To evaluate the mean residence lifetime (τ_m) of the water molecule coordinated to the metal center of complexes **1-4**, temperature dependent ^{17}O-NMR was performed. Plotting only the paramagnetic contribution of the observed ^{17}O-NMR transverse relaxation rate of water gave the expected bell-shaped curves for each complex (**Figure 3.3**). This data was then subjected to the fitting parameters outlined in the Experimental Procedures section.[26-28] The fitted ^{17}O vs. temperature (T) profiles revealed the τ_m values displayed in **Table 3.1**. Notice that the values for **1-4** are relatively close to each other, and decidedly higher than the previously reported optimal value for Gd(III) MR contrast agents of 10 ns.[23]

Although these times are substantially slower than DOTA and DTPA, such a discrepancy can be explained. Substitution of an acetate arm to an amide linkage (as in the case of **1-4**) lessens the normal steric crowding around the metal center and decreases the overall molecular charge of the metalated complexes.[29, 30] Both factors negatively affect τ_m, and such values are similar to those obtained for other amidated DOTA and DTPA structures.[31-33] Normally deviation from optimal τ_m values would cause concern, but in this case, small molecule chelates at high fields (> 20 MHz), the relaxivity value is dominated by another parameter, the rotational correlation motion (τ_R).[34] Consequently, the dependence on τ_R in this system is so dominant that it nearly alleviates any decrease in relaxivity that could have resulted from the less-than-optimal τ_m.[30]

In Vitro Disulfide Cleavage Assay

To assess thiol-mediated release of the chelated Gd(III) from the disulfide-linked arginine oligomer, varying equivalents of GSH were added to a solution of **4** and the cleavage product was quantified via HPLC-MS. The samples were made by adding increasing amounts of GSH, from 0.25:1 to 4:1 (GSH : 4), to a stock solution of **4** (1.0 mM in DPBS). These samples

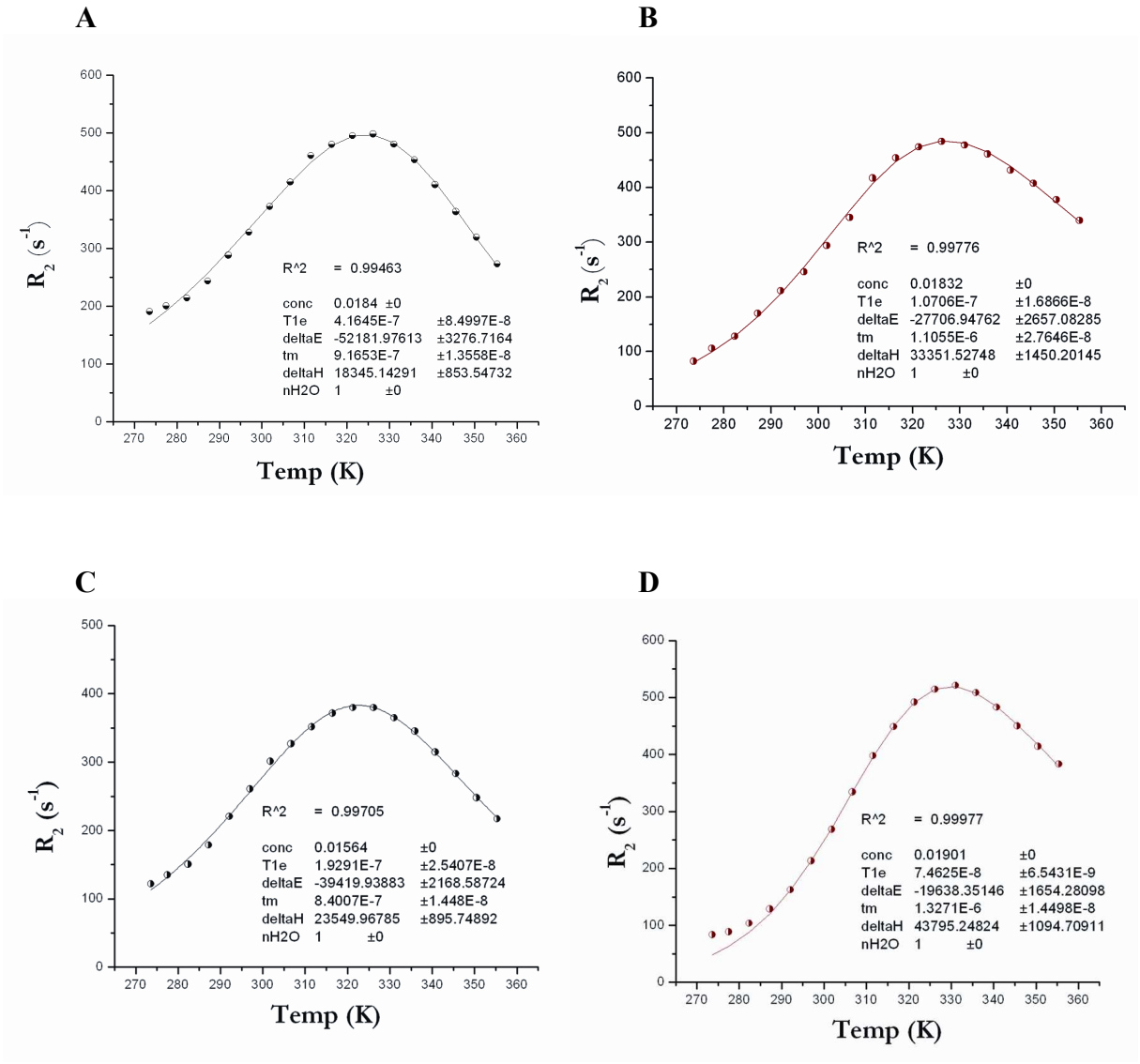

Figure 3.3 Determination of τ_m by ^{17}O transverse relaxation rate measurements of disulfide functionalized MRI contrast agents **1**-**4** at 25 °C. (A) Raw ^{17}O data and τ_m fitting of compound **1**, (B) compound **2**, (C) compound **3**, and (D) compound **4**. The relaxation data were fit to these four parameters: τ_m (water exchange rate), $\Delta H^{\ddagger}$ (activation enthalpy), T_{1e} (electronic relaxation rate), and ΔE_{T1e} (activation energy of T_{1e}). Black is used to highlight DOTA chelates, while red is used to highlight DTPA chelates.

were made on a staggered timeline so that each sample could be incubated in a 37 °C waterbath for 4 h, mimicking the conditions present in the later described cell culture environment, prior to LC-MS analysis. Separation was accomplished by a gradient ramp starting with 0% MeCN which reached 60% MeCN at 40 min before returning to 0% MeCN. The speculated cleavage reaction (**Figure 3.4**) was tracked by plotting the total ion count (TIC) of the desired product (Gd(III)-DTPA-GSH, m/z = 912^{+} amu) and the multiply-charged starting material (**4**, m/z = 3, 673^{+} amu) as their concentrations changed in response to GSH addition (**Figure 3.5**). The molecular ions chromatograms (912^{+} and 673^{+}) were then integrated so that the total area under the curve could be calculated (**Table 3.2**).

Cellular Retention

To elucidate uptake and retention of complexes **1**-**4**, confluent cultures of NIH/3T3 cells were incubated with 0.10 mM of **1**-**4** for 4 h. After a 4 h incubation, the cells were washed three times with DPBS (time = 0, Initial Amt.), placed in fresh media, and allowed to equilibrate for 1 h. Three cell samples and aliquots of the corresponding cell media were then removed for analysis. This procedure was repeated 4 more times for a total of 5 washes, where the last wash was allowed to leach for 24 h. To provide an accurate representation of contrast agent location, each cell culture well was treated as a single system consisting of two Gd(III)-containing phases: (i.) the cells and (ii.) the external media. After each sample was quantified via ICP-MS, this method allowed for the overall assessment of accumulated, retained, and leached Gd(III) for the cells at five consecutive time points. This data shows that prior to any leaching, non-disulfide complexes **1** and **2** show increased uptake efficacy over **3** and **4** (**Table 3.3**). However, closer examination of **Table 3.3** shows that after the washes, cells treated with **1** and **2** lose a significant amount of Gd(III), more than those treated with **3** and **4**. These absolute quantities were then

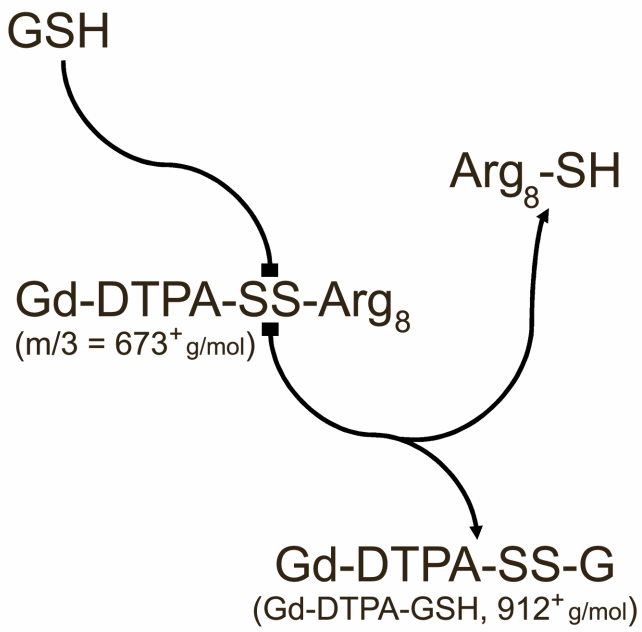

Figure 3.4 Reduction of Gd(III)-DTPA-SS-Arg_8 (**4**) by GSH

.

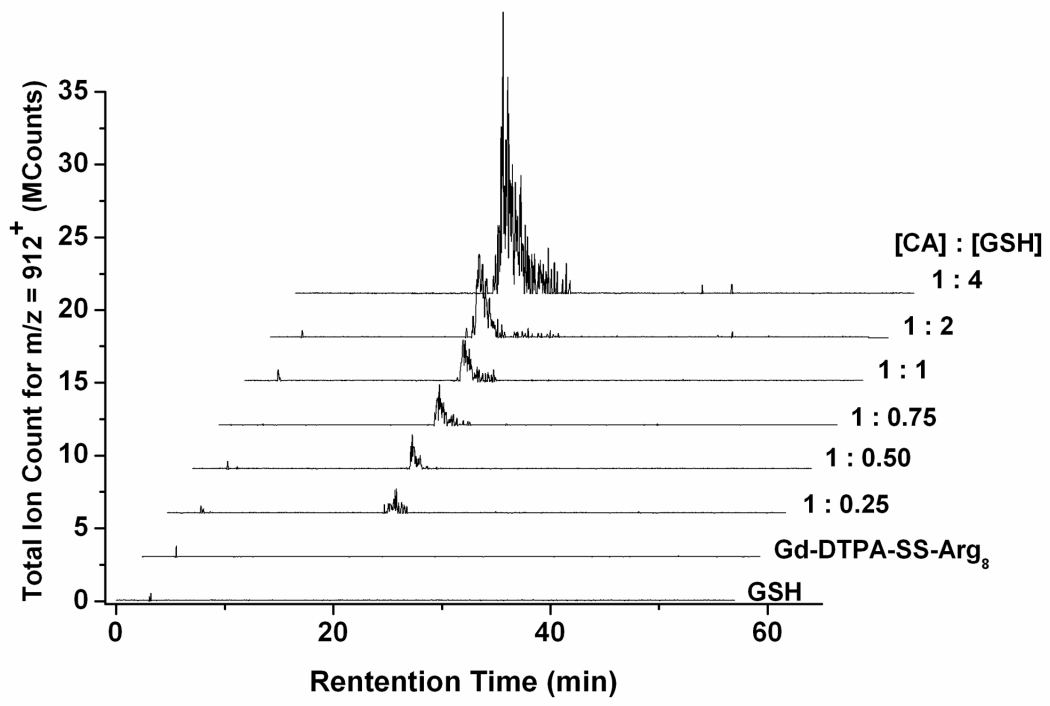

Figure 3.5 HPLC-MS visualized cleavage of contrast agent **4** with a free thiol. Treatment of **4** with increasing concentrations of GSH leads to disulfide exchange and subsequent product formation (Gd(III)-DTPA-GSH, m/z = 912^{+}).

Table 3.2 Quantified cleavage of Gd(III)-DTPA-SS-Arg_8 (**4**) via disulfide exchange with GSH.

[**4**] : [GSH]	Starting Material **4** (Gd(III)-DTPA-SS-Arg_8) (TIC*10^8 of *m/z* = 3; 673^+)	Product Gd(III)-DTPA-GSH (TIC*10^8 of *m/z* = 1; 912^+)
1 : 4.0	0.414	5.94
1 : 2.0	0.687	2.37
1 : 1.0	1.60	0.719
1 : 0.75	1.90	0.739
1 : 0.50	2.06	0.469
1 : 0.25	2.14	0.210
4	2.68	NA[a]
GSH	NA	NA

[a] NA = not applicable, no discernable peak to integrate

divided by their respective initial concentrations (those collected at time = 0) in order to elucidate the relative amount of each agent retained within the system (**Figure 3.6**). As can be readily seen in **Figure 3.6**, the incorporation of a disulfide linkage between the transduction moiety and Gd(III) chelate of these cell-permeable contrast agents drastically improves cellular retention (e.g. from 15 → 40% in the case of **1** vs. **3** in the NIH/3T3 cell line).

Synchrotron Radiation X-Ray Fluorescence (SR-XRF) Analysis

Synchrotron based XRF analysis was performed to determine the cellular association of complexes **1-4**. For each sample, three to five randomly chosen areas (100 x 100 μm) were raster-scanned at high speed (10 ms dwell time) to determine cell density within that region. From these randomly chosen areas, the one with the greatest cell coverage was raster scanned with longer dwell times to acquire a multi-cell containing image with high resolution (60 x 60 μm with 0.25 μm^2 pixel size). This image acquisition procedure was followed for all the collected and displayed elemental maps. Following our previous report, these high-resolution elemental maps provide pixel by pixel data sets that globally confirm, map, and quantify the Gd distribution within each sampled area. An example of this data is displayed in **Figure 3.7** where the leaching and non-leaching data of **2** and **4** in the NIH/3T3 cell line is compared. Fluorescence maps of inherent biological elements (e.g., P and S) accompany each Gd image to prove cellular existence and provide boundaries. The overlay column combines the data from the three elemental maps (P, S, and Gd columns) to provide information on the areas of multi-element overlap. Owing to the proximity of the Gd and Fe fluorescence energy levels, it is important to deconvolute potential peak overlap between Fe and Gd fluorescence. This was accomplished using modified gaussian curves that were fitted at each scan position to the

Table 3.3 Total quantities of **1**-**4** associated with NIH/3T3 cells in culture after a 1.0 mM incubation for 4 h.

	NIH/3T3 Cell Line [a]			
Complex	**1**	**2**	**3**	**4**
Initial Amt.	13.6 ±0.36	15.3 ±1.0	2.45 ±0.22	2.23 ±0.04
Wash 1 (1 h)	3.39 ±0.03	3.87 ±0.15	1.18 ±0.09	1.12 ±0.16
Wash 2 (2 h)	3.04 ±0.21	3.58 ±0.03	1.16 ±0.02	1.07 ±0.02
Wash 3 (3 h)	2.77 ±0.26	3.27 ±0.10	1.05 ±0.02	0.97 ±0.07
Wash 4 (4 h)	2.37 ±0.22	3.26 ±0.24	1.03 ±0.05	0.94 ±0.04
Wash 5 (24 h)	2.04 ±0.08	2.59 ±0.06	0.97 ±0.06	0.92 ±0.03

[a] Units are in moles*10^{-11} and error is given as one standard deviation of its respective value.

* Cell culture was performed by Keith MacRenaris.

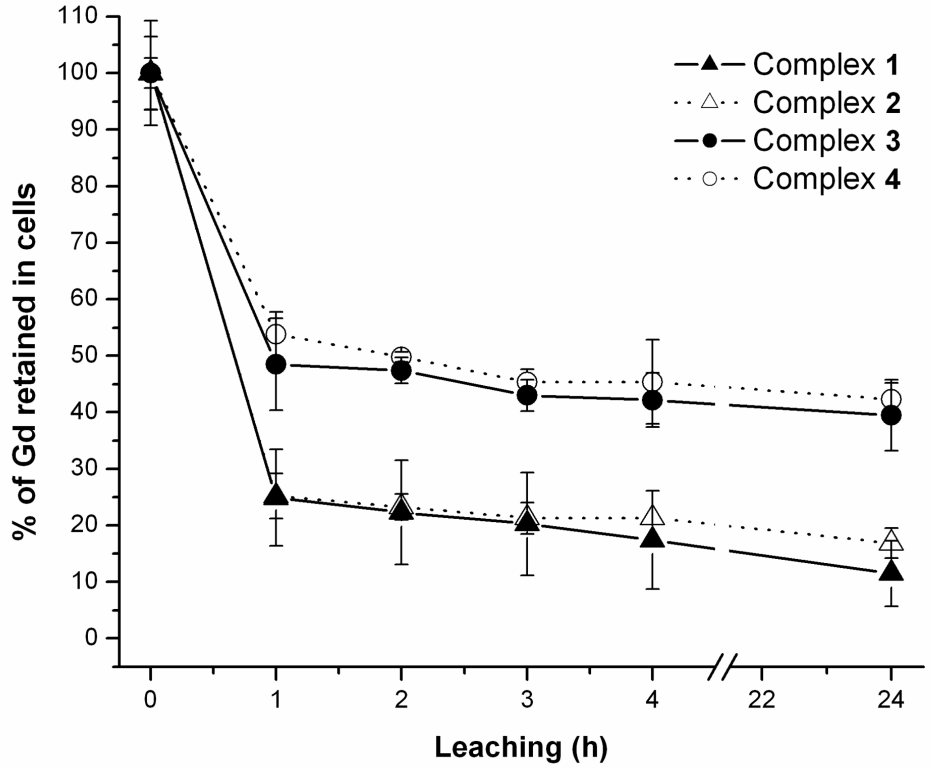

Figure 3.6 The percentage of Gd(III) associated with the NIH/3T3 cells as a function of the initial uptake concentration. DPBS washes were done on the hour leaching time points displayed. The contrast agents are represented as: **1** (closed triangles), **2** (open triangles), **3** (closed circles), and **4** (open circles). Comparison of closed data point markers allows facile correlation of the two DOTA-based ligands as does open data point markers for the two DTPA-based ligands.

acquired X-ray fluorescence spectra.[35] Images of complexes **1** and **3** are displayed in **Figure 3.8**. The top two rows of images displayed in **Figures 3.7** and **3.8** clearly show the extent to which leaching has depleted the NIH/3T3 cells of associated gadolinium when treated with the non-disulfide contrast agents (**1** or **2**). Conversely, when the cells are treated with disulfide linked contrast agents (**3** or **4**), they retain a large amount of gadolinium post-leach (bottom 2 rows of each figure).

MR Imaging and T_1 Analysis

In order to assess the feasibility of the disulfide linkage to increase cell retention and maintain MR image contrast over an extended time period, NIH/3T3 cells were again incubated with 1.0 mM of **1**-**4**. After the cells were harvested and placed in glass capillary tubes, they were imaged via MRI. Shown in **Figure 3.9A**, the cells incubated with complexes **1** and **2** exhibit a significantly brighter signal than the control cells. However, after following the washing procedure outlined for the SR-XRF and ICP-MS data (4 h, with washes at the hours) the cells incubated with **1** and **2** have a drastically lower intensity in the MR image. This loss of intensity, due to leaching of the contrast agent, is much less in the case of the cells incubated with complexes **3** and **4**. Shown in **Figure 3.9B**, these cells display intensities that when compared to their respective non-leached samples, are visually similar and show almost no loss of signal intensity.

Discussion

Arginine- bound cell-permeable contrast agents **3** and **4** were prepared via thiol-activated pyridyl intermediates to create cell-permeable MR-active conjugates that are linked to cell transduction moieties via a disulfide bond. These agents are structurally similar to **1** and **2**, however, unlike their non-disulfide counterparts (**1** and **2**), contrast agents **3** and **4** must be

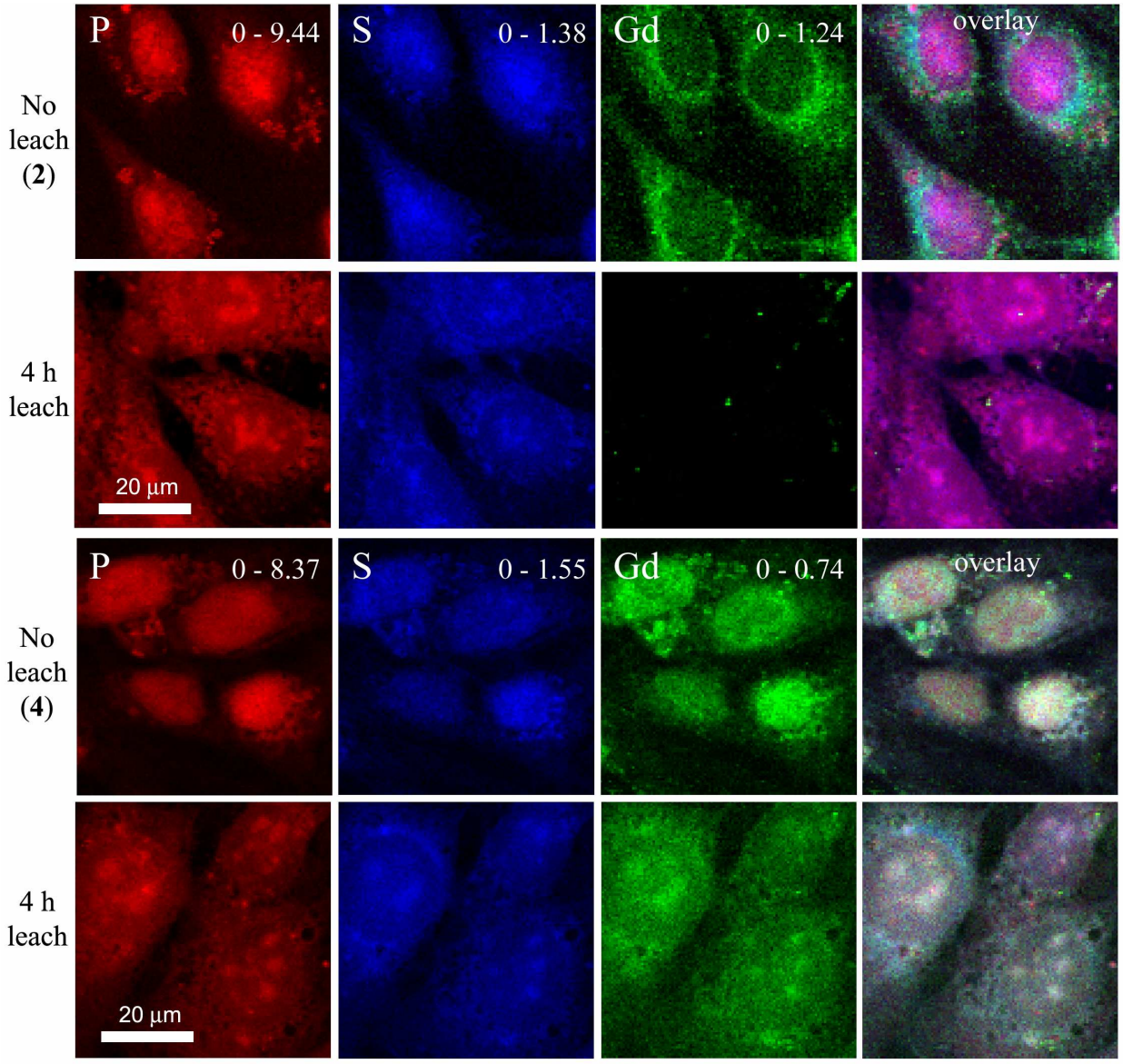

Figure 3.7 XRF images of NIH/3T3 cells treated with contrast agents **2** and **4**. Images are shown for time = 0 (No leach) and after 4 h (of leaching). Phosphorus is mapped in red, sulfur in blue, and gadolinium in green. The scale bars represent 20 µm. Note that each column of images is scaled to its respective maximum value (displayed at the upper right corner and given in $\mu g/cm^2$).

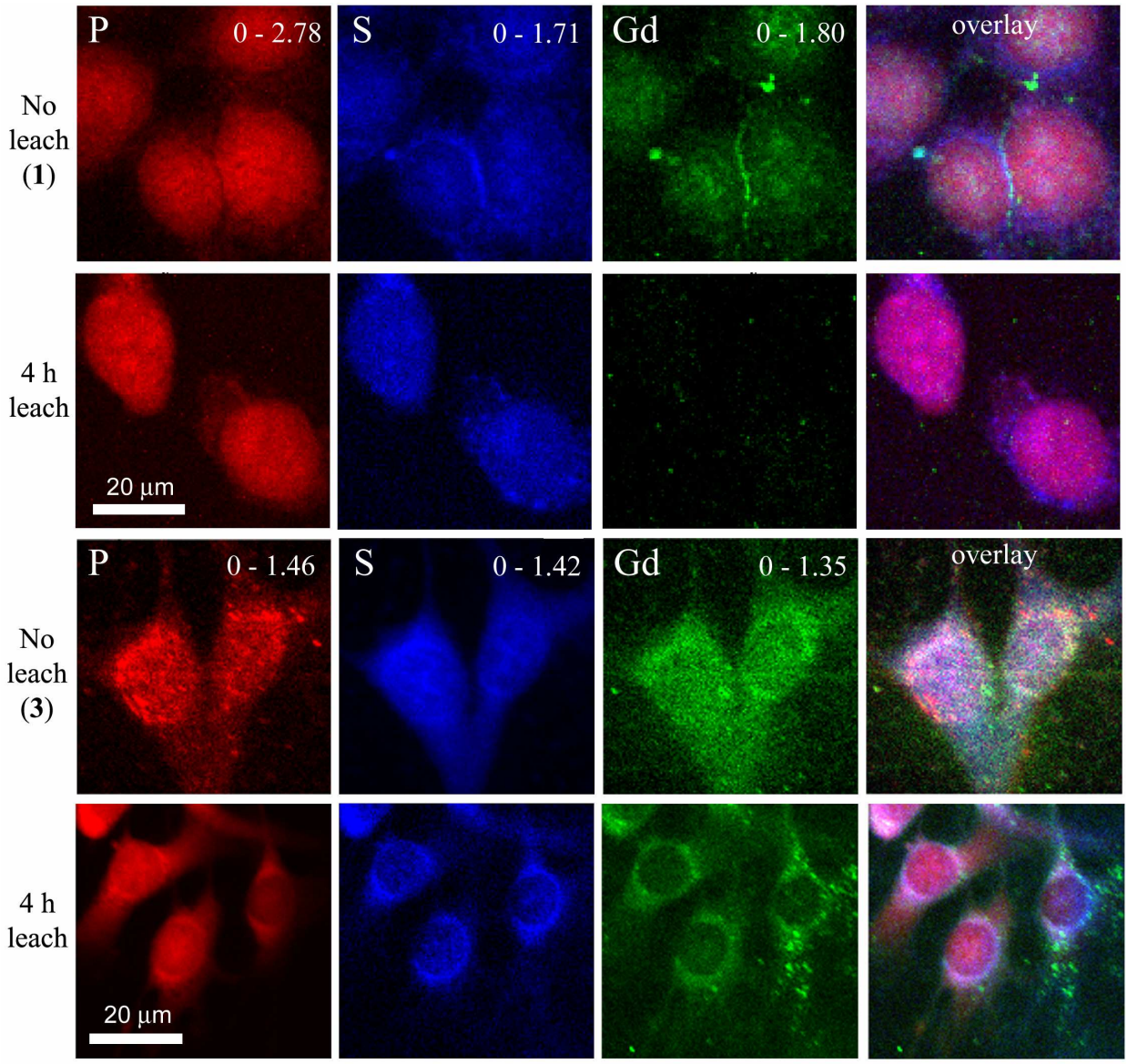

Figure 3.8 XRF images of NIH/3T3 cells treated with contrast agents **1** and **3**. Images are shown for time = 0 (No leach) and after 4 h (of leaching). Phosphorus is mapped in red, sulfur in blue, and gadolinium in green. The scale bars represent 20 µm. Note that each column of images is scaled to its respective maximum value (displayed at the upper right corner and given in $\mu g/cm^2$).

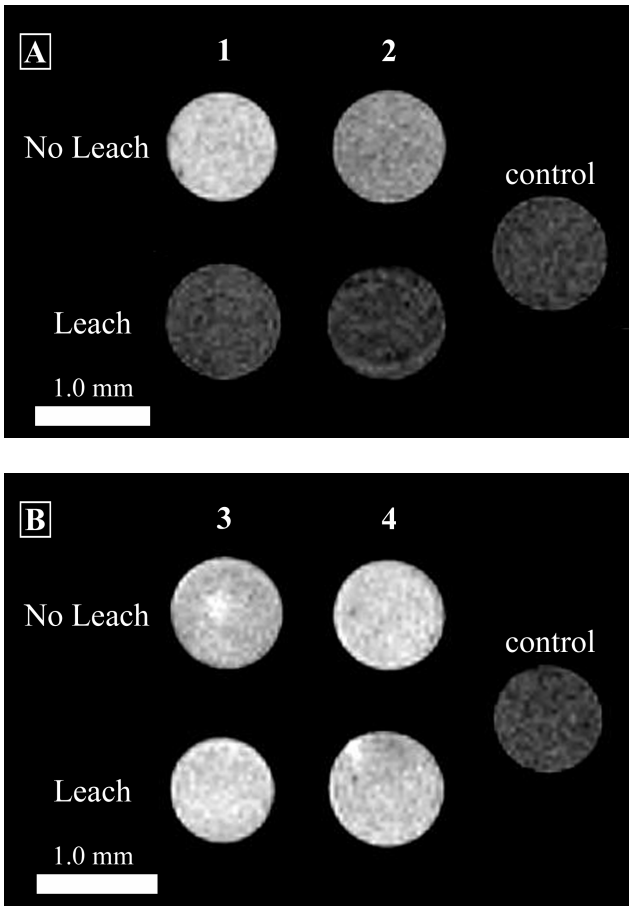

Figure 3.9 T_1-weighted MR images of NIH/3T3 cells incubated with complexes **1**-**4**. The 'Leach' rows are the cell populations that were allowed to leach for 4 h with washes of DPBS at the hours. The control cells were not incubated with contrast agent but were harvested and packed following the same procedure. (A) Image of the cell-permeable contrast agents, **1** and **2**. (B) Image of the disulfide-cleavable cell-permeable contrast agents, **3** and **4**. Images were acquired at 14.1 T within a FOV of 10 x 10 mm (matrix size 256 x 256) and a slice thickness of 1.0 mm. The scale bar represents 1.0 mm. T_1 values and student *t*-tests confirming statistically significant differences are given on the following page.

Sample name	**Avg. T_1** time (ms)	**Std. Dev.** (ms)		***t* test comparison** (value x *to* value y)	**Meets 95% confidence level?**
Fig. 3.9A: **1** *No Leach*	1847	94		contrast agent **1** No Leach *to* Leach	Yes
Fig. 3.9A: **1** *Leach*	2773	123		contrast agent **2** No Leach *to* Leach	Yes
Fig. 3.9A: **2** *No Leach*	2415	99		contrast agent **3** No Leach *to* Leach	No
Fig. 3.9A: **2** *Leach*	2824	138		contrast agent **4** No Leach *to* Leach	No
Fig. 3.9A: **control**	3017	111			
Fig. 3.9B: **3** *No Leach*	1687	63		contrast agent **1** Leach *to* Control	Yes
Fig. 3.9B: **3** *Leach*	1899	78		contrast agent **2** Leach *to* Control	Yes
Fig. 3.9B: **4** *No Leach*	1671	35		contrast agent **3** Leach *to* Control	Yes
Fig. 3.9B: **4** *Leach*	1834	59		contrast agent **4** Leach *to* Control	Yes
Fig. 3.9B: **control**	2912	72			

Fig. 3.9-cont. T_1 values and student *t*-tests confirming statistically significant differences. Student's *t*-tests were calculated in Origin 7 SR2 (Origin Lab, Northampton, MA) at a 95% confidence level with 8 degrees of freedom, independent testing, and a null hypothesis value (minimum acceptable time difference) of 100 ms. At least 5 slices per sample were averaged.

coupled to their respective Gd(III) chelating moieties off-resin and under strict pH and equivalents control. Although such procedures do negatively impact the overall synthetic time frame, yields remain acceptable. Once conjugated to the end-capped Arg_8-Cys, compounds **8** and **9** are metaled with $Gd(OH)_3$ to provide a set of cell-permeable MR contrast agents with anti-leaching properties.

The small, yet possibly significant changes made to **1** and **2** in order to incorporate the disulfide bond were then tested to determine their affect on relaxometric properties. As can be seen from **Table 3.1**, the coordination environment around the Gd(III) ion, expressed by the *q*, τ_m, and relaxivity measurements, has not been significantly changed in spite of the synthetic differences between non-disulfide (**1** and **2**) and disulfide (**3** and **4**) agents. Even under large pH variations, relaxivity still remains relatively constant (**Figure 3.2**). Such characterization and stability makes all four contrast agents excellent choices for exploitation as cell labeling compounds in a non-leaching environment (**Table 3.3**, Initial Amount).

Before subjecting the disulfide functionalized agents to cell culture models, time was taken to explore their cleavage tendencies in vitro. As is seen in **Figure 3.4**, each disulfide functionalized agent should undergo exchange or reduction with endogenous thiols, especially GSH.[12] Such mechanisms should cleave the Gd(III) chelate from its cell-penetrating polyarginine oligomer and leave the chelated Gd(III) with no mode of cellular exit. The longevity of the disulfide linkage was tested by incubating agent **4** at 37 °C in the presence of increasing quantities of GSH. **Table 3.2** shows the full quantification of this cleavage assay; however, **Figure 3.5** provides a qualitative picture of the results. As the amount of GSH increases, so does the amount of cleaved product (Gd(III)DTPA-GSH) detected via HPLC-MS, whereas the amount of detected starting material (**4**) decreases. This trend continues through

ratios of [GSH] : [**4**] that reach 4:1. This data tells us that although disulfide cleavage begins at very low GSH concentrations, only 0.25 equivalents, complete cleavage is not obtained even at GSH concentrations that are 4 times that of the contrast agent. Such kinetics, although not optimal, do allow some insight into the cell retention properties experienced when these agents were tested in NIH/3T3 cell culture.

Shown in **Table 3.3**, the cellular uptake of **1**-**4**, when incubated with a standardized initial concentration, demonstrates that **1** and **2** accumulate within the NIH/3T3 cells with greater efficiency than **3** and **4** (Initial Amt., **Table 3.3**). This observation is most likely attributed to the inherent nature of the cell line, and possible hydrogen bonding of the Gd(III) ion to the guanidinium groups of the arginine oligomer when the Gd(III) chelate is conjugated via the cysteine's side chain (**3** and **4**) instead of the peptide's semi-rigid backbone (**1** and **2**).[16] The latter hypothesis of metal to arginine back-binding would decrease the number of surface-displayed guanidinium groups available to facilitate membrane translocation, which has been shown to negatively impact cell uptake.[19, 36]

Closer examination of the initial uptake values of **1** vs. **2** shows that the NIH/3T3 cell line prefers the negatively charged DTPA over the neutral DOTA chelate when the structure of the transduction moiety is held constant. Conversely, in the case of **3** vs. **4**, the neutral DOTA chelate is preferred over the charged DTPA. However, the uptake discrepancies between arginine-bound DOTA and DTPA were expected and have been previously reported.[16] In contrast to the lower initial uptake amounts, the percentage of gadolinium retained in the cells post-leaching, last row in **Table 3.3**, implies that incorporation of the disulfide bond into **3** and **4** has a significant positive effect on long term contrast agent retention. Represented in **Figure 3.6**, the role of the disulfide moiety as it pertains to retention of the cell-permeable contrast agents is

made obvious: addition of the reactive disulfide linkage (**3** and **4**) increases the cell retention of the Gd(III) chelate 3.5 and 2.5 fold over the non-disulfide counterparts (**1** and **2**), respectively.

To supplement and co-validate the bulk ICP-MS measurements, cells incubated with **1**-**4** were evaluated by SR-XRF. Due to the forbidden transitions of lanthanide fluorescence and the difficulties associated with mapping intracellular metals without the use of cell transport property altering organic fluorophores, SR-XRF mapping was used. SR-XRF microprobes offer submicron resolution and quantifiable elemental data on desired subcellular regions of interest that are easily displayed in a two-dimensional, intensity weighted image.[37] As shown in **Figure 3.7**, the cells labeled with **2** and **4** and fixed at time = 0 (No leach, figure rows 1 and 3), show a significant amount of associated gadolinium. In contrast, row 2 and 4 of the figure (4 h leach for **2** and **4**, respectively) have quite drastic differences in their amounts of gadolinium fluorescence. The 4 h leach images for complex **2** show only trace amounts of gadolinium, whereas, the corresponding images of cells treated with 4 display a relatively large amount of gadolinium, comparable to the distribution acquired in the cases of no leaching. This visualized signal longevity is in agreement with the ICP-MS measurements, and can only be attributed to the incorporation of the disulfide linkage between the Gd(III) chelate and the arginine moiety.

With the data provided, it is obvious that incorporation of the disulfide linkage has a positive effect on the cell retention of contrast agents **3** and **4**. However, due to the decreased sensitivity of MRI (versus ICP-MS and SR-XRF) towards Gd(III) concentration, the utility of **1**-**4** to increase MR image intensity after the leaching process was tested. This assessment was done by incubating **1**-**4** (1.0 mM) on 2 populations of NIH/3T3 cells. One population was not allowed to leach, while the second was subjected to the leaching protocol outlined in the Experimental Procedures. Comparison of the images in **Figure 3.9A** to those in **3.9B** clearly

shows that cells incubated with **3** and **4** hold their image contrast enhancement to a much greater extent than those incubated with **1** and **2** (over the leaching period). These images augment the SR-XRF data by visualizing the extent to which increased cell retention of the Gd(III)-based contrast agents increases the resulting image contrast longevity via MRI. However, the Gd(III) amounts obtained from the cell studies (**Table 3.3**) predicts that the MR image enhancement should not have been as drastic.

Therefore, it is hypothesized that **1** and **2** have significantly different intracellular fates than **3** and **4**. Further speculation is that **1** and **2** have been degraded or processed by cell cycles that leave the Gd(III) ion non-specifically bound to the recycling membrane (either endosomal or lysosomal) and difficult to remove unless subjected to harsh conditions (i.e. the formaldehyde fixation and dehydration procedure followed for the SR-XRF samples). This would also explain the high T_1 values and reduced MR image intensity in **Figure 3.9A** (leach) despite the Gd(III) measurements displayed in **Table 3.3**. If **1** and **2** are non-specifically bound to the internal membrane or likewise sequestered in lysosomes, the image intensity and resultant T_1 values will decrease due to reduced Gd(III) access to the bulk water. Such encapsulation creates a membrane shielding effect where the contrast agent has access to only a small number of rapidly exchanging inner sphere water molecules. This phenomenon has been previously observed within artificial systems such as those involving LIPOCEST contrast agents, and more importantly, within certain subcellular compartments.[38, 39]

Conclusions

In conclusion, DOTA and DTPA-based cell-permeable contrasts that show increased cell retention and longevity via disulfide bond incorporation and exploitation of intracellular thiol concentrations have been synthesized. The agents' relaxometric properties, pH stability, in vitro

cleavage kinetics, and cell retention have been explored via multiple complementary techniques, and those results have been highlighted. As expected, **3** and **4** show increased cell retention (ICP-MS), single cell association (SR-XRF), and viability as MRI contrast agents (MR images). As a result, these agents could be used to ectopically label cell populations and provide long-term contrast enhancement for cell tracking and lineage analysis using MRI.

Future Directions

Due to the substantial decrease in contrast agent uptake when the arginine oligomer was conjugated to the chelate via a disulfide bond, various other cell penetrating peptides that are perhaps more tolerant to structural modifications can be synthesized and tested for cell uptake. Similar to the arginine modified contrast agents described in this chapter, the penetratin, human immunodeficiency virus (HIV-1-TAT), and chimeric (e.g. transportan) cell penetrating peptide families can be built on the solid phase and could offer a MR contrast agent that is more efficient at transducing cell memebranes.[40-43] However, if the previously discussed hydrogen bonding scenario between the Gd(III) ion and the guanidinium groups is the cause of decreased cell uptake, then synthesis of a longer arginine oligomer (i.e. 12-mer) may alleviate the problem.

In a more biological approach, the cells could be grown in a sulfur-free environment (commercially available sulfur- and serum-free media) before incubation with the disulfide contrast agents.[44] Such precautions should reduce the concentration of free, extracellular thiols that could cleave the arginine oligomer from the conjugated contrast agent. Although the sulfur and serum starved cell cultures might experience adverse downstream effects of the limited culture conditions, such a study would explain the modest uptake values of **3** and **4**.

Experimental Procedures

All reagents and solvents were of the highest purity attainable from Sigma-Aldrich (Milwaukee, WI) and Fluka (Sigma-Aldrich Chemie GmbH, Switzerland) unless otherwise noted. Modified Wang resin and amino acids were purchased from Novabiochem (San Diego, CA). NIH/3T3 cells were purchased from the American Type Culture Collection (ATCC; Manassas, VA). Also purchased from ATCC were DMEM, with 4 mM L-glutamine modified to contain 4.5 g/L glucose and 1.5 g/L sodium carbonate and EMEM, with Earle's BSS and 2 mM L-glutamine modified to contain 1.0 mM sodium pyruvate, 0.1 mM nonessential amino acids, and 1.5 g/L sodium bicarbonate. FBS and CBS, and 0.25% trypsin/EDTA solution were purchased from ATCC. Vent-cap flasks, multiwell plates, cell scrapers, and DPBS w/o calcium and magnesium were purchased from Fisher Scientific.

^{1}H and ^{13}C NMR spectra were obtained on a Varian Inova spectrometer at 500 and 125 MHz, respectively. Compounds were dissolved in D_2O (4.80 ppm used as internal references for NMR spectra). Due to solubility issues associated with the peptide-chelate conjugates, ^{13}C NMR spectra were collected in D_2O and a relative reference was used for each sample (first carbon resonance is always given a value of 24.42 ppm). Mass spectrometry samples were analyzed using electrospray ionization (ESI), single quadrupole mass spectrometry on a Varian 1200L spectrometer or matrix assisted laser desorption ionization time-of-flight (MALDI-TOF) mass spectrometry on an Applied Biosystems Voyager-DE Pro. Results reported for *m/z* are for $[M+H^+]^+$ or $[M-H^+]^-$ unless stated otherwise. Elemental Analyses were performed at Desert Analytics Laboratory, Tuscon, AZ.

ICP-MS was performed on a computer-controlled Thermo Elemental (Waltham, MA) PQ ExCell Inductively Coupled Plasma Mass Spectrometer. All standards and samples contain 5

ng/mL of a multi-element internal standard (Spex CertiPrep, Metuchen, NJ) consisting of Bi, Ho, In, Li, Sc, Tb, Y and 3% nitric acid (v/v). Gadolinium standards were prepared in concentrations of 0.05, 0.10, 0.25, 0.50, 1.0, 5.0, 10, 25, and 50 ng/mL. Analysis was accomplished running 1 survey run and 3 main runs (peak jumping, 100 sweeps per run) using ^{156}Gd and ^{157}Gd isotopes and interpolating through ^{209}Bi and ^{115}In internal standards.

Complex Gd(III)-DOTA-Arg_8 (**1**), Gd(III)-DTPA-Arg_8 (**2**), and S-(2-Aminoethylthio)-2-thiopyridine hydrochloride (AETP) were synthesized following previously published procedures and 1,4,7-tris(acetic acid-*tert*-butyl ester)-10-acetic acid-1,4,7,10-tetraazacyclododecane (DOTA-tris-TB) was purchased from Macrocyclics (Dallas, TX).[16, 45, 46]

HPLC-MS

Analytical reverse phase HPLC-MS was performed on a computer controlled Varian Prostar system consisting of a 410 autosampler equipped with a 100 μL sample loop, two 210 pumps with 5 mL/min heads, a 363 fluorescence detector, a 330 photodiode array (PDA) detector, and a 1200L single quadrupole ESI-MS. All separations were executed with a 1.0 mL/min flow rate using a Waters 4.6 x 250 mm 5 μm Atlantis C18 column, with a 3.1:1 split directing one part to the MS and 3.1 parts to the series-connected light and fluorescence detectors. Mobile phases consisted of Millipore Synthesis grade water (solvent A) and HPLC-grade MeCN (solvent B). Preparative HPLC was accomplished using a Varian Prostar system. Two Prostar 210 pumps with 25 mL/min heads fed a 5 mL manual inject sample loop. Detection was performed after a 20:1 split by a two-channel Prostar 325 UV-visible detector and, on the low-flow side, a HP 1046A fluorescence detector. The mobile phases were the same as in the HPLC-MS instrument. Preparative runs were on a Waters 19 x 250 mm 10 μm Atlantis C18 column.

Relaxivity (r_1)

A 2 mM stock solution of **1**-**4**, Gd(III)-DTPA, or Gd(III)-DOTA in 100 mM PBS buffer at pH 7.41 were serially diluted to give 500 μL of each of the five approximate concentrations for each compound: 0.15, 0.3, 0.5, 1.0, and 2.0 mM. The T_1 of each sample was determined at 60 MHz (1.5 T) and 37 °C using an inversion recovery pulse sequence on a Bruker mq60 Minispec (Bruker Canada; Milton, Ontario, Canada) and at 600 MHz (14.1 T) and ambient temperature using a saturation recovery pulse sequence on a Bruker Omega 600WB spectrometer (Bruker BioSpin; Billerica, MA). Reproducibility of the T_1 data was ± 0.3%. Ten microliters of each sample was then analyzed for exact gadolinium concentration using ICP-MS. The inverse of the longitudinal relaxation time (T_1) was plotted against the concentration obtained from ICP-MS and fit to a straight line. All lines were fit with $R^2 > 0.998$. This was performed for each sample in duplicate.

Determination of q by Luminescence Lifetime Measurements

Terbium(III) complexes (**10**-**13**) were dissolved in H_2O and D_2O. The emission was monitored at 544 nm with excitation at 229 nm on a Hitachi F4500 Fluorescence Spectrophotometer operating in phosphorescence lifetime mode. Twenty-five scans were averaged and fit to a monoexponential decay ($R^2 > 0.98$) to give the phosphorescent lifetimes which were entered into this equation (corrected for one amide oscillator, where k is given in ms^{-1}): $q = 5.0 (k_{H2O} - k_{D2O} - 0.06)$.[47, 48]

Determination of τ_m by ^{17}O Transverse Relaxation Rate Measurements

Samples of **1**-**4** were prepared at 15-20 mM concentrations in 1% ^{17}O enriched water (Medical Isotopes, Inc.; Pelham, NH) adjusted to pH 7.40. Lock was achieved by means of an external D_2O standard. ^{17}O spectra were obtained at 54 MHz (number of averaged transients was 160 – 320 and relaxation delay was 400 ms) at temperatures ranging from 1 °C to 85 °C in 5 °C

increments. The ^{17}O transverse relaxation rate was determined by obtaining the line width (in Hz) at half of the peak height, $\Delta\nu_{1/2}$, of the ^{17}O water signal and later fitting the data.[26-28] Using the known sample concentrations and *q* values, the relaxation data were fit to these four parameters at 25 °C: τ_m (water exchange rate), $\Delta H^{\ddagger}$ (activation enthalpy), T_{1e} (electronic relaxation rate), and ΔE_{T1e} (activation energy of T_{1e}).[49]

Cell Culture Conditions

All cell lines, media, sera, buffers, and dissociation reagents were purchased from the ATCC as previously stated. NIH/3T3 cells (CRL-1658) were grown in DMEM (with 4 mM L-glutamine, 4,5 g/L glucose, 1 mM sodium pyruvate, 1.5 g/L sodium carbonate, and phenol red supplemented with 10% CBS). Cells were grown in a humidified incubator at 37 °C and 5% CO_2. Cells were washed with DPBS (without calcium and magnesium) and dissociated with a 0.25% trypsin-EDTA solution. All flasks and multi-well plates were Corning brand, tissue culture treated, and sterile. The studies for each contrast agent and time point were performed at least in triplicate

Cells were counted and viability was assessed using a Guava EasyCite Mini Personal Cell Analyzer (Guava Technologies; Hayward, CA). Cell samples were diluted 10 fold with Guava ViaCount reagent (total volume is 200 μL) and allowed to stain at room temperature for at least 5 minutes (no longer than 20 minutes) vortexed and measured. Each sample was measured using the Guava ViaCount software module using 1000 counts per run doing 2 separate runs per sample. Instrument reproducibility was assessed daily following the manufacturer's suggested protocol using GuavaCheck reagent and the corresponding software module.

ICP-MS assessment of the cell associated gadolinium was determined by collecting and processing all cell and media samples via this procedure: addition of 70% (v/v) nitric acid in water, vortexing (~ 5 min), and digestion at 65 °C for at least four hours. Samples were then added to a 15 mL conical tube along with internal standard and water to give a final nitric acid concentration (v/v) of 3%.

Synchrotron Radiation X-Ray Fluorescence (SR-XRF) Analysis

NIH/3T3 cells were grown to 65% confluency on silicon nitride windows (membrane thickness: 500 nm and frame size: 5.0 mm x 5.0 mm, Silson Ltd.; Northampton, England) in Corning brand 24 well cell culture treated plates. Each well had 2 silicon nitride windows (one incubation sample and one leach sample). Cells were incubated with 3.0 mM of compounds **1**-**4** (post 0.2 μm syringe filtration) for 4 hours. Samples were then rinsed three times with DPBS and one window was removed for processing (incubation sample) while one window was allowed to incubate with fresh media for 4 more hours followed by processing (leached sample). Windows were processed by cell fixation in 3.7% formalin for 5 minutes at room temperature, rinsing with DPBS (1x), rinsing with Millipore water (1x), rinsing in 100% ethanol (1x), and drying overnight (18 h, room temp.). The silicon nitride windows were then mounted onto a kinematic specimen mount for both visible light and X-ray fluorescence microscopy. The samples were examined on a light microscope (Leica DMXRE), and the cells to be scanned with SR-XRF were located on the window relative to a reference point (one of the four window corners) using a high spatial resolution motorized x/y stage (Ludl Bioprecision).

Scanning SR-XRF microscopy was carried out at the 2-ID-E beamline of the Advanced Photon Source at Argonne National Laboratory (IL, USA). Hard X-rays from an undulator source were monochromatized using a single bounce Si <111> monochromator. The energy was

selected to allow for efficient excitation of the Gd L-lines, and also to enable the detection of the P, S, Fe, and Zn K-lines. A Fresnel zone plate (320 μm diameter, focal length f = 250 mm, X-radia; Concord, CA) was used to focus the monochromatic X-ray beam to a spot size of ~ 0.4 x 0.3 μm^2 on the specimen. The sample was raster scanned through the beam at room temperature under a helium atmosphere. At each scan position, a full fluorescence spectrum was acquired using an energy dispersive germanium detector (Ultra-LEGe detector, Canberra; Meriden, CT). Elemental content was determined by comparison of fitted sample spectra with NBS thin film standards 1832 and 1833 (NIST; Gaithersburg, MD) using MAPS software supplemented with fitting of fluorescence spectra at every pixel.[35]

MR Imaging and T_1 Analysis

MR measurements were performed on a General Electric/Bruker Omega 600WB 14.1 T imaging spectrometer fitted with Accustar shielded gradient coils at ambient temperature (~ 25 °C). Spin lattice relaxation times (T_1) were measured using a saturation recovery pulse sequence with static T_E (10.18 ms) and variable T_R (127.5, 165, 200, 300, 500, 1000, 2000, 5000, 7500, 10000 ms) values. Two independent trials were run per sample and at least 5 slices were quantified per trial. Student's *t*-tests were calculated in Origin 7 SR2 (Origin Lab; Northampton, MA) at a 95% confidence level with 8 degrees of freedom and a null hypothesis value (minimum acceptable time difference) of 100 ms. Images were acquired using a T_1-weighted, spin-echo pulse sequence (T_E = 10.18, T_R = 750 ms) on freshly harvested cells that were spun down (at *250g*) within glass capillary tubes for 5 min prior to image acquisition. Total time from harvest to image acquisition was 1-2 h.

Synthesis of end-modified Arg_8-Cys (**5**)

Polystyrene-based Wang resin containing a fluorenyl-methoxy-carbonyl (Fmoc) protected arginine residue (2.00 g, 0.580 mmol/g) was swelled in CH_2Cl_2 for 10 min (x 3) and washed with peptide synthesis grade *N*,*N*-dimethylformamide (DMF) (4 x 10 min). The resin was treated three times with a solution of 20% piperdine in DMF (10 min) and the deprotected resin was washed with DMF (4 x 10 min). In a separate vial, Fmoc protected pentamethyldihydrobenzofuran-5-sulfonyl (Pbf)-arginine (1.505 g 2.320 mmol), *N*,*N*,*N*′,*N*′-tetramethyl-*O*-(7-azabenzotriazol-1-yl)uronium hexafluorophosphate (HATU) (0.881 g, 2.32 mmol), and *N*,*N*-diisopropylethylamine (DIEA) (0.748 g, 5.80 mmol) were dissolved in approximately 3 mL of DMF. The resulting solution was added to the deprotected resin and nitrogen was bubbled through the mixture for 6-8 h. The peptide solution was removed from the resin which was subsequently rinsed with DMF (4 x 10 min). This procedure was repeated a total of seven times in order to achieve the synthesis of an 8 amino acid polyarginine oligomer bound to the Wang resin (3.96 g).

The Arg_8 functionalized resin (2.00 g, 0.29 mmol/g, 0.58 mmol) was deprotected with the piperdine solution and washed with DMF as described above. In a separate vial, Fmoc protected trityl (Trt)-cysteine (0.725 g, 1.16 mmol) and 2, 4, 6-trimethylpyridine (0.154 g, 1.27 mmol) were dissolved in a minimal amount of DMF. The resulting solution was added to the deprotected resin and nitrogen was bubbled through the mixture for 6-8 h. The peptide solution was removed and the resin was washed with DMF (4 x 10 min each). The resin bound Arg_8-Cys oligomer was deprotected with the piperdine solution, and washed with DMF. The resin was resuspended in a solution of acetic anhydride (0.118 g, 1.160 mmol), DIEA (0.374 g, 2.90 mmol) and DMF (3 mL). Bubbling nitrogen through this mixture for 4 h effectively capped the

peptide's N-terminus. Upon removal of the capping solution, the resin was washed with DMF, CH_2Cl_2, and MeOH (4 x 10 min each). Following the methanol washes, the resin was dried under vacuum. A solution of 95% trifluoroacetic acid (TFA), 2.5% ethane dithiol (EDT), 1.5% H_2O, and 1.0% triisopropylsilane (TIS) (50 mL) was added to the resin and nitrogen was bubbled through the mixture for 1 h. The resin was filtered and to the filtrate was added methyl *tert*-butyl ether (MTBE) (40 mL) to precipitate a white solid that was subsequently washed with MTBE (3 x). The solid was dissolved in 30 mL of water and freeze-dried to yield white flaky crystals of the end modified peptide, Arg_8-Cys (0.692 g, 84%). ^{1}H NMR (D_2O @ pH 1.0): δ = 1.22-1.40 (m, 16H), 1.50 (dd, *J* = 8.5, 5.5 Hz, 16H), 1.59-1.69 (m, 2H), 1.74 (d, *J* = 6.0 Hz, 3H), 2.89 (m, 16H), 3.95-4.10 (m, 8H); ^{13}C NMR (D_2O @ pH 1.0): δ = 24.42, 27.50, 28.03, 39.36, 40.52, 52.26, 53.25, 156.57, 172.61, 173.44, 174.84; with ESI-MS (*m/z*): 1413.58; calc. for $C_{53}H_{105}N_{33}O_{11}S+H^+$: 1413.68.

Synthesis of 1,4,7-Tris(carboxymethyl)-10-(N-[2-(pyridin-2-yldithio)ethyl]acetamide)-1,4,7,10-tetraazacyclododecane (**6**)

DOTA-tris-TB (0.600 g, 1.05 mmol), HATU (1.197 g, 3.150 mmol), and anhydrous DIEA (0.683 g, 5.25 mmol) were dissolved in 4.0 mL of anhydrous DMF and allowed to stir for 10 min under a nitrogen atmosphere while AETP (0.466 g, 2.10 mmol) was dissolved in 2.0 mL of anhydrous DMF. After the 10 min activation time, the AETP solution was added via syringe and the mixture was allowed to stir for 5 h while being monitored by TLC [KNO_3─H_2O─MeCN (1:9:90)]. Upon reaction completion the solution was evaporated *in vacuo*. The resulting yellow residue was stirred overnight in 95% TFA, 2.5% TIS, and 2.5% H_2O (30 mL). The reaction mixture was concentrated to approx. 10 mL by application of a steady stream of dry nitrogen across the top of the vessel. The crude product was precipitated by addition of MTBE (40 mL)

and was subsequently washed with MTBE (3 x). The yellow solid was dried *in vacuo* to yield 1.12 g of crude product.

The crude mixture was submitted to preparatory HPLC with the Waters Atlantis column. The solid was brought up in H_2O and purified using the following method: begin at 0% B, ramp to 3% B over 1 min, hold at 3% B for 15 min, then ramp to 20% B over 7 min and hold for 8 min, followed by a wash to 100% B before returning to 0% B. The desired fractions (retention time: 32.20 min by UV at 235, 280 nm) were collected and freeze-dried to yield the product as a white solid (0.410 g, 68%). ^{1}H NMR (D_2O): δ = 2.96-3.10 (m, 11H), 3.41-3.51 (m, 13H), 3.79 (q, *J* = 16.5 Hz, 4H), 7.33 (t, *J* = 4.5 Hz, 1H), 7.88 (d, *J* = 3.5 Hz, 2H), 8.40 (d, *J* = 4.5 Hz, 1H); ^{13}C NMR (D_2O): δ = 37.05, 38.13, 48.22, 48.46, 50.94, 51.64, 53.73, 55.51, 56.59, 121.92, 122.26, 139.56, 148.50, 158.48, 170.02, 171.96, 175.07; ESI-MS (*m/z*): 573.26; calc. for $C_{23}H_{36}N_6O_7S_2$ $+H^+$: 573.70; with Anal. Calcd for $C_{23}H_{36}N_6O_7S_2$ • Na • 1.5 H_2O: C, 44.36; H, 6.31; N, 13.50; S, 10.30. Found: C, 44.20; H, 6.17; N, 13.38; S, 10.98.

Synthesis of [(2-{carboxymethyl-[2-(carboxymethyl-{[2-(pyridin-2-yldisulfanyl)-ethylcarbamoyl]-methyl}-amino)-ethyl]-amino}-ethyl)-amino]-acetic acid (**7**)

DTPA dianhydride (2.00 g, 5.60 mmol) was dissolved in 100 mL of anhydrous DMSO and allowed to stir under a nitrogen atmosphere while AETP (0.672 g, 3.040 mmol) was dissolved in a stirring solution of anhydrous DMSO (25 mL) and anhydrous DIEA (1.067 g, 8.210 mmol). The AETP solution was slowly added to the DTPA dianhydride solution via syringe pump over 5 h. Upon complete addition, the resulting solution was stirred for an additional hour before being quenched with H_2O (100 mL) and concentrated *in vacuo*. The resulting residue was brought up in H_2O and submitted to preparatory HPLC with the Waters Atlantis column using the following method: begin at 0% B, ramp to 100% B over 35 min

followed by a wash at 100% B for 5 min before returning to 0% B. The desired fractions (retention time: 10.28 min by UV at 235, 280 nm) were collected and freeze-dried to yield the product as a white solid (1.07 g, 63%). ^{1}H NMR (D_2O): δ = 3.04 (t, *J* = 5.5 Hz, 2H), 3.24-3.35 (m, 6H), 3.54 (t, *J* = 6.0 Hz, 2H), 3.59 (t, *J* = 6.0 Hz, 2H), 3.69 (s, 2H), 3.75-3.90 (m, 8H), 7.57 (t, *J* = 6.5 Hz, 1H), 8.05 (d, *J* = 8.5 Hz, 1H), 8.15 (t, *J* = 8.5 Hz, 1H), 8.53 (d, *J* = 5.5 Hz, 1H); ^{13}C NMR (D_2O): δ = 37.45, 37.94, 50.30, 51.24, 52.52, 52.09, 54.48, 56.52, 57.04, 57.21, 123.29, 123.95, 142.71, 145.62, 157.07, 168.74, 170.56, 172.17, 172.78; ESI-MS (*m/z*): 560.19; calc. for $C_{21}H_{31}N_5O_9S_2$-H^+: 560.63; with Anal. Calcd for $C_{21}H_{31}N_5O_9S_2$ • Na: C, 43.14; H, 5.34; N, 11.98; S, 10.97. Found: C, 42.70; H, 5.21; N, 12.02; S, 11.29.

Synthesis of DO3A-SS-Arg$_8$ (**8**)

Compound **6** (0.160 g, 0.306 mmol) was added to end-modified Arg_8-Cys (**5**) (0.432 g, 0.306 mmol) dissolved in 30 mL of degassed phosphate buffer (10 mM, pH 8.0). The solution was stirred under nitrogen atmosphere at room temperature. The reaction was monitored by analytical HPLC and found to be complete after 72 h. An aliquot (2.5 mL) of the solution was removed for characterization while the remaining material (27.5 mL) was carried onto the synthesis of Gd(III)-DOTA-SS-Arg_8 (**3**). Dialysis (M_{wt} cut-off 1,000) against Millipore H_2O (4 L x 4 days), yielded 3 mL of a translucent liquid that was 0.2 μm syringe filtered and freeze-dried to yield a white solid (0.389 g, 74%). ^{1}H NMR (D_2O) shows the disappearance of all aromatic protons. ^{13}C NMR (D_2O): δ = 24.42, 28.16, 28.88, 37.11, 38.17, 40.65, 40.79, 48.44, 50.71, 51.90, 53.59, 54.91, 55.52, 56.66, 156.86, 170.04, 172.19, 172.80, 173.75, 175.41; ESI-MS (*m/z*): 1875.31; calc. for $C_{70}H_{136}N_{38}O_{18}S_2$+$H^+$: 1875.21.

Synthesis of DTPA-SS-Arg$_8$ (**9**)

Compound **7** (0.175 g, 0.312 mmol) was added to end-modified Arg$_8$-Cys (3) (0.440 g, 0.312 mmol) dissolved in 30 mL of degassed phosphate buffer (10 mM, pH 8.0). The solution was stirred under nitrogen atmosphere at room temperature. The reaction was monitored by analytical HPLC and found to be complete after 72 h. An aliquot (2.5 mL) of the solution was removed for characterization while the remaining material (27.5 mL) was carried onto the synthesis of Gd(III)-DTPA-SS-Arg$_8$ (**4**). Dialysis (M_{wt} cut-off 1,000) against Millipore H_2O (4 L x 4 days), yielded 4 mL of a translucent liquid that was 0.2 μm syringe filtered and freeze-dried to yield a white solid (0.351 g, 66%). ^{1}H NMR (D_2O) shows the disappearance of all aromatic protons. ^{13}C NMR (D_2O): δ = 24.42, 28.20, 38.79, 40.66, 50.53, 52.19, 53.44, 53.53, 54.94, 55.19, 57.88, 58.91, 156.84, 172.70, 172.97, 173.60, 174.32, 178.33; ESI-MS (*m/z*): 1864.21; calc. for $C_{69}H_{131}N_{37}O_{20}S_2+H^+$: 1864.14.

Synthesis of Gd(III)-DOTA-SS-Arg$_8$ (**3**)

To the remaining aliquot of DO3A-SS-Arg$_8$ (**8**) (27.5 mL, 0.285 mmol), was added $Gd(OH)_3$ (0.064 g, 0.314 mmol). The reaction mixture was brought to pH 6.0 with 1.0 M NaOH and allowed to stir for 7 d at room temperature under a nitrogen atmosphere. Dialysis (M_{wt} cut-off 1,000) against Millipore H_2O (4 L x 4 days), yielded 30 mL of a translucent liquid that was brought to pH 11.0 with concentrated NH_4OH. This suspension was 0.2 μm syringe filtered and freeze-dried to yield a white powder which was found to be (**3**) (0.453 g, 78%) by ESI-MS (*m/z*): 2029.44 (*m/1*), 1014.70 (*m/2*), 677.43 (*m/3*) 508.26 (*m/4*) with Gd isotope pattern; calc. for $C_{71}H_{133}GdN_{38}O_{18}S_2+H^+$: 2029.44.

Synthesis of Gd(III)-DTPA-SS-Arg$_8$ (**4**)

To the remaining aliquot of DTPA-SS-Arg$_8$ (**9**) (27.5 mL, 0.286 mmol), was added $Gd(OH)_3$ (0.064 g, 0.315 mmol). The reaction mixture was brought to pH 6.0 with 1.0 M NaOH and allowed to stir for 7 d at room temperature under a nitrogen atmosphere. Dialysis (M_{wt} cut-off 1,000) against Millipore H_2O (4 L x 4 days), yielded 30 mL of a translucent liquid that was brought to pH 11.0 with concentrated NH_4OH. This suspension was 0.2 μm syringe filtered and freeze-dried to yield a white powder which was found to be (**4**) (0.484 g, 84%) by ESI-MS (*m/z*): 2017.30 (*m/1*), 1008.55 (*m/2*), 672.99 (*m/3*), 505.12 (*m/4*), 404.38 (*m/5*) with Gd isotope pattern; calc. for $C_{69}H_{127}GdN_{37}O_{20}S_2+H^+$: 2017.36.

Synthesis of Tb(III)-DOTA-Arg$_8$ (**10**)

The terbium analogue of **1** was synthesized using previously outlined metalation procedures and substituting $Tb(OH)_3$ for $Gd(OH)_3$.[45] The resulting white solid was found to be 10 (45.7 mg, 42%) by ESI-MS (*m/z*): 1810.85 (*m/1*), 906.07 (*m/2*), 604.24 (*m/3*), 453.47 (*m/4*); calc. for $C_{64}H_{121}N_{36}O_{16}Tb+H^+$: 1810.80.

Synthesis of Tb(III)-DTPA-Arg$_8$ (**11**)

The terbium analogue of **2** was synthesized using previously outlined metalation procedures and substituting $Tb(OH)_3$ for $Gd(OH)_3$.[16] The resulting white solid was found to be 11 (42.0 mg, 52%) by ESI-MS (*m/z*): 1798.63 (*m/1*), 899.91 (*m/2*), 600.26 (*m/3*), 450.47 (*m/4*); calc. for $C_{62}H_{115}N_{35}O_{18}Tb+H^+$: 1798.73.

Synthesis of Tb(III)-DOTA-SS-Arg$_8$ (**12**)

The terbium analogue of **3** was synthesized using compound **8** (10.0 mg, 0.005 mmol), $Tb(OH)_3$ (1.23 mg, 0.006 mmol), and the same metalation procedure previously described for **3**

(6.0 mg, 60%). ESI-MS (m/z): 2031.01 (*m/1*), 1016.00 (*m/2*), 677.73 (*m/3*) 508.54 (*m/4*), 407.12 (*m/5*); calc. for $C_{71}H_{133}N_{38}O_{18}S_2Tb+H^+$: 2031.12.

Synthesis of Tb(III)-DTPA-SS-Arg$_8$ (**13**)

The terbium analogue of **4** was synthesized using compound **9** (10.0 mg, 0.005 mmol), $Tb(OH)_3$ (1.23 mg, 0.006 mmol), and the same metalation procedure previously described for **4** (5.9 mg, 55%). ESI-MS (*m/z*): 2019.02 (*m/1*), 1010.01 (*m/2*), 673.64 (*m/3*) 505.43 (*m/4*), 404.65 (*m/5*); calc. for $C_{69}H_{127}N_{37}O_{20}S_2Tb+H^+$: 2019.04.

CHAPTER 4:

Targeted Intracellular Delivery of a Nanoparticle Contrast Agent for MRI

The text in this chapter was taken in part from:

Endres, P. J.; Paunesku, T.; Vogt, S.; Meade, T. J.; Woloschak, G. E., DNA-TiO_2 Nanoconjugates Labeled with Magnetic Resonance Contrast Agents. *J. Am. Chem. Soc.* **2007,** 129, (51), 15760-15761.

Introduction

Recent efforts to develop nano-scale materials for use as biocompatible delivery scaffolds of drugs and imaging agents have produced significant advances in the area of multifunctional probes.[1-5] These new materials provide the means to chaperone and concentrate both drugs and contrast agents in specific organs, tissues and cells.[6, 7] Primarily, superparamagnetic iron oxide (SPIO) nanoparticles, known for their ability to enhance signal contrast in T_2-weighted magnetic resonance (MR) images, have dominated reports employing this approach.[8-17] These agents typically result in negative contrast enhancement, and occasionally their inherent magnetic susceptibility leads to background artifacts.[18] Conversely, T_1 contrast agents do not suffer from this phenomenon; however, there are very few examples of paramagnetic (T_1) labeled nanoparticles that combine therapeutics with an MR reporter.[19, 20]

In conjunction, recent work from our collaborators shows that TiO_2 nanoparticles decorated with modified DNA oligonucleotides function in a targeted and therapeutic capacity.[21, 22] Targeting is accomplished via oligonucleotide hybridization to an intracellular organelle's matching DNA sequence, and therapeutic activity is elicited by light-induced scission of the semi-conducting, nanoparticle-bound DNA. Considering these properties, attachment of a T_1-contrast agent to such a targeted nanoparticle would allow the visualization of certain genomic sequences in cells and tissues via MRI. Knowing that cancer is a result of DNA mutations, one can envision that a therapeutic MR probe targeting only mutant, oncogene sequences would have a significant impact on the therapeutic and diagnostic communities. To investigate this, DNA labeled nanoconjugates have been functionalized with a Gd(III)-based contrast agent to produce a biocompatible, therapeutically active delivery scaffold that is detectable by routine T_1-weighted MR imaging (**Scheme 4.1**).[22]

Scheme 4.1 Functionalization of TiO_2 nanoparticles with a dopamine-bound MRI contrast agent (**1**).

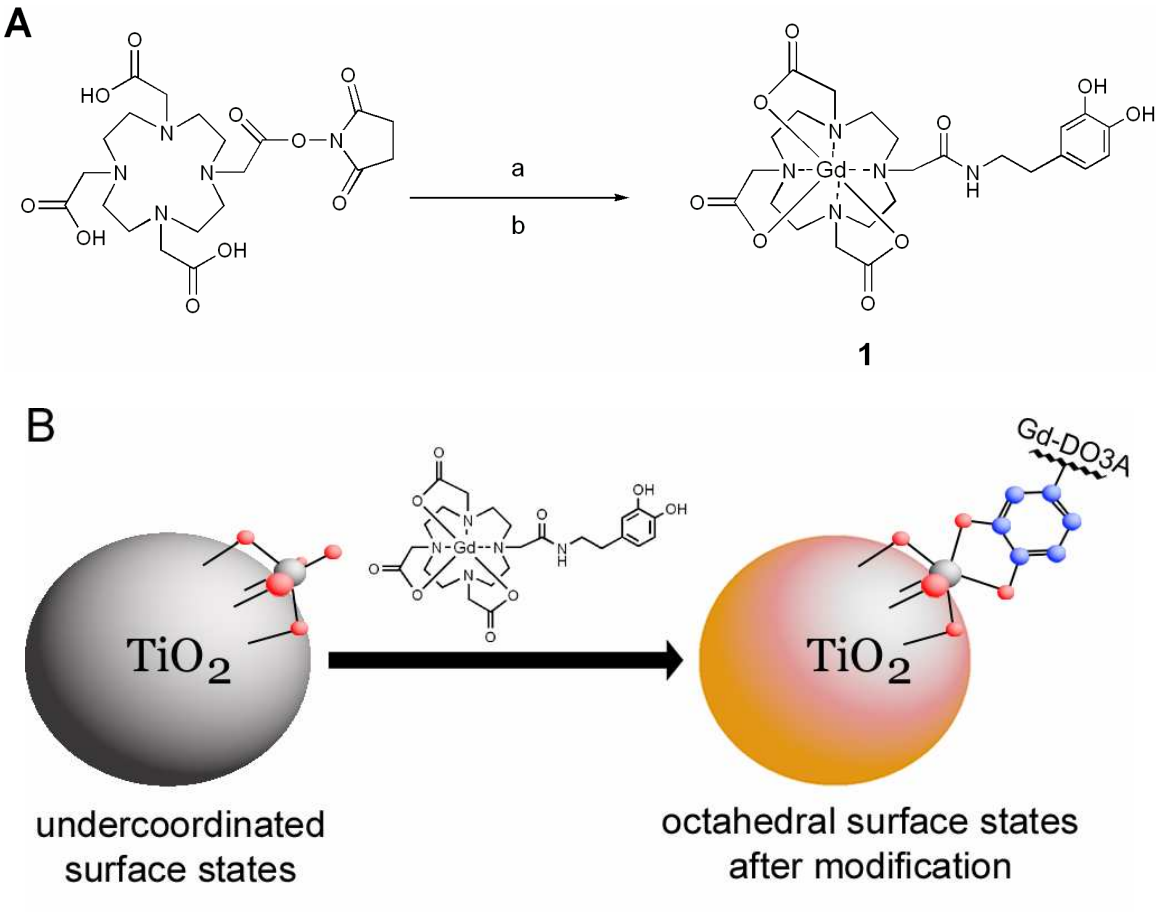

(A) Synthetic route to a dopamine-modified MR contrast agent (**1**); (a) dopamine, DIEA, DMF; (b) $GdCl_3$, H_2O pH 4.5, 45 °C. (B) Functionalization of TiO_2 nanoparticles with **1**.

Results

Synthesis of the Nanoparticle-based Contrast Agent

The synthesis of a dopamine-modified contrast agent (DOPA-DO3A, **1**) was accomplished by coupling the commercially available succinimidyl ester activated-1,4,7,10-tetraazacyclododecane- 1,4,7-tetraacetic acid (DOTA-mono-NHS) to dopamine hydrochloride. Metalation with $GdCl_3$ and purification were carried out under strict pH control as the catechol in the metalated complex (**1**) is easily oxidized at pH values above 5.

Preparation of the TiO_2 nanoparticles (3-5 nm) was performed following previously published procedures.[21, 23, 24] Nanoconjugates were prepared so that, on the surface of each nanoparticle, 1-5 dopamine-modified DNA oligonucleotides could be attached (**Scheme 4.2**). A glycidyl isopropyl ether coating was used to reduce the surface reactivity of the nanoconjugates, rendering them non-reactive with the vast majority of biological molecules. The DNA-TiO_2 nanoconjugates were analyzed by ICP-MS to determine the total amount of Ti. The Ti concentration was used to calculate the concentration of nanoconjugates, and subsequently, the concentration of active sites available for dopamine binding.[23, 24]

TiO_2 Nanoparticle Functionalization and Characterization

Following characterization (HPLC, ESI-MS, and EA), varying amounts of the dopamine modified contrast agent (**1**) were reacted with TiO_2 nanoparticles in the presence and absence of surface conjugated oligonucleotides (**Table 4.1**). Coupling **1** to the nanoparticle was initially detected by a distinct color change resulting from a red shift in nanoparticle absorption between the white, unmodified nanoparticles to the orange/brown, modified nanoparticles.[23] In addition, formation of the DOPA-DO3A- nanoparticles was confirmed by UV and IR spectroscopy. The modified nanoparticles revealed a characteristic rise in UV light absorption towards

Scheme 4.2 Synthesis of control DNA-TiO_2 nanoconjugates and DNA-DOPA-DO3A-TiO_2 nanoconjugates.

A

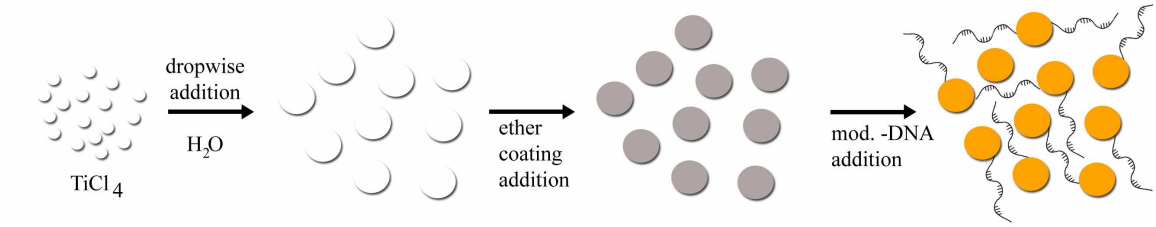

B

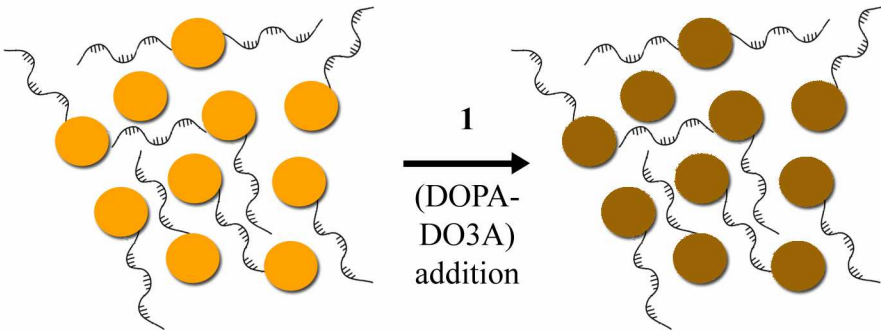

(A) Preparation of the DNA-TiO_2 nanoconjugates (3-5 nm) following previously published procedures.[21-23] (B) Preparation of the DNA-DOPA-DO3A-TiO_2 nanoconjugates.

Table 4.1 Table of binding efficiencies: TiO_2 nanoparticle active sites to **1**.[a]

Equiv. Ratio [Ti binding sites]:[1]	% NP Active Sites Functionalized
1:0.2	3.0±0.2
1:0.6	3.2±0.1
1:1.0	4.6±0.2
1:1.4	4.0±0.5
1:5.0	4.2±0.2

[a] All functionalization reactions were carried out in triplicate.

higher energies (200-360 nm) that is attributable to formation of dopamine-TiO_2, semi-conducting nanocomposites (**Figure 4.1**).[23, 24] Similarly, the modified nanoconjugates showed a 20% increase in IR absorption over control nanoparticles in the carbon-carbon double bond and aromatic stretching frequencies of 1540-1680 cm^{-1} (**Figure 4.2**).

To determine the relaxivity of the DOPA-DO3A-TiO_2 nanoconjugates, the slope of the line generated by plotting the inverse of the T_1 relaxation time versus Gd(III) concentration was measured. The resulting graph yielded a relaxivity per Gd(III) ion of 3.5±0.1 $mM^{-1}s^{-1}$. Therefore, based on the Ti:Gd ratio acquired from ICP-MS, each individual nanoparticle has an average relaxivity of 61.0±1.7 $mM^{-1}s^{-1}$.

Synchrotron Radiation X-Ray Fluorescence (SR-XRF) Analysis

The cellular distribution and single cell association of the DNA-DOPA-DO3A-TiO_2 nanoconjugates was evaluated by SR-XRF.[25] As stated in Chapter 2, the acquired high-resolution elemental maps provided pixel by pixel data sets that were used to globally confirm, map, and quantify the Gd and Ti distributions within each sample. In addition, a DNA oligonucleotide targeted to the mitochondrial genome was used to functionalize the nanoparticles. This targeting sequence was specific for the sense strand of a NADH dehydrogenase 2 (ND2) mitochondrial gene present in the rat PC12 cell line: 5' carboxy dT-cacgacaccttagcaccaacttac (ND2s).[22] The results display colocalized Ti and Gd fluorescence signals in the cytoplasm, but not in the nuclei of the nanoparticle-incubated cells (**Figure 4.3**).

A

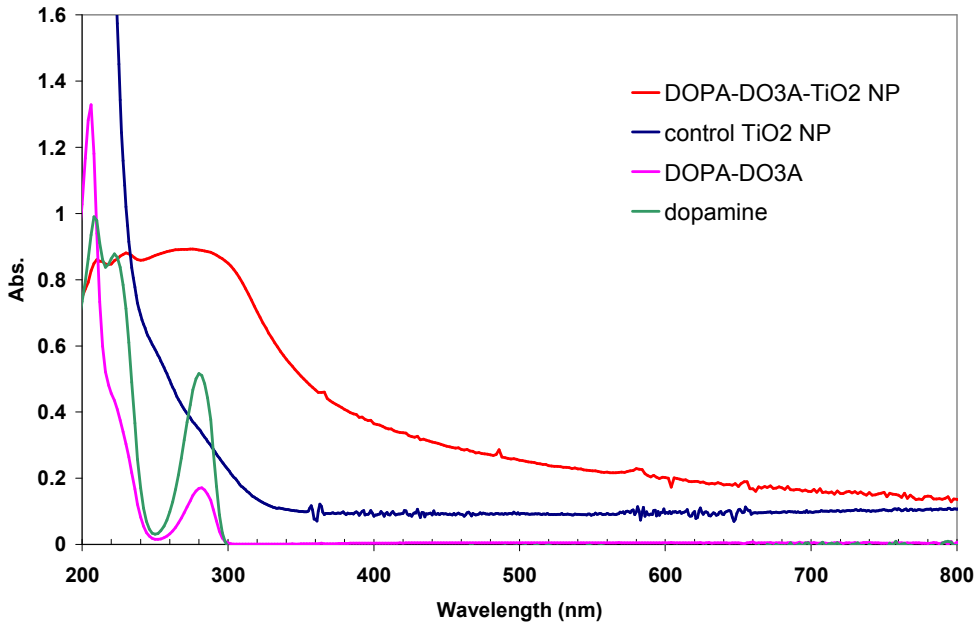

B

Solvent	λ_{ex}	λ_{em}	ε (M^{-1} cm^{-1})
Millipore H_2O	282	314	2040
MOPS (pH 7.41)	282	314	2049

Figure 4.1 UV-Visible spectra of **1** and DNA-DOPA-DO3A-TiO_2 nanoconjugates. (A) UV-Visible traces of the TiO_2 nanoconjugates were taken in H_2O to confirm that **1** was binding to the nanoparticles in a semi-conducting fashion (DOPA-DO3A-TiO_2 NP – 1.25 mM; TiO_2 NP – 1.25 mM; **1** – 0.10 mM; dopamine – 0.10 mM). The spectra and sample concentrations are shown below the spectra. (B) The extinction coefficients of **1** were calculated by plotting the concentration of the compound vs. the total absorbance and fitting the data to a linear function. Five concentrations were used to construct the trend line, giving an R^2 value of >0.99 for the fitting.

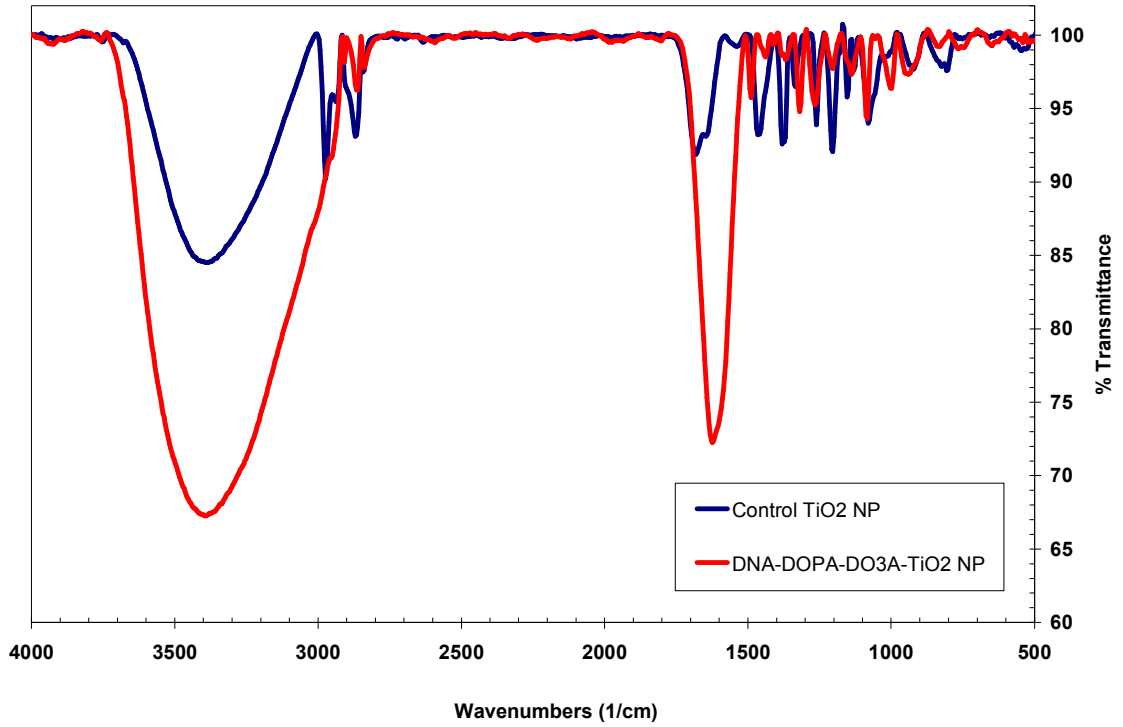

Figure 4.2 IR spectra of **1** and DNA-DOPA-DO3A-TiO_2 nanoconjugates. FT-IR was used to verify and confirm the presence of **1** on the surface of the TiO_2 nanoconjugates. The samples were prepared as a 5-10% weight mixture in KBr powder, and the spectra were collected by DRIFT spectroscopy.

MR Imaging and T_1 Analysis

To assess the viability of **1** to enhance the MR image contrast of the TiO_2 nanoparticles, DOPA-DO3A-TiO_2 nanoconjugates at varying [**1**]:[TiO_2 active site] ratios were gravity packed in glass capillary tubes and imaged using a T_1-weighted spin-echo imaging sequence (**Figure 4.4**). As expected, the TiO_2 nanoconjugates functionalized with **1** display a brighter signal and lower T_1 values than the control nanoparticles. Subsequently, cultures of human prostate cells (PC3M) were incubated with 1.0 μM of the nanoconjugates and imaged via MRI (**Figure 4.5**). Comparison of the images and data from **Figure 4.5** reveals that although Gd(III) loading of the nanoconjugates does not elicit a statistically significant change in T_1 values or image intensity, the cells incubated with the DNA-DOPA-DO3A nanoconjugates display contrast enhancement over the control cells.

Discussion

The TiO_2 nanoparticles were surface modified by exploiting their selective reactivity to ortho-substituted enediol ligands (such as ascorbic acid, alizarin, and dopamine).[23] These reactions form semi-conducting, photocatalytically cleavable bonds between the Ti atoms of the nanoparticles and the oxygen atoms of the binding ligands, allowing for the surface conjugation of dopamine-modified DNA. This nanoparticle-bound DNA retains its subcellular targeting capabilities, while remaining stable enough to allow in vivo compartmental accumulation before photocatalytic cleavage is induced.[22] Therefore, addition of other dopamine-bound moieties, e.g. the described MR-active agent, allows this scaffold to become multi-functional.

As reported in **Table 4.1**, conjugation of **1** to the DNA-modified nanoconjugates occurs in a linear relationship to the equivalents added. The success of the conjugation reaction

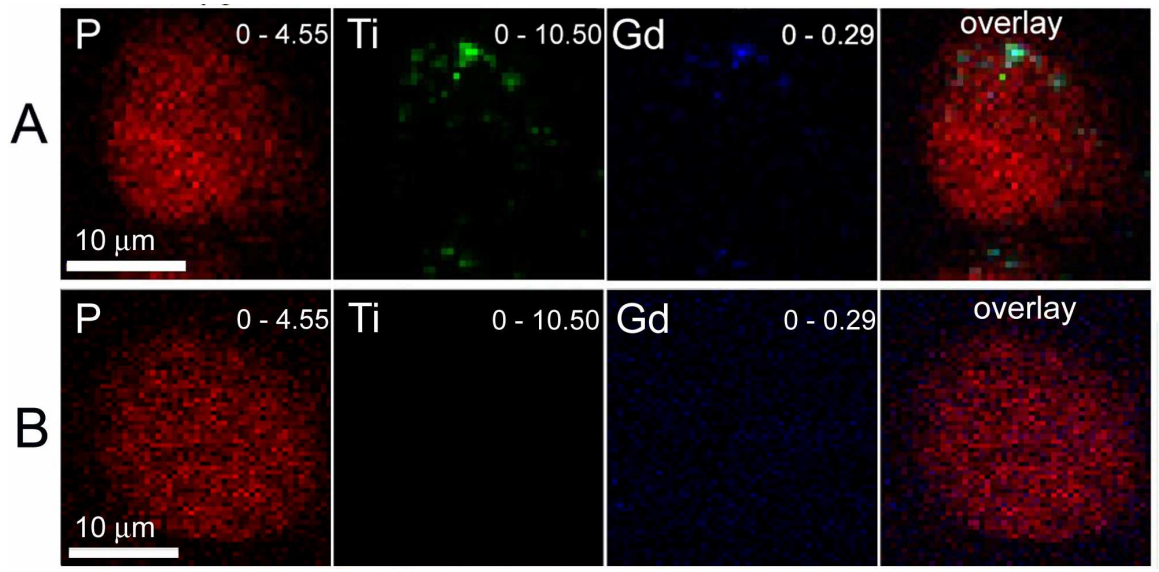

Figure 4.3 Selected SR-XRF images of PC12 cells incubated with the DNA-DOPA-DO3A-TiO_2 nanoconjugates. (A) PC12 cells transfected with DNA-DOPA-DO3A modified nanoconjugates; (B) control, non-transfected PC12 cells. Phosphorus is red, titanium is green, and gadolinium is blue. The scale bars represent 10 µm. Note that each image is scaled to its respective maximum value (displayed at the upper right corner and given in $\mu g/cm^2$).

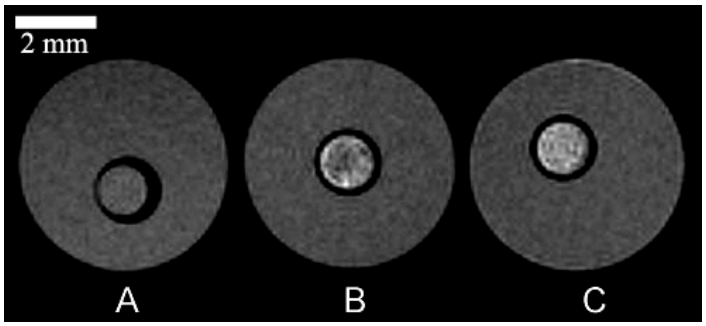

Figure 4.4 T_1-weighted MR images of the DNA-DOPA-DO3A-TiO_2 nanoconjugates. (A) DNA-modified TiO_2 nanoconjugates (T_1 = 3386±98 ms); (B) DNA-nanoconjugates with 3.4% DOPA-DO3A coverage (T_1 = 502±25 ms); (C) DNA-nanoconjugates with 4.8% DOPA-DO3A coverage (T_1 = 235±8 ms). The outer rings are DI water and were used as an external phantom (T_1 = 3547±60 ms). The scale bar represents 2.0 mm (within a field of view of 20 mm and a slice thickness of 1.0 mm). One trial was run per sample and 5 slices were quantified per trial. Student's *t*-tests were calculated with 4 degrees of freedom and a null hypothesis value (minimum acceptable time difference) of 100 ms.

Sample name	Avg. T_1 time (ms)	Std. Dev. (ms)		*t* test comparison	*t* test results	Meets 95% confidence level?
Fig. 4.4: A	3386	98		A to B	47.677	Yes
Fig. 4.4: B	502	25		A to C	53.744	Yes
Fig. 4.4: C	235	8		B to C	11.019	Yes

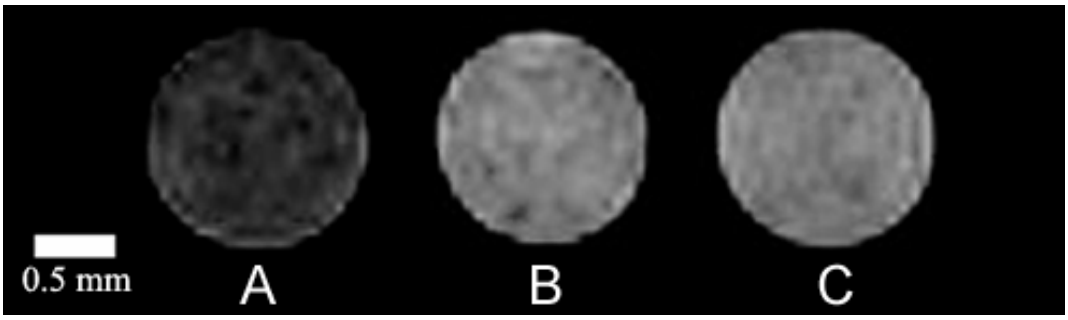

Figure 4.5 T_1-weighted MR images of PC3M cells incubated with the DNA-DOPA-DO3A-TiO_2 nanoconjugates. (A) Control PC3M cells (T_1 = 3527±48 ms); (B) PC3M cells incubated with 1.0 μM DNA-DOPA-DO3A-nanoconjugates with 1.8% **1**:TiO_2 active site coverage (T_1 = 2178±88 ms); (C) PC3M cells incubated with 1.0 μM DNA-DOPA-DO3A-nanoconjugates with 4.4% **1**:TiO_2 active site coverage (T_1 = 2356±100 ms). The scale bar represents 0.5 mm (at 14.1 T within a FOV of 20 mm and a slice thickness of 0.5 mm). T_1 values were confirmed to be statistically different via student t-tests with 7 degrees of freedom and a null hypothesis value (minimum acceptable time difference) of 100 ms.

Sample name	Avg. T_1 time (ms)	Std. Dev. (ms)		*t* test comparison	*t* test results	Meets 95% confidence level?
Fig. 4.5: A	3527	48		A to B	30.987	Yes
Fig. 4.5: B	2178	88		A to C	48.679	Yes
Fig. 4.5: C	2356	100		B to C	3.194	Yes

.

(assessed by the ICP-MS of Ti and Gd in purified trials of varying [**1**]:[TiO_2 active site] equivalents) increases linearly until the ratio of [**1**]:[TiO_2 active sites] reaches 1.0. At a 1:1 equivalence ratio, the conjugation reaction plateaus, giving a value of 4.6±0.2% of functionalized TiO_2 active sites at ratios extending to 5:1. This is most likely due to steric effects as the available TiO_2 active sites may be blocked by the DNA oligonucleotides and the freely rotating, surface-conjugated DOPA-DO3A contrast agents.[26]

Similar to other small molecule clinical contrast agents, the per Gd(III) relaxivity of the nanoconjugates is 3.5±0.1 $mM^{-1}s^{-1}$.[27] However, the maximum overall calculated relaxivity of 61.0±1.7 $mM^{-1}s^{-1}$ for each nanoconjugate is a significant increase in relaxivity. Such an increase allows for quantitative gradient detection of various DOPA-DO3A-nanoparticle loadings via MRI (**Figure 4.4**).

The cellular distribution and single cell association of the DOPA-DO3A-TiO_2 nanoconjugates was evaluated by X-ray fluorescence.[25] SR-XRF data, when deconvulated and standardized, provides high resolution (0.3 x 0.3 μm), two-dimensional images that can be employed to map locations and total elemental concentrations in a desired subcellular region of interest.[21] Therefore, this imaging modality allows direct visualization of the optically undetectable nanoconjugates while simultaneously providing cellular outlines and contrast agent location (phosphorus and gadolinium, respectively).[25, 28]

Presence of nanoconjugates in the cytoplasmic but not the nuclear regions suggests localization in either the targeted organelle, mitochondria, or possibly endosomes (this oligonucleotide has previously shown sequence specificity in this cell line).[7] Colocalization of the Ti and Gd fluorescence signals reveals that the DOPA-DO3A-TiO_2 nanoconjugates are

biologically stable and that their presence inside cells is responsible for the increase in MR image intensity versus control untreated cells (**Figure 4.3**).[25]

To assess the biocompatibility and MR image contrast of the modified nanoparticles in vitro, PC3M cells were imaged after incubation with the nanoconjugates (**Figure 4.5**). Comparison of the images reveals that the cells incubated with the DOPA-DO3A nanoconjugates display contrast enhancement over control cells. Corroborating the nanoconjugate phantom images and XRF images, the PC3M cell images in **Figure 4.5** demonstrate the utility of quantitative T_1 analysis and SR-XRF to predict viable contrast enhancement via MR imaging.

Conclusions and Future Directions

In conclusion, Gd(III)-modified DNA-TiO_2 semi-conducting nanoparticles that are detectable in cells by MR imaging have been synthesized. The labeled particles appear to be retained at specific locations inside cells by the conjugated DNA oligonucleotides hybridizing to intracellular targets, hence creating the first nanoparticle system capable of targeting specific DNA sequences while being simultaneously detected by MR imaging.[22] As a result, it is anticipated that any dopamine functionalized molecule (e.g., cell-penetrating peptides for passive cell membrane transport) can be linked to this modified TiO_2 nanoparticle scaffold allowing non-invasive monitoring of cells containing target molecules and removal of target gene sequences pending TiO_2 excitation. Thus, there are ongoing solid phase peptide syntheses of various cell-penetrating peptides functionalized with a dopamine moiety to facilitate passive membrane transport of the nanoconjugates.

Experimental Procedures

All reagents and solvents were of the highest purity attainable from Aldrich (Milwaukee, WI) and Macrocyclics (Dallas, TX) unless otherwise noted. London finder gold grids (200 mesh)

coated with a polymer backing (formvar) were purchased from Electron Microscopy Sciences (Hatfield, PA). Stem coaxial inserts with 1.5 mm ODs were hand made from 9 in. Pasteur pipets available from Fisher Scientific (Hampton, NH). Mass spectrometry samples were analyzed using electrospray ionization (ESI), single quadrupole mass spectrometry on a Varian 1200L. Results reported for *m/z* are for $[M+H^+]^+$ or $[M-H^+]^-$ unless stated otherwise. Elemental Analysis was performed at Desert Analytics Laboratory (Tuscon, AZ).

Inductively coupled plasma mass spectrometry (ICP-MS) was performed on a computer controlled PQ ExCell Inductively Coupled Plasma Mass Spectrometer (ICP-MS) standardized with eight concentrations spanning the range of 0-50 ppb Gd(III). Five parts per billion In(III) was used as the internal standard for all runs.

UV-visible spectroscopy was performed on a HP 8452A diode array spectrometer at 25 °C. Resolution was set at 2 nm. IR spectra were acquired on a Thermo Nicolet Nexus 870 FT-IR spectrometer in diffuse reflectance infrared fourier transform (DRIFT) mode at 25 °C. The samples were prepared as a 5-10% weight mixture in KBr powder. Automatic baseline correction was used. Resolution was set at 4 cm^{-1}.

HPLC-MS

Analytical HPLC-MS was performed on a computer controlled Varian Prostar system consisting of a 410 autosampler equipped with a 100 μL sample loop, two 210 pumps with 5 mL/min heads, a 363 fluorescence detector, a 330 photodiode array (PDA) detector, and a 1200L single quadrupole ESI-MS. All separations were executed with a 1.0 mL/min flow rate using a Waters 4.6 x 250 mm 5 μm Atlantis-T3 C18 column and a 3.1:1 split directing one part to the MS and 3.1 parts to the series-connected light and fluorescence detectors. Mobile phases consisted of Millipore Synthesis grade water (and HPLC-grade acetonitrile (MeCN). Preparative

HPLC was accomplished using a Varian Prostar system. Two Prostar 210 pumps with 25 mL/min heads fed a 5 mL manual inject sample loop. Detection was performed after a 20:1 split by a two-channel Prostar 325 UV-visible detector and, on the low-flow side, a HP 1046A fluorescence detector. The mobile phases were the same as in the HPLC-MS instrument. Preparative runs were on a Waters 19 x 250 mm 10 μm Atlantis-T3 C18 column.

Cell Culture Experiments

PC3M (human prostate cancer) and PC12 (rat pheochromocytoma) cells were grown according to the instructions recommended by American Type Culture Collection (ATCC) to 80% confluence and at that time incubated in serum-free medium for 16 h. Transfection was done by electroporation: 1-3x10^6 cells were electroporated with 5-15 μL of 10 μM nanoconjugate solution (with 2-6 oligonucleotides per particle) using the Mammozapper™ apparatus (Tritech, Carlsbad, CA) following the manufacturer's instructions. The electroporated cells were resuspended in 8 mL of complete medium and allowed to attach to the tissue culture dishes for 2 h; at that time, cells were washed free of excess nanoconjugates by removing the medium, rinsing with new complete medium, and then adding 10 mL of fresh medium. The cells were allowed to incubate for 24 h before they were harvested for imaging.

MR Imaging and T_1 Analysis

MR measurements were performed on a General Electric/Bruker Omega 600WB 14.1 T imaging spectrometer fitted with Accustar shielded gradient coils at 25 °C. Spin-lattice relaxation times (T_1) were measured using a saturation recovery pulse sequence with a static T_E (7.43 ms) and variable T_R (127.5, 165, 200, 300, 500, 1000, 2000, 5000, 7500, 10000 ms). Two independent trials were run per sample and 4-5 slices were quantified per trial. Student's *t*-tests were calculated in Origin 7 SR2 (Origin Lab, Northampton, MA) at a 95% confidence level with

7 degrees of freedom and a null hypothesis value (minimum acceptable time difference) of 100 ms. Images were acquired using a T_1-weighted spin-echo pulse sequence on nanoparticles or freshly harvested cells that were allowed to gravity pack within the capillary tubes for 12 h prior to image acquisition. The longitudinal water proton relaxation rate at 60 MHz was measured by using a Bruker mq60 NMR Analyzer (Bruker Canada, Milton, Ont. Canada) operating at 1.5 T, by means of the standard inversion-recovery technique. Reproducibility of the T_1 data was ± 0.3%. The temperature was maintained at 37 °C.

Synchrotron Radiation X-Ray Fluorescence (SR-XRF) Analysis

Synchrotron based scanning X-ray fluorescence microscopy was carried out at the 2-ID-E beamline of the Advanced Photon Source at Argonne National Laboratory (IL, USA). Hard X-rays (10 keV) from an undulator source were monochromatized using a single bounce Si <111> monochromator. A Fresnel zone plate (320 μm diameter, focal length f = 250 mm, X-radia, Concord, CA) was used to focus the monochromatic X-ray beam to a spot size of ~0.3 x 0.3 μm^2 on the specimen. The sample was raster scanned through the beam at room temperature under a helium atmosphere. At each scan position, a full fluorescence spectrum was acquired using an energy dispersive germanium detector (Ultra-LEGe detector, Canberra, Meriden, CT). Elemental content was determined by comparison of fitted sample spectra with NBS thin film standards 1832 and 1833 (NIST, Gaithersburg, MD) using MAPS software supplemented with fitting of fluorescence spectra at every pixel.[21, 29]

Relaxivity of the DNA-DOPA-DO3A-TiO_2 Nanoconjugates

The relaxivity of the nanoconjugates was assessed by preparing variable nanoconjugate sample concentrations and embedding them in fast-gelling 1.0% (w/v) agarose. The agarose (2% w/v) was maintained at 50 °C while differing concentrations of nanoconjugates were added to

create samples (1.0 mL total volume) of 1.0% agarose. Upon nanoparticle addition, the solution was thoroughly mixed and allowed to gel in an ice water bath at 0 °C for 5 min. Following gelation, the samples were maintained at 37 °C while the T_1 values were analyzed. The T_1 values of the gelled samples were then plotted against the ICP-MS determined Gd concentration within the samples. The linear slope of the data gave the relaxivity per Gd(III) ion.

Synthesis of gadolinium (III) 4,7-Bis-carboxymethyl-10-{[2-(3,4-dihydroxy-phenyl)-ethylcarbamoyl]-methyl}-1,4,7,10-tetraazacyclododecyl-acetic acid (DOPA-DO3A, **1**)

Dopamine hydrochloride (247 mg, 1.31 mmol) was dissolved in 2 mL of dimethylsulfoxide (DMSO) and the resulting solution was added to a stirring solution of DOTA-mono-NHS (500 mg, 0.77 mmol), *N*,*N*'-diisopropylethylamine (DIEA) (158 mg, 1.23 mmol) and DMSO (10 mL) under a nitrogen atmosphere. ***Note: Depending on the manufacturing process, a variable amount of CF_3COOH and HPF_6 is associated with the mono-NHS-DO3A. The amount of CF_3COOH is typically 3 equivalents. The amount of HPF_6 is typically 1 equivalent.*** The reaction mixture was allowed to stir for 5 h. Aliquots of the mixture were tested via ESI-MS for reaction completion. Once the reaction was complete, the solution was concentrated in vacuo and resuspended in Millipore H_2O. Immediately after resuspension, the $GdCl_3$ (285 mg, 0.77 mmol) was added to the reaction vessel. The temperature was raised to 45 °C and the pH was adjusted to 4.5 with 1 M NaOH. The metalation was allowed to proceed at these conditions for 72 h. Following metalation, the reaction mixture was again concentrated in vacuo to yield the crude product mixture.

The crude mixture was submitted to preparatory HPLC with the Waters Atlantis-T3 column. The solid was brought up in H_2O and purified using the following method: start at 100% H_2O, ramp to 100% MeCN over 35 min and hold for 5 min before returning to 100% H_2O.

The desired fractions (retention time: 10.9 min by UV at 218 and 280 nm) were collected and freeze-dried to yield the product (**1**) as a white solid (442 mg, 83%). ESI-MS calcd for $C_{24}H_{34}GdN_5O_9$ $[M-H]^-$: 693.160, found 693.145; calcd. for $[M+H]^+$: 695.160, found 695.160. Anal. Calcd. for $C_{24}H_{34}GdN_5O_9 + CF_3COOH + 2\ H_2O$: C, 37.01; H, 4.66; N, 8.30. Found: C, 37.14; H, 4.42; N, 8.49.

Synthesis of the DNA-TiO_2 nanoconjugates

The DNA-TiO_2 nanoconjugates were synthesized and then purified via dialysis (4 x 4L over 4 days with 1,000 mol. wt. cutoff) against Millipore H_2O as outlined.[21-23]

Synthesis of the DNA-DOPA-DO3A-TiO_2 nanoconjugates

The DNA-TiO_2 nanoconjugates were analyzed by ICP-MS to determine the total amount of Ti. The Ti concentration was then used to calculate the concentration of nanoconjugates, and subsequently, the concentration of active sites available for dopamine binding.[24] Once the concentration of binding sites was known, compound **1** was added to the DNA-TiO_2 nanoconjugate solution in a 1:1 equivalence ratio for [Ti binding sites]:[**1**]. The DNA-DOPA-DO3A-TiO_2 nanoconjugates were then purified via dialysis (4 x 4L over 4 days with 1,000 mol. wt. cutoff) against Millipore H_2O as previously.

CHAPTER 5:

Towards Optimization of MR Contrast Agent Relaxivity via Ring-Opening Metathesis Polymerization

Introduction

As discussed in the previous chapters, magnetic resonance imaging (MRI) is a routine imaging technique that has gained great importance in the clinical diagnostic community.[1] Its high spatial resolution (10 μm in research settings) and unsurpassed ability to distinguish soft tissues make MR imaging a viable option to other traditional diagnostic techniques.[2] Nevertheless, an overriding disadvantage of MRI as compared to other radiological imaging modalities is its relatively low sensitivity to exogenous contrast agents. Therefore, MR has difficulty exploiting many of the newly developed contrast agents that have been shown to elicit specific and selective image contrast enhancement on a molecular level.[3-13] However, by increasing the effectiveness of these agents, especially those based upon clinically approved, Gd(III)-DOTA and Gd(III)-DTPA complexes, another step in the optimization of diagnostic MR imaging can be recognized.[14]

The overall efficacy of a Gd(III)-based MRI contrast agent depends on several parameters: external magnetic field strength, electronic properties of the Gd(III) ion (T_{1e}), number of Gd(III)-coordinated water molecules (q), water exchange rate (τ_m), molecular rotational diffusion (τ_R), and the Gd(III)-water distance.[12, 14] (The importance and optimization of these parameters are outlined in Chapter 1.) Termed relaxivity, it is the cumulative effect of these parameters which gives contrast agents their ability to enhance MR image intensities.[14] However, because relaxivity is such an intricate and complex relationship of parameters, it is advantageous to focus on one or two limiting characteristics rather than trying to optimize the system as a whole. Consequently, relaxivity at high fields (> 20 MHz) has been recognized to be highly dependent on molecular rotational correlation time, τ_R, with a secondary emphasis on water exchange rate, τ_m (**Figure 5.1**).[5, 14]

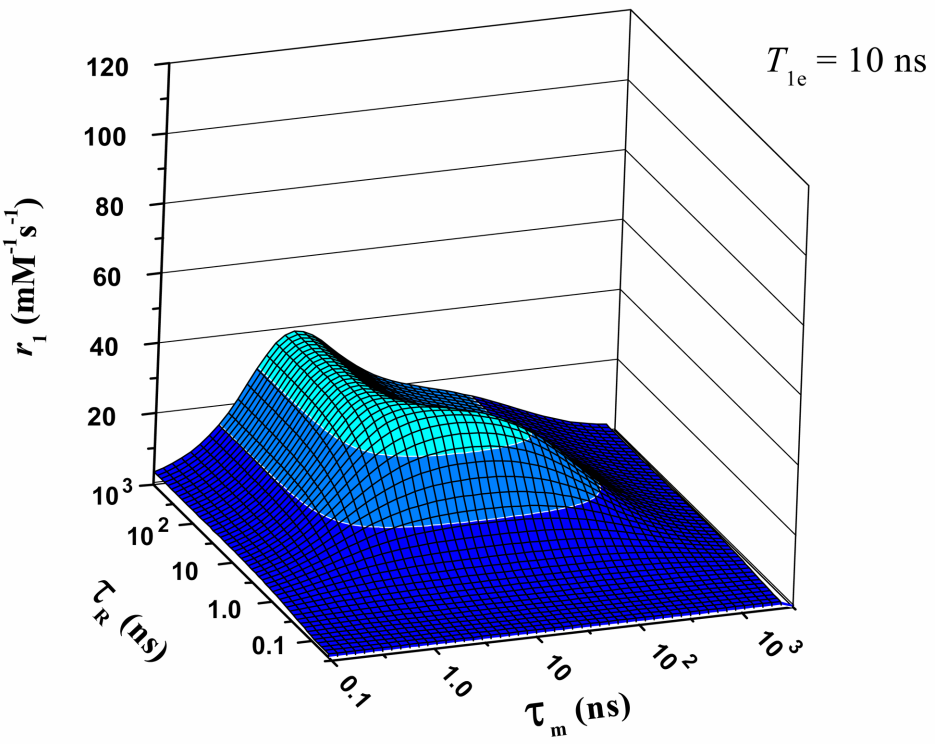

Figure 5.1 Relaxivity calculated as a function of τ_m and τ_R for static T_{1e} at 60 MHz. Optimization of τ_R in the presence of optimum τ_m values allows relaxivity to be maximized (T_{1e} = 10 ns and q = 1). Reproduced with permission from reference 14.

There are numerous reports of fast tumbling Gd(III)-DTPA and Gd(III)-DOTA complexes that have been conjugated to high molecular weight polymers, liposomes, proteins, and nanoparticles in order to produce increased relaxivities by slowing molecular tumbling.[5, 15-20] These high molecular weight agents have optimized τ_R, thereby allowing τ_m, a rate mainly dependent on the Gd(III) chelate and steric crowding around the metal center, to become the critical parameter for achieving maximum relaxivities.[14]

Although these macromolecular agents are effective, they are often difficult to characterize and many are built upon scaffolds which can not be further functionalized (i.e. fluorescent probes for covalidation of in vivo images or cell transduction moieties and targeting domains for molecular and selective MR imaging). However, developments in ring-opening metathesis polymerization (ROMP) with ruthenium-alkylidene catalysts have provided an attractive system to eliminate both of these problems.[21, 22]

Reports have shown that ROMP affords polymers of highly-controlled, well-defined lengths that can display multiple functionalities as well as biological activities.[23-25] This functional group tolerance and length precision were important initial considerations for this work. Additionally, such flexibility and control was augmented by the potential to link multiple Gd(III)-based T_1 contrast agents together while simultaneously increasing their per ion relaxivity via τ_R optimization. These advantages make metathesis-polymerized, Gd(III)-DOTA- and DTPA-based MR contrast agents highly desirable synthetic targets. Therefore, this chapter is devoted to the synthesis, characterization, and preliminary results of a polymer-based MR contrast agent built upon a norbornene scaffold that allows facile monomer and polymer characterization as well as incorporation of multiple covalent functionalities.

Scheme 5.1 Synthesis of norbornene functionalized contrast agents **1** and **6-9**.

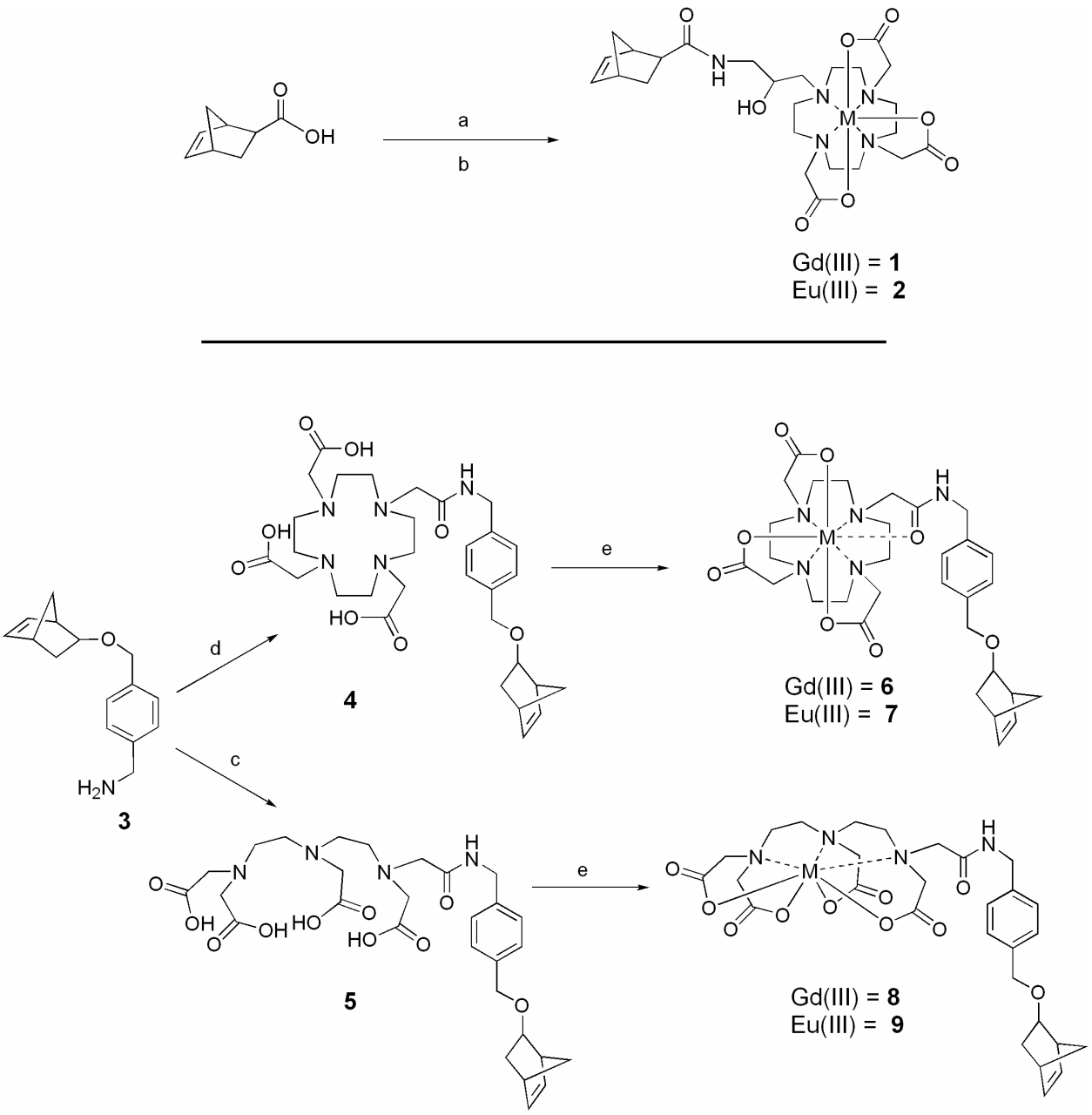

(a) $(COCl)_2$, CH_2Cl_2, 0 °C; (b) Gd(III) or Eu(III)-1,4,7-tris(carboxymethyl)-10-(3-amino-2-hydroxypropyl)-1,4,7,10-tetraazacyclododecane,[26] TEA, DMF, 60 °C; (c) DTPA-dianhydride, DMSO; (d) DOTA-mono-NHS, DIEA, DMF; (e) MCl_3, H_2O pH 6.0.

Results

Synthesis of the ROMP-Accessible Contrast Agent Monomers

The norbornene-based monomer (**1**) was synthesized by coupling the *in situ* activated bicyclo[2.2.1]hept-5-ene-2-*exo*-carboxylic acid to the previously reported amine-functionalized Gd(III)-contrast agent (**Scheme 5.1**).[26] A second set of monomers (**4** and **5**) was generated by treating diethlyenetriaminepentaacetic acid-dianhydride (DTPA-dianhydride) or 1,4,7,10-tetraazacyclododecane-1,4,7,10-tetraacetic acid mono-*N*-hydroxysuccinimidyl ester (DOTA-mono-NHS) with amine **3** (**Scheme 5.1**). Although the condensation reaction leading to **5** yielded di-amidated norbornene monomers, precautions were taken to minimize the formation of this byproduct (Experimental Procedures). To ensure complete metalation, all three monomers were reacted with $EuCl_3$ or $GdCl_3$, purified, and characterized via HPLC-MS and elemental analysis (EA) prior to polymerization. This procedure provided water soluble monomers and removed post-ROMP metalation reactions, thus eliminating any unmetalated monomer units within the polymer.

Monomer Relaxivity, *q*, and τ_m

The relaxivity measurements (r_1, $mM^{-1}s^{-1}$) provided in **Table 5.1** show the relative enhancement of the water proton relaxation rates per Gd(III) ion for complexes **1**, **6**, and **8**. As expected, these values are all relatively close to the commercially available, small-molecule contrast agents, Gd(III)-DTPA (Magnevist) and Gd(III)-DOTA (Dotarem). Similarly, when the Eu(III) analogs (complexes **2**, **7**, and **9**) were subjected to fluorescence measurements, *q* values similar to those reported for Gd(III)-DTPA and Gd(III)-DOTA were revealed.[27] These measurements provided the following data (ms^{-1}): **2**: $k_{H2O} = 1.791$, $k_{D2O} = 0.661$; **7**: $k_{H2O} = 1.545$, $k_{D2O} = 0.439$; **9**: $k_{H2O} = 1.585$, $k_{D2O} = 0.409$. The calculated *q* values are displayed in **Table 5.1**.

Table 5.1 Relaxometric properties of the ROMP-accessible MRI contrast agent monomers **1**, **6**, and **8** at pH 7.4 and 37 °C.

	Relaxivity ($mM^{-1}s^{-1}$)[a] 60 MHz (1.5 T)	q	τ_m (ns)[b]
1	3.5	1.0	378
6	3.6	1.0	748
8	4.2	1.0	1069
Gd(III)-DOTA	3.2	1.2[c]	243[d]
Gd(III)-DTPA	3.8	1.2[c]	303[d]

[a] Measured in H_2O, and calculated per Gd(III) ion, [b] calculated at 25 °C, [c] data from reference 27, [d] data from reference 28.

A

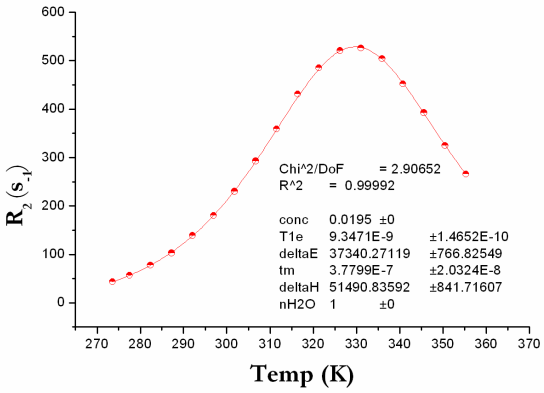

B

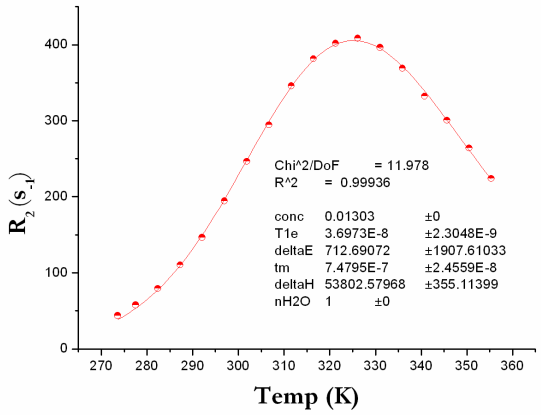

C

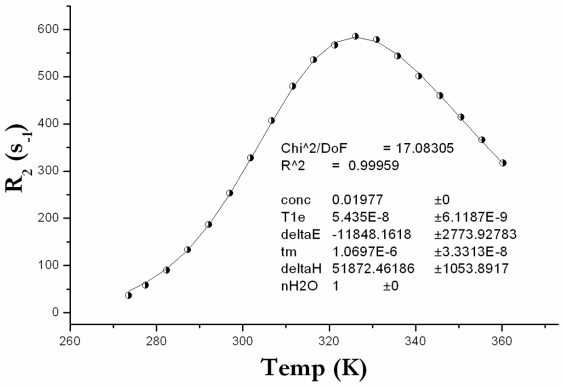

Figure 5.2 Determination of τ_m by ^{17}O transverse relaxation rate measurements of ROMP-accessible MRI contrast agents (A) **1**, (B) **6**, and (C) **8** at 25 °C. Notice that in each case the calculated τ_m curve closely fits the experimentally acquired relaxation data (red is used to highlight DOTA chelates, while black is used to highlight DTPA chelates).

As with most small molecule DOTA and DTPA-based contrast agents where one carboxylic acid arm has been replaced with an amide or β-hydroxyl, these values all reflect one bound water molecule within an error of ±0.5.[6, 14]

To evaluate the mean residence lifetime (τ_m) of the water molecule coordinated to the metal center of complexes **1**, **6**, and **8**, temperature dependent, line-broadening ^{17}O-NMR was performed. The data was fit according to equations derived by Swift and Connick using these four parameters: τ_m (water exchange rate), $\Delta H^{\ddagger}$ (activation enthalpy), T_{1e} (electronic relaxation rate), and ΔE_{T1e} (activation energy of T_{1e}) (**Figure 5.2**).[29-31] Notice that substitution of an acetate arm by an amide linkage, as with complexes **6** and **8**, has significantly increased the lifetime of the bound water molecule as compared to **1**, Gd(III)-DTPA, or Gd(III)-DOTA (e.g. 243 → 748 ns, in the case of Gd(III)-DOTA → complex **6**, **Table 5.1**). Although undesirable, this negative impact on τ_m via chelate arm amidation was described in Chapter 3 and has been reported elsewhere.[6, 14, 32]

Polymerization and Characterization

To assess the ROMP activity of the contrast agent monomers, complex **1** was reacted with Grubbs catalyst ($Ru(PCy_3)_2$=CHPh) in varying monomer to catalyst ratios to yield incremental block lengths (**Scheme 5.2A**). Construction of the homopolymers was afforded by quick initiation, as evidenced by a characteristic solution color change. However, slow propagation and decreased solubility of the growing polymer chains yielded mixtures of desired product and starting material, regardless of solvent conditions or polymerization times (e.g. CH_2Cl_2:MeOH (9:1), $CHCl_3$:MeOH (9:1), or DMF with a maximum duration of 90 min before catalyst deactivation). Therefore, post polymerization and precipitation, each reaction mixture was submitted to size-exclusion chromatography on Sephadex G-15 media to remove the

Scheme 5.2 Synthesis of multimeric MRI contrast agent via ROMP. [a]

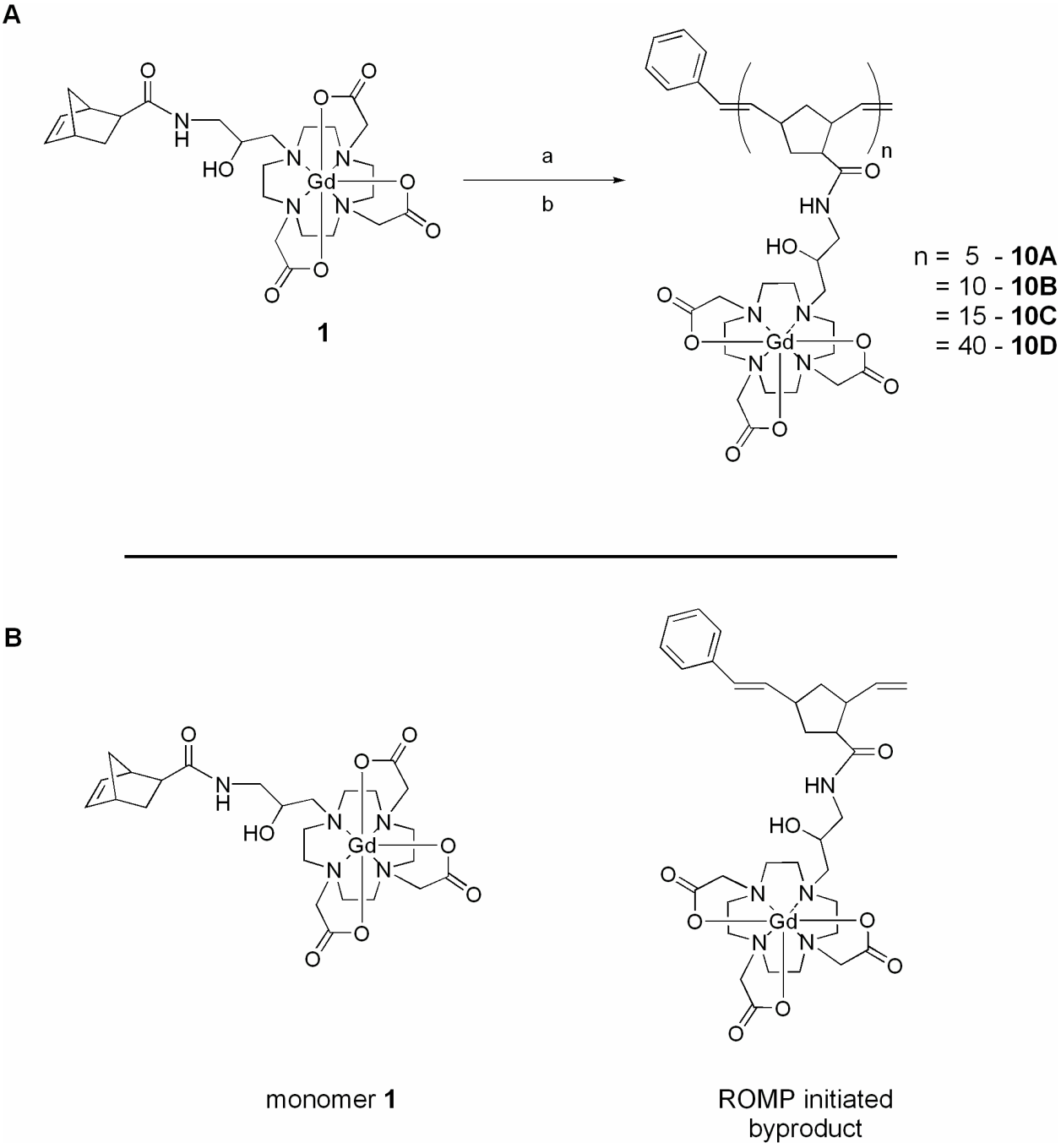

(A) Polymerization of **1**, (a) $Ru(PCy_3)_2$=CHPh, $CHCl_3$:MeOH (9:1); (b) CH_2=$CHOCH_2CH_3$. (B) Byproducts of reaction (A). [*]Polymerizations were perfomed by DeeDee Smith.

Table 5.2 Properties of MRI contrast agent polymers **10A-D**.

	Theoretical block length	Theoretical Mol. Wt.	Actual block length	Actual Mol. Wt. (GPC)[a]	PDI
10A	5	3,574	5	3,339	1.32
10B	10	7,044	10	6,586	1.14
10C	15	10,514	15	10,087	1.12
10D	40	27,864	14	9,653	1.12

[a] The observed difference between the experimental and calculated Mol. Wt. values can be attributed to a decreased hydrodynamic radius with respect to linear, polystyrene gel permeation chromatography (GPC) standards.

A

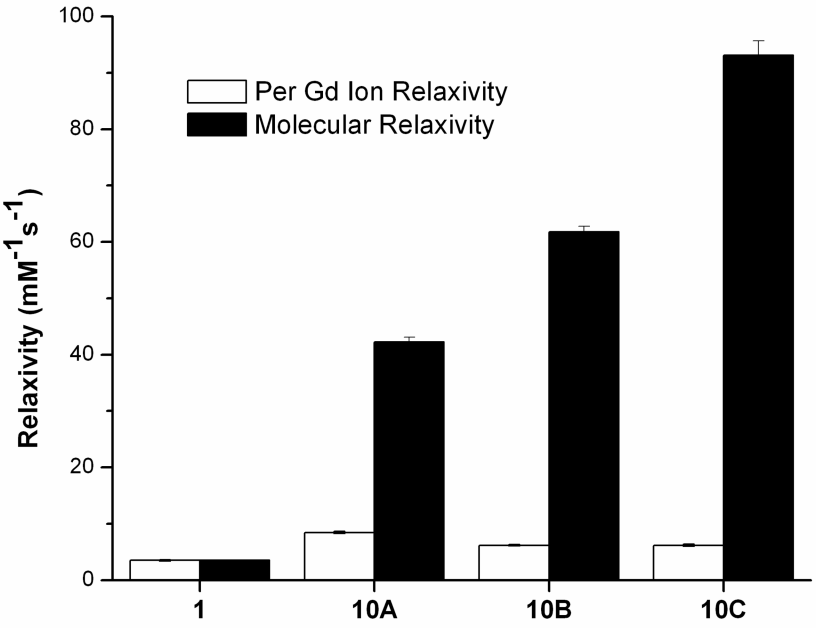

B

	Relaxivity per Gd(III) ($mM^{-1}s^{-1}$)	Relaxivity per molecule ($mM^{-1}s^{-1}$)
10A	8.46 ±0.06	42.3 ±0.8
10B	6.18 ±0.10	61.8 ±1.0
10C	6.21 ±0.16	93.2 ±2.5

Figure 5.3 Relaxometric properties of the polymeric MRI contrast agents in H_2O, pH 7.4 at 60 MHz and 37 °C. (A) Bar chart of Gd(III) ionic and molecular relaxivities. (B) Measured and calculated Gd(III) ionic and molecular relaxivities. (Polymer **10D** was omitted due to synthetic issues that limited block length.)

starting material and the possible low molecular weight byproducts. These collected fractions were analyzed via HPLC to determine the species present. Although a substantial amount of the desired polymer was recovered (e.g. 55% for **10A**), HPLC-MS revealed that the two most prevalent byproducts were ROMP-initiated and uninitiated monomer (**Scheme 5.2B**). Furthermore, the block length of the homopolymers appears to be limited to approximately 15 units, regardless of the concentration of monomer present or the reaction time allowed (**Table 5.2**). However, because the collected and purified polymers displayed synthetically acceptable polydispersity indices (average PDI of 1.2), the relaxivities of the varying-length polymers were explored.[21, 22]

Polymer Relaxivities

To determine the effect of chain length on the relaxivity of the contrast agent polymers, the slope of the line generated by plotting the inverse of the T_1 relaxation time versus Gd(III) concentration was measured. Transition from the monomeric species (**1**) to a short oligomer of 5 (**10A**) yielded a per Gd(III) relaxivity of 8.46±0.06. As the chain length was increased to yield oligomers of 10 (**10B**) and 15 (**10C**), the relaxivity per Gd(III) dropped to 6.18±0.10 and 6.21±0.16, respectively. These values are on average 2.2-fold higher than clinically approved Gd(III)-DOTA (**Figure 5.3**). Similarly, overall molecular relaxivities increase with the incorporation of multiple chelated Gd(III) ions, giving polymer **10C** a relaxivity that is 29-fold that of clinical agents. (Polymer **10D** was omitted from these studies due to synthetic issues that limited block length.)

Discussion

Synthetically, each monomer presented unique challenges. Due to the highly-activated acid chloride formed *in situ*, monomer **1** had to be metalated prior to the norbornene conjugation

reaction (**Scheme 5.1**). Metalation eliminated the possibility of esterification between the alcohol functionality of the chelate starting material and the acid chloride by coordinating the hydroxyl moiety to the Gd(III) metal.[14] However, this limits synthetic versatility by forcing metalation early in the 4-step literature procedure to synthesize the amine functionalized chelate, 1,4,7-tris(carboxymethyl)-10-(3-amino-2-hydroxypropyl)-1,4,7,10-tetraazacyclododecane.[26] Optimally, preparation of a metal chelating ligand can be completed in its entirety before the lanthanide is added. This approach allows preparation of an array of metalated complexes without the need to repeat a multi-step synthesis. Therefore, the synthetic schemes leading to lanthanide complexes **6-9** were designed differently.

Monomers **6-9** were synthesized using a common starting material, compound **3**. Specifically, monomers **6** and **7** were built from an activated DOTA derivative, while monomers **8** and **9** were built from DTPA-dianhydride. This made each set of metalated complexes available from a single precursor, compound **4** or **5**, respectively (**Scheme 5.1**). Such an approach allows versatility in the final product, as metalation with various lanthanide salts yields complexes that can later be used to determine various molecular parameters such as *q* values, solution phase NMR structures, and relaxivity.[12, 33, 34]

Upon successful synthesis and characterization of the contrast agent monomers, each was subjected to *q*, τ_m, and relaxivity measurements (Experimental Procedures). This data, summarized in **Table 5.2**, conforms to other previously explored small molecule contrast agents.[6] The per Gd(III) ion relaxivities at 37 °C and 60 MHz are all near the reported range of 3-4 $mM^{-1}s^{-1}$, as are the *q* values, which reflect the expected value of 1.0±0.5.[6, 14] Due to the amidation within **6** and **8**, the τ_m values encompass a much wider numerical range.[6, 12, 32] Originally chosen for this parameter and the amine functionality of its literature precursor,

monomer **1** has a τ_m value that is 2 and 3-fold shorter than monomers **6** and **8**, respectively. Although such differences are hidden by the strong dependence of this system on τ_R, the goal of the ROMP scaffold is to optimize τ_R, therefore, it is important to remain cognizant of τ_m, because these values will eventually require attention (**Figure 5.1**).[12, 14]

The initial polymerization studies of **1** have revealed promising results. Although polymerization is possible, chain length in CH_2Cl_2:MeOH or $CHCl_3$:MeOH mixtures appears to be limited to a maximum of 15 units. Additionally, yields are less than quantitative, indicating that either decreased polymer chain solubility or some aspect of the monomer is hindering the metathesis reaction. Therefore, extensive HPLC purification was used to identify and discard any possible *endo*-isomer impurities from the monomer starting material (the *endo* isomer of norbornene is known to slow ROMP-based reactions).[35] However, subsequent polymerizations with the re-purified *exo*-monomer of **1** afforded insignificant changes in the polymerization results. Further investigation by the Nguyen group with similar monomers have since provided evidence that α-amide functionalized norbornene molecules can display a slower reaction rate than α-oxo species.[36] Therefore, monomers **6** and **8** were designed and synthesized from compound **3**, eliminating the amide moiety speculated to be hindering polymerization while increasing both monomers' organic solubility by adding the benzyl linkage. While these monomers are currently undergoing polymerization studies, polymers **10A-10C** were subjected to relaxivity measurements.

To evaluate the efficacy of **10A-10C** to shorten the T_1 of bulk water protons, the relaxivity of each polymer was determined (**Figure 5.3**). Considering the directly proportional relationship between increased molecular weight and relaxivity, the values acquired for **10A-C** show the expected positive increase in relaxivity upon ruthenium-catalyzed ROMP.[12, 14]

However, after addition of more than 5 monomer units, the per Gd(III) relaxivity of the polymers decreases, maintaining an average value of 6.2 $mM^{-1}s^{-1}$ for block lengths extending to 15. Such behavior has yet to be explained, but one possible conjecture is that the added length of **10B** and **10C** allow the polymers increased fluidity as compared to **10A**. Increased fluidity negatively impacts molecular anisotropy and consequently, τ_R.[37] However, this data is preliminary, and detailed studies aimed at explaining this trend are presented in the Future Directions section of this chapter.

Conclusions

By designing and synthesizing MRI contrast agents functionalized with various norbornene moieties, this work shows that metathesis polymerization is capable of creating easily characterizable, high molecular weight, Gd(III)-based contrast agents with low polydispersities. In addition, these novel contrast agents are multi-meric, affording relaxivities that are up to 29-fold greater than the currently available clinical agents. Furthermore, the versatility of ROMP has not only allowed the synthesis of several high relaxivity MR contrast agents, but it has provided insight into the optimization of τ_R in linear polymeric systems. Although this system requires more in-depth study, the strategy of using ROMP to create multi-valent contrast agent structures has been successful and will support future work on the synthesis of highly-versatile, multi-modal contrast agents for MR imaging.

Future Directions

To explore the hypothesis that the α-amide of monomer **1** is responsible for the slight deactivation of the ruthenium catalyst, the polymerization studies of monomers **6** and **8** must be completed. Furthermore, the polymerization reactions of **6** and **8** will provide insight on whether decreased polymer solubility as a result of growing chain length is halting ROMP at 15 subunits.

Additional evidence on the optimization of the rotational correlation time as a function of polymer weight can also be recorded from the variable chain length polymers of these slow water exchange monomers. Such data will elucidate the cause of the phenomenon observed in **10A-C**, where an increase in molecular weight led to a decrease in per Gd(III) relaxivity. When this relaxivity decrease and the slow polymerization rate can be explained, a ROMP-accessible monomer that exhibits a near-optimal τ_m will be synthesized.

By exploiting work done by both Congreve and Duimstra, **Scheme 5.3A** outlines the simple, two-step synthesis of a contrast agent monomer that should display $q = 1$ and a near-optimal water exchange rate due to steric bulk placed around the Gd(III) ion by the large norbornene substituent.[7, 38] However, if α-amide moieties are proven to slow ruthenium-catalyzed ROMP, **Scheme 5.3B** outlines a lengthier synthetic route to a complementary monomer that is built from **3** and should display drastically improved τ_m values, via confined chelate geometry, over **6** and **8**.[39]

To allow the ROMP scaffold cell membrane permeability and further applicability in the field of molecular MR imaging, **Scheme 5.4** shows the synthesis of a norbornene-based, polyarginine monomer. By utilizing the ability of ruthenium-catalyzed ROMP to create well-defined diblock copolymers, attachment of one or two polyarginine monomers should provide **10A-C** or various other contrast agent polymers, with the ability to transduce cell membranes and consequently label cultured cells for detection via routine MR imaging.[40, 41]

Scheme 5.3 Synthesis of two ROMP-accessible MRI contrast agents with optimized water exchange rates.

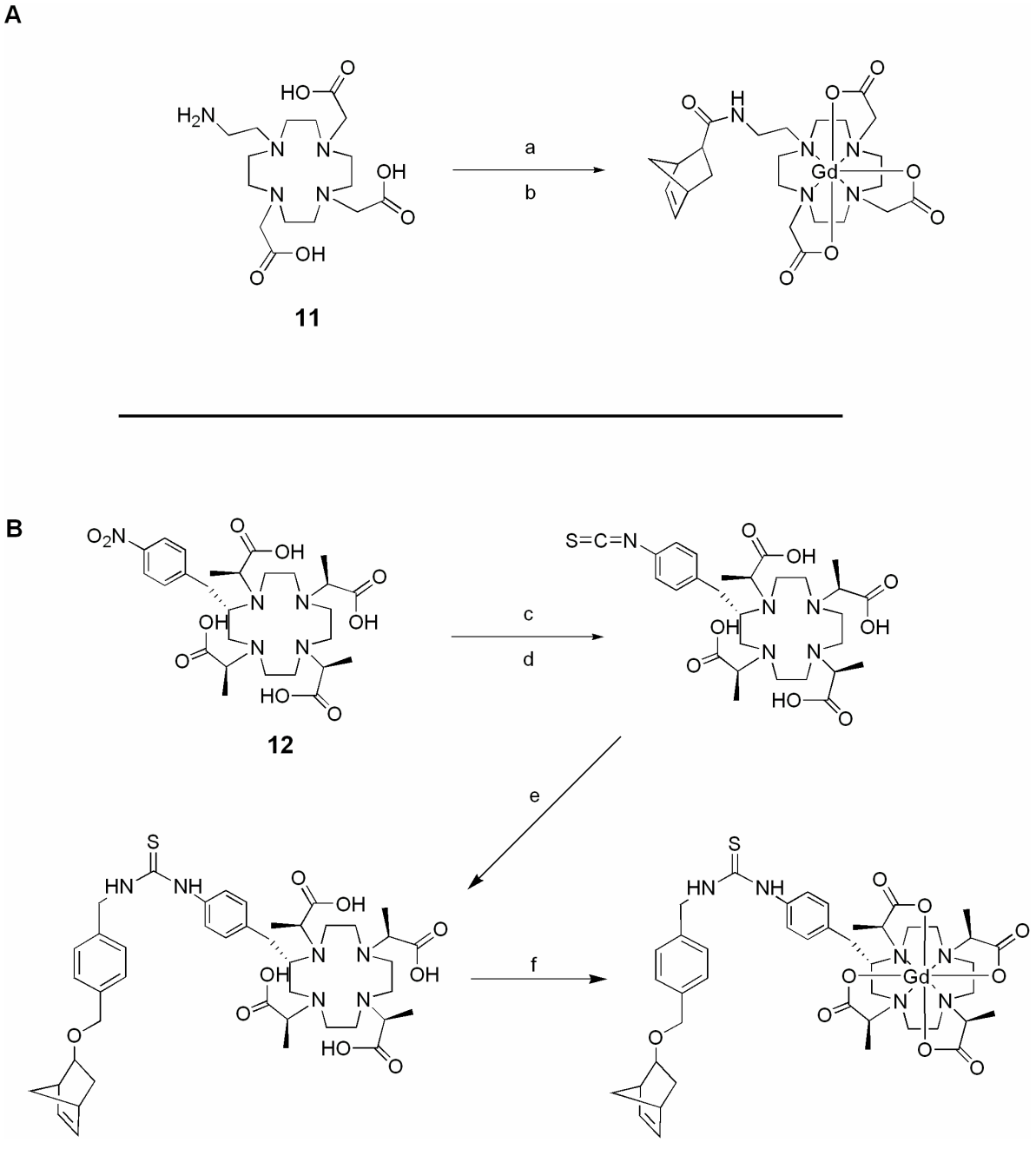

(a) (compound **11**),[7] bicyclo[2.2.1]hept-5-ene-2-*exo*-carboxylic acid, $(COCl)_2$, CH_2Cl_2, 0 °C; (b) $GdCl_3$, H_2O pH 6.0, 60 °C; (c) (compound **12**),[39] Pd/C, H_2; (d) K_2CO_3, $CSCl_2$, $CHCl_3$, 0 ºC; (e) **3**, DMSO, 80 ºC; (f) $GdCl_3$, H_2O pH 6.0, 60 °C.

Scheme 5.4 Synthesis of a polyarginine ROMP-accessible monomer for facilitating cell transduction of block copolymers.

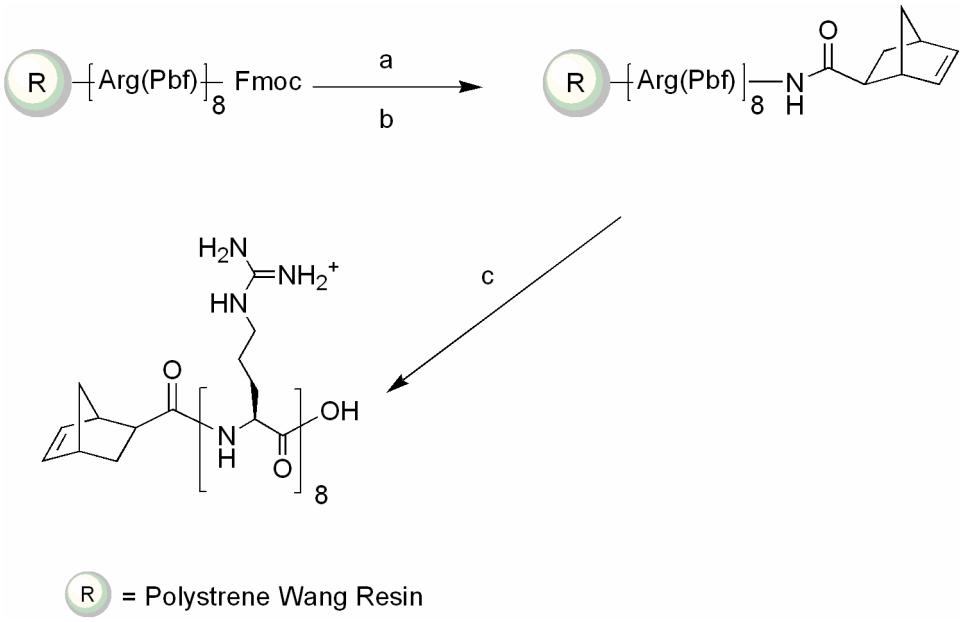

(a) Piperdine; (b) bicyclo[2.2.1]hept-5-ene-2-*exo*-carboxylic acid, HATU, DIEA; (c) 95% TFA, 2.5% H_2O, 2.5% TIS

Experimental Procedures

All reagents and solvents were of the highest purity attainable from Sigma-Aldrich (Milwaukee, WI) or Strem Chemicals (Newburyport, MA) unless otherwise noted. ^{1}H and ^{13}C NMR spectra were obtained on a Varian Inova spectrometer at 400 and 100 MHz, respectively. Mass spectrometry samples were analyzed using ESI, single quadrupole mass spectrometry on a Varian 1200L spectrometer (Varian Inc.; Walnut Creek, CA). High resolution MS (HR-MS) samples were analyzed on an Agilent Technologies ESI-quadrupole TOF spectrometer (Agilent Technologies; Santa Clara, CA). Results reported for *m/z* are for $[M+H^+]^+$ or $[M-H^+]^-$ unless stated otherwise. Elemental Analyses were performed at Desert Analytics Laboratory (Tuscon, AZ).

ICP-MS was performed on a computer-controlled Thermo Elemental (Waltham, MA) PQ ExCell Inductively Coupled Plasma Mass Spectrometer. All standards and samples contain 5 ng/mL of a multi-element internal standard (Spex CertiPrep, Metuchen, NJ) consisting of Bi, Ho, In, Li, Sc, Tb, Y and 3% nitric acid (v/v). Gadolinium standards were prepared in concentrations of 0.05, 0.10, 0.25, 0.50, 1.0, 5.0, 10, 25, and 50 ng/mL. Analysis was accomplished running 1 survey run and 3 main runs (peak jumping, 100 sweeps per run) using ^{156}Gd and ^{157}Gd isotopes and interpolating through ^{209}Bi and ^{115}In internal standards.

Molecular weights relative to polystyrene standards were measured either by LARK Enterprises (Webster, MA) or on a Waters gel-permeation chromatograph (GPC) equipped with Breeze software, a 717 autosampler, Shodex KF-G guard column, KF-803L and KF-806L columns in series, a Waters 2440 UV detector, and a 410 RI detector. HPLC-grade THF was used as the eluent at a flow rate of 1.0 mL/min and the instrument was calibrated using polystyrene standards (Aldrich, 15 standards, 760-1,800,000 Daltons).

1,4,7,10-Tetraazacyclododecane-1,4,7,10-tetraacetic acid mono(*N*-hydroxysuccinimide ester) (DOTA-NHS) was purchased from Macrocyclics (Dallas, TX). Gd(III) and Eu(III)-1,4,7-tris(carboxymethyl)-10-(3-amino-2-hydroxypropyl)-1,4,7,10-tetraazacyclododecane were synthesized following a previously published procedure, as was compound **3**, 4-[(bicyclo[2.2.1.]hept-5-en-2-*exo*-yloxy)-methyl]benzylamine.[24, 26]

HPLC-MS

Analytical reverse phase HPLC-MS was performed on a computer controlled Varian Prostar system consisting of a 410 autosampler equipped with a 100 μL sample loop, two 210 pumps with 5 mL/min heads, a 363 fluorescence detector, a 330 photodiode array (PDA) detector, and a 1200L single quadrupole ESI-MS. All separations were executed with a 1.0 mL/min flow rate using a Waters 4.6 x 250 mm 5 μm Atlantis C18 column, with a 3.1:1 split directing one part to the MS and 3.1 parts to the series-connected light and fluorescence detectors. Mobile phases consisted of Millipore Synthesis grade water (solvent A) and HPLC-grade MeCN (solvent B). Preparative HPLC was accomplished using a Varian Prostar system. Two Prostar 210 pumps with 25 mL/min heads fed a 5 mL manual inject sample loop. Detection was performed after a 20:1 split by a two-channel Prostar 325 UV-visible detector and, on the low-flow side, a HP 1046A fluorescence detector. The mobile phases were the same as in the HPLC-MS instrument. Preparative runs were on a Waters 19 x 250 mm 10 μm Atlantis C18 column.

Relaxivity (r_1)

A 2 mM stock solution of each compound was serially diluted to give 500 μL of each of the five approximate concentrations: 0.15, 0.3, 0.5, 1.0, and 2.0 mM. The T_1 of each sample was determined at 60 MHz (1.5 T) and 37 °C using an inversion recovery pulse sequence on a Bruker mq60 Minispec (Bruker Canada; Milton, Ontario, Canada). Reproducibility of the T_1 data was ±

0.3%. Ten microliters of each sample was then analyzed for exact gadolinium concentration using ICP-MS. The inverse of the longitudinal relaxation time (T_1) was plotted against the concentration obtained from ICP-MS and fit to a straight line. All lines were fit with $R^2 > 0.998$. The measurements were performed in duplicate for each sample.

Determination of q by Luminescence Lifetime Measurements

The Eu(III) complexes were dissolved in D_2O and H_2O. The emission was monitored at 614 nm with excitation at 395 nm on a Hitachi F4500 Fluorescence Spectrophotometer operating in phosphorescence lifetime mode. Twenty-five scans were averaged and fit to a monoexponential decay ($R^2 > 0.98$) to give the phosphorescent lifetimes which were entered into this equation (corrected for one amide oscillator): $q = 1.0 (k_{H2O} - k_{D2O} - 0.25 - 0.075)$.[33, 42] These values were reproduced in duplicate with varying mole fractions of H_2O and D_2O as outlined.[33]

Determination of τ_m by ^{17}O Transverse Relaxation Rate Measurements

Samples were prepared at 15-20 mM concentrations in 1% ^{17}O enriched water (Medical Isotopes, Inc.; Pelham, NH) adjusted to pH 7.40. Lock was achieved by means of an external D_2O standard. ^{17}O spectra were obtained at 54 MHz (number of averaged transients was 160 – 320 and relaxation delay was 400 ms) at temperatures ranging from 1 °C to 85 °C in 5 °C increments. The ^{17}O transverse relaxation rate was determined by obtaining the line width (in Hz) at half of the peak height, $\Delta\nu_{1/2}$, of the ^{17}O water signal and later fitting the data.[29-31] Using the known sample concentrations and q values, the relaxation data were fit to these four parameters at 25 °C: τ_m (water exchange rate), $\Delta H^{\ddagger}$ (activation enthalpy), T_{1e} (electronic relaxation rate), and ΔE_{T1e} (activation energy of T_{1e}).[5]

Synthesis of Gd(III)-1-{3-[(bicyclo[2.2.1]hept-5-ene-2-exo-carbonyl)-amino]-2-hydroxy-propyl}-4,7,10-tris-carboxymethyl-1,4,7,10-tetraazacyclododecane (**1**)

Following a procedure similar to Stille and coworkers, bicyclo[2.2.1]hept-5-ene-2-*exo*-carboxylic acid (360 mg, 2.61 mmol) was dissolved in 10 mL of degassed, anhydrous CH_2Cl_2 under an argon atmosphere.[43] The stirring solution was cooled to 0 °C before adding the oxalyl chloride (219 mg, 1.74 mmol). This solution was allowed to warm to room temperature overnight before being concentrated *in vacuo*. The resulting oil was resuspended in a solution of Gd(III)-1,4,7-tris(carboxymethyl)-10-(3-amino-2-hydroxypropyl)-1,4,7,10-tetraazacyclododecane (500 mg, 0.871 mmol) in anhydrous DMF (6 mL). After the mixture was resuspended, anhydrous TEA (176 mg, 1.74 mmol) was added. This mixture was brought to 60 °C and this temperature was maintained for 8 h. Upon cooling, the yellowish solution was concentrated *in vacuo* and was brought up in 1:1, MeCN:H_2O. This crude mixture was submitted to preparatory HPLC with the Waters Atlantis T3 column using the following method: start at 0% B, ramp to 100% B over 35 min followed by a wash at 100% B for 5 min before returning to 0% B. The desired fractions (retention time: 15.40 min by UV at 220 nm) were collected and freeze-dried to yield the product as a white solid (244 mg, 40%). HR-ESI-MS (*m/z*): 695.2036; calc. for $C_{25}H_{38}GdN_5O_8+H^+$: 695.2039.

Synthesis of Eu(III)-1-{3-[(bicyclo[2.2.1]hept-5-ene-2-exo-carbonyl)-amino]-2-hydroxy-propyl}-4,7,10-tris-carboxymethyl-1,4,7,10-tetraazacyclododecane (**2**)

Following a procedure similar to Stille and coworkers, bicyclo[2.2.1]hept-5-ene-2-*exo*-carboxylic acid (50 mg, 0.362 mmol) was dissolved in 5 mL of degassed, anhydrous CH_2Cl_2 under an argon atmosphere.[43] The stirring solution was cooled to 0 °C before adding the oxalyl chloride (30.4 mg, 0.241 mmol). This solution was allowed to warm to room temperature overnight before being concentrated *in vacuo*. The resulting oil was resuspended in a solution of Eu(III)-1,4,7-tris(carboxymethyl)-10-(3-amino-2-hydroxypropyl)-1,4,7,10-

tetraazacyclododecane (68.4 mg, 0.121 mmol) in anhydrous DMF (3 mL). Shortly after the mixture was resuspended, anhydrous TEA (24.0 mg, 0.241 mmol) was added. This mixture was brought to 60 °C for 8 h. Upon cooling, the yellowish solution was concentrated *in vacuo* and was brought up in 1:1, MeCN:H_2O. This crude mixture was submitted to preparatory HPLC with the Waters Atlantis T3 column using the following method: start at 0% B, ramp to 100% B over 35 min followed by a wash at 100% B for 5 min before returning to 0% B. The desired fractions (retention time: 15.58 min by UV at 220 nm) were collected and freeze-dried to yield the product as a white solid (31.0 mg, 37%). HR-ESI-MS (*m/z*): 690.2015; calc. for $C_{25}H_{38}EuN_5O_8+H^+$: 690.2011.

Synthesis of (4-{[4-(Bicyclo[2.2.1]hept-5-en-2-exo-yloxymethyl)-benzylcarbamoyl]-methyl}-7,10-bis-carboxymethyl-1,4,7,10-tetraazacyclododec-1-yl)-acetic acid (**4**)

DOTA-mono-NHS (100 mg, 0.199 mmol), 4-[(bicyclo[2.2.1.]hept-5-en-2-*exo*-yloxy)-methyl]benzylamine (**3**, 59.4 mg, 0.259 mmol), and DIEA (257 mg, 1.99 mmol) were dissolved in 15 mL of anhydrous DMF. The reaction mixture was allowed to stir under a nitrogen atmosphere for 3 h before being concentrated in vacuo. The resulting oil was brought up in H_2O and submitted to preparatory HPLC with the Waters Atlantis T3 column using the following method: start at 0% B, ramp to 60% B over 35 min, a second ramp to 100% B over 10 min, and finally a wash at 100% B for 5 min before returning to 0% B. The desired fractions (retention time: 41.84 min by UV at 220, 264 nm) were collected and freeze-dried to yield the product as a white solid (82.4 mg, 68%). ^{1}H NMR (DMSO): δ = 1.30-1.34 (m, 1H), 1.45-1.52 (m, 2H), 16.0-1.62 (m, 2H), 2.68-3.01 (m, 18H), 3.16-3.34 (m, 9H), 3.51 (m, 1H), 3.53 (s, 1H), 3.92 (s, 1H), 4.26 (s, 1H), 4.39-4.53 (m, 2H), 5.93-5.95 (m, 1H), 6.18-6.21 (m, 1H), 7.20-7.40 (m, 4H), 8.77 (bs, 1H); ^{13}C NMR (DMSO): δ = 34.16, 39.86, 41.54, 42.65, 43.02, 45.68, 45.81, 50.11, 50.21,

50.89, 51.45, 55.60, 55.98, 58.23, 70.09, 79.20, 127.83, 127.47, 127.56, 128.29, 133.20, 137.14, 138.46, 140.52, 168.70, 169.83, 170.44; ESI-MS (*m/z*): 616.289; calc. for $C_{31}H_{45}N_5O_8$+H^+: 616.280; with Anal. Calcd. for $C_{31}H_{45}N_5O_8$: C, 60.47; H, 7.37; N, 11.37. Found: C, 60.40; H, 7.00; N, 11.60.

Synthesis of [(2-{[2-({[4-(Bicyclo[2.2.1]hept-5-en-2-exo-yloxymethyl)-benzylcarbamoyl]-methyl}-carboxymethyl-amino)-ethyl]-carboxymethyl-amino}-ethyl)-carboxymethyl-amino]-acetic acid (**5**)

DTPA-dianhydride (779 mg, 2.18 mmol) was dissolved in 100 mL of anhydrous DMSO. This solution was stirred vigorously while H_2O (39.2 mg, 2.18 mmol) in DMSO (20 mL) was added via syringe pump over 2.5 h. Then a solution of 4-[(bicyclo[2.2.1.]hept-5-en-2-*exo*-yloxy)-methyl]benzylamine (**3**, 250 mg, 1.09 mmol) dissolved in 20 mL of DMSO was added to the reaction mixture over 4 h. The resulting solution was allowed to stir for an additional 2 h before 20 mL of H_2O was added to quench any remaining anhydride. After concentration *in vacuo*, the crude oil was redissolved in H_2O and submitted to preparatory HPLC with the Waters Atlantis T3 column using the following method: start at 0% B, ramp to 60% B over 35 min, a second ramp to 100% B over 10 min, and finally a wash at 100% B for 5 min before returning to 0% B. The desired fractions (retention time: 18.62 min by UV at 220, 254 nm) were collected and freeze-dried to yield the product as a white solid (197 mg, 30%). ^{1}H NMR (DMSO): δ = 1.25-1.29 (m, 1H), 1.39-1.50 (m, 2H), 1.57 (d, *J* = 8.4 Hz, 1H), 2.46 (s, 5H), 2.83-2.96 (m, 11H), 3.28-3.49 (m, 11H), 4.24 (dd, *J* = 11.6, 14.4 Hz, 2H), 5.91 (m, 1H), 6.16 (m, 1H), 7.21 (s, 4H), 8.57 (bs, 1H); ^{13}C NMR (DMSO): δ = 34.15, 41.87, 45.67, 45.82, 50.50, 51.86, 54.50, 54.80, 55.00, 57.50, 61.77, 62.40, 70.07, 79.14, 127.13, 127.51, 131.56, 133.19, 137.27, 138.64, 140.48, 169.49, 170.34, 172.56, 172.65; ESI-MS (*m/z*): 605.280; calc. for $C_{29}H_{40}N_4O_{10}$+H^+: 605.274;

with Anal. Calcd. for $C_{29}H_{40}N_4O_{10}$ • 2 H_2O: C, 54.37; H, 6.92; N, 8.74. Found: C, 54.27; H, 6.49; N, 9.19.

The fractions containing the diamidated product (retention time: 26.26 min by UV at 220, 254 nm) were also collected and freeze-dried (152 mg, 17%). %). ^{1}H NMR (DMSO): δ = 1.30-1.33 (m, 2H), 1.43-1.50 (m, 4H), 1.61 (d, *J* = 8.0 Hz, 2H), 2.77-2.80 (m, 12H), 2.80-2.91 (m, 12H), 3.51 (d, *J* = 6.4, 2H), 4.26 (d, *J* = 6.0, 4H), 4.46 (dd, *J* = 11.6, 14.4 Hz, 4H), 5.94 (m, 2H), 6.19 (m, 2H), 7.22 (m, 8H), 8.55 (bs, 2H); ^{13}C NMR (DMSO): δ = 34.15, 39.86, 41.73, 45.67, 45.82, 51.04, 52.16, 55.01, 57.53, 70.06, 79.15, 127.09, 127.49, 133.18, 137.29, 138.57, 140.47, 169.90, 170.37, 171.34, 172.64; ESI-MS (*m/z*): 816.418; calc. for $C_{44}H_{42}N_5O_{10}$+H^+: 816.411; with Anal. Calcd. for $C_{44}H_{42}N_5O_{10}$ • Na: C, 62.99; H, 6.85; N, 8.35. Found: C, 62.89; H, 6.55; N, 8.52.

Synthesis of Gd(III)- 1-{[4-(Bicyclo[2.2.1]hept-5-en-2-exo-yloxymethyl)-benzyl-carbamoyl]-methyl}-4,7,10-tris-carboxymethyl-1,4,7,10-tetraazacyclododecane (**6**)

Compound **4** (35.0 mg, 0.0570 mmol) and $GdCl_3$ (31.6 mg, 0.0860 mmol) were dissolved in 5 mL of H_2O. The pH was adjusted to 6.0 with NH_4OH and then the solution was heated to 50 °C for 12 h. Once the solution had cooled to room temperature, the pH was raised to 11.0 to precipitate any unchelated Gd(III). The solution was then filtered through a 0.2 μm syringe filter before being submitted to preparatory HPLC with the same column and method as compound **3**. The desired fractions (retention time: 42.40 min by UV at 220, 264 nm) were collected and freeze-dried to yield the product as a white solid (41.0 mg, 94%). ESI-MS (*m/z*): 769.298; calc. for $C_{31}H_{42}GdN_5O_8$-H^+: 769.227; with Anal. Calcd. for $C_{31}H_{42}GdN_5O_8$ • Na • 2 H_2O: C, 44.92; H, 5.59; N, 8.45. Found: C, 44.58; H, 5.50; N, 8.67.

Synthesis of Eu(III)- 1-{[4-(Bicyclo[2.2.1]hept-5-en-2-exo-yloxymethyl)-benzyl-carbamoyl]-methyl}-4,7,10-tris-carboxymethyl-1,4,7,10-tetraazacyclododecane (**7**)

Compound **4** (15.0 mg, 0.0244 mmol) and $GdCl_3$ (10.7 mg, 0.0293 mmol) were dissolved in 5 mL of H_2O. The pH was adjusted to 6.0 with NH_4OH and then the solution was heated to 50 °C for 12 h. Once the solution had cooled to room temperature, the pH was raised to 11.0 to precipitate any unchelated Eu(III). The solution was then filtered through a 0.2 μm syringe filter before being submitted to preparatory HPLC with the same column and method as compound **4**. The desired fractions (retention time: 41.02 min by UV at 220, 264 nm) were collected and freeze-dried to yield the product as a white solid (11.0 mg, 59%). ESI-MS (*m/z*): 764.205; calc. for $C_{31}H_{42}EuN_5O_8$-H^+: 764.225; with Anal. Calcd. for $C_{31}H_{42}EuN_5O_8 \bullet NH_4 \bullet H_2O$: C, 46.50; H, 6.04; N, 10.50. Found: C, 45.10; H, 6.10; N, 10.80.

Synthesis of Gd(III)- [(2-{[2-({[4-(Bicyclo[2.2.1]hept-5-en-2-exo-yloxymethyl)-benzylcarbamoyl]-methyl}-carboxymethyl-amino)-ethyl]-carboxymethyl-amino}-ethyl)-carboxymethyl-amino]-acetic acid (**8**)

Compound **5** (150 mg, 0.248 mmol) and $GdCl_3$ (138 mg, 0.373 mmol) were dissolved in 10 mL of H_2O. The pH was adjusted to 6.0 with NH_4OH and then the solution was heated to 50 °C for 12 h. Once the solution had cooled to room temperature, the pH was raised to 11.0 to precipitate any unchelated Gd(III). The solution was then filtered through a 0.2 μm syringe filter before being freeze-dried. The resulting crude product was dissolved in 10 mL of H_2O with 5 μL of TFA to aid solubility. This solution was submitted to preparatory HPLC with the same column and method as compound **5**. The desired fractions (retention time: 19.00 min by UV at 220, 254 nm) were collected and freeze-dried to yield the product as a white solid (185 mg, 98%).

ESI-MS (*m/z*): 759.112; calc. for $C_{29}H_{36}GdN_4O_{10}+H^+$: 759.167; with Anal. Calcd. for $C_{29}H_{36}GdN_4O_{10}$ • TFA: C, 42.70; H, 4.28; N, 6.43. Found: C, 42.80; H, 4.00; N, 6.70.

Synthesis of Eu(III)- [(2-{[2-({[4-(Bicyclo[2.2.1]hept-5-en-2-exo-yloxymethyl)-benzylcarbamoyl]-methyl}-carboxymethyl-amino)-ethyl]-carboxymethyl-amino}-ethyl)-carboxymethyl-amino]-acetic acid (**9**)

Compound **5** (30.0 mg, 0.0497 mmol) and $EuCl_3$ (27.3 mg, 0.0745 mmol) were dissolved in 5 mL of H_2O. The pH was adjusted to 6.0 with NH_4OH and then the solution was heated to 50 °C for 12 h. Once the solution had cooled to room temperature, the pH was raised to 11.0 to precipitate any unchelated Eu(III). The solution was then filtered through a 0.2 μm syringe filter before being freeze-dried. The resulting crude product was dissolved in 5 mL of H_2O with 2 μL of TFA to aid solubility. This solution was submitted to preparatory HPLC with the same column and method as compound **5**. The desired fractions (retention time: 19.20 min by UV at 220, 254 nm) were collected and freeze-dried to yield the product as a white solid (35.2 mg, 94%). ESI-MS (*m/z*): 752.142; calc. for $C_{29}H_{36}EuN_4O_{10}$-H^+: 752.164; with Anal. Calcd. for $C_{29}H_{36}EuN_4O_{10}$ • TFA: C, 42.92; H, 4.97; N, 6.90. Found: C, 43.30; H, 4.70; N, 6.80

*General Polymerization Reaction (Synthesis of **10A**)*

In an inert-atmosphere glovebox, monomer **1** (20.0 mg, 0.0288 mmol) was weighed into a 20-mL scintillation vial equipped with a magnetic stirring bar. A 9:1 mixture of dry $CHCl_3$/CH_3OH (2 mL) was added, followed by a solution of the $Ru(PCy_3)_2$=CHPh catalyst (4.7 mg, 0.0057 mmol) in 9:1, dry $CHCl_3$:CH_3OH (1 mL). The mixture was stirred for 90 min at room temperature. The polymerization was terminated with the addition of ethyl vinyl ether (1 mL). The crude homopolymer of **10A** was isolated as an off-white solid by precipitation in cold pentanes (200 mL) and concentration *in vacuo*. This reaction mixture was then dissolved in H_2O

and purified via size-exclusion chromatography on Sephadex-G15. The product containing fractions were identified via HPLC-MS and combined to yield **10A** as a white solid (11.0 mg, 55%).

REFERENCES

Chapter 1:
References

1. Merbach, A. E.; Toth, E.; Editors, *The Chemistry of Contrast Agents in Medical Magnetic Resonance Imaging*. 2001; p 471 pp.

2. Bloembergen, N.; Morgan, L. O., Proton relaxation times in paramagnetic solutions. Effects of electron spin relaxation. *J. Chem. Phys.* **1961**, 34, 842-50.

3. Solomon, I.; Bloembergen, N., Nuclear magnetic interactions in the HF molecule. *J. Chem. Phys.* **1956**, 25, 261-6.

4. Caravan, P.; Ellison, J. J.; McMurry, T. J.; Lauffer, R. B., Gadolinium(III) chelates as MRI contrast agents: Structure, dynamics, and applications. *Chem. Rev.* **1999**, 99, (9), 2293-2352.

5. Caravan, P., Strategies for increasing the sensitivity of gadolinium-based MRI contrast agents. *Chem. Soc. Rev.* **2006**, 35, (6), 512-523.

6. Cossy, C.; Helm, L.; Powell, D. H.; Merbach, A. E., A change in coordination number from nine to eight along the lanthanide(III) aqua ion series in solution: A neutron diffraction study. *New J. Chem.* **1995**, 19, (1), 27-35.

7. Aime, S.; Botta, M.; Fasano, M.; Terreno, E., Prototropic and water-exchange processes in aqueous solutions of Gd(III) chelates. *Acc. Chem. Res.* **1999**, 32, (11), 941-949.

8. Fries, P. H.; Belorizky, E., Electronic relaxation of paramagnetic metal ions and NMR relaxivity in solution: Critical analysis of various approaches and application to a Gd(III)-based contrast agent. *J. Chem. Phys.* **2005**, 123, (12), 124510/1-124510/15.

9. Schaefle, N.; Sharp, R., Four complementary theoretical approaches for the analysis of NMR paramagnetic relaxation. *J. Magn. Reson.* **2005**, 176, (2), 160-170.

10. Jacques, V.; Desreux, J. F., New classes of MRI contrast agents. *Top. Curr. Chem.* **2002**, 221, (Contrast Agents I), 123-164.

11. Chan, K. W.-Y.; Wong, W.-T., Small molecular gadolinium(III) complexes as MRI contrast agents for diagnostic imaging. *Coord. Chem. Rev.* **2007**, 251, (17-20), 2428-2451.

12. Aime, S.; Botta, M.; Garino, E.; Crich, S. G.; Giovenzana, G.; Pagliarin, R.; Palmisano, G.; Sisti, M., Non-covalent conjugates between cationic polyamino acids and Gd(III) chelates: A route for seeking accumulation of MRI-contrast agents at tumor targeting sites. *Chem-Eur. J.* **2000**, 6, (14), 2609-2617.

13. Dirksen, A.; Langereis, S.; de Waal, B. F. M.; van Genderen, M. H. P.; Meijer, E. W.; de Lussanet, Q. G.; Hackeng, T. M., Design and synthesis of a bimodal target-specific contrast agent for angiogenesis. *Org. Lett.* **2004**, 6, (26), 4857-4860.

14. Kubicek, V.; Rudovsky, J.; Kotek, J.; Hermann, P.; Vander Elst, L.; Muller, R. N.; Kolar, Z. I.; Wolterbeek, H. T.; Peters, J. A.; Lukes, I., A bisphosphonate monoamide analogue of DOTA: A potential agent for bone targeting. *J. Am. Chem. Soc.* **2005**, 127, (47), 16477-16485.

15. Anelli, P. L.; Bertini, I.; Fragai, M.; Lattuada, L.; Luchinat, C.; Parigi, G., Sulfonamide-functionalized gadolinium DTPA complexes as possible contrast agents for MRI: A relaxometric investigation. *Eur. J. Inorg. Chem.* **2000**, (4), 625-630.

16. Lauffer, R. B.; McMurry, T. J.; Dunham, S. O.; Scott, D. M.; Parmelee, D. J.; Dumas, S. Bioactivated diagnostic imaging contrast agents. 97-US4804
9736619, 19970325., 1997.

17. Nivorozhkin, A. L.; Kolodziej, A. F.; Caravan, P.; Greenfield, M. T.; Lauffer, R. B.; McMurry, T. J., Enzyme-activated Gd^{3+} magnetic resonance imaging contrast agents with a prominent receptor-induced magnetization enhancement. *Angew. Chem. Int. Edit.* **2001**, 40, (15), 2903-2906.

18. Louie, A. Y.; Huber, M. M.; Ahrens, E. T.; Rothbacher, U.; Moats, R.; Jacobs, R. E.; Fraser, S. E.; Meade, T. J., In vivo visualization of gene expression using magnetic resonance imaging. *Nat. Biotechnol.* **2000**, 18, (3), 321-325.

19. Duimstra, J. A.; Femia, F. J.; Meade, T. J., A gadolinium chelate for detection of β-glucuronidase: A self-immolative approach. *J. Am. Chem. Soc.* **2005**, 127, (37), 12847-12855.

20. Urbanczyk-Pearson, L. M.; Femia, F. J.; Smith, J.; Parigi, G.; Duimstra, J. A.; Eckermann, A. L.; Luchinat, C.; Meade, T. J., Mechanistic investigation of β-galactosidase-activated MR contrast agents. *Inorg. Chem.* **2008**, 47, (1), 56-68.

21. Gerweck, L. E.; Seetharaman, K., Cellular pH gradient in tumor versus normal tissue: Potential exploitation for the treatment of cancer. *Cancer Res.* **1996**, 56, (6), 1194-8.

22. Zhang, S.; Wu, K.; Sherry, A. D., A novel pH-sensitive MRI contrast agent. *Angew. Chem. Int. Edit.* **1999**, 38, (21), 3192-3194.

23. Aime, S.; Barge, A.; Botta, M.; Howard, J. A. K.; Kataky, R.; Lowe, M. P.; Moloney, J. M.; Parker, D.; de Sousa, A. S., Dependence of the relaxivity and luminescence of gadolinium and europium amino-acid complexes on hydrogencarbonate and pH. *Chem. Comm.* **1999**, (11), 1047-1048.

24. Kalman, F. K.; Woods, M.; Caravan, P.; Jurek, P.; Spiller, M.; Tircso, G.; Kiraly, R.; Bruecher, E.; Sherry, A. D., Potentiometric and relaxometric properties of a gadolinium-based MRI contrast agent for sensing tissue pH. *Inorg. Chem.* **2007**, 46, (13), 5260-5270.

25. Sitharaman, B.; Wilson, L. J., Gadofullerenes and gadonanotubes: A new paradigm for high-performance magnetic resonance imaging contrast agent probes. *J. Biomed. Nanotechn.* **2007**, 3, (4), 342-352.

26. Laus, S.; Sitharaman, B.; Toth, E.; Bolskar, R. D.; Helm, L.; Wilson, L. J.; Merbach, A. E., Understanding paramagnetic relaxation phenomena for water-soluble gadofullerenes. *J. Phys. Chem. C.* **2007**, 111, (15), 5633-5639.

27. Toth, E.; Bolskar, R. D.; Borel, A.; Gonzalez, G.; Helm, L.; Merbach, A. E.; Sitharaman, B.; Wilson, L. J., Water-soluble gadofullerenes: Toward high-relaxivity, pH-responsive MRI contrast agents. *J. Am. Chem. Soc.* **2005**, 127, (2), 799-805.

28. Aime, S.; Ascenzi, P.; Comoglio, E.; Fasano, M.; Paoletti, S., Molecular recognition of R- and T-states of human adult hemoglobin by a paramagnetic Gd(III) complex by means of the measurement of solvent water proton relaxation rate. *J. Am. Chem. Soc.* **1995**, 117, (36), 9365-6.

29. Aime, S.; Digilio, G.; Fasano, M.; Paoletti, S.; Arnelli, A.; Ascenzi, P., Metal complexes as allosteric effectors of human hemoglobin: An NMR study of the interaction of the gadolinium(III) bis(m-boroxyphenylamide)diethylenetriaminepentaacetic acid complex with human oxygenated and deoxygenated hemoglobin. *Biophys. J.* **1999**, 76, (5), 2735-2743.

30. Livramento, J. B.; Toth, E.; Sour, A.; Borel, A.; Merbach, A. E.; Ruloff, R., High relaxivity confined to a small molecular space: A metallostar-based, potential MRI contrast agent. *Angew. Chem. Int. Edit.* **2005**, 44, (10), 1480-1484, S1480/1-S1480/4.

31. Li, W.-h.; Fraser, S. E.; Meade, T. J., A calcium-sensitive magnetic resonance imaging contrast agent. *J. Am. Chem. Soc.* **1999**, 121, (6), 1413-1414.

32. Major, J. L.; Parigi, G.; Luchinat, C.; Meade, T. J., The synthesis and in vitro testing of a zinc-activated MRI contrast agent. *Proc. Natl. Acad. Sci. U. S. A.* **2007**, 104, (35), 13881-13886, S13881/1-S13881/9.

33. Hanaoka, K.; Kikuchi, K.; Urano, Y.; Narazaki, M.; Yokawa, T.; Sakamoto, S.; Yamaguchi, K.; Nagano, T., Design and synthesis of a novel magnetic resonance imaging contrast agent for selective sensing of zinc ion. *Chem. Biol.* **2002**, 9, 1027-1032.

34. Wolff, S. D.; Balaban, R. S., Magnetization transfer contrast (MTC) and tissue water proton relaxation in vivo. *Magn. Reson. Med.* **1989**, 10, (1), 135-44.

35. Ward, K. M.; Aletras, A. H.; Balaban, R. S., A new class of contrast agents for MRI based on proton chemical exchange dependent saturation transfer (CEST). *J. Magn. Reson.* **2000**, 143, (1), 79-87.

36. Zhang, S.; Merritt, M.; Woessner Donald, E.; Lenkinski Robert, E.; Sherry, A. D., PARACEST agents: Modulating MRI contrast via water proton exchange. *Acc. Chem. Res.* **2003**, 36, (10), 783-90.

37. Aime, S.; Castelli, D. D.; Terreno, E., Novel pH-reporter MRI contrast agents. *Angew. Chem. Int. Edit.* **2002**, 41, (22), 4334-4336.

38. Zhang, S.; Malloy, C. R.; Sherry, A. D., MRI thermometry based on PARACEST agents. *J. Am. Chem. Soc.* **2005**, 127, (50), 17572-17573.

39. Liu, G.; Li, Y.; Pagel, M. D., Design and characterization of new irreversible responsive PARACEST MRI contrast agent that detects nitric oxide. *Magn. Reson. Med.* **2007**, 58, (6), 1249-1256.

40. Trokowski, R.; Zhang, S.; Sherry, A. D., Cyclen-based phenylboronate ligands and their Eu^{3+} complexes for sensing glucose by MRI. *Bioconjug. Chem.* **2004**, 15, (6), 1431-1440.

41. Woods, M.; Woessner Donald, E.; Sherry, A. D., Paramagnetic lanthanide complexes as PARACEST agents for medical imaging. *Chem. Soc. Rev.* **2006**, 35, (6), 500-11.

42. Yoo, B.; Pagel, M. D., A PARACEST MRI contrast agent to detect enzyme activity. *J. Am. Chem. Soc.* **2006**, 128, (43), 14032-14033.

43. Xu, J.; Franklin, S. J.; Whisenhunt, D. W., Jr.; Raymond, K. N., Gadolinium complex of tris[(3-hydroxy-1-methyl- 2-oxo-1,2-didehydropyridine-4-carboxamido)ethyl]-amine: A New Class of gadolinium magnetic resonance relaxation agents. *J. Am. Chem. Soc.* **1995**, 117, (27), 7245-6.

44. Sunderland, C. J.; Botta, M.; Aime, S.; Raymond, K. N., 6-Carboxamido-5,4-hydroxypyrimidinones: A new class of heterocyclic ligands and their evaluation as gadolinium chelating agents. *Inorg. Chem.* **2001**, 40, (26), 6746-6756.

45. Raymond, K. N.; Pierre, V. C., Next generation, high relaxivity gadolinium MRI agents. *Bioconjug. Chem.* **2005**, 16, (1), 3-8.

46. Pierre, V. C.; Botta, M.; Aime, S.; Raymond, K. N., Substituent effects on Gd(III)-based MRI contrast agents: Optimizing the stability and selectivity of the complex and the number of coordinated water molecules. *Inorg. Chem.* **2006**, 45, (20), 8355-8364.

47. Allen, M. J.; Raines, R. T.; Kiessling, L. L., Contrast agents for magnetic resonance imaging synthesized with ring-opening metathesis polymerization. *J. Am. Chem. Soc.* **2006**, 128, (20), 6534-6535.

48. Doble, D. M. J.; Botta, M.; Wang, J.; Aime, S.; Barge, A.; Raymond, K. N., Optimization of the relaxivity of MRI contrast agents: Effect of poly(ethylene glycol) chains on the water-exchange rates of Gd(III) complexes. *J. Am. Chem. Soc.* **2001**, 123, (43), 10758-10759.

49. Sieving, P. F.; Watson, A. D.; Rocklage, S. M., Preparation and characterization of paramagnetic polychelates and their protein conjugates. *Bioconjug. Chem.* **1990**, 1, (1), 65-71.

50. Desser, T. S.; Rubin, D. L.; Muller, H. H.; Qing, F.; Khodor, S.; Zanazzi, G.; Young, S. W.; Ladd, D. L.; Wellons, J. A.; Kellar, K. E., Dynamics of tumor imaging with Gd-DTPA-polyethylene glycol polymers: Dependence on molecular weight. *J. Magn. Reson. Imaging* **1994**, 4, (3), 467-72.

51. Toth, E.; Helm, L.; Kellar, K. E.; Merbach, A. E., High-pressure NMR kinetics. Part 87. Gd(DTPA-bisamide)alkyl copolymers: A hint for the formation of MRI contrast agents with very high relaxivity. *Chem-Eur. J.* **1999**, 5, (4), 1202-1211.

52. Modo, M.; Cash, D.; Mellodew, K.; Williams Steven, C. R.; Fraser Scott, E.; Meade Thomas, J.; Price, J.; Hodges, H., Tracking transplanted stem cell migration using bifunctional, contrast agent-enhanced, magnetic resonance imaging. *Neuroimage* **2002**, 17, (2), 803-11.

53. Rohrer, M.; Bauer, H.; Mintorovitch, J.; Requardt, M.; Weinmann, H.-J., Comparison of magnetic properties of MRI contrast media solutions at different magnetic field strengths. *Invest. Radiol.* **2005**, 40, (11), 715-24.

Chapter 2:
References

1. Toga, A. W.; Mazziotta, J. C., *Brain Mapping: The Methods*. Academic Press: San Diego, CA, 2002; p 877.

2. Allen, M. J.; MacRenaris, K. W.; Venkatasubramanian, P. N.; Meade, T. J., Cellular delivery of MRI contrast agents. *Chem. Biol.* **2004**, 11, (3), 301-307.

3. Louie, A. Y.; Huber, M. M.; Ahrens, E. T.; Rothbacher, U.; Moats, R.; Jacobs, R. E.; Fraser, S. E.; Meade, T. J., In vivo visualization of gene expression using magnetic resonance imaging. *Nat. Biotechnol.* **2000**, 18, (3), 321-325.

4. Merbach, A. E.; Toth, E., *The Chemistry of Contrast Agents in Medical Magnetic Resonance*. John Wiley & Sons, Ltd.: New York, 2001.

5. Aime, S.; Botta, M.; Terreno, E., Gd(III)-based contrast agents for MRI. *Adv. Inorg. Chem.* **2005**, 57, 173-237.

6. Allen, M. J.; Meade, T. J., Magnetic Resonance Contrast Agents for Medical and Molecular Imaging. In *Metal Ions in Biological Systems*, Sigel, A.; Sigel, H., Eds. Marcel Dekker Inc.: New York, 2004; Vol. 42, pp 1-28.

7. Brown, M. A.; Semelka, R. C., *MRI Basic Principles and Applications*. Wiley-Liss, Inc.: New York, 1999.

8. Torchilin, V.; Babich, J.; Weissig, V., Liposomes and micelles to target the blood pool for imaging purposes. *J. Liposome Res.* **2000**, 10, (4), 483-499.

9. Kresse, M.; Wagner, S.; Pfefferer, D.; Lawaczeck, R.; Elste, V.; Semmler, W., Targeting of ultrasmall superparamagnetic iron oxide (USPIO) particles to tumor cells in vivo by using transferrin receptor pathways. *Magn. Reson. Med.* **1998**, 40, (2), 236-242.

10. Moore, A.; Josephson, L.; Bhorade, R. M.; Basilion, J. P.; Weissleder, R., Human transferrin receptor gene as a marker gene for MR imaging. *Radiology* **2001**, 221, (1), 244-250.

11. Kayyem, J. F.; Kumar, R. M.; Fraser, S. E.; Meade, T. J., Receptor-targeted co-transport of DNA and magnetic resonance contrast agents. *Chem. Biol.* **1995**, 2, (9), 615-620.

12. Konda, S. D.; Aref, M.; Wang, S.; Brechbiel, M.; Wiener, E. C., Specific targeting of folate-dendrimer MRI contrast agents to the high affinity folate receptor expressed in ovarian tumor xenografts. *Magn. Reson. Mater Phy.* **2001**, 12, (2-3), 104-113.

13. Reddy, J. A.; Allagadda, V. M.; Leamon, C. P., Targeting therapeutic and imaging agents to folate receptor positive tumors. *Curr. Pharm. Biotechnol.* **2005**, 6, (2), 131-150.

14. Sun, C.; Sze, R.; Zhang, M., Folic acid-PEG conjugated superparamagnetic nanoparticles for targeted cellular uptake and detection by MRI. *J. Biomed. Mater. Res.* **2006**, 78A, (3), 550-557.

15. Futaki, S.; Suzuki, T.; Ohashi, W.; Yagami, T.; Tanaka, S.; Ueda, K.; Sugiura, Y., Arginine-rich peptides: An abundant source of membrane-permeable peptides having potential as carriers for intracellular protein delivery. *J. Biol. Chem.* **2001**, 276, (8), 5836-5840.

16. Allen, M. J.; Meade, T. J., Synthesis and visualization of a membrane-permeable MRI contrast agent. *J. Biol. Inorg. Chem.* **2003**, 8, (7), 746-750.

17. Futaki, S.; Goto, S.; Sugiura, Y., Membrane permeability commonly shared among arginine-rich peptides. *J. Mol. Recognit.* **2003**, 16, (5), 260-264.

18. Futaki, S., Membrane-permeable arginine-rich peptides and the translocation mechanisms. *Adv. Drug Deliver. Rev.* **2005**, 57, (4), 547-558.

19. Kaplan, I. M.; Wadia, J. S.; Dowdy, S. F., Cationic TAT peptide transduction domain enters cells by macropinocytosis. *J. Control. Release* **2005**, 107, (3), 571-572.

20. Lewin, M.; Carlesso, N.; Tung, C.-H.; Tang, X.-W.; Cory, D.; Scadden, D. T.; Weissleder, R., TAT peptide-derivatized magnetic nanoparticles allow in vivo tracking and recovery of progenitor cells. *Nat. Biotechnol.* **2000**, 18, (4), 410-414.

21. Gump, J. M.; Dowdy, S. F., TAT transduction: The molecular mechanism and therapeutic prospects. *Trends Mol. Med.* **2007**, 13, (10), 443-448.

22. Jenkins, R.; Gedcke, D.; Gould, R. W., *Quantitative X-ray Spectrometry*. 2nd ed.; Marcel Dekker, Inc.: New York, 1995; Vol. 20, p 504.

23. Beekman Freek, J.; McElroy David, P.; Berger, F.; Gambhir Sanjiv, S.; Hoffman Edward, J.; Cherry Simon, R., Towards in vivo nuclear microscopy: Iodine^{125} imaging in mice using micro-pinholes. *Eur. J. Nucl. Med. Mol. I.* **2002**, 29, (7), 933-938.

24. Jarver, P.; Langel, U., The use of cell-penetrating peptides as a tool for gene regulation. *Drug Discov. Today* **2004**, 9, (9), 395-402.

25. Caravan, P.; Ellison, J. J.; McMurry, T. J.; Lauffer, R. B., Gadolinium(III) chelates as MRI contrast agents: Structure, dynamics, and applications. *Chem. Rev.* **1999**, 99, (9), 2293-2352.

26. Allen, M. J. Delivery and activation of contrast agents for magnetic resonance imaging. California Institute of Technology, Pasadena, 2004.

27. Fahrni, C. J., Biological applications of X-ray fluorescence microscopy: Exploring the subcellular topography and speciation of transition metals. *Curr. Opin. Chem Bio.* **2007**, 11, (2), 121-127.

28. Takenouchi, K.; Tabe, M.; Watanabe, K.; Hazato, A.; Kato, Y.; Shionoya, M.; Koike, T.; Kimura, E., Novel pendant-type macrocyclic bifunctional chelating agents: (Carboxymethyl)amino derivatives of 2-(4-nitrobenzyl)-1,4,7,10-tetraazacyclododecane-*N*,*N*',*N*'',*N*'''-tetraacetic acid and their complex formation with yttrium(III). *J. Org. Chem.* **1993**, 58, (24), 6895-6899.

29. McMurry, T.; Brechbiel, M.; Kumar, K.; Gansow, O., Convenient synthesis of bifunctional tetraaza macrocycles. *Bioconjug. Chem.* **1992**, 3, 108-117.

30. Corson, D. T.; Meares, C. F., Efficient multigram synthesis of the bifunctional chelating agent (S)-1-*p*-isothiocyanatobenzyl-diethylenetriamine pentaacetic acid. *Bioconjug. Chem.* **2000**, 11, (2), 292-299.

31. Vogt, S., MAPS: A set of software tools for analysis and visualization of 3D X-ray fluorescence data sets. *J. Phys. IV* **2003**, 104, (X-Ray Microscopy), 635-638.

32. Fuchs, S. M.; Raines, R. T., Pathway for polyarginine entry into mammalian cells. *Biochemistry* **2004**, 43, (9), 2438-2444.

33. Skovronsky, D. M.; Zhang, B.; Kung, M.-P.; Kung, H. F.; Trojanowski, J. Q.; Lee, V. M. Y., In vivo detection of amyloid plaques in a mouse model of Alzheimer's disease. *Proc. Natl. Acad. Sci. U. S. A.* **2000**, 97, (13), 7609-7614.

34. Kung, H. F.; Lee, C.-W.; Zhuang, Z.-P.; Kung, M.-P.; Hou, C.; Ploessl, K., Novel stilbenes as probes for amyloid plaques. *J. Am. Chem. Soc.* **2001**, 123, (50), 12740-12741.

35. Jainchill, J. L.; Aaronson, S. A.; Todaro, G. J., Murine sarcoma and leukemia viruses: Assay using clonal lines of contact-inhibited mouse cells. *J. Virol.* **1969**, 4, (5), 549-553.

36. Gaush, C. R.; Hard, W. L.; Smith, T. F., Characterization of an established line of canine kidney cells (MDCK). *Proc. Soc. Exp. Biol. Med.* **1966**, 122, (3), 931-935.

37. Ralph, P.; Nakoinz, I., Antibody-dependent killing of erythrocyte and tumor targets by macrophage-related cell lines: Enhancement by PPD and LPS. *J. Immunol.* **1977**, 119, (3), 950-954.

38. Collection, A. T. C. ATCC homepage: The Global Bioresource Center. http://www.atcc.org/ (2/1/2006),

39. Misfeldt, D. S.; Hamamoto, S. T.; Pitelka, D. R., Transepithelial transport in cell culture. *Proc. Natl. Acad. Sci. U. S. A.* **1976**, 73, (4), 1212-1216.

40. Irvine, J. D.; Takahashi, L.; Lockhart, K.; Cheong, J.; Tolan, J. W.; Selick, H. E.; Grove, J. R., MDCK (Madin-Darby canine kidney) cells: A tool for membrane permeability screening. *J. Pharm. Sci.* **1999**, 88, (1), 28-33.

41. Di Fabrizio, E.; Romanato, F.; Gentill, M.; Cabrini, S.; Kaulich, B.; Susini, J.; Barrett, R., High-efficiency multilevel zone plates for key X-rays. *Nature* **1999**, 401, (6756), 895-898.

42. Yun, W.; Lai, B.; Cai, Z.; Maser, J.; Legnini, D.; Gluskin, E.; Chen, Z.; Krasnoperova, A. A.; Vladimirsky, Y.; Cerrina, F.; Di Fabrizio, E.; Gentili, M., Nanometer focusing of hard X-rays by phase zone plates. *Rev. Sci. Instrum.* **1999**, 70, (5), 2238-2241.

43. Twining, B.; Baines, S.; Fisher, N.; Maser, J.; Vogt, S.; Jacobsen, C.; Tovar-Sanchez, A.; Sanudo-Wilhelmy, S., Quantifying trace elements in individual aquatic protist cells with a synchrotron X-Ray fluorescence microprobe. *Anal. Chem.* **2003**, 75, (15), 3806-3816.

44. Al-Taei, S.; Penning, N. A.; Simpson, J. C.; Futaki, S.; Takeuchi, T.; Nakase, I.; Jones, A. T., Intracellular traffic and fate of protein transduction domains HIV-1 TAT peptide and octaarginine. Implications for their utilization as drug delivery vectors. *Bioconjug. Chem.* **2006**, 17, (1), 90-100.

45. Parker, D., Excitement in f block: Structure, dynamics and function of nine-coordinate chiral lanthanide complexes in aqueous media. *Chem. Soc. Rev.* **2004**, 33, (3), 156-165.

46. Parker, D., Luminescent lanthanide sensors for pH, *p*O2 and selected anions. *Coord. Chem. Rev.* **2000**, 205, 109-130.

47. Turro, C.; Fu Patty, K. L.; Bradley Patricia, M., Lanthanide ions as luminescent probes of proteins and nucleic acids. *Met. Ions Biol. Syst.* **2003**, 40, 323-53.

48. Reifernberger, J. G.; Ge, P.; Selvin, P. R., Progress in lanthanides as luminescent probes. *Rev. Fluorescence* **2005**, 2, 399-431.

49. Hemmilae, I.; Laitala, V., Progress in lanthanides as luminescent probes. *J. Fluorescence* **2005**, 15, (4), 529-542.

50. Selvin, P. R., Principles and biophysical applications of lanthanide-based probes. *Annu. Rev. Biophys. Biomol. Struct.* **2002**, 31, 275-302.

51. Quenneville, J.; Martinez, T. J., *Ab initio* study of cis-trans photoisomerization in stilbene and ethylene. *J. Phys. Chem. A.* **2003**, 107, (6), 829-837.

52. Amatatsu, Y., *Ab initio* study on the electronic structures of stilbene at the conical intersection. *Chem. Phys. Lett.* **1999**, 314, (3,4), 364-368.

53. Khokhryakov, A. A.; Khokhlova, A. M., Electronic absorption spectra of the Ce^{3+} ions in halide melts. *Radiochem.* **2003**, 45, (6), 559-561.

54. Carnall, W. T.; Fields, P. R.; Rajnak, K., Electronic energy levels in the trivalent lanthanide aquo ions. I. Pr^{3+}, Nd^{3+}, Pm^{3+}, Sm^{3+}, Dy^{3+}, Ho^{3+}, Er^{3+}, and Tm^{3+}. *J. Chem. Phys.* **1968**, 49, (10), 4424-42.

55. Kaczkan, M.; Malinowski, M., Inhomogeneity of Ho^{3+} activated $SrLaGa_3O_7$ and $SrLaGaO_4$ crystals studied by fluorescence line narrowing technique. *Optical Mater.* **2005**, 28, (1-2), 119-122.

56. Van Uitert, L. G.; Dearborn, E. F.; Grodkiewicz, W. H., Quenching interactions involving the first excited states of gadolinium, ytterbium, erbium, thulium, and holmium in sodium rare earth tungstates. *J. Chem. Phys.* **1968**, 49, (10), 4400-3.

57. Freshney, I. R., *Culture of Animal Cells: A Manual of Basic Technique, 4th Edition*. 4th. ed.; John Wiley and Sons, Inc: New York, 2000.

Chapter 3:
References

1. Caravan, P., Strategies for increasing the sensitivity of gadolinium based MRI contrast agents. *Chem. Soc. Rev.* **2006**, 35, (6), 512-523.

2. Chan, K. W.-Y.; Wong, W.-T., Small molecular gadolinium(III) complexes as MRI contrast agents for diagnostic imaging. *Coord. Chem. Rev.* **2007**, 251, (17-20), 2428-2451.

3. Aime, S.; Cabella, C.; Colombatto, S.; Geninatti Crich, S.; Gianolio, E.; Maggioni, F., Insights into the use of paramagnetic Gd(III) complexes in MR-molecular imaging investigations. *J. Magn. Reson. Imaging* **2002**, 16, (4), 394-406.

4. Winter, P. M.; Caruthers, S. D.; Wickline, S. A.; Lanza, G. M., Molecular imaging by MRI. *Curr. Cardiol. Rep.* **2006**, 8, (1), 65-9.

5. Louie, A. Y.; Huber, M. M.; Ahrens, E. T.; Rothbacher, U.; Moats, R.; Jacobs, R. E.; Fraser, S. E.; Meade, T. J., In vivo visualization of gene expression using magnetic resonance imaging. *Nat. Biotechnol.* **2000**, 18, (3), 321-5.

6. Endres, P. J.; Paunesku, T.; Vogt, S.; Meade, T. J.; Woloschak, G. E., DNA-TiO_2 nanoconjugates labeled with magnetic resonance contrast agents. *J. Am. Chem. Soc.* **2007**, 129, (51), 15760-15761.

7. Saccavini, J. C.; Curtet, C.; Bohy, J.; Tellier, C.; Bourgoin, C.; Lhoste, J. M., Magnetic resonance imaging studies on nude mice grafted with colorectal adenocarcinoma using gadolinium-labeled monoclonal antibody. *Invest. Radiol.* **1988**, 23, (Suppl. 1), S292-S293.

8. Caravan, P.; Cloutier, N. J.; Greenfield, M. T.; McDermid, S. A.; Dunham, S. U.; Bulte, J. W. M.; Amedio, J. C., Jr.; Looby, R. J.; Supkowski, R. M.; Horrocks, W. D., Jr.; McMurry, T. J.; Lauffer, R. B., The interaction of MS-325 with human serum albumin and its effect on proton relaxation rates. *J. Am. Chem. Soc.* **2002**, 124, (12), 3152-3162.

9. Major, J. L.; Parigi, G.; Luchinat, C.; Meade, T. J., The synthesis and in vitro testing of a zinc-activated MRI contrast agent. *Proc. Natl. Acad. Sci. U. S. A.* **2007**, 104, (35), 13881-13886, S13881/1-S13881/9.

10. Saborowski, O.; Simon, G. H.; Raatschen, H.-J.; Wendland, M. F.; Fu, Y.; Henning, T.; Baehner, R.; Corot, C.; Chen, M.-H.; Daldrup-Link, H. E., MR imaging of antigen-induced arthritis with a new, folate receptor-targeted contrast agent. *Contrast Med. Mol. Imag.* **2007**, 2, (2), 72-81.

11. Kalman, F. K.; Woods, M.; Caravan, P.; Jurek, P.; Spiller, M.; Tircso, G.; Kiraly, R.; Bruecher, E.; Sherry, A. D., Potentiometric and relaxometric properties of a gadolinium-based MRI contrast agent for sensing tissue pH. *Inorg. Chem.* **2007**, 46, (13), 5260-5270.

12. Meister, A.; Anderson, M. E., Glutathione. *Annu. Rev. Biochem.* **1983**, 52, 711-60.

13. Hong, R.; Han, G.; Fernandez, J. M.; Kim, B.-j.; Forbes, N. S.; Rotello, V. M., Glutathione-mediated delivery and release using monolayer protected nanoparticle carriers. *J. Am. Chem. Soc.* **2006**, 128, (4), 1078-1079.

14. Han, G.; Chari Nandini, S.; Verma, A.; Hong, R.; Martin Craig, T.; Rotello Vincent, M., Controlled recovery of the transcription of nanoparticle-bound DNA by intracellular concentrations of glutathione. *Bioconjug. Chem.* **2005**, 16, (6), 1356-9.

15. Carrera, C.; Digilio, G.; Baroni, S.; Burgio, D.; Consol, S.; Fedeli, F.; Longo, D.; Mortillaro, A.; Aime, S., Synthesis and characterization of a Gd(III) based contrast agent responsive to thiol containing compounds. *Dalton T.* **2007**, (43), 4980-4987.

16. Endres, P. J.; MacRenaris, K. W.; Vogt, S.; Allen, M. J.; Meade, T. J., Quantitative imaging of cell-permeable magnetic resonance contrast agents using X-ray fluorescence. *Mol. Img.* **2006**, 5, (4), 485-97.

17. Allen, M. J.; MacRenaris, K. W.; Venkatasubramanian, P. N.; Meade, T. J., Cellular delivery of MRI contrast agents. *Chem. Biol.* **2004**, 11, (3), 301-307.

18. Futaki, S., Membrane-permeable arginine-rich peptides and the translocation mechanisms. *Adv. Drug Deliver. Rev.* **2005**, 57, (4), 547-558.

19. Futaki, S.; Suzuki, T.; Ohashi, W.; Yagami, T.; Tanaka, S.; Ueda, K.; Sugiura, Y., Arginine-rich peptides: An abundant source of membrane-permeable peptides having potential as carriers for intracellular protein delivery. *J. Biol. Chem.* **2001**, 276, (8), 5836-5840.

20. Glogard, C.; Stensrud, G.; Aime, S., Novel radical-responsive MRI contrast agent based on paramagnetic liposomes. *Magn. Reson. Chem.* **2003**, 41, (8), 585-588.

21. Botta, M.; Aime, S.; Barge, A.; Bobba, G.; Dickins, R. S.; Parker, D.; Terreno, E., Ternary complexes between cationic Gd(III) chelates and anionic metabolites in aqueous solution: An NMR relaxometric study. *Chem-Eur. J.* **2003**, 9, (9), 2102-2109.

22. Urbanczyk-Pearson, L. M.; Femia, F. J.; Smith, J.; Parigi, G.; Duimstra, J. A.; Eckermann, A. L.; Luchinat, C.; Meade, T. J., Mechanistic investigation of β-galactosidase-activated MR contrast agents. *Inorg. Chem.* **2008**, 47, (1), 56-68.

23. Caravan, P.; Ellison, J. J.; McMurry, T. J.; Lauffer, R. B., Gadolinium(III) chelates as MRI contrast agents: Structure, dynamics, and applications. *Chem. Rev.* **1999**, 99, (9), 2293-2352.

24. Bryden, C. C.; Reilley, C. N., Europium luminescence lifetimes and spectra for evaluation of 11 europium complexes as aqueous shift reagents for nuclear magnetic resonance spectrometry. *Anal. Chem.* **1982**, 54, (4), 610-15.

25. Powell, D. H.; Ni Dhubhghaill, O. M.; Pubanz, D.; Helm, L.; Lebedev, Y. S.; Schlaepfer, W.; Merbach, A. E., High-pressure NMR kinetics. Part 74. Structural and dynamic parameters obtained from ^{17}O NMR, EPR, and NMRD studies of monomeric and dimeric Gd^{3+} complexes

of interest in magnetic resonance imaging: An integrated and theoretically self-consistent approach. *J. Am. Chem. Soc.* **1996**, 118, (39), 9333-9346.

26. Terreno, E.; Botta, M.; Boniforte, P.; Bracco, C.; Milone, L.; Mondino, B.; Uggeri, F.; Aime, S., A multinuclear NMR relaxometry study of ternary adducts formed between heptadentate Gd(III) chelates and L-lactate. *Chem-Eur. J.* **2005**, 11, (19), 5531-5537.

27. Aime, S.; Botta, M.; Crich, S. G.; Giovenzana, G.; Pagliarin, R.; Sisti, M.; Terreno, E., NMR relaxometric studies of Gd(III) complexes with heptadentate macrocyclic ligands. *Magn. Reson. Chem.* **1998**, 36, (Spec. Issue), S200-S208.

28. Swift, T. J.; Connick, R. E., NMR (nuclear magnetic resonance)-relaxation mechanisms of ^{17}O in aqueous solutions of paramagnetic cations and the lifetime of water molecules in the first coordination sphere. *J. Chem. Phys.* **1962**, 37, 307-20.

29. Jaszberenyi, Z.; Moriggi, L.; Schmidt, P.; Weidensteiner, C.; Kneuer, R.; Merbach, A. E.; Helm, L.; Toth, E., Physicochemical and MRI characterization of Gd^{3+}-loaded polyamidoamine and hyperbranched dendrimers. *J. Bio. Inorg. Chem.* **2007**, 12, (3), 406-420.

30. Merbach, A. E.; Toth, E.; Editors, *The Chemistry of Contrast Agents in Medical Magnetic Resonance Imaging*. 2001; p 471 pp.

31. Kubicek, V.; Rudovsky, J.; Kotek, J.; Hermann, P.; Vander Elst, L.; Muller, R. N.; Kolar, Z. I.; Wolterbeek, H. T.; Peters, J. A.; Lukes, I., A bisphosphonate monoamide analogue of DOTA: A potential agent for bone targeting. *J. Am. Chem. Soc.* **2005**, 127, (47), 16477-16485.

32. Laurent, S.; Parac-Vogt, T. N.; Kimpe, K.; Thirifays, C.; Binnemans, K.; Muller, R. N.; Vander Elst, L., Bis(phenylethylamide) derivatives of Gd-DTPA as potential receptor-specific MRI contrast agents. *Eur. J. Inorg. Chem.* **2007**, (14), 2061-2067.

33. Zhang, S.; Jiang, X.; Sherry, A. D., Modulation of the lifetime of water bound to lanthanide metal ions in complexes with ligands derived from 1,4,7,10-tetraazacyclododecane tetraacetate (DOTA). *Helv. Chim. Acta* **2005**, 88, (5), 923-935.

34. Lauffer, R. B., Paramagnetic metal complexes as water proton relaxation agents for NMR imaging: Theory and design. *Chem. Rev.* **1987**, 87, (5), 901-27.

35. Vogt, S., MAPS: A set of software tools for analysis and visualization of 3D X-ray fluorescence data sets. *J. Phys. IV* **2003**, 104, (X-Ray Microscopy), 635-638.

36. Futaki, S.; Goto, S.; Sugiura, Y., Membrane permeability commonly shared among arginine-rich peptides. *J. Mol. Recognit.* **2003**, 16, (5), 260-264.

37. Twining, B. S.; Baines, S. B.; Fisher, N. S.; Maser, J.; Vogt, S.; Jacobsen, C.; Tovar-Sanchez, A.; Sanudo-Wilhelmy, S. A., Quantifying trace elements in individual aquatic protist cells with a synchrotron X-ray fluorescence microprobe. *Anal. Chem.* **2003**, 75, (15), 3806-3816.

38. Aime, S.; Castelli, D. D.; Terreno, E., Highly sensitive MRI chemical exchange saturation transfer agents using liposomes. *Angew. Chem. Int. Edit.* **2005**, 44, (34), 5513-5515.

39. Bulte, J. W. M.; Douglas, T.; Witwer, B.; Zhang, S.-C.; Strable, E.; Lewis, B. K.; Zywicke, H.; Miller, B.; van Gelderen, P.; Moskowitz, B. M.; Duncan, L. D.; Frank, J. A., Magnetodendrimers allow endosomal magnetic labeling and in vivo tracking of stem cells. *Nat. Biotechnol.* **2001**, 19, (12), 1141-1147.

40. Herbig, M. E.; Weller, K. M.; Merkle, H. P., Reviewing biophysical and cell biological methodologies in cell penetrating peptide (CPP) research. *Crit. Rev. Ther. Drug Carrier Syst.* **2007**, 24, (3), 203-255.

41. Chen, L.; Harrison, S. D., Cell-penetrating peptides in drug development: Enabling intracellular targets. *Biochem. Soc. Trans.* **2007**, 35, (4), 821-825.

42. Prochiantz, A., Cell permeable peptides and messenger proteins, from a serendipitous observation to a new signaling mechanism. *Handbook of Cell-Penetrating Peptides (2nd Edition)* **2007**, 239-244.

43. Magzoub, M.; Graeslund, A., Cell-penetrating peptides: Small from inception to application. *Q. Rev. Biophys.* **2004**, 37, (2), 147-195.

44. Zong, Y.; Guo, J.; Ke, T.; Mohs, A. M.; Parker, D. L.; Lu, Z.-R., Effect of size and charge on pharmacokinetics and in vivo MRI contrast enhancement of biodegradable polydisulfide Gd(III) complexes. *J. Control. Release* **2006**, 112, (3), 350-356.

45. Allen, M. J.; Meade, T. J., Synthesis and visualization of a membrane-permeable MRI contrast agent. *J. Bio. Inorg. Chem.* **2003**, 8, (7), 746-750.

46. Ebright, Y. W.; Chen, Y.; Kim, Y.; Ebright, R. H., S-[2-(4-azidosalicylamido)ethylthio]-2-thiopyridine: Radioiodinatable, cleavable, photoactivatable crosslinking agent. *Bioconjug. Chem.* **1996**, 7, (3), 380-384.

47. Beeby, A.; Clarkson, I. M.; Dickins, R. S.; Faulkner, S.; Parker, D.; Royle, L.; de Sousa, A. S.; Williams, J. A. G.; Woods, M., Non-radiative deactivation of the excited states of europium, terbium and ytterbium complexes by proximate energy-matched OH, NH and CH oscillators: An improved luminescence method for establishing solution hydration states. *J. Chem. Soc., Perkin Trans. 2* **1999**, (3), 493-504.

48. Quici, S.; Cavazzini, M.; Marzanni, G.; Accorsi, G.; Armaroli, N.; Ventura, B.; Barigelletti, F., Visible and near-infrared intense luminescence from water-soluble lanthanide [Tb(III), Eu(III), Sm(III), Dy(III), Pr(III), Ho(III), Yb(III), Nd(III), Er(III)] complexes. *Inorg. Chem.* **2005**, 44, (3), 529-537.

49. Caravan, P.; Parigi, G.; Chasse, J. M.; Cloutier, N. J.; Ellison, J. J.; Lauffer, R. B.; Luchinat, C.; McDermid, S. A.; Spiller, M.; McMurry, T. J., Albumin binding, relaxivity, and

water exchange kinetics of the diastereoisomers of MS-325, a Gadolinium(III)-based magnetic resonance angiography contrast agent. *Inorg. Chem.* **2007**, 46, (16), 6632-6639.

Chapter 4:
References

1. Horak, D.; Babic, M.; Jendelova, P.; Herynek, V.; Trchova, M.; Pientka, Z.; Pollert, E.; Hajek, M.; Sykova, E., D-Mannose-modified iron oxide nanoparticles for stem cell labeling. *Bioconjug. Chem.* **2007**, 18, (3), 635-644.

2. Zhang, Y.; So, M. K.; Rao, J., Protease-modulated cellular uptake of quantum dots. *Nano Lett.* **2006**, 6, (9), 1988-1992.

3. Tkachenko, A. G.; Xie, H.; Liu, Y.; Coleman, D.; Ryan, J.; Glomm, W. R.; Shipton, M. K.; Franzen, S.; Feldheim, D. L., Cellular trajectories of peptide-modified gold particle complexes: Comparison of nuclear localization signals and peptide transduction domains. *Bioconjug. Chem.* **2004**, 15, (3), 482-490.

4. Xu, X.-H. N.; Brownlow, W. J.; Kyriacou, S. V.; Wan, Q.; Viola, J. J., Real-time probing of membrane transport in living microbial cells using single nanoparticle optics and living cell imaging. *Biochemistry* **2004**, 43, (32), 10400-10413.

5. Bull, S. R.; Guler, M. O.; Bras, R. E.; Meade, T. J.; Stupp, S. I., Self-assembled peptide amphiphile nanofibers conjugated to MRI contrast agents. *Nano Lett.* **2005**, 5, (1), 1-4.

6. Winter, P. M.; Caruthers, S. D.; Wickline, S. A.; Lanza, G. M., Molecular imaging by MRI. *Curr. Cardiol. Rep.* **2006**, 8, (1), 65-9.

7. Maysinger, D., Nanoparticles and cells: Good companions and doomed partnerships. *Organic & Biomolecular Chemistry* **2007**, 5, (15), 2335-2342.

8. Winter, P. M.; Caruthers, S. D.; Yu, X.; Song, S.-K.; Chen, J.; Miller, B.; Bulte, J. W. M.; Robertson, J. D.; Gaffney, P. J.; Wickline, S. A.; Lanza, G. M., Improved molecular imaging contrast agent for detection of human thrombus. *Magn. Reson. Med.* **2003**, 50, (2), 411-416.

9. Dobson, J., Magnetic nanoparticles for drug delivery. *Drug Dev. Res.* **2006**, 67, (1), 55-60.

10. Lind, K.; Kresse, M.; Debus, N. P.; Muller, R. H., A novel formulation for superparamagnetic iron oxide (SPIO) particles enhancing MR lymphography: Comparison of physicochemical properties and the in vivo behaviour. *J. Drug Target.* **2002**, 10, (3), 221-230.

11. Nitin, N.; LaConte, L. E. W.; Zurkiya, O.; Hu, X.; Bao, G., Functionalization and peptide-based delivery of magnetic nanoparticles as an intracellular MRI contrast agent. *J. Biol. Inorg. Chem.* **2004**, 9, (6), 706-712.

12. Zhao, M.; Kircher, M. F.; Josephson, L.; Weissleder, R., Differential conjugation of TAT peptide to superparamagnetic nanoparticles and its effect on cellular uptake. *Bioconjug. Chem.* **2002**, 13, (4), 840-844.

13. Atanasijevic, T.; Shusteff, M.; Fam, P.; Jasanoff, A., Calcium-sensitive MRI contrast agents based on superparamagnetic iron oxide nanoparticles and calmodulin. *Proc. Natl. Acad. Sci. U. S. A.* **2006**, 103, (40), 14707-14712.

14. Hong, J.; Xu, D.; Yu, J.; Gong, P.; Ma, H.; Yao, S., Facile synthesis of polymer-enveloped ultrasmall superparamagnetic iron oxide for magnetic resonance imaging. *Nanotechnology* **2007**, 18, (13), 135608/1-135608/6.

15. Neuberger, T.; Schoepf, B.; Hofmann, H.; Hofmann, M.; Von Rechenberg, B., Superparamagnetic nanoparticles for biomedical applications: Possibilities and limitations of a new drug delivery system. *J. Magn. Magn. Mater.* **2005**, 293, (1), 483-496.

16. Na, H. B.; Lee, J. H.; An, K.; Park, Y. I.; Park, M.; Lee, I. S.; Nam, D.-H.; Kim, S. T.; Kim, S.-H.; Kim, S.-W.; Lim, K.-H.; Kim, K.-S.; Kim, S.-O.; Hyeon, T., Development of a T_1 contrast agent for magnetic resonance imaging using MnO nanoparticles. *Angew. Chem.* **2007**, 46, (28), 5397-5401.

17. Frullano, L.; Meade, T. J., Multimodal MRI contrast agents. *J. Biol. Inorg. Chem.* **2007**, 12, (7), 939-949.

18. Bulte, J. W. M.; Kraitchman, D. L., Iron oxide MR contrast agents for molecular and cellular imaging. *NMR Biomed.* **2004**, 17, (7), 484-499.

19. Voisin, P.; Ribot, E. J.; Miraux, S.; Bouzier-Sore, A.-K.; Lahitte, J.-F.; Bouchaud, V.; Mornet, S.; Thiaudiere, E.; Franconi, J.-M.; Raison, L.; Labrugere, C.; Delville, M.-H., Use of lanthanide-grafted inorganic nanoparticles as effective contrast agents for cellular uptake imaging. *Bioconjug. Chem.* **2007**, 18, (4), 1053-1063.

20. Guccione, S.; Li, K. C. P.; Bednarski, M. D., Vascular-targeted nanoparticles for molecular imaging and therapy. *Methods Enzymol.* **2004**, 386, (Imaging in Biological Research, Part B), 219-236.

21. Paunesku, T.; Rajh, T.; Wiederrecht, G.; Maser, J.; Vogt, S.; Stojicevic, N.; Protic, M.; Lai, B.; Oryhon, J.; Thurnauer, M.; Woloschak, G., Biology of TiO_2-oligonucleotide nanocomposites. *Nat. Mat.* **2003**, 2, (5), 343-346.

22. Paunesku, T.; Vogt, S.; Lai, B.; Maser, J.; Stojicevic, N.; Thurn, K. T.; Osipo, C.; Liu, H.; Legnini, D.; Wang, Z.; Lee, C.; Woloschak, G. E., Intracellular distribution of TiO_2-DNA oligonucleotide nanoconjugates directed to nucleolus and mitochondria indicates sequence specificity. *Nano Lett.* **2007**, 7, (3), 596-601.

23. Rajh, T.; Chen, L. X.; Lukas, K.; Liu, T.; Thurnauer, M. C.; Tiede, D. M., Surface restructuring of nanoparticles: An efficient route for ligand-metal oxide crosstalk. *J. Phys. Chem. B.* **2002**, 106, (41), 10543-10552.

24. Rajh, T.; Nedeljkovic, J. M.; Chen, L. X.; Poluektov, O.; Thurnauer, M. C., Improving optical and charge separation properties of nanocrystalline TiO_2 by surface modification with vitamin C. *J. Phys. Chem. B.* **1999**, 103, (18), 3515-3519.

25. Endres, P. J.; MacRenaris, K. W.; Vogt, S.; Allen, M. J.; Meade, T. J., Quantitative imaging of cell-permeable magnetic resonance contrast agents using X-ray fluorescence. *Mol. Img.* **2006**, 5, (4), 485-97.

26. Toth, E.; Helm, L.; Merbach, A. E., Relaxivity of MRI contrast agents. *Top. Curr. Chem.* **2002**, 221, (Contrast Agents I), 61-101.

27. Caravan, P.; Ellison, J. J.; McMurry, T. J.; Lauffer, R. B., Gadolinium(III) chelates as MRI contrast agents: Structure, dynamics, and applications. *Chem. Rev.* **1999**, 99, (9), 2293-2352.

28. Twining, B.; Baines, S.; Fisher, N.; Maser, J.; Vogt, S.; Jacobsen, C.; Tovar-Sanchez, A.; Sanudo-Wilhelmy, S., Quantifying trace elements in individual aquatic protist cells with a synchrotron X-Ray fluorescence microprobe. *Anal. Chem.* **2003**, 75, (15), 3806-3816.

29. Vogt, S., MAPS: A set of software tools for analysis and visualization of 3D X-ray fluorescence data sets. *J. Phys. IV* **2003**, 104, (X-Ray Microscopy), 635-638.

Chapter 5:
References

1. Jacques, V.; Desreux, J. F., New classes of MRI contrast agents. *Top. Curr. Chem.* **2002**, 221, (Contrast Agents I), 123-164.

2. Jacobs, R. E.; Ahrens, E. T.; Meade, T. J.; Fraser, S. E., Looking deeper into vertebrate development. *Trends Cell Biol.* **1999**, 9, (2), 73-6.

3. Aime, S.; Castelli, D. D.; Terreno, E., Novel pH-reporter MRI contrast agents. *Angew. Chem. Int. Edit.* **2002**, 41, (22), 4334-4336.

4. Aime, S.; Ascenzi, P.; Comoglio, E.; Fasano, M.; Paoletti, S., Molecular recognition of R- and T-states of human adult hemoglobin by a paramagnetic Gd(III) complex by means of the measurement of solvent water proton relaxation rate. *J. Am. Chem. Soc.* **1995**, 117, (36), 9365-6.

5. Caravan, P.; Parigi, G.; Chasse, J. M.; Cloutier, N. J.; Ellison, J. J.; Lauffer, R. B.; Luchinat, C.; McDermid, S. A.; Spiller, M.; McMurry, T. J., Albumin binding, relaxivity, and water exchange kinetics of the diastereoisomers of MS-325, a gadolinium(III)-based magnetic resonance angiography contrast agent. *Inorg. Chem.* **2007**, 46, (16), 6632-6639.

6. Chan, K. W.-Y.; Wong, W.-T., Small molecular gadolinium(III) complexes as MRI contrast agents for diagnostic imaging. *Coord. Chem. Rev.* **2007**, 251, (17-20), 2428-2451.

7. Duimstra, J. A.; Femia, F. J.; Meade, T. J., A gadolinium chelate for detection of β-glucuronidase: A self-immolative approach. *J. Am. Chem. Soc.* **2005**, 127, (37), 12847-12855.

8. Louie, A. Y.; Huber, M. M.; Ahrens, E. T.; Rothbacher, U.; Moats, R.; Jacobs, R. E.; Fraser, S. E.; Meade, T. J., In vivo visualization of gene expression using magnetic resonance imaging. *Nat. Biotechnol.* **2000**, 18, (3), 321-5.

9. Major, J. L.; Parigi, G.; Luchinat, C.; Meade, T. J., The synthesis and in vitro testing of a zinc-activated MRI contrast agent. *Proc. Natl. Acad. Sci. U. S. A.* **2007**, 104, (35), 13881-13886, S13881/1-S13881/9.

10. Nivorozhkin, A. L.; Kolodziej, A. F.; Caravan, P.; Greenfield, M. T.; Lauffer, R. B.; McMurry, T. J., Enzyme-activated Gd^{3+} magnetic resonance imaging contrast agents with a prominent receptor-induced magnetization enhancement. *Angew. Chem. Int. Edit.* **2001**, 40, (15), 2903-2906.

11. Sitharaman, B.; Wilson, L. J., Gadofullerenes and gadonanotubes: A new paradigm for high-performance magnetic resonance imaging contrast agent probes. *J. Biomed. Nanotechn.* **2007**, 3, (4), 342-352.

12. Merbach, A. E.; Toth, E.; Editors, *The Chemistry of Contrast Agents in Medical Magnetic Resonance Imaging*. 2001; p 471 pp.

13. Anelli, P. L.; Bertini, I.; Fragai, M.; Lattuada, L.; Luchinat, C.; Parigi, G., Sulfonamide-functionalized gadolinium DTPA complexes as possible contrast agents for MRI: A relaxometric investigation. *Eur. J. Inorg. Chem.* **2000**, (4), 625-630.

14. Caravan, P.; Ellison, J. J.; McMurry, T. J.; Lauffer, R. B., Gadolinium(III) chelates as MRI contrast agents: Structure, dynamics, and applications. *Chem. Rev.* **1999**, 99, (9), 2293-2352.

15. Shu, C.-Y.; Ma, X.-Y.; Zhang, J.-F.; Corwin, F. D.; Sim, J. H.; Zhang, E.-Y.; Dorn, H. C.; Gibson, H. W.; Fatouros, P. P.; Wang, C.-R.; Fang, X.-H., Conjugation of a water-soluble gadolinium endohedral fulleride with an antibody as a magnetic resonance imaging contrast agent. *Bioconjug. Chem.* **2008**, 19, (3), 651-655.

16. Karfeld, L. S.; Bull, S. R.; Davis, N. E.; Meade, T. J.; Barron, A. E., Use of a genetically engineered protein for the design of a multivalent MRI contrast agent. *Bioconjug. Chem.* **2007**, 18, (6), 1697-1700.

17. Endres, P. J.; Paunesku, T.; Vogt, S.; Meade, T. J.; Woloschak, G. E., DNA-TiO_2 nanoconjugates labeled with magnetic resonance contrast agents. *J. Am. Chem. Soc.* **2007**, 129, (51), 15760-15761.

18. Terreno, E.; Cabella, C.; Carrera, C.; Delli Castelli, D.; Mazzon, R.; Rollet, S.; Stancanello, J.; Visigalli, M.; Aime, S., From spherical to osmotically shrunken paramagnetic liposomes: An improved generation of LIPOCEST MRI agents with highly shifted water protons. *Angew. Chem. Int. Edit.* **2007**, 46, (6), 966-968.

19. Aime, S.; Castelli, D. D.; Lawson, D.; Terreno, E., Gd-loaded liposomes as T_1, susceptibility, and CEST agents, all in one. *J. Am. Chem. Soc.* **2007**, 129, (9), 2430-2431.

20. Sieving, P. F.; Watson, A. D.; Rocklage, S. M., Preparation and characterization of paramagnetic polychelates and their protein conjugates. *Bioconjug. Chem.* **1990**, 1, (1), 65-71.

21. Lynn, D. M.; Mohr, B.; Grubbs, R. H., Living ring-opening metathesis polymerization in water. *J. Am. Chem. Soc.* **1998**, 120, (7), 1627-1628.

22. Schwab, P.; France, M. B.; Ziller, J. W.; Grubbs, R. H., A series of well-defined metathesis catalysts - synthesis of $[RuCl_2(=CHR')(PR_3)_2]$ and their reactions. *Angew. Chem.* **1995**, 34, (18), 2039-41.

23. Kiessling, L. L.; Strong, L. E., Bioactive polymers. *Topics in Organometallic Chemistry* **1998**, 1, (Alkene Metathesis in Organic Synthesis), 199-231.

24. Bertin, P. A.; Watson, K. J.; Nguyen, S. T., Indomethacin-containing nanoparticles derived from amphiphilic polynorbornene: A model ROMP-based drug encapsulation system. *Macromolecules* **2004**, 37, (22), 8364-8372.

25. Allen, M. J.; Raines, R. T.; Kiessling, L. L., Contrast agents for magnetic resonance imaging synthesized with ring-opening metathesis polymerization. *J. Am. Chem. Soc.* **2006**, 128, (20), 6534-6535.

26. Glogard, C.; Stensrud, G.; Aime, S., Novel radical-responsive MRI contrast agent based on paramagnetic liposomes. *Magn. Reson. Chem.* **2003**, 41, (8), 585-588.

27. Bryden, C. C.; Reilley, C. N., Europium luminescence lifetimes and spectra for evaluation of 11 europium complexes as aqueous shift reagents for nuclear magnetic resonance spectrometry. *Anal. Chem.* **1982**, 54, (4), 610-15.

28. Powell, D. H.; Ni Dhubhghaill, O. M.; Pubanz, D.; Helm, L.; Lebedev, Y. S.; Schlaepfer, W.; Merbach, A. E., High-pressure NMR kinetics. Part 74. Structural and dynamic parameters obtained from ^{17}O NMR, EPR, and NMRD studies of monomeric and dimeric Gd^{3+} complexes of interest in magnetic resonance imaging: An integrated and theoretically self-consistent approach. *J. Am. Chem. Soc.* **1996**, 118, (39), 9333-9346.

29. Aime, S.; Botta, M.; Crich, S. G.; Giovenzana, G.; Pagliarin, R.; Sisti, M.; Terreno, E., NMR relaxometric studies of Gd(III) complexes with heptadentate macrocyclic ligands. *Magn. Reson. Chem.* **1998**, 36, (Spec. Issue), S200-S208.

30. Swift, T. J.; Connick, R. E., NMR (nuclear magnetic resonance)-relaxation mechanisms of ^{17}O in aqueous solutions of paramagnetic cations and the lifetime of water molecules in the first coordination sphere. *J. Chem. Phys.* **1962**, 37, 307-20.

31. Terreno, E.; Botta, M.; Boniforte, P.; Bracco, C.; Milone, L.; Mondino, B.; Uggeri, F.; Aime, S., A multinuclear NMR relaxometry study of ternary adducts formed between heptadentate GdIII chelates and L-lactate. *Chem-Eur. J.* **2005**, 11, (19), 5531-5537.

32. Jaszberenyi, Z.; Moriggi, L.; Schmidt, P.; Weidensteiner, C.; Kneuer, R.; Merbach, A. E.; Helm, L.; Toth, E., Physicochemical and MRI characterization of Gd^{3+}-loaded polyamidoamine and hyperbranched dendrimers. *J. Bio. Inorg. Chem.* **2007**, 12, (3), 406-420.

33. Beeby, A.; Clarkson, I. M.; Dickins, R. S.; Faulkner, S.; Parker, D.; Royle, L.; de Sousa, A. S.; Williams, J. A. G.; Woods, M., Non-radiative deactivation of the excited states of europium, terbium and ytterbium complexes by proximate energy-matched OH, NH and CH oscillators: An improved luminescence method for establishing solution hydration states. *J. Chem. Soc., Perkin Trans. 2* **1999**, (3), 493-504.

34. Urbanczyk-Pearson, L. M.; Femia, F. J.; Smith, J.; Parigi, G.; Duimstra, J. A.; Eckermann, A. L.; Luchinat, C.; Meade, T. J., Mechanistic investigation of β-galactosidase-activated MR contrast agents. *Inorg. Chem.* **2008**, 47, (1), 56-68.

35. Wolfe, P. S.; Wagener, K. B., Investigation of organoboronates in metathesis polymerization *Macromolecules* **1999**, 32, (24), 7961 -7967.

36. Smith, D., Recent work has shown that conjugating Indomethacin to bicyclo[2.2.1]hept-5-ene-2-*exo*-carboxylic acid via amidation affords a monomer with a drastically reduced rate of polymerization. In Northwestern University: 2008.

37. Chung, S. E.; Chung, I. J., Rotational diffusion coefficient of rodlike polymer with a slight flexibility in semidilute and concentrated solutions. *Polym. Bull.* **1989**, 21, (1), 105-12.

38. Congreve, A.; Parker, D.; Gianolio, E.; Botta, M., Steric control of lanthanide hydration state: Fast water exchange at gadolinium in a mono-amide 'DOTA' complex. *Dalton Trans.* **2004**, (9), 1441-1445.

39. Woods, M.; Kovacs, Z.; Zhang, S.; Sherry, A. D., Towards the rational design of magnetic resonance imaging contrast agents: Isolation of the two coordination isomers of lanthanide DOTA-type complexes. *Angew. Chem. Int. Edit.* **2003**, 42, (47), 5889-5892.

40. Allen, M. J.; MacRenaris, K. W.; Venkatasubramanian, P. N.; Meade, T. J., Cellular delivery of MRI contrast agents. *Chem. Biol.* **2004**, 11, (3), 301-307.

41. Endres, P. J.; MacRenaris, K. W.; Vogt, S.; Allen, M. J.; Meade, T. J., Quantitative imaging of cell-permeable magnetic resonance contrast agents using X-ray fluorescence. *Mol. Img.* **2006**, 5, (4), 485-97.

42. Quici, S.; Cavazzini, M.; Marzanni, G.; Accorsi, G.; Armaroli, N.; Ventura, B.; Barigelletti, F., Visible and near-infrared intense luminescence from water-soluble lanthanide [Tb(III), Eu(III), Sm(III), Dy(III), Pr(III), Ho(III), Yb(III), Nd(III), Er(III)] complexes. *Inorg. Chem.* **2005**, 44, (3), 529-537.

43. Stille, J. R.; Santarsiero, B. D.; Grubbs, R. H., Rearrangement of bicyclo[2.2.1]heptane ring systems by titanocene alkylidene complexes to bicyclo[3.2.0]heptane enol ethers. Total synthesis of (±)-$\Delta^{9(12)}$-capnellene. *J. Org. Chem.* **1990**, 55, (3), 843-62.

Appendix:

Molecular Imaging Journal Cover

Featured Article:

Endres, P. J.; MacRenaris, K. W.; Vogt, S.; Allen, M. J.; Meade, T. J., Quantitative Imaging of Cell-Permeable Magnetic Resonance Contrast Agents Using X-Ray Fluorescence. *Mol. Img.* **2006,** 5, (4), 485-497.

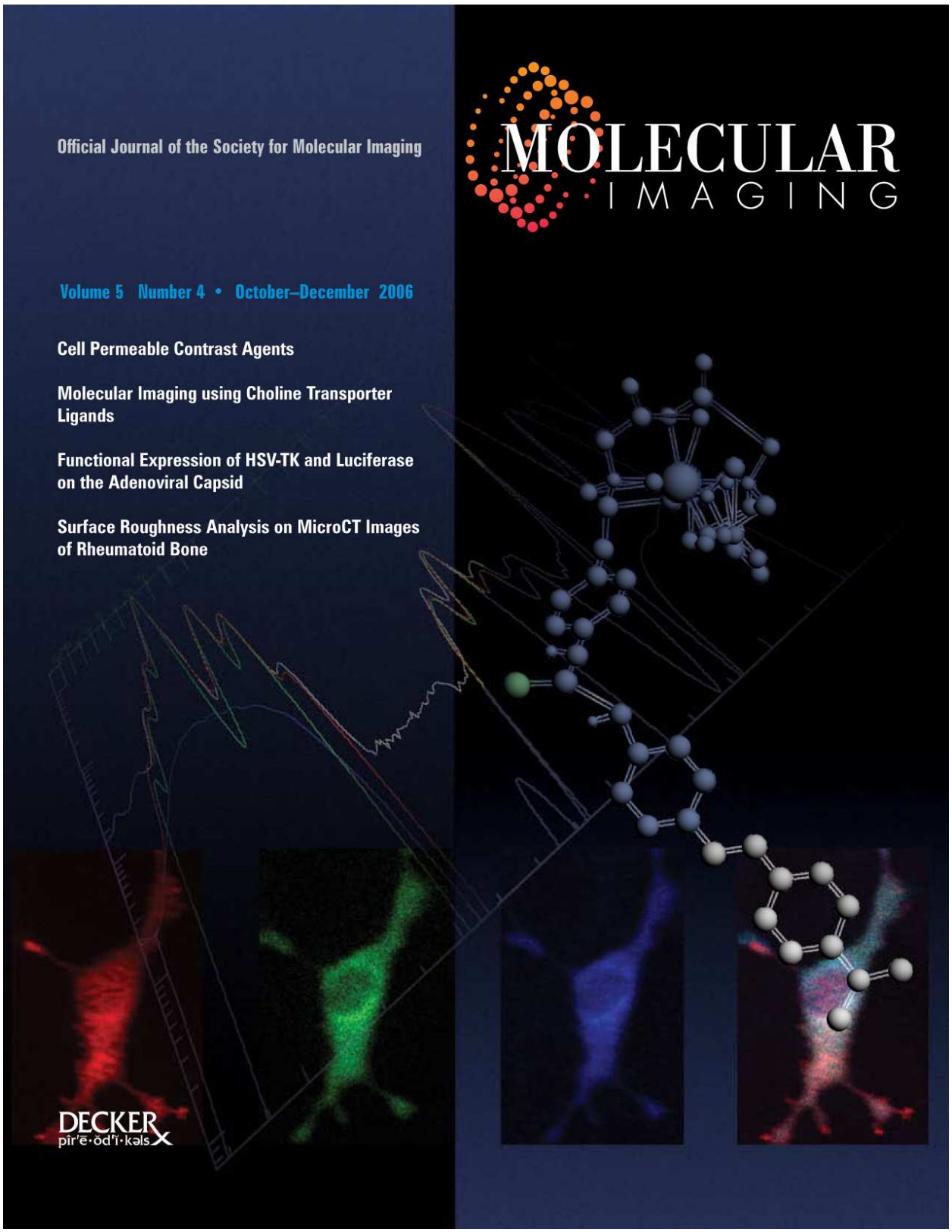
Official Journal of the Society for Molecular Imaging
MOLECULAR
IMAGING
Volume 5 Number 4 • October–December 2006
Cell Permeable Contrast Agents
Molecular Imaging using Choline Transporter Ligands
Functional Expression of HSV-TK and Luciferase on the Adenoviral Capsid
Surface Roughness Analysis on MicroCT Images of Rheumatoid Bone
DECKER
pîr'ē·ŏd'ĭ·kəls